Humboldt-Universität zu Berlin

DISSERTATION

Analytical Characterization of Porous Geomaterials
Reference Assessment in some Sedimentary Rocks

zur Erlangung des akademischen Grades doctor rerum naturalium (Dr. rer. nat.)
im Fach Chemie

angereicht an der Matematisch-Naturwissenschaftlichen Fakultät I

von

Rodolphe Robert

Präsident der Humboldt-Universität:
Prof. Dr. Jürgen Mlynek

Dekan der Mathemathisch-Naturwissenschlichen Fakultät I:
Prof. Thomas Buckhout, PhD

Gutachter:
1. Prof. Dr. sc. nat. Manfred Meisel (Vorsitzender)
2. Prof. Dr. Dr. h. c. Adolf Zschunke
3. Prof. Dr. Claude Dubois
4. Prof. Dr. Klaus Meyer
5. Prof. Dr. rer. nat. Jürgen Liebscher
6. Prof. Dr. rer. nat. Reinhard Stößer

Datum der mündlichen Prüfung: 17. September 2004

Zusammenfassung:

In der vorliegenden Arbeit wurden fünf typische Sedimentgesteine, zwei Sandsteine („Grès a Meules“, Fontainebleau), eine Kreide und zwei Kalksteine (Tuffeau, Vuillicin) im Hinblick auf ihre Porosität, Mineralbestand und Transporteigenschaften von Flüssigkeiten und Gasen untersucht. Porenvolumen, -größe, -verteilung und -form sowie die spezifische Oberfläche wurden mit Hilfe von Wasser- und Quecksilberporosimetrie, Gasadsorption sowie Bildanalyse bestimmt. Durch den komplexen Einsatz der oben genannten Untersuchungsmethoden mit ihren unterschiedlichen Nachweisgrenzen im Mikro-, Meso- und Makrobereich konnte ein umfassendes Bild über die Porengröße und -verteilung sowie über die Homogenität der Sedimente gewonnen werden. Außerdem wurden Computertomographie, Röntgen-Refraktometrie, Licht- und Elektronmikroskopie angewendet und Permeabilitätsmessungen sowie Messungen der Wasseraufnahme mittels der Kapillaraufstiegsmethode an Bohrkernen durchgeführt. Die Untersuchung der Porenstruktur und der Transporteigenschaften wurde mit Mineralanalysen gekoppelt, die mit Hilfe von Röntgendiffraktometrie, Elektronmikroskopie und der Herstellung von Dünnschliffen durchgeführt wurden. Die experimentellen Ergebnisse wurden mit Hilfe von bestehenden Porenmodelle (Zylinder- und Kugelporenmodell, Kozeny-Carman- und Marshall-Modell, PORE-COR-Modell) interpretiert.

Das Ziel der Arbeit bestand zuerst in der Aufklärung von Zusammenhängen zwischen Porenstruktur, Mineralzusammensetzung und Transporteigenschaften. Mehrere Zusammenhänge zwischen Mineralart und Porenstruktur konnten nachgewiesen werden. Insbesondere wurde der Einfluss von Tonmineralien auf die Porenstruktur, die Permeabilität und die kapillare Wasseraufnahme nachgewiesen. Der Einfluss der Porenstrukturparameter auf die Wasser- und Gastransporteigenschaften wurde am Beispiel ausgewählter Sedimentgesteine ebenfalls nachgewiesen. Auf der Basis der experimentellen Ergebnisse wurden für die einzelnen Sedimentgesteine typische Porenmodelle entwickelt, die den Zusammenhang zwischen Porenstruktur im weitesten Sinne und den Transporteigenschaften bezüglich Wasser und Gasen wiedergeben. Ein wichtiger Aspekt der Arbeit war die Fragestellung, ob ausgewählte Sedimentgesteine als Referenz- bzw. Standardmaterialien für die Bewertung von Messverfahren oder von anderen Geomaterialien dienen können. Dazu wurden umfassende Homogenitätsuntersuchungen durchgeführt. Es zeigte sich, dass eine Gesteinsart (Vuillecin-Kalkstein) unabhängig von der Probengröße inhomogen war und daher in keinem Falle als Geo-Standard in Betracht kommen kann. Bei den anderen hier untersuchten Sedimentgesteinen wurde gefunden, dass sie für Messverfahren, die ein relativ großes Probenvolumen (> 15 cm^3) benötigen (z. B. die Wasserporosimetrie oder die Kapillaraufstiegsmethode an Bohrkernen) als hinreichend homogen bezüglich des Einsatzes als mögliche Geo-Referenzmaterialien einzustufen sind. Damit könnten sie u. a. zur Entwicklung oder Überprüfung z. B. von Modellen für Transporteigenschaften von Geomaterialien oder als Untersuchungsmaterial für Ringversuche verwendet werden. Im Falle von Messverfahren, die ein kleineres Probenvolumen (weniger als 2 oder 3 cm^3) voraussetzen, beispielsweise die Gasadsorption oder die Quecksilberporosimetrie, war die gefundene Homogenität aller fünf hier untersuchten Sedimentgesteine nicht mehr ausreichend, um als Kandidatenmaterial für eine Referenzmaterial-Zertifizierung zu dienen. Dies spiegelte sich deutlich in den wesentlich größeren Streuungen der Messresultate gegenüber „synthetischen“ zertifizierten Referenzmaterialien für die Gas-adsorption und die Hg-Porosimetrie wieder. Damit entfällt auch ein möglicher Einsatz für die Kalibrierung von Messapparaturen oder für Methodenvalidierungen.

Sedimentgestein
Referenzmaterial
Porenstruktur
Homogenität
Transporteigenschaft

Abstract:

In this study, five typical sedimentary rocks, two sandstones (Fontainebleau, "Grès à Meules"), a chalk and two limestones (tuffeau, Vuillecin) were analyzed with regards to their porous structure, mineral structure and fluid transport properties. Structure parameters such as porous volume, size and distribution of the pores and the pore accesses, and specific surface area were measured using water porosimetry, mercury porosimetry, gas adsorption, x-ray refraction, as well as image analyses. Other techniques, namely X-ray computed tomography, optical and electron microscopy permitted us to visualize the porous and/or mineral structure of the rocks. Gas permeability measurements and capillary water imbibition analyses were also realized. Moreover, SEM, X-ray diffraction and analyses of thin sections made it possible to obtain additional information about the mineral structure of the rocks. The application of existing pore models (cylindrical and spherical pore models, Kozeny-Carman's and Marshall's models, PORE-COR model) has helped us to interpret the experimental results.

The aim of these investigations was first to link the characteristics of the porous structure and the mineral structure with each over and together with the fluid transport properties. Relationships of the mineral contents to the porous structure and the fluid transport properties of the rocks were established. In particular, the role of clay mineral concentrations was exposed. The porous structure parameters, on which the fluid transport properties significantly depend, were identified regarding the degree of their influence. On the basis of these experimental results, sketches that show the main characteristics of the rocks were elaborated. Furthermore, specific ideal pore models were schematized. These models describe the fluid transport behavior of the rocks either for gas flow or water imbibition.

The second main goal for this characterization's work was to express if or not these geomaterials could become useful reference materials. It was shown that the degrees of homogeneity of the rocks were low in comparison with any existing certified reference materials, which are industrially synthesized. For this major reason, the possibilities of the elaboration of useful reference values using the rocks were found to be restraint. It was evident that one of the rocks (Vuillecin limestone) had a too low homogeneity degree to be reasonably used in any way as reference material. The variations of many structure parameters of the other rocks were low for big samples (over 15 cm^3). In this first case, certified reference values could be elaborated using methods such as the water porosimetry or the capillary water imbibition kinetics. Such reference values would be useful in the field of geomaterial research for qualitative inter-comparisons and for the control or the development of pore models applied to the analysis of fluid transport properties. For small sample volumes (generally below 2 or 3 cm^3) measured using techniques such as mercury porosimetry or gas adsorption, the accuracy of the structure parameters was low in comparison with actual synthetic reference materials. In this second case, the rocks were found to be not suitable for the elaboration of reference values with the aim of applications such as the calibration of instruments, the efficiency test of apparatus, the validation of methods.

Sedimentary Rock
Reference Material
Porous Structure
Homogeneity
Transport Properties

Résumé :

Cette investigation a consisté à étudier cinq faciès typiques de roches sédimentaires – Grès de Fontainebleau, « Grès à meules », craie, tuffeau, Calcaire de Vuillecin – à partir d'analyses de leur structure poreuse et minérale et de mesures de leurs propriétés de transport de fluides.

Les caractéristiques du réseau poreux (porosité, densité minérale, volume poreux, taille de pores et d'accès aux pores, surface spécifique) ont été mesurées à l'aide de méthodes telles que la porosimétrie à l'eau ou au mercure, l'adsorption de gaz ou encore l'analyse d'images. D'autres techniques (lames minces colorées, tomographie RX, MEB, réfraction RX) ont permis une visualisation de la structure poreuse des roches. Des mesures de perméabilité et des propriétés d'imbibition capillaire ont été également réalisées. La caractérisation de la structure poreuse et la détermination des propriétés de transport de fluides de ces roches ont été couplées à des analyses pétrographiques et minéralogiques (lames minces, MEB, DRX). L'application de modèles de pores (modèle de pores cylindriques ou sphériques, modèles de Kozeny-Carman et de Marshall, modèle PORE-COR) a aidé à l'interprétation des résultats expérimentaux.

L'intérêt premier a été de relier les nombreuses données acquises (valeurs et variations des paramètres de structure, images, données pétrographiques, etc.) afin d'établir les relations existant entre les caractéristiques du réseau poreux de ces roches sédimentaires et leurs propriétés physiques. Il a été montré comment la taille et l'arrangement des grains déterminent la structure des pores et leur distribution. La présence et l'abondance relative d'espèces minérales particulières, notamment de minéraux argileux, jouent également un rôle important dans l'architecture du réseau poreux et dans la détermination propriétés de transport de fluides. Les autres paramètres de structure qui influencent significativement les propriétés de transport de fluides ont été identifiés et répertoriés suivant leur degré d'importance. La synthèse de ces résultats a mené, d'une part, à la réalisation d'esquisses décrivant de manière simple les caractéristiques pétrographiques et physiques des roches. D'autre part, des schémas de modèles de structures idéales de pores ont pu être élaborés. Ceux-ci permettent de décrire le cheminement des fluides à travers la roche et le rôle des différentes structures de porosité dans les processus de transfert capillaire et/ou d'écoulement en milieu saturé.

Un second aspect majeur de ce travail a été d'estimer les possibilités d'établissement de valeurs de référence chez ce type de géomatériaux. Il a été démontré que le degré d'homogénéité de la structure poreuse des roches était bien plus faible que celui de matériaux de référence de synthèse actuels. Le calcaire de Vuillecin, présente un degré d'homogénéité de structure trop faible pour pouvoir envisager une quelconque « standardisation ». Les variations des paramètres analysés pour les quatre autres roches sont généralement faibles pour des volumes analysés importants (à partir d'environ 15 cm^3). Ceci pourrait permettre d'établir des références pour des méthodes telles que porosimétrie à l'eau, cinétique d'imbibition capillaire et pour des applications comme le contrôle ou le développement de modèles de structures de pores décrivant les propriétés de transport de fluides dans les géomatériaux. Dans le cas de petits volumes analysés, généralement inférieurs à environ 2 ou 3 cm^3, généralement testés par les techniques telles que la porosimétrie au mercure ou l'adsorption de gaz, la précision des valeurs de paramètres de structure est beaucoup faible que celle des matériaux synthétiques de référence. Il a été conclu que, dans ce cas, les roches sédimentaires ne permettent pas l'élaboration de valeurs de référence pour des applications telles que le calibrage d'appareils de mesures, les tests de performance d'instruments ou encore la validation de méthodes de mesures.

Contents

Introduction

Reference samples and reference materials are very useful in analytical measurements either for the accuracy and the qualitative analysis of results or for the development of analytical measurement techniques. The necessity to compare analytical chemistry results between laboratories and between countries was felt in 1906, when the US National Bureau of Standards (NBS) initiated a program to provide reference materials, originally as standard samples (ZSCHUNKE A. (Ed.), 2000). Since then, the use of reference materials has extended in many countries, and nowadays their need is still urgent. To attempt to fulfill this large international demand, institutions use certification procedures to provide Certified Reference Materials (CRMs), which are all synthetically manufactured. Unfortunately, “Certified Reference Geomaterials (Geo-CRMs)” do not exist and yet natural materials are actually of great interest. This interest concerns a large range of scientific fields.

The natural alteration of rocks modifies their structure and properties. Consequences are visible on the monuments’ stones, on which climatic constraints engender significant damages. The research of new reserves of energy (geothermics, nuclear fuel, oil and gas) requires the study of geological sites. For instance, the deep storage of nuclear wastes needs a good knowledge of the candidate rocks; the extraction of petroleum requires information about the properties of the considered rocks (mainly porosity, permeability). These main topics are the current motives for the qualitative and quantitative analysis of the mineral and porous structure and of the properties of geomaterials (especially sedimentary rocks) throughout analytical measurements. Moreover, the understanding of the porous structure and of the transport mechanisms, for which analysis is possible in laboratories, also means the development and application of adapted theoretical models, which describe the main physical processes.

Due to the actual interest of natural rocks and to the great international demand of references, the view of “reference geomaterials” was the reason for this study. The goal was to characterize the structure of some selected sedimentary rocks (two sandstones, two limestones and a chalk) and to link the determined characteristics with each other.

A given degree of homogeneity is the main condition for a material to eventually become a reference material. Thus, it was important to assess the porous structure homogeneity of the sedimentary rocks throughout their characterization in order to achieve a classification of them according to their homogeneity degree. Afterwards, the results of this characterization were used to determine the possibility of the establishment of “reference geomaterials” and to eventually express the possible applications. That means providing answers to questions such as:

1. Which techniques, parameters and properties could be concerned in an eventual certification?
2. In which limits could one of the sedimentary rocks be referenced?
3. Which interesting applications could be possible from the eventual establishment of “reference samples” using the sedimentary rocks?

This study was centered on the determination of values and variations of the porous structure parameters of the rocks. Moreover, fluid transport properties were studied. These analyzed properties were the capillary water imbibition properties and the gas permeability. The assessment of the porous structure homogeneity needed the determination of its limits and the identification of causes of heterogeneities. This was done analyzing first the measured variations (standard deviations, distributions…) in the porous structure characteristics and in the properties. Secondly, the Representative Elemental Volume (REV, smallest homogeneous sample volume) had to be identified by analyzing the porous structure of the rocks at different scales (50-cm-cubic-block, core of several cubic centimeters, small samples of one or of less than one cubic centimeter).

The characterization of the rocks also necessitated the analysis of their mineral structure, which may certainly have an influence on the porous structure and the properties of the rocks. Therefore, another aim of the study was also to determine this influence.

The rocks were compared in order to understand the differences that could be eventually pointed out concerning their characteristics (porous, as well as mineral) and their properties.

Comparisons between the measurement techniques were necessary for the control of the results and for the estimation of the repeatability and the accuracy of the results. Combinations and correlations between the methods were also helpful in understanding the variations in the porous structure characteristics and in the properties of the rocks.

The porous structure characterization of the rocks and the analysis of their fluid transport properties required the application of porous structure models. With this application, it was possible to summarize the results of the characterization in a general view (establishment of diagrams and sketches, which could describe the characteristics and properties of the sedimentary rocks or which could help to predict their properties considering their characteristics).

Definitions of terms in connection with the Reference Materials (RM), the sedimentary rocks and the porosity of rocks were given in the first chapter. A small explanation was made concerning the problems that could occur while analyzing the substance “rock”. In the same chapter, the sedimentary rocks that have been selected for this study were presented (geographic and stratigraphic location). A preliminary qualitative and semi-quantitative petrographical analysis of the porous and mineral structure of the rocks was carried out using microscopy techniques (optical and electron microscopy).

In the second chapter, analytical measurement techniques (water and mercury porosimetry, gas adsorption, image analysis, X-ray tomography and X-ray refraction) were used to determine values and standard deviations of the porous structure parameters of the rocks, namely:

- the porosity,
- the bulk and mineral density,
- the specific pore volume,
- the mean pore access size,
- the specific surface area.

The results were exposed and discussed per measurement methods, and the theory of each technique was described before its application to the five rocks.

The fluid transport properties of the rocks were investigated in the third chapter with the help of the results of the porous structure characteristics’ measurements. Existing porous structure models and expressions that could correlate the properties of each rock were applied (Kozeny-Carman’s and Marshall’s models, Pore-Cor simulation…).

The results of the characterization of the sedimentary rocks were summarized in a last chapter. In the latter, conclusions were given concerning i) the homogeneity degree of the sedimentary rocks, ii) the relations between the mineral structure of a rock and its porous structure and properties, iii) the problem of the establishment's possibility and utility of "reference geomaterials". This chapter ends by discussing the perspectives following these conclusions.

1. Material presentation and petrographical analysis

1.1. Introduction to the study of the porous structure of sedimentary rocks

1.1.1. Definition and role of the reference materials

The fundamental terms used in connection with reference materials are defined in ISO Guide 30 (1992):

- Reference Material (RM): material or substance one or more of whose property values are sufficiently homogeneous and well established to be used for the calibration of an apparatus, the assessment of a measurement method, or for assigning values to materials.
- Certified Reference Material (CRM): reference material, accompanied by a certificate[1], one or more of whose property values are certified by a procedure which establishes its traceability[2] to an accurate realization of the unit in which the property values are expressed, and for which each certified values is accompanied by an uncertainty statement at stated level of confidence.

The reference materials are usually used for the calibration of measuring systems, the assessment of analytical procedures, the performance test of instruments, the definition of measurement scales, and also for inter-laboratory comparisons and for qualitative and quantitative analyses of materials (ZSCHUNKE A.(Ed.), 2000). Then, to correctly fulfill these topics, the main condition for a candidate material to become a RM or a CRM is an accurate degree of homogeneity of its structure or/and properties.

1.1.2. Sedimentary rocks: Generalities, definitions and diagenetic processes

More than 50% of the earth surface is covered by a blanket of sediment, which makes up about 6% of the total earth's crust. Sedimentary rocks are the results of weathering and sedimentation processes: igneous, metamorphic and also previously deposited sediment rocks are broken down physically and chemically, and the residual material is transported as debris and in solution and accumulates at the locus of deposition and/or precipitation (SCHÖN J.H., 1996).

Therefore, it can be distinguished, after occurrence and origin, two main types of sedimentary rocks: the clastic or fragmental sedimentary rocks (e.g. sandstones, shales), and the chemical and biochemical sedimentary rocks (e.g. carbonates, evaporates).

Because quartz is one of the most resistant minerals in the crust it becomes enriched in sedimentary rocks, whereas minerals like feldspars, amphiboles or mica are in general less abundant. The last type of minerals is mainly very fine-grained phyllosilicates with grain diameters of less than 0.02 mm (clay mineral group).

---

[1] The certificate of a reference material and possibly an additional report reveal important information on quality aspects (ZSCHUNKE A. (Ed.), 2000):

- property values and their uncertainty ranges;
- traceability information (in conformity with ISO (TAG4) WG 3; 1992);
- measurement techniques, the use of primary methods and the procedure for data evaluation;
- instruction for the correct use of the reference material;
- stability, transportation and storage instructions;
- state of homogeneity (minimum sample size);
- declaration of conformity with standards and guides (e.g. ISO Guides 30-35).

[2] The traceability is defined as the property of the result of a measurement or the value of a standard whereby it can be related to stated references, usually national or internal standards, through an unbroken chain of comparisons all having stated uncertainties.

The structure (mineral skeleton and voids) of a sedimentary rock is the result of its own petrofabric (SCHÖN J.H., 1996; GROLIER J. et al., 1990). Many factors acting on the sedimentation influenced the primary framework and porosity of a rock (Fig. 1):

- The “grain sorting”[1] is a factor linked to the transport of the sedimentary particles. The particles acquire a specific form (generally a round form) during their carrying and they are more or less far displaced according to their primary size and weight, leading to a natural sorting in grain size.
- Environmental conditions during the sediment deposit (sea level, detrital input…) also influence the primary structure of a rock, mainly leading to different more-or-less thick layers in a massif.
- The deposition of various mineral contents also occurred during the sedimentation.
- The grain size and shape of the particles that accumulates are also of any importance in the primary structure of a rock.

During the history of the rock, many factors contribute to modifications of the primary porosity:

- Dissolution/precipitation due to fluid-mineral interaction induces changes in the size and shape of the primary voids (pores and throats).
- The burial genesis is linked to pressure, which mainly induces grain compaction and porosity reduction.

The study of the microstructure of sedimentary rocks relates to several scientific fields, such as geosciences (mineralogy, petrography, petrology) and physical measurements. Due to the origin of the rocks, the study of their porous structures involves specific samplings and appropriate methodologies.

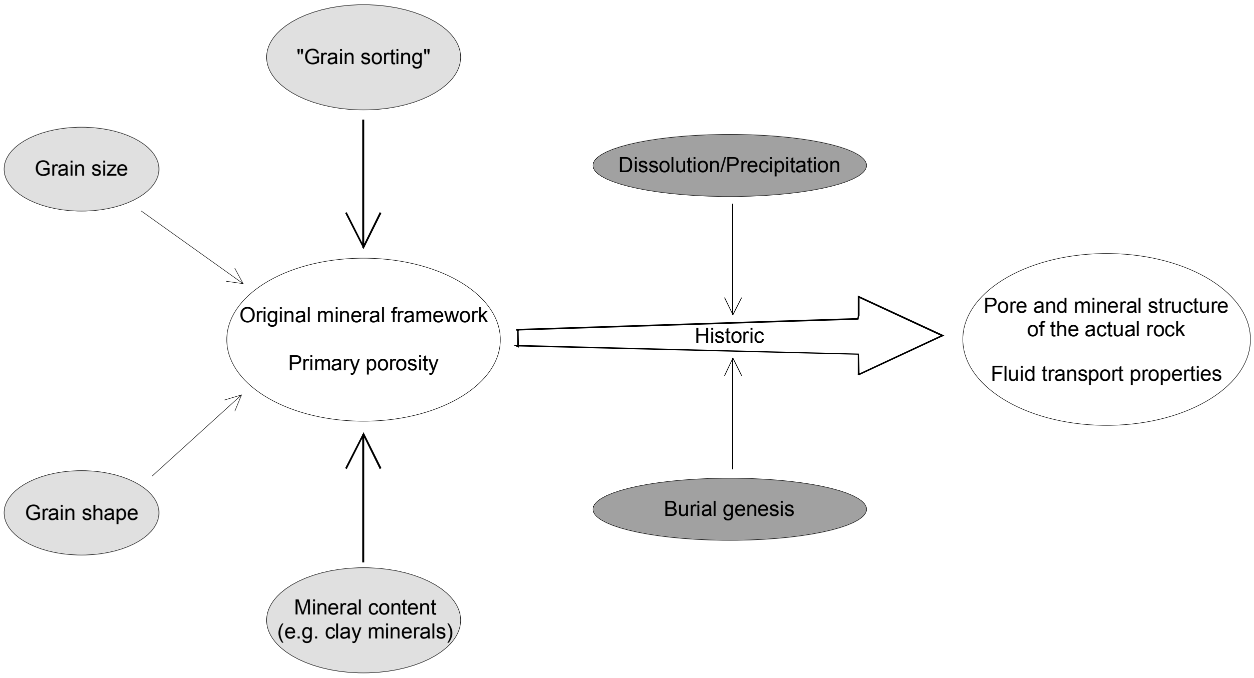

Fig. 1 – Factors that influence the porous structure of a rock during its diagenesis.

---

[1] Sorting (So, track sorting coefficient): the coefficient of sorting is defined as So = $(d_{25}/d_{75})^{1/2}$, where d25 is the grain size (mm) of 25 quartile and d_{75} is the grain size of 75 quartile; a clastic sediment can be called *very-well sorted* when the coefficient So is <1.4, *well sorted* with 1.4 to 1.87, and *poorly sorted* > 1.87 (SCHÖN J.H., 1996)

1.1.3. Sampling

The heterogeneity of the substance “rock” encompasses the general problem of different scales when using various techniques to characterize the porous structure. Two important points must be considered to avoid the well known problems of scaling and “representative volume”.

1.1.3.1. Sampling into a layer

The deposition of particles during sedimentation leads to the arrangement of the sediments in layers in relation to different geological environments, and layer heterogeneity occurs in a massif whatever sedimentary rock. This study was restrained to one 50x50x50-cm^3-block of each rock sampled in only one specific layer of the working face of the site quarry of the rock.

1.1.3.2. Iterative sampling

This study involved the use of several different measurement methods (mercury porosimetry, gas adsorption, water porosimetry …), requiring appropriate sizing of the experimental samples. In the aim of characterizing a rock, fundamental problems of measurement methods and “representative volume” make it necessary to increase the number of measurements until stable averages and minimal standard deviations are reached. Therefore, sets of laboratory sample cores were randomly drilled in each block at optimal dimensions, which were determined through preliminary measurements using a few samples of different sizes.

1.1.4. Sedimentary rocks and analysis methods used for this study

Five sedimentary rocks, two sandstones (Fontainebleau and “Grès à meules” sandstones), a chalk (Mons chalk), and two limestones (tuffeau and Vuillecin limestones), were chosen for this study. The Fontainebleau sandstone is a rock known to be homogeneous. This sandstone has been already used for many studies. The “Grès à meules” sandstone, the Mons chalk and the tuffeau limestone have been less studied, but some characteristics of these rocks have been already determined in analyses, which have been made separately, using a few methods. The Vuillecin limestone has been rarely studied and its structure and properties were poorly known at the time of this study.

Firstly, each selected material was described in terms of mineralogy, petrography, and porous structure characteristics (in this chapter). That required the following qualitative and/or semi-quantitative methods:

- mineralogical analysis by X-Ray Diffraction (XRD),
- optical microscopy on thin sections of a rock impregnated with a colored resin,
- Scanning Electron Microscopy (SEM).

Secondly, the porous structure of the material was quantitatively characterized throughout analytical measurements using (Chapter 2):

- water porosimetry,
- mercury porosimetry,
- gas adsorption,
- analysis of Back-Scattered Electron (BSE) images,
- X-ray Computed Tomography (CT),
- X-ray absorption/refraction characterization.

Then, fluid transport properties were analyzed by (Chapter 3):

- capillary water imbibition kinetics,
- gas permeability measurement.

Comparisons and correlations between the methods helped to characterize the porous structure of the rocks. They were governed by the application field of each method (Fig. 2). Because of its large range of applications, mercury porosimetry was frequently used for comparison and correlation.

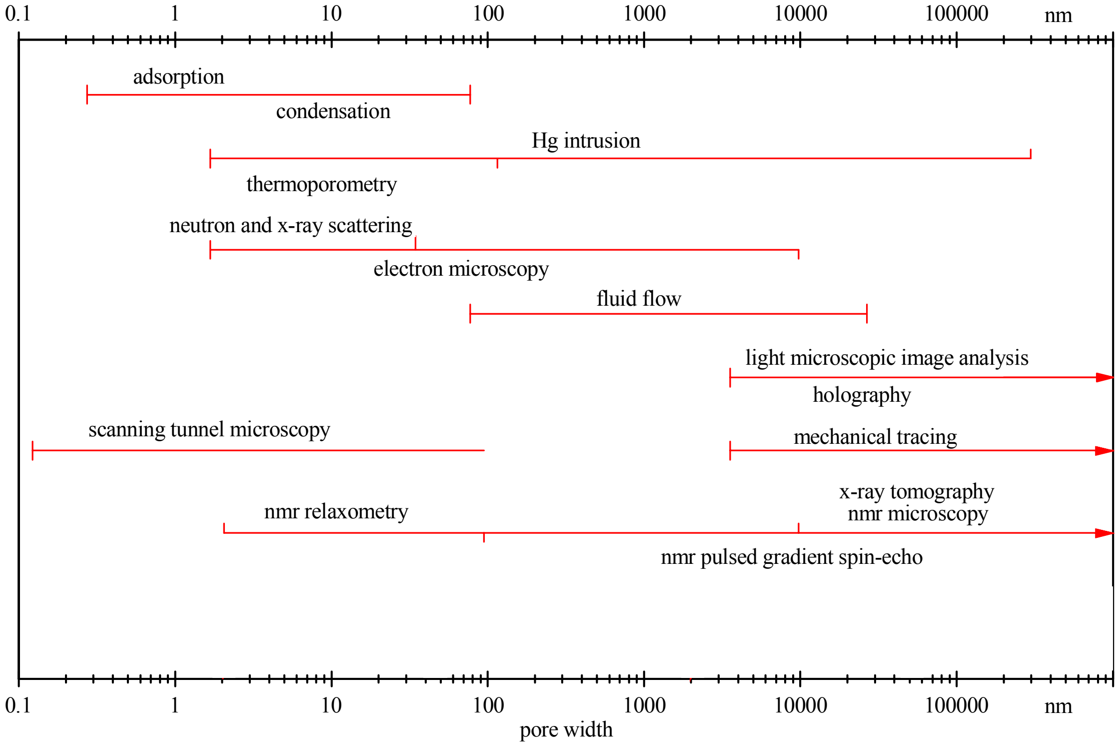

Fig. 2 – Measuring ranges of important characterizing methods for measuring pore widths (MEYER et al., 1994).

1.1.5. Porosity terminology

1.1.5.1. Pore classification

The pore classification recommended by IUPAC (Fig. 3) was not found to be adapted to this study, especially for the first part, which was based on a qualitative description of the materials porous structure by optical microscopy. Thus, we adopted a simplified classification proposed by geologists. It is linked to optical microscopy and its resolution, as well as to the observations of thin sections of rocks impregnated with a colored resin. This classification defines:

- macropores: pores individually distinguished under the optical microscope,
- micropores: pores not individually distinguished (they generally constitute discernable microporous areas).

Many authors have chosen different limits between the two classes: for example, CHOQUETTE P.W. & PRAY L.C. (1970) proposed a pore diameter limit of 0.25 mm while PITTMAN E.D. (1972) suggested a lower limit of 10 µm. For simplicity, we chose 15 µm as the pore diameter limit between the macropores and the micropores (Fig. 3), i.e. between macroporosity and microporosity. This value corresponds to the pore diameter accessible by mercury porosimetry under atmospheric pressure (0.1 MPa).

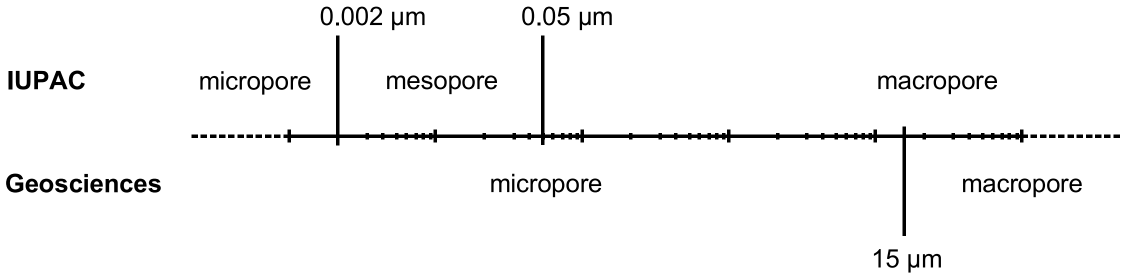

Fig. 3 – Pore classification proposed by IUPAC; pore classification commonly used in the geosciences (petroleum sciences) and adopted for this study.

1.1.5.2. Porosity terms

Porosity

This word stands for either the porous system, globally its morphology and its structure, or the ratio of the volume of porous spaces (V_P) to the total, or bulk volume (V_B) of the rock sample:

$$\text{POROSITY} = \frac{V_P}{V_B} \quad (1)$$

The porosity is usually expressed as a percentage (%).

Open (N_O) and closed (N_C) porosity

The porosity related to the continual porous network connected to the outside of the analyzed sample, represents the open porosity (Fig. 4). It is also called the connecting porosity. The porosity related to strictly closed pores, not connected to the outside, is called the closed or storage porosity.

Total porosity (N)

The total porosity is the sum of the open porosity and the closed porosity:

$$N = N_O + N_C \quad (2)$$

Fluid invading techniques (mercury porosimetry, gas adsorption, water porosimetry) only investigate the open porosity. Fortunately, the closed porosity, currently associated to singular fluid inclusions, **is negligible in most of the sedimentary rocks** (BOURBIÉ T. et al., 1986; SCHÖN J.H., 1996). During this study, **the porosity measurements were assumed to give information about the total porosity N of the rocks**, keeping in mind the limits of each applied method.

Free (N_F) and trapped (N_{TR}) porosity

Porosity that is freely accessible to a fluid under atmospheric pressure is called free porosity (N_F). The other part of the porosity (not freely accessible by a fluid) represents the trapped porosity:

$$N = N_{TR} + N_F \quad (3)$$

The interpretation of these types of porosity needs trapping theories about the phenomenon that occurs during the application of the fluid invasion method.

1.2. Material origin and petrography

1.2.1. Geographic origin and stratigraphic position of the materials

All the materials that were used in this study are Mesozoic or Cenozoic sedimentary rocks (Fig. 5): the Fontainebleau and the "Grès à Meules" sandstones are silicoclastic rocks; the Mons chalk and the Vuillecin limestone are calcareous rocks; and the Marigny-Brizay Tuffeau limestone is a silico-calcareous rock.

Fontainebleau sandstone

The Fontainebleau sandstone formation corresponds to eolian sands that were deposited during the Middle Oligocene in the Paris Basin (RASPLUS, 1987). They form a set of paleodunes around the town of Fontainebleau and over a narrow band south of the Seine river (Appendix A, Fig. A). The Fontainebleau sandstone formation, whose entire thickness ranges between 40 and 70 m, presents more or less ferruginous layers at its bottoms while at the top the sandstones become leached and white. They are composed of more than 99 % quartz grains that were sometimes deeply cemented by quartz overgrowths due to water migration (THIRY and BERTRAND-AYRAULT, 1988). This extensive silicification has induced the development of discontinuous and mineralogical homogeneous sandstone bodies within the sand masses. The sandstone studied in this thesis comes from a quarry near Milly-la-Forêt (Essonne, France).

"Grès à Meules" sandstone

The Triassic sandstones belong to the Buntsandstein outcrop in the northern end of the Vosges massif (Appendix A, Fig. B). About 500 m thick, they consist in coarse grain sandstones with low clay content. These coarse grain sandstones are inter-layered with conglomerates in their lower and their middle parts. The cohesion of these sandstones is made up of quartz overgrowths. Above these stratigraphic layers are the "Grès à Meules" sandstone, which belongs to the Voltzia Sandstone formation and the upper-Buntsandstein (PERRIAUX J., 1961; GALL J.-C. et al., 1977). Despite its thinness (10 to 15 m), the low dip angle of the westward layers leads to very wide outcrop zones in Northern Alsace where the main part of the sandstone quarries are found; the sandstones tested in this study comes from the Druligen area (Bas-Rhin, France).

Mons chalk

The Mons Basin (Belgium) is an extension of the Paris Basin toward the Southeast (Appendix A, Fig. C). This small sedimentary basin (15 by 30 km) situated between the Ardennes and the Brabant massifs corresponds to a syncline in which cretaceous end tertiary deposits lie in non-conformity on the relicts of the northern Hercynian range (VANDYCKE S. et al., 1991). The chalk studied comes from the northern border of the quarry of Hainault-Sambre, which belongs to the CBR (Belgium Cement Company) and is situated in the Southeast of Mons in the Harmignies area. This Campanian chalk is part of the Obourg chalk formation, which is represented in the quarry by about 15 m of white chalk (ROBASZINSKY F. & CHRISTENSEN W.K., 1989).

Tuffeau limestone

Impure Turonian chalky (base of Lower Cretaceous) limestones, usually called "tuffeau", outcrop in the Loire river valley and the southwestern part of Paris Basin (Appendix A, Fig. A). They correspond to an accumulation of bioclasts and rock fragments brought to the sea by the rivers, and which were cemented to each other during the diagenesis. The kind of limestone used in this study comes from the C3b formation of the ROCAMAT quarry near Marigny-Brizay (Vienne, West of France).

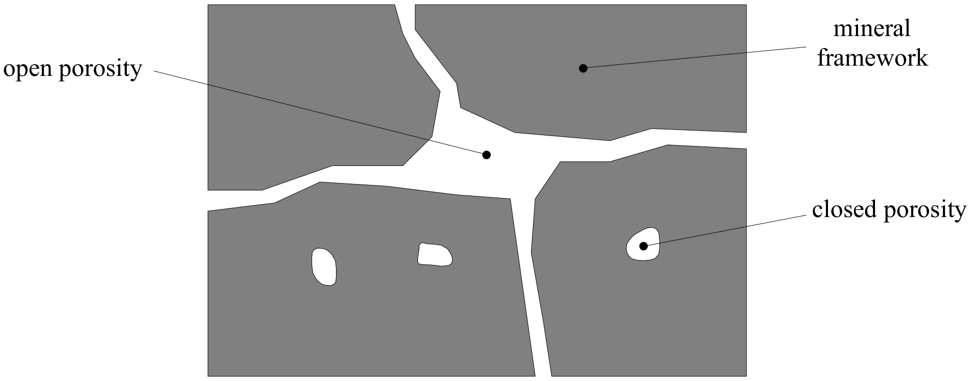

Fig. 4 – Open and closed porosity in a 2-D represented material (COSTER L. & CHERMANT J.L., 1989).

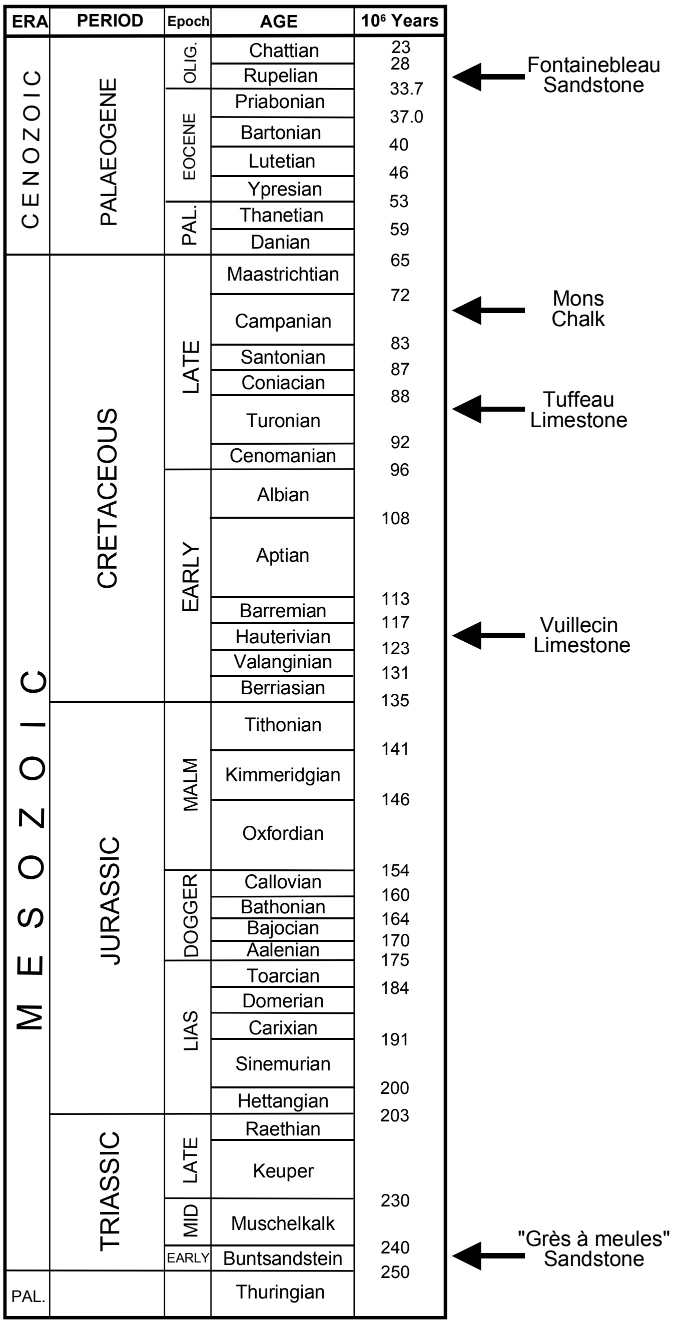

ERA	PERIOD	Epoch	AGE	10^6 Years
CENOZOIC	PALAEOGENE	OLIG.	Chattian	23 28
			Rupelian	33.7
		EOCENE	Priabonian	37.0
			Bartonian	40
			Lutetian	46
			Ypresian	53
		PAL.	Thanetian	59
			Danian	65
MESOZOIC	CRETACEOUS	LATE	Maastrichtian	72
			Campanian	83
			Santonian	87
			Coniacian	88
			Turonian	92
			Cenomanian	96
		EARLY	Albian	108
			Aptian	113
			Barremian	117
			Hauterivian	123
			Valanginian	131
			Berriasian	135
	JURASSIC	MALM	Tithonian	141
			Kimmeridgian	146
			Oxfordian	154
		DOGGER	Callovian	160
			Bathonian	164
			Bajocian	170
			Aalenian	175
		LIAS	Toarcian	184
			Domerian	
			Carixian	191
			Sinemurian	200
			Hettangian	203
	TRIASSIC	LATE	Raethian	
			Keuper	230
		MID	Muschelkalk	240
		EARLY	Buntsandstein	250
PAL.			Thuringian	

Fig. 5 – Position of the five sedimentary rocks on the geological time table.

Vuillecin limestone

The Jura Range (CHAUVE P., 1975) looks like a big arc mainly composed of Mesozoic sedimentary rocks, whose convexity is turned toward the Northeast (Appendix A, Fig. D). The Vuillecin limestone, also called “Pierre jaune de Neuchâtel” (yellow stone of Neuchâtel) is typical of the Late Hauterivian (Lower Cretaceous) rocks, which outcrop in the form of 5-to-50-cm-thick beds, over a thickness of 40 m in the upper Jura Range near the town of Pontarlier (Doubs, Northeast of France). The rock used in this study comes from working faces of small holes situated northwest of Pontarlier in a village called Vuillecin. These small quarries have provided the stones used for the building of numerous monuments in Pontarlier, such as the Town Hall, St Trophine’s Church and St Pierre’s Gate. This limestone, usually organized into 10-to-30-cm-thick beds with cross-bedding, corresponds to an accumulation of water-worn shell fragments cemented by calcisparite crystals.

1.2.2. Petrography and mineralogy of the rocks and description of their porosity

The petrographical and mineralogical analysis of each rock was carried out in three steps.

First, a powdered whole sample and its fine fraction (< 2 µm) were analyzed by XRD (X-ray Diffraction) in order to semi-quantify the mineral composition.

Second, the rock was described in terms of its petrography and porous structure characteristics. Thin sections of a sample impregnated with colored resin (Appendix B) were observed by optical microscopy.

Then, the broken surface of a rock sample was observed by SEM. A JEOL JSM-5600 instrument using secondary electron detection, gave images of the broken surface at a lower scale than under the optical microscope, which made it possible to identify some pore size classes in relation to the mineral framework.

Fontainebleau sandstone

This sandstone is a quartzarenite (FOLK R.L., 1974) composed of very well sorted quartz grains with a median diameter of about 300 µm. During diagenesis, they were strongly cemented by syntaxial quartz overgrowths, which gave them their euhedral shapes. An iron and/or manganese oxide coating may be enclosed between the detrital grain and its authigenic overgrowth. Grains are mainly in contact with their neighbors by long crystal faces, which may be embedded.

These extensive quartz overgrowths (about 12% of the volume of the rock) induced the strong reduction and the development of their polyhedral structure (Image board A, Fig. A and C). The shape of the inter-granular porous spaces becomes simpler as the pores decrease in size: pores with triangular shapes are often present (Image board A, Fig. D). Spatial variations in the silicification intensity and the arrangement of the packing of the grains (more-or-less compact) are responsible for porous space heterogeneity on the thin section: in some areas, clusters of 5 to 10 quartz grains are completely silicified.

In other places, this assemblage of subhedral and euhedral quartz is not perfect, and long pores with straight borders can be observed. Some detrital grains and quartz overgrowths have been locally corroded; thus, large inter-granular pores are delimited by concavo-convex or crenate contours (Image board A, Fig. A).

In the thin section, the porosity of this sandstone consists of a geometrical network of canals with median lengths quite similar to the quartz grain diameters. Their widths usually range between 30 to 110 µm, but sometimes they can reach up to 200 and 300 µm. The pores have typical polyhedral shapes where the grains have been strongly cemented by quartz overgrowths.

Without extensive silicification and after dissolution, these sandstones could have bigger and more irregularly shaped pores.

The trapped porosity (Image board A, Fig. B) is located in these big pores, whatever their shape. The free porosity consists of the small inter-granular pores and the small canals or constrictions that provide the connection between the pores. All these porous structures compose a continuous and homogenous porous network throughout the rock.

Because of large sized grains and pores, most of the structure was already investigated by optical microscopy. The SEM study confirmed the previous observations. Images of strongly cemented areas (Image board A, Fig. D) of various sizes (from one to several millimeters) confirm that they often contain residual pore spaces with a polyhedral shape. These pores are often connected by small elongated capillaries with diameters from less than 1 to several micrometers.

These observations made it possible to confirm and/or interpret further results of the physical properties. In fact:

- the low porosity values (§2.1.2.1.) are strictly linked to extensive silicification;
- the scattering of the B value coefficient (from capillary water imbibition kinetics; § 3.1.) may be related to a modification in the size of the connections (canals that connect the pores with each other): a small variation in the quartz overgrowth amount has more impact on the pore access sizes than on the volume porosity;
- the pore connection sizes remain big enough (hydraulic diameter of about 30 µm) to preserve a good connectivity throughout the porous medium, which allows for a fast and continuous water absorption of the free porosity;
- the development of quartz overgrowths increases the difference between the macropore diameters and the pore access diameters, which is the cause of the high percentage of trapped porosity in this sandstone (§ 2.1.).

Thus, in spite of its great mineralogical homogeneity, this sandstone shows some heterogeneity in its porous medium due to the high amount of quartz overgrowths and their distribution throughout the rock. If they do not affect the connectivity network, they have a direct impact on the capillary properties and greatly contribute to the variations in the physical parameters.

“Grès à Meules” sandstone

Viewed from a thin section, this sandstone presents a great mineral variety (Image board B, Fig. A). It is composed of quartz grains (78%) about 120 µm long, clay minerals (8.5%), iron oxide and hydroxide, potassium-feldspars (also written K-feldspars; 13.5%) and some micas. A fine fraction (< 2 µm) contains illite (78% in mass of the fine fraction), chlorite (12%) and kaolinite (10%).

Stratification is underlined by the orientation of the long detrital muscovite and the large diameters of some of the quartz and feldspars. Clay minerals, and especially the illite whose contents may range between 5 and 10%, are the main components of the matrix located in the inter-granular pore spaces, which wind between the other mineral phases. The cohesion of the sandstone is due to the existence of this clayey matrix and the sutured contacts of some quartz grains. Significant amounts of small granules of iron oxide and hydroxide pigment this clayey matrix. Sometimes they are concentrated at the borders of the macropores, but always in association with the clay minerals.

On colored thin sections, the compact appearance of this sandstone looks quite deceptive in comparison with its porosity (Image board B, Fig. A). If the free porosity (colored in red) is quite visible in some inter-granular macropores, the main porosity is located in the clayey matrix.

Because of the microporous structure of this matrix, the resin color is not easily distinguished. However, under reflected light, the microporosity appears significant. The trapped porosity (colored in blue) takes place in most of the network's macropores often in association with the clay minerals and iron oxide/hydroxide concentrations (Image board B, Fig. B). SEM images show in detail the different mineral components of the clayey matrix, like kaolinite and illite (Image board B, Fig. D). In some cases, the clay minerals rim the detrital grains (Image board B, Fig. C) and/or are more concentrated in the throats. These clay concentrations strongly reduce the size of the throats pores. In other cases, clay minerals completely fill the inter-granular porous spaces, leading to micropores of various sizes (evaluated from 1 µm to several nanometers).

In the "Grès à Meules" sandstone, the porous structures may be simplified as to be an abundant free microporosity, which isolates areas mainly made up of trapped macropores. Contrary to the Fontainebleau sandstone, in spite of petrographical heterogeneities, it is the mineral variety, and more precisely the presence of the clayey matrix, that contributes to a homogenization of the porous medium due to the development of this free porosity. This characteristic of "homogeneity" would explain the low dispersion of the different physical parameters measured in this rock.

Mons chalk

The Obourg chalk, which was used in this study, is white and corresponds to a mudstone in DUNHAM's classification (1962) or to a biomicrite in FOLK's classification (1959, 1962). Bioclasts are mostly foraminifera and lamellibranchiata. Their repartition in the chalk is quite homogeneous except in some enriched beds. Some fractures filled by calcimicrite cement are sometimes present. The clay fraction < 2 µm, which constitutes less than 1 % of the rock's total volume, contains illite (25%) and irregular illite-smectite mixed layers (75%). The chalk nano-facies are made up an accumulation of complete or broken coccoliths and primary anhedral particles (MACHHOUR et al., 2002). Coccolith plates and primary particle surfaces look smooth and their contours are regular. The micrite elements are arranged without any preferred orientation. SEM images (Image board C, Fig. D) show that the primary anhedral particles are often isolated (the structure is punctic type). Most of them have lengths of about 1 or 2 µm; some other particles can be larger (to 5 µm) or smaller (about 0.5 µm). Some modifications of the nano-facies are sometimes observable: changes in the borders of primary particles and coccolith plates (regular to irregular); a modification in the shape of the primary particles (anhedral to subhedral); and an increase in the number of secondary particles. The creation of this number is linked to the combination of coccolith fragments and primary particles. Numerous primary and secondary particles show solution or crystal growth features.

The porosity of this chalk mainly consists of a free microporosity (Image board C, Fig. A) located between the calcimicrite crystals of the bioclasts (foraminifera shells, coccoliths …) and the cement (SIZUN J.-P. et al. 2002). These micropores are well-sorted. Their mean diameter ranges from 1 to 5 µm (Image board C, Fig. D). Nevertheless, small amounts of pores reach sizes as low as about several hundred nanometers. Some geodesic (vugs) or intra-particle macropores are also present in foraminifera cells or on the emplacement of dissolved bioclasts (Image board C, Fig. C). Trapped porosity (Image board C, Fig. B) takes place in some of them. Nevertheless, their low abundance in the chalk does not contribute to an increase in the porosity.

"Tuffeau" limestone

This "tuffeau" or Marigny-Brizay limestone is a light marly siliceous limestone (SCOLARI & LILLE's classification, 1973) that can be classified as a bio-arenite with siliceous and micrite cement, pelletoidal and loosely packed textures (ROBASZINSKI et al., 1982). This limestone (Image board D, Fig. A) mainly consists of calcite (48%; bioclast, micrite and sparite cement), of silica (quartz: 23%, opal-Cristobalite-Tridymite (opal-CT): 13%), of K-feldspar (2%) and of clay minerals (smectites and glauconite: 14%). Some micas (biotites and muscovites) are present in traces. Quartz and feldspar grains and bioclasts are very well sorted around 100 µm. The mineral fraction < 2 µm contains illite (15%), smectites (85%) and traces of clinoptilolite.

The porous network of this rock consists of the juxtaposition of free microporous areas and macropores linked to trapped porosity (Image board D, Fig.B). The pores range in diameter from 5 to 10 µm and are connected by narrower accesses; they are defined by the arrangement of opal-CT spherules. The presence of coarser detrital grains (quartz, K-feldspars, micas, glauconite, bioclasts…) disturbs the opal-CT packing and creates bigger macropores. The microporosity is made of inter-granular micropores located between the calcite crystals of the micritic grains, or in the spaces between the opal-CT spherule lamellas by the micropores linked to the grain surface roughness and by the microporous area due to the phyllosilicate mineral concentrations (clays and micas). SEM images show various microporous structures linked to the different minerals (Image board D, Fig. C):

- opal-CT spherules delimit macropores; they have a lamellar structure and contain micropores with diameters from several nanometer to about 1 µm (Image board D, Fig. D);
- clay mineral concentrations (illite, smectite) reduce the size of the pores and their throats and contribute to the development of trapped porosity (Image board D, Fig. F), as seen for the "Grès à Meules" sandstone. They contain micropores of various sizes along the nanometre scale;
- micropores with diameters of about 1 µm or 2 µm, and even sometimes less than 1 µm, are located in micritic calcite areas;
- micropores with diameters less than 0.1 µm are located in glauconite grains (intra-granular porosity) and between the crystalline layers of exfoliated muscovite (Image board D, Fig. E).

Vuillecin limestone

The Vuillecin limestone consists of numerous fragments of bryozoans, molluscs and echinoderms (crinoids, urchin spines), ooliths, oncholiths and micritic intraclasts cemented by sparite and microsparite calcite (Image board E, Fig. A). The fragment sizes, relatively variable (10 to more than 300 µm), and their angular shape indicate that the rock is immature.

The nature of the components and the cement content led us to class this limestone as a packstone (DUNHAM's classification, 1962) and a biosparite (FOLK R.L., 1962). From a mineralogical point of view, this rock is mainly made of calcite, with traces of quartz and goethite. The fine fraction < 2 µm shows illite (35 %), irregular illite-smectite mixed layers (56 %), kaolinite (6 %), chlorite (3 %) and traces of goethite.

The porous network of this limestone consists of:

- microporous areas related to micritic areas;
- remaining inter-granular macropores located in the calcisparite cement areas;
- secondary macropores developed by solution and/or recrystallization of ooliths and bioclasts.

In some cases, the nucleus and the cortex of ooliths have been totally dissolved to form spherical macropores. Some bioclasts show solution marks, which have induced the development of macropores.

Microporous areas and macropores (< 10 % of the total volume of the rock) are often isolated from each other and only connected by the thin spaces situated between the calcite crystals of the cement. The porous network made up of these porous structures depends on the distribution of the porous fragments in the rock, and looks relatively heterogeneous at the thin section scale, as also remarked at a lower scale by SEM analysis (Image board E, Fig. B).

Moreover, detailed SEM observations of the micritic and sparitic areas made it possible to distinguish pore sizes:

- from 10 to 200 µm: pores delimited by sparitic calcite crystals (Image board E, Fig. C);
- about a few µm: pores between the microsparitic crystals of the cement (Image board E, Fig. D);
- lower than 1 µm: pores between the micritic calcites (cement and allochems).

1.3. Summary

This preliminary part of the study was a qualitative overview of the structure of the selected rocks (mineralogy, petrography and porous structure characteristics), which was summarized in Table 1. Qualitative information about the petrography and the porosity characteristics of the rocks (porosity type and evaluated pore size range) was useful in understanding the results of the measurements exposed in the next section (water saturation ability, mercury porosimetry curves, transport properties…). Two materials – Fontainebleau sandstone and Mons chalk – have shown relatively small ranges of evaluated pore sizes, while the three others have shown larger pore size ranges (from macropores to micropores). These two rocks seemed to be the more homogeneous materials (mineral and porous structure homogeneity). The porous structure of the other rocks seemed to be less homogeneous due to more complex mineral structures (different mineral components, various grain sizes). Then, these five rocks were adequately chosen for this study because they were representative of a large panel of porous structures and of degrees of homogeneity. However, noticeable similarities were pointed out. In spite of these similarities, the materials have shown different fluid transport properties, as seen in the third chapter. Then, questions deserved to be raised, for example:

- why do the two sandstones (Fontainebleau and "Grès à Meules"), which are mainly made of quartz, have quite different pore sizes and permeabilities?
- why do the Vuillecin limestone and the Mons chalk, which are almost only made of calcite and which mainly contain micropores, have totally different capillary water imbibition properties?

The importance of clay minerals (amount and nature) in the structure of a porous medium was soon emphasized in this section. Clays are always associated to microporous areas and have influence on the spatial distribution of pores. Thus, they must have strong influence on quantitative measurements.

Legend of Table 1:

MP : macropore
µP : micropore

▥ ? : no pore size evaluation

Table 1 – Summary of the conclusions from the petrographical analysis: each rock and its porosity characteristics.

			Porous network description
Rock Name	Rock type	Mineral composition	Porosity description
Font. sandstone	Quartzarenite	Quartz	Inter-granular MP Inter-granular µP Q grain microroughness
"Grès à Meules" sandstone	Feldspathic sublitharenite	Quartz Feldspar Clay minerals	Inter-granular MP Clayey matrix-µP
Mons chalk	Mudstone or biomicrite	Calcite	Vugular MP Calcite inter-crystal µP
Tuffeau limestone	Siliceous bio-arenite	Calcite Quartz Clay minerals	Vugular & inter-granular MP Clayey matrix-µP Calcite inter-crystal µP Intra-granular µP
Vuillecin limestone	Packstone or biosparite	Calcite	Vugular MP Calcisparite inter-crystal MP microsparitic & micritic cement inter-crystal µP

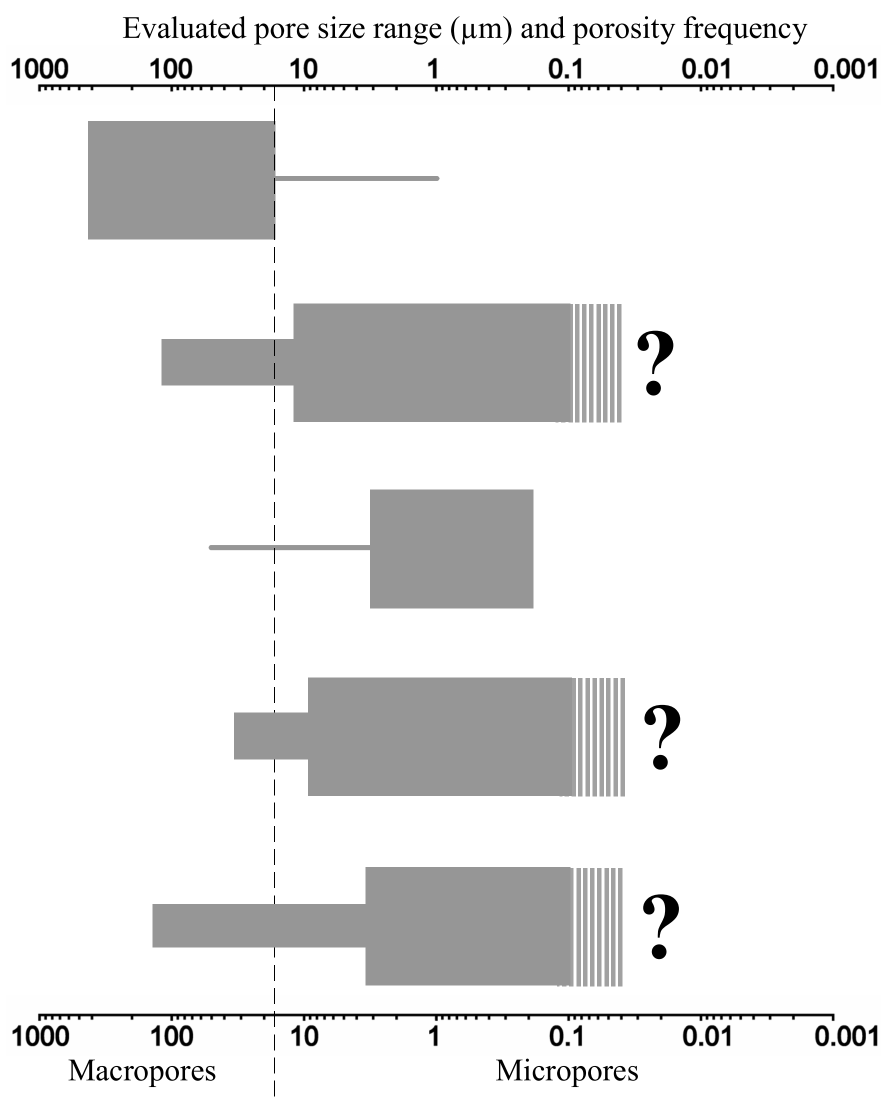

2. Quantitative analysis of the porous structures of the rocks

Petrophysical measurements were carried out on each material using three main approaches: statistical determinations of the porous structure parameters, visualization of the porous media and analysis of the transport properties (Fig. 6). Water porosimetry gave the first information about the porosity and the water saturation ability of the rocks using big samples (from 25 to 50 cm³). Sets of smaller samples (from 1 to 2 cm³), used for statistical analyses, were first investigated by water porosimetry and helium pycnometry (non-destructive methods), and then by mercury porosimetry (destructive method). Other sets of small samples were used for the gas adsorption experiments. The sizes of the samples were chosen so that controls and parameter correlations could be made between the different methods. Techniques like the BSE image analysis and the X-ray computed tomography made it possible to visualize the structures of the rocks.

2.1. Water porosimetry

With its low viscosity and high wettability, water is a simple means of investigation for porous media. Different water absorption methods were required in this study to obtain information about the porous volume and the type of porosity: total porosity, “free” or “trapped” porosity.

2.1.1. Theoretical aspects

2.1.1.1. Total water porosity N_W

The recommendations proposed by RILEM (1980) were followed for the tests made in this study.

The technique of the total water porosity measurement is based on the absorption of water inside the total connected porous volume of a sample, in an airless environment. The experimental device usually used is composed of two parts (Fig. 7): one provides a vacuum environment and the other ensures the water supply (degassed distilled water). The sample is first dried at 60°C until it reaches a stable weight. Then, it is degassed under vacuum at $2\ 10^{-2}$ Torr (2.6 Pa) for 24 hours in an airtight enclosure. It is progressively water imbibed from its base, under a dynamic vacuum, following the wet fringe rise in the sample (BOUSQUIE P., 1979).

Three weights of the sample are measured during the experiment:

- the dry sample weight (w_s),
- the hydrostatic sample weight (w_1: weight of the immersed water-saturated sample).
- the water-saturated sample weight (w_2),

The total porosity is the ratio of the void volume to the sample bulk volume (Relation *1*). Because the density of water is $\rho_{H_2O} = 1$ g cm^{-3}, the bulk volume V_B is expressed as the weight difference (Archimedes’s principle):

$$V_B = \frac{w_2 - w_1}{\rho_{H_2O}} = w_2 - w_1 \qquad (4)$$

The total porosity (%) is given by:

$$N_W = \frac{w_2 - w_s}{w_2 - w_1} \times 100 \qquad (5)$$

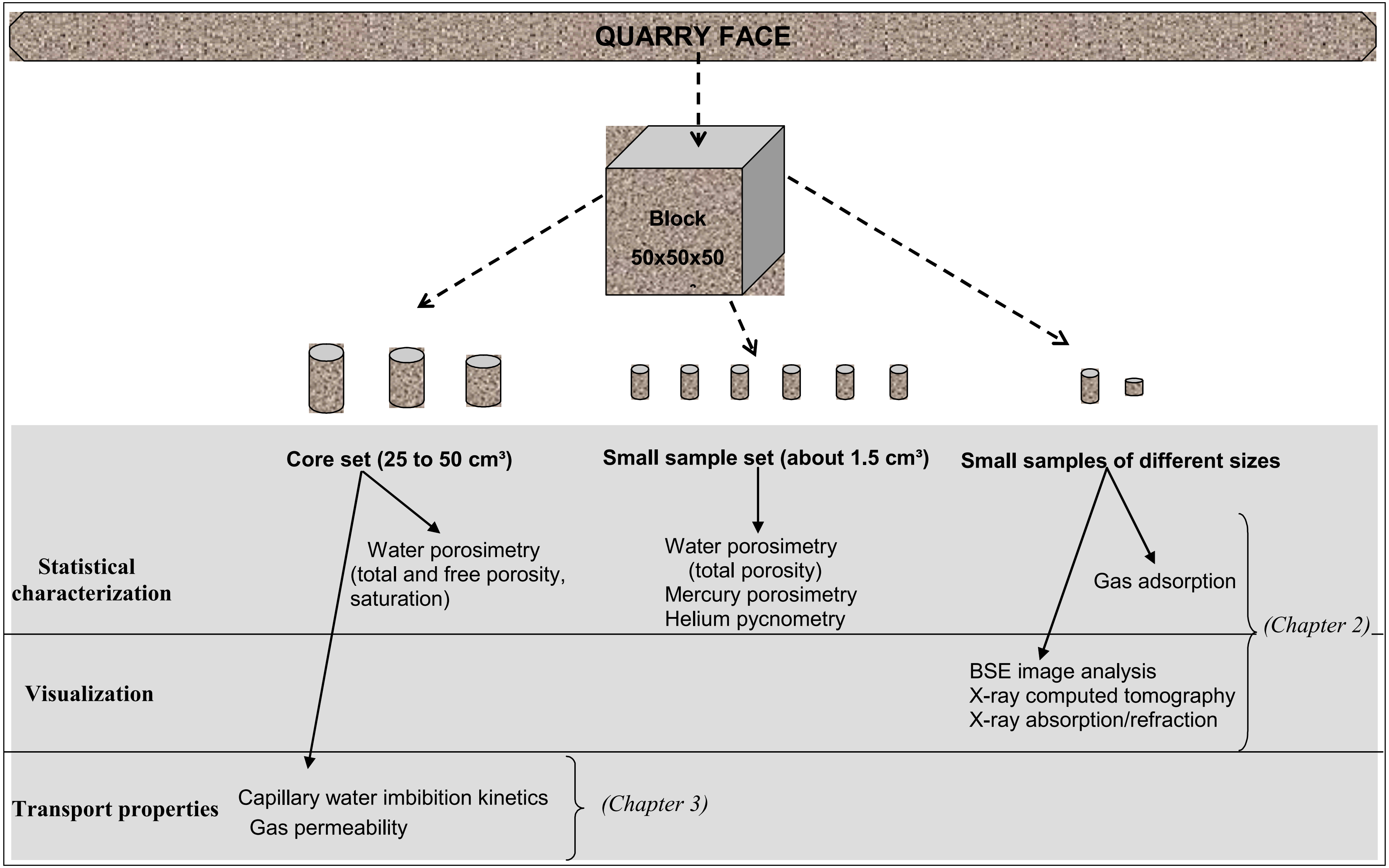

Fig.6 – Diagram of the investigation os each sedimentary rock (arrowed dashed line: sampling; arrowed bold line: measurement).

2.1.1.2. “Free” porosity N_{48}

The 48 hours porosity (N_{48}) is the porosity that is freely accessible to water under atmospheric conditions (French norm NF B.10.513). N_{48} is also called the “free” or “imbibable” porosity, because it is assimilated to N_F in Relation *3* (§1.1.3.2).

The sample is previously dried at 60°C until it obtains a stable weight (w_s). A quarter of the sample is put in water for one hour. Afterwards, half of the sample is immersed for 23 hours; finally, the entire sample is immersed for 24 hours (Fig. 8). The weight of the imbibed sample is measured at the end of the experiment (w_{48}).

The 48 hours porosity (N_{48}) is obtained from the following relation:

$$N_{48} = \frac{w_{48} - w_s}{w_2 - w_1} \times 100 \qquad (6)$$

2.1.1.3. Trapped water porosity $N_{TR,W}$

During the free porosity measurements, gas (air, water vapour) occupies the non-water invaded part of the porous volume. According to Relation *3*, the trapped porosity can be calculated as the difference:

$$N_{TR,W} = N_W - N_{48} \qquad (7)$$

The trapped porosity is often expressed as a percentage of the total porosity. This percentage of trapped porosity $N^*_{TR,W}$ is given dividing the trapped porosity $N_{TR,W}$ by the total porosity N_W.

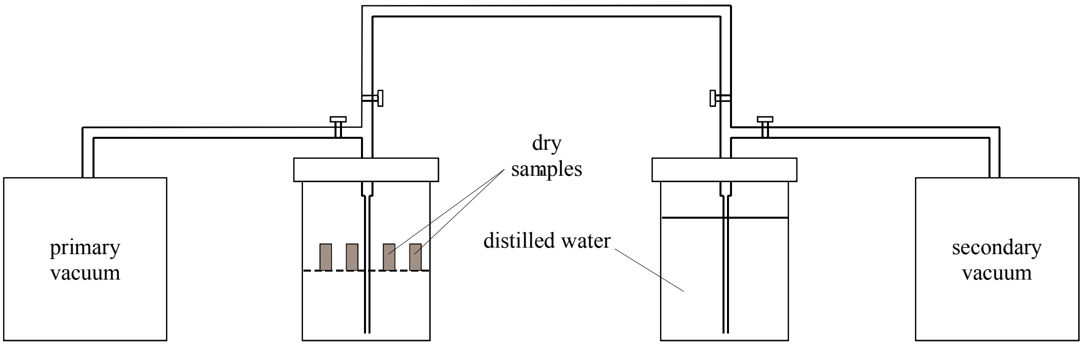

Fig. 7 – Diagram of the device for the total water porosity measurements.

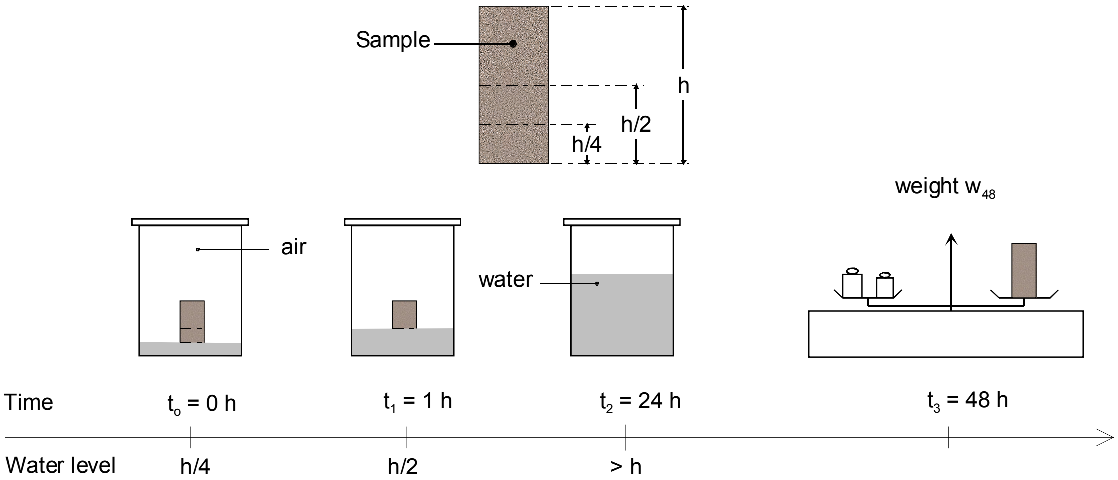

Fig. 8 – Diagram of the device used for the 48 hours porosity measurement (ROUSSET TOURNIER B., 2001). h: sample height; w_{48}: water imbibed sample weight after 48 hours.

2.1.1.4. Hirschwald's coefficient S_{48}

The Hirschwald's coefficient is the saturation ratio of the sample obtained from the 48 hours porosity test. It quantifies the proportion of the porous network that is freely accessible to water under natural absorption conditions:

$$S_{48} = \frac{N_{48}}{N_W} \quad (8)$$

The saturation ratio (≤ 1) is linked to the connectivity of the porous structure: a high saturation coefficient often means a high connectivity. Pore and throat sizes also influence the rock saturation ability since the pore-to-throat-size ratio is an important factor in the air trapping phenomenon (MERZ J.D., 1991), which is explained in the following paragraph.

2.1.1.5. Air trapping mechanisms

BOUSQUIE P. (1979) proposed two main air trapping mechanisms linked to porous structure properties, which take into consideration the different wettabilities of air and water:

Mode 1: water rises along the rough surface of a pore (Fig. 9a) to the upper capillary, inducing a trapping of air in the middle of the pore (BOUSQUIE P., 1979; DULLIEN F.A.L. et al., 1983).

Mode 2: the porous network can be simplified into a network of pores and throats. According to the theory of hydrodynamics, when the difference between the throat and pore sizes is high, water flows slowly into the pore. It flows faster through small parallel connected throats and back into the pore through an upper entrance ("bypass"), inducing a trapping of air (Fig. 9b). This explains that the pore-to-throat size ratio influences how much air is trapped: the higher the ratio, the lower the water saturation.

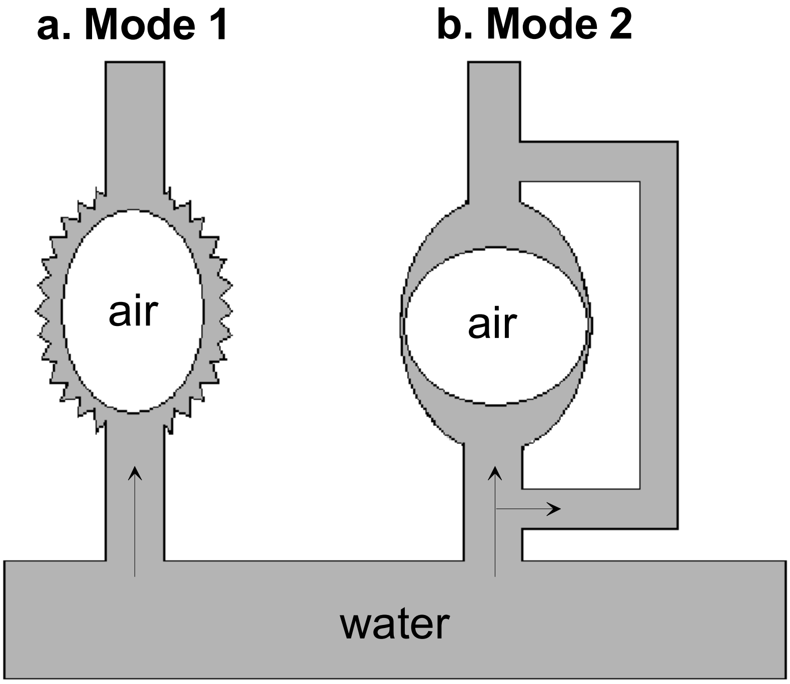

Fig. 9 – Air trapping modes according to BOUSQUIE P. (1979) – a.: trapping induced by roughness; b.: "bypass" trapping.

2.1.2. Results and discussion

As shown in Table 2, there are two highly porous materials (Mons chalk, 43% and tuffeau limestone, 46%), a moderately porous one ("Grès à Meules" sandstone, 21%) and two lowly porous materials (Fontainebleau sandstone and Vuillecin limestone, both with about 12%). Four of the materials show low relative standard deviations ($\sigma_{R,NW}$) in their total porosity (Fontainebleau sandstone: 1.4%; "Grès à Meules" sandstone: 0.8%; Mons Chalk: 0.3% and tuffeau limestone: 1.8%). The Vuillecin limestone presents higher deviations: 5.7%.

From one material to the next, various percentages of trapped porosity ($N^{*}_{TR,W}$) were recorded (Fontainebleau sandstone: 44%; "Grès à Meules" sandstone: 33%; Vuillecin limestone: 29%; tuffeau limestone: 17%; Mons chalk: 7%). Inverse variations can be observed for the Hirschwald's coefficient (S_{48}): it is high for the chalk (0.93) and the tuffeau limestone (0.84), lower for the Vuillecin limestone (0.71) and the "Grès à Meules" sandstone (0.68) and significantly low for the Fontainebleau sandstone (0.56).

These variations could be linked to the different structures of the rocks porous networks.

Fontainebleau sandstone

The petrographical analysis has shown the presence of some quartz grains with rough surfaces. This micro-roughness can induce air trapping in the macropores delimited by such grains (Mode 1). However, given the large quantity of trapped air in this material, Mode 1 cannot be the only mechanism at work here.

In comparison with the other materials, the low saturation coefficient and the large quantity of trapped porosity of this sandstone are due to a large trapping of air according to the "bypass" mechanism (Mode 2). Silicification has induced pore and throat size modifications in different zones of the rock during the diagenesis. These modifications were observed on the thin sections and SEM images. In a previous study, Hirschwald's coefficients and total porosities were determined for Fontainebleau sandstone samples originating from different places in the massif[1]. The samples had various porosities (ranging from 5 to 20 %), which were linked to different degrees of silicification. For this study, these data were used again and plotted in Figure 10. The diagram shows that S_{48} increases linearly with the total porosity. It shows that the part of trapped porosity increases with the amount of quartz overgrowths. Thus, the degree of silicification inside a sandstone from Fontainebleau influences the type of porosity, trapped or free, that characterizes its porous network. Two features explain this correlation (Fig. 11):

- Diagenesis silicification preferentially occurred in the dihedral parts of the pores delimited by grains, because of the presence of residual water. The size of the throats was reduced in a more extensive way than the pore sizes: this enhanced the difference between the pore and throat sizes.
- Diagenesis silicification occurred in preferential zones of the rock (for instance zones where grains are slightly smaller and close to each other). That induced the presence of strongly cemented zones juxtaposed to slightly cemented areas, which were observed by petrographical analysis. During an imbibition under atmospheric pressure, water can bypass the bigger pores and flows through the more cemented areas, which contain smaller pores and narrower throats (air trapping Mode 1).

Thus, the low water saturation (in comparison with the other rocks) of the studied Fontainebleau sandstone is linked to the silicification degree of the rock. Moreover, it is important to note that the low water saturation does not mean a low connectivity of the porous network but is mainly due to a mean pore-to-throat size ratio, which may be high.

---

[1] Measurements made for some other studies in the laboratory "Laboratoire de Pétrophysique du Centre de Géochimie de la Surface (CNRS)" in Strasbourg (no related publication).

Table 2 – Averaged water porosimetry data: total porosity (N_W), free porosity (N_{48}), trapped porosity ($N_{TR,W}$, and $N^*_{TR,W}$ as a percentage of the total porosity) and water saturation (S_{48}). The data obtained from each sample were reported in Appendix C.

	Fontainebleau sandstone	"Grès à Meules" sandstone	Mons chalk	Tuffeau limestone	Vuillecin limestone
Number of samples	4	4	11	7	8
N_W (%)	12.45	21.21	43.67	46.31	11.77
σ_{N_W}	0.18	0.18	0.12	0.82	0.67
σ_{R,N_W} (%)	1.4	0.8	0.3	1.8	5.7
N_{48} (%)	6.98	14.25	40.57	38.37	8.31
$\sigma_{N_{48}}$	0.35	0.41	0.35	2.18	0.40
$\sigma_{R,N_{48}}$ (%)	5.0	2.9	0.9	5.7	4.8
$N_{TR,W}$ (%)	5.47	6.96	3.10	7.94	3.46
$\sigma_{N_{TR,W}}$	0.18	0.58	0.33	2.26	0.32
$N^*_{TR,W}$ (%)	43.9	32.8	7.4	17.2	29.4
$\sigma_{R,N^*_{TR,W}}$ (%)	3.3	8.3	10.5	28.4	9.2
S_{48}	0.56	0.68	0.93	0.84	0.71
$\sigma_{S_{48}}$	0.02	0.03	0.01	0.04	0.01
$\sigma_{R,S_{48}}$ (%)	3.8	3.8	0.8	5.3	2.0

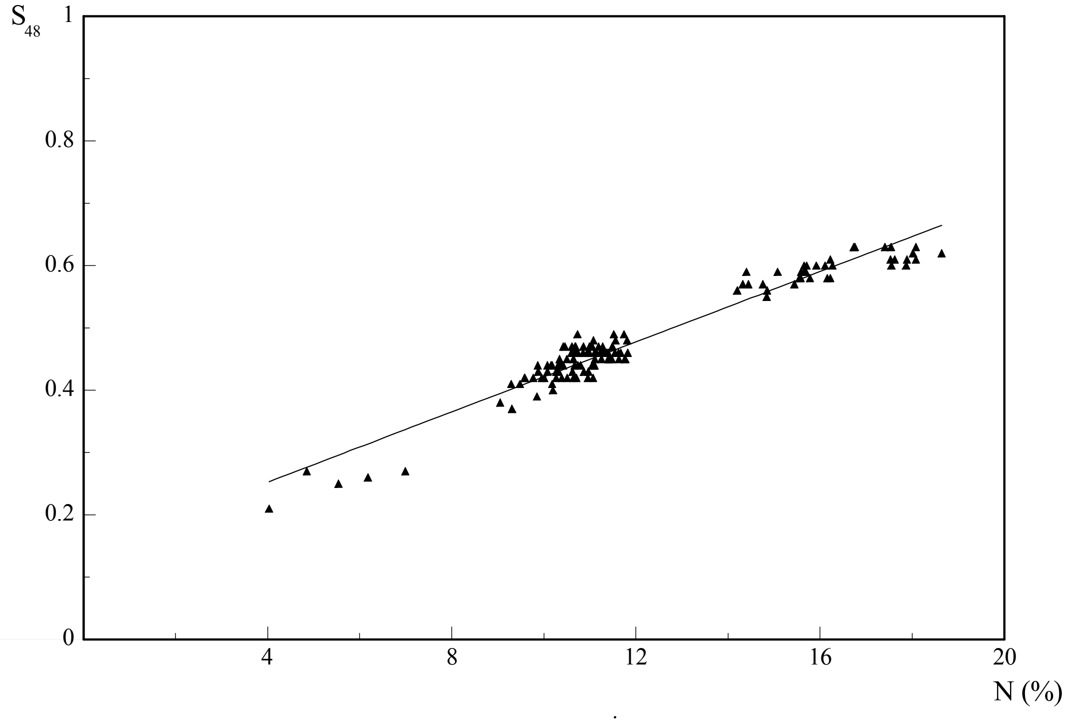

Fig. 10 – Hirschwald's coefficient versus the total porosity (data obtained by water porosimetry for samples of different types of Fontainebleau sandstones).

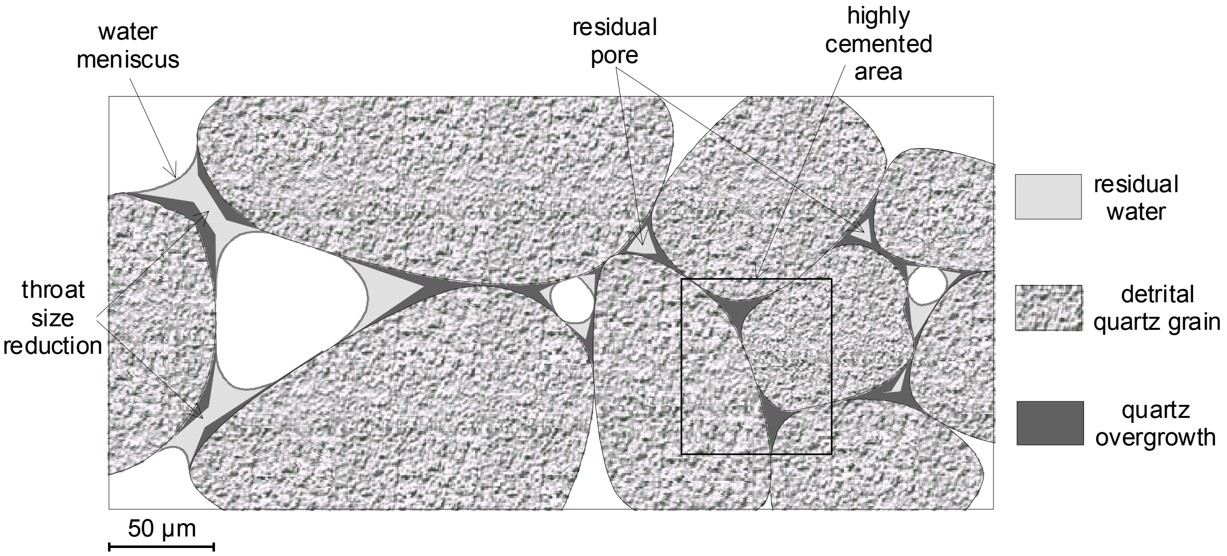

Fig. 11 – Silicification mechanism in the Fontainebleau sandstone during the diagenesis: water remained at the dihedral parts of the pores, where quartz overgrowths induced typical euhedral shapes of the grains and pores; throat size reduction occurred and highly cemented areas were created – The scale was approximately set according to the evaluated mean size of the grains.

“Grès à Meules” sandstone

Unlike the Fontainebleau sandstone, the smaller amount of trapped air and a higher saturation coefficient of the “Grès à Meules” sandstone can be explained by the presence of clay minerals, which were revealed by XRD analysis. As observed on thin sections, clays fill the inter-granular voids (pores and throats) and induce free microporous areas. Thus, they can enhance the water saturation.

On the other hand, numerous macropores are isolated, and air trapping can occur during water absorption according to Mode 2, as well as to Mode 1, due to clays at their surfaces.

Then, the clay minerals govern the water saturation ability in the “Grès à Meules” sandstone. On one hand, they enhance the amount of free porosity. On the other hand, they allow air to be trapped in macropores; this explains the lower water saturation than that of rocks like the chalk and the tuffeau limestone.

Mons chalk

The petrographical analysis has shown that the porous structure of this material mainly consists in a microporous network with a relatively small range of pore sizes. The high saturation coefficient can be explained by the fact that the pores and throats of the microporous network have mean sizes of the same order. A confirmation for this was given after the determination of the mean hydraulic diameter by mercury porosimetry and the determination of the mean pore size by image analysis (a comparison with the Fontainebleau sandstone was made, since the two rocks present opposite water saturation abilities and they seem to have different pore-to-throat size ratios). Hence, almost the entire microporous network is accessible to water under atmospheric conditions, and air trapping by bypass occurs only in a few isolated macropores.

Thus, compared to the other rocks, the water saturation parameters made us classify the chalk as the rock with the most homogeneous porous structure.

Tuffeau limestone

Although the porous structure of this limestone is complex, its saturation coefficient is relatively high. That means a high connectivity of its porous network. As qualitatively observed by petrographical analysis, the microporous network is made of different classes of pores. In each class, pores and throats with sizes of the same order may strongly contribute to the high saturation ability of this limestone.

The low trapped porosity was associated with some isolated macropores, which are often bordered by opal-CT spherules. More significant than in the Mons chalk (Mode 2), trapping of air inside this limestone must be mainly due to the micro-roughness of these opal-CT spherules (Mode 1).

Vuillecin limestone

The saturation coefficient of this limestone (0.7) is lower than that of the chalk (0.9). Both materials are composed of calcite and the main part of their porosity is located between the calcite crystals. Differences in their structure, deduced from the petrographical analysis, justify the different saturation coefficients:

- When the chalk contains a few macropores, a higher amount of macropores (pores in place of dissolved bioclasts or residual macropores in sparite areas) enhances the trapped porosity in the Vuillecin limestone.
- Contrary to the chalk, cementation has largely occurred in the Vuillecin limestone. This cementation has induced the juxtaposition of microporous and macroporous zones. The cemented zones, as well as the micrite areas, which contain throats that are smaller than pores, allow air to be trapped inside the numerous macropores (Mode 2).

Thus, if a large part of the porous network of the rock (70%) is freely accessible to water under atmospheric conditions, the juxtaposition of numerous microporous and macroporous zones induces a lower water saturation ability than that of the chalk (only one narrow class of micropores with similar pore and throat sizes).

2.2. Mercury porosimetry

2.2.1. Theory

The principles of mercury porosimetry has been described by numerous authors (DULLIEN F. A. L., 1979; PAUL A. WEBB and CLYDE ORR, 1996; CARLOS A. LEÓN y LEÓN, 1998; TSAKIROGLOU C.D. and PAYATAKES A.C., 1998; PAUL A. WEBB, 2001). The principles that have been adopted for this study are described in detail below.

2.2.1.1. Washburn’s relation

At room temperature, mercury is a non-wetting fluid that can be used for most porous materials with any technological interest. This fact led WASHBURN (1921) to propose that injecting mercury into a porous material could be used to measure pore-size distributions. He formulated a model that described the mercury injection into a cylindrical pore with a diameter D. The force F_I necessary for expelling mercury, and the one F_E needed to push it into the pore under external pressure P, are respectively expressed by:

$$F_I = \pi \, D\gamma \cos\theta \quad (9)$$

$$F_E = \frac{\pi \, D^2 P}{4} \quad (10)$$

with θ as the contact angle of the mercury on the material, and γ the surface tension of the mercury.

Thus, at the equilibrium under pressure P, the balance of the two forces (*9* and *10*) leads one to establish the following expression of the diameter D of a cylindrical pore filled by mercury:

$$D = \frac{-4\gamma\cos\theta}{P} \qquad (11)$$

2.2.1.2. Measured and calculated parameters

During a mercury porosimetry measurement, mercury is forced step-by-step into the porous spaces of the sample under increasing pressure. At each step, the pressure P^i and the corresponding volume V^i_p invaded by mercury are measured. Characteristics of the sample like the total specific porous volume ($V^*_{p,Hg}$), the skeletal density (or mineral density, $d_{M,Hg}$) and the total porosity (N_{Hg}) are directly deduced from the mercury intrusion data.

Washburn's relation *11* correlates the applied pressure and the pore access diameter: the cumulative specific pore volume can be plotted versus the pore access diameter (Fig. 12). The diagram of dV/dlnD (called the Log-differential pore volume) versus the pore access diameter gives information about the pore access size distribution. Characteristics like the median and the average pore access diameters (D_{50} and D_{AV}), the hydraulic diameter (D_H) and the specific surface area (S_{Hg}) are calculated from the data of the measured injected volume and of the applied pressure (see the definitions of the calculated parameters in Appendix D).

2.2.1.3. Hysteresis and mercury trapping mechanism

Under given pressure P, mercury invades a certain pore volume of the sample. Afterwards, if the applied pressure decreases, a quantity of mercury is trapped within the porous spaces. Under identical pressure, the volume of mercury in the sample is greater for the withdrawal than for the injection.

The trapped mercury volume V_R (residual volume) measured after the mercury withdrawal at pressure 0.1 MPa (i.e. for a washburn's diameter of about 15 µm), corresponds to a trapped mercury porosity $N_{TR,Hg}$ (Fig. 12). During the mercury injection under an increasing pressure, the pore access sizes govern the entry of mercury into the pores, whereas, under a decreasing pressure, the pore sizes control the withdrawal of mercury. The percentage of trapped porosity $N^*_{TR,Hg}$ is given dividing the trapped porosity $N_{TR,Hg}$ by the total porosity N_{Hg}

WARDLAW N.C. & MCKELLAR M. (1981) have studied how the shape and the hysteresis of the mercury injection, withdrawal and re-injection curves are influenced by the geometry and the connections of the pores in glass micro-models and in sedimentary rocks. The authors give experimental evidence about two main porous system characteristics as critical factors in the displacement of the mercury, and in particular, in its trapping during withdrawal:

- the greater the pore-to-throat size ratio, the greater the volume of trapped mercury;
- the volume of trapped mercury is as high as the number of non-random heterogeneities that can be, for example, zones of large pores isolated in a continuous network of smaller pores.

2.2.2. Experimental

Before the analysis by mercury porosimetry, the sets of the small samples were investigated by water total porosimetry (theory in §2.1.1.1.) and the mineral densities were determined by helium pycnometry. To compare them with the mercury porosimetry data, two parameters were calculated from the water total porosimetry data in addition to N_W (Relation *5*), the total specific porous volume $V^*_{p,W}$ and the mineral density $d_{M,W}$ (normalized to the density of water $\rho_{H2O} = 1$ g cm^{-3}; thus without dimension), which are given using the following relations:

$$V^*_{p,\,W} = \frac{w_2 - w_S}{\rho_{H_2O} w_S} = \frac{w_2 - w_S}{w_S} \qquad (12)$$

$$d_{M,\,W} = \frac{w_S}{w_S - w_1} \qquad (13)$$

Let us reiterate here that w_S is the weight of the dry sample, w_1 the hydrostatic sample weight, and w_2 the weight of the water-saturated sample.

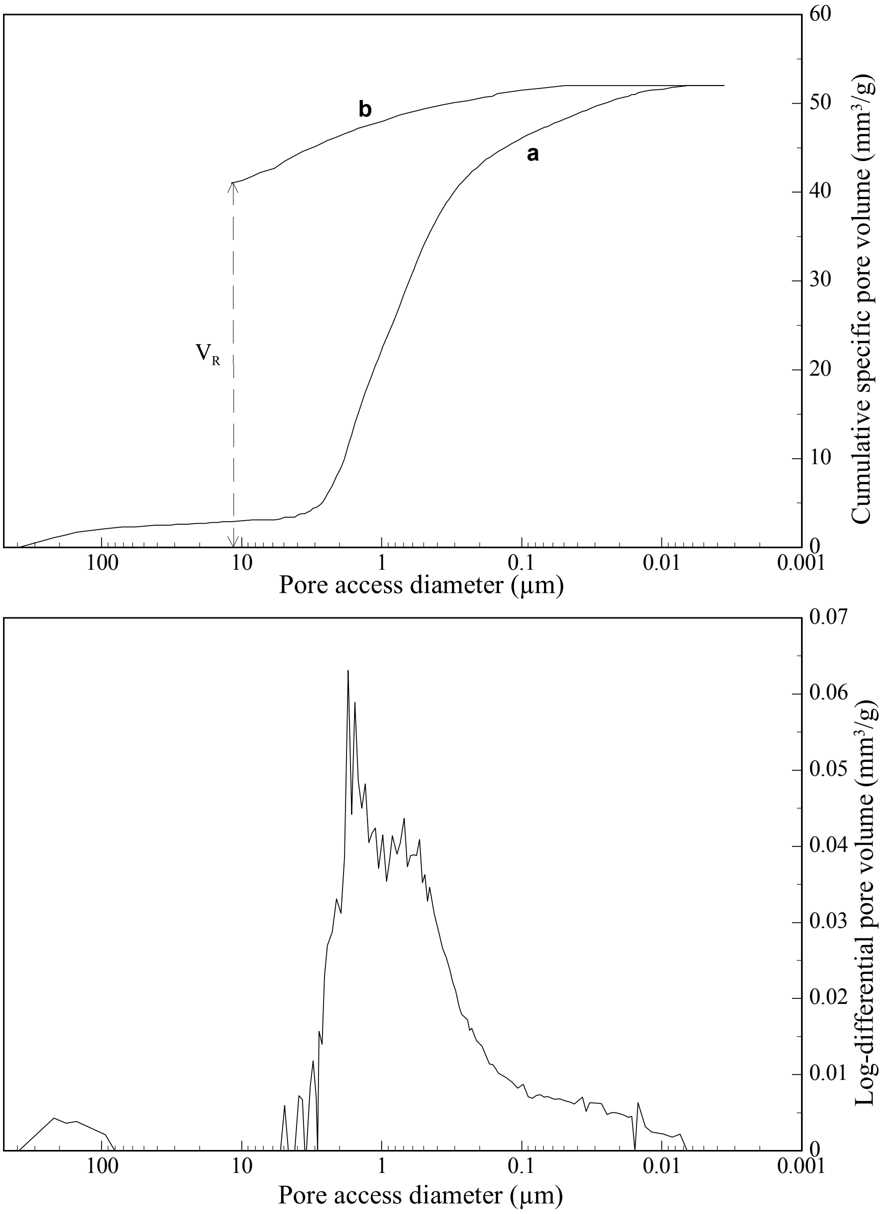

Fig. 12 – Example of mercury porosimetry curves obtained from a porous rock sample (Vuillecin limestone) – Top diagram: cumulative pore volume-pore access diameter curve plotted for an injection (a) and a withdrawal (b) of mercury; V_R is the residual volume, which corresponds to the trapped mercury porosity – Bottom diagram: pore access diameter distribution plotted from the injection data.

The mercury porosimetry measurements were performed using an Autopore III Porosimeter (Micromeritics). Each sample was put into an adequate penetrometer, and pressure was applied step-by-step from 0.001 MPa to 400 MPa (corresponding to the pore access diameters from 400 µm to 4 nm). Afterwards, the pressure decreased from 400 MPa to 0.1 MPa, in order to analyze the mercury withdrawal from the sample.

The surface tension of the mercury is 0.485 N m^{-1} (485 dynes cm^{-1}). The value of the contact angle θ between the mercury and a solid surface depends on the solid surface chemical composition, cleanliness and roughness, and on the purity of the mercury. RITTER H.L. & DRAKE L.C. (1945) originally chose an average contact angle of 140°, representative of a wide variety of materials. In fact, for many materials, this is a rough approximation that can induce errors up to 50% in the estimated pore sizes (ALLEN T., 1997). For the five sedimentary rocks of this study, the contact angles were chosen according to the recommendations reported in the bibliography and to the rock mineral compositions (Appendix E shows various contact angles for some minerals): 145.5° for the chalk and the Vuillecin limestone, 143.5° for the tuffeau limestone and 139° for the Fontainebleau and the "Grès à Meules" sandstones.

Due to the clay mineral concentrations, the samples of the tuffeau limestone and the "Grès à Meules" sandstone were first dried until stable weights, at 80°C under vacuum for 48 hours. Such conditions were necessary for the investigation of almost the entire pore volume of these materials. The samples of the other rocks were dried for 24 hours under vacuum at 70°C.

2.2.3. Results – Comparison with the water porosimetry and the helium pycnometry

The mercury porosimetry curves (the cumulated or log differential volume versus the pore access diameter) of the five rocks are represented in Figures 13 and 14 (only four curves for each rock have been presented for clarity's sake).

The mean value and the maximum and minimum values of the calculated parameters, as their relative standard deviations, are given in Table 3. For better convenience during the interpretation of the mercury porosimetry results, the total specific porous volume was always determined in mm^3g^{-1} and the bulk and mineral densities were normalized to the density of water.

2.2.3.1. Mercury porosimetry curves

Four of the materials show unimodal pore access diameter distributions with maxima at 30 µm and 9 µm for the Fontainebleau and the "Grès à Meules" sandstones and 0.8 µm and about 1 µm for the chalk and the Vuillecin limestone, respectively. The tuffeau limestone differs from the others in its seemingly bimodal pore access diameter distribution: two maxima were recorded at 10 µm and 10 nm.

Both the Fontainebleau sandstone and the Mons chalk show a relatively narrow pore access diameter distribution (Fig. 13a and 14a), while wide pore access diameter distributions can be observed for the other rocks. Most of the "Grès à Meules" sandstone curves and the tuffeau limestone curves (Fig. 13b and 14b) suggest that these two rocks contain only a few pore accesses with diameters below 4 nm.

2.2.3.2. Specific pore volume, porosity and density

Table 3 shows that the mercury porosimetry parameters are quite similar to those of the water porosimetry. Comparing the two methods, the porosity difference is less than 1% for the tuffeau limestone and the "Grès à Meules" sandstone. This proves that the pore accesses with diameters below 4 nm correspond to a small part of the total porosity of these rocks (less than 2 and 4% in the limestone and the sandstone, respectively). In most cases the water porosity (N_W) is higher than the mercury porosity (N_{Hg}). The unusual feature of the Fontainebleau sandstone ($N_{Hg} > N_W$) is due to the large size of the pores: a slight volume of water was loosed during the sample weighing, which induced an under-evaluation of the total water porosity. Using samples with large volumes could avoid this effect; however, this particular study required the use of small volumes.

The densities (obtained from the water and the mercury porosimetry, and from the helium density measurements) of the Fontainebleau sandstone, the Mons chalk and the Vuillecin limestone are quite comparable with those of the pure mono-crystal of quartz (2.65) and calcite (2.70), respectively. This confirms the mono-mineral composition of these materials.

The relative standard deviation of the pore volume, the porosity and the mineral density are relatively low for all the materials except the Vuillecin limestone. Deviations of more than 10% were recorded for the Vuillecin limestone. That means that this rock's porous structure is more heterogeneous than the others'.

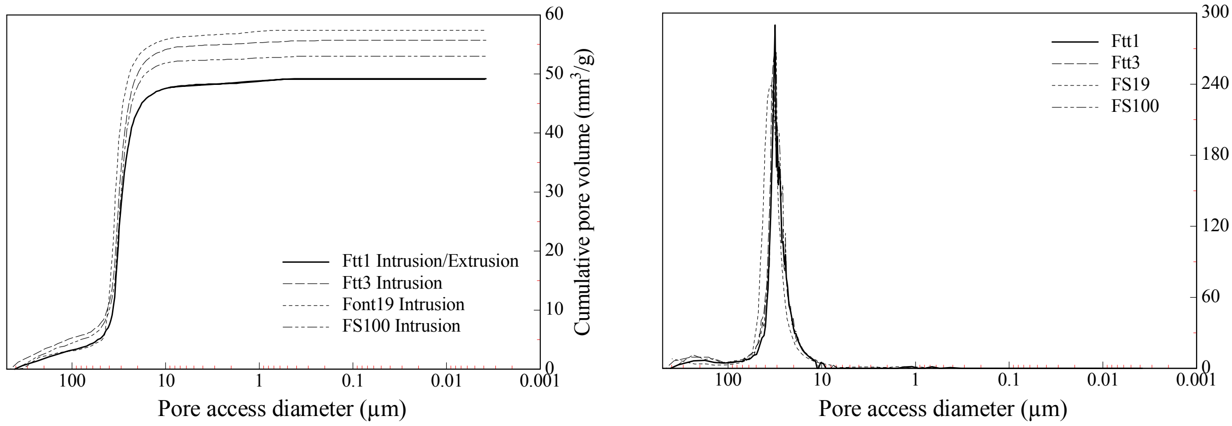
a. Fontainebleau sandstone

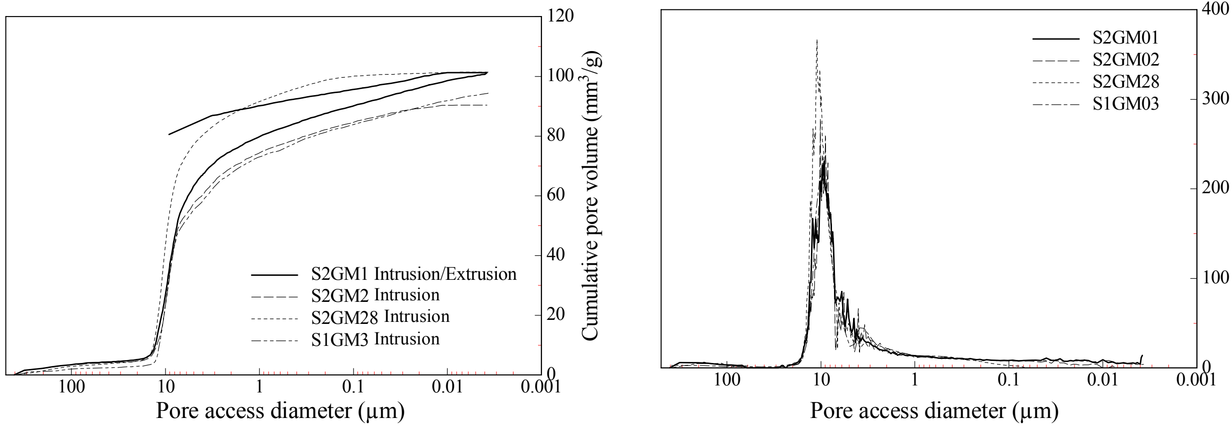
b. "Grès à meules" sandstone

Fig. 13 – Cumulative pore volume curves (on left) and pore access diameter distributions (on right) of the two sandstones – Solid lines: one mercury intrusion/withdrawal cycle; dashed lines: mercury injection without withdrawal.

a. Mons chalk

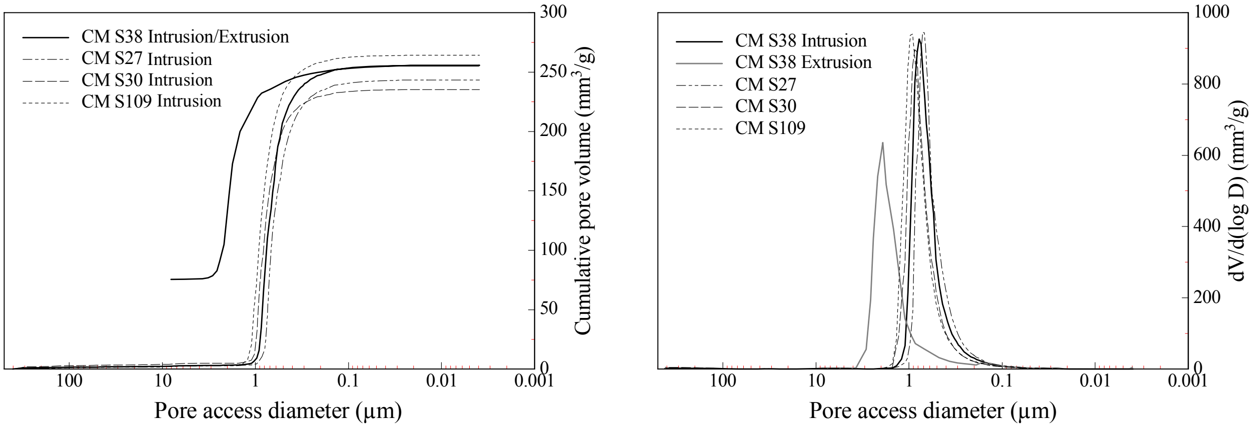

b. Tuffeau limestone

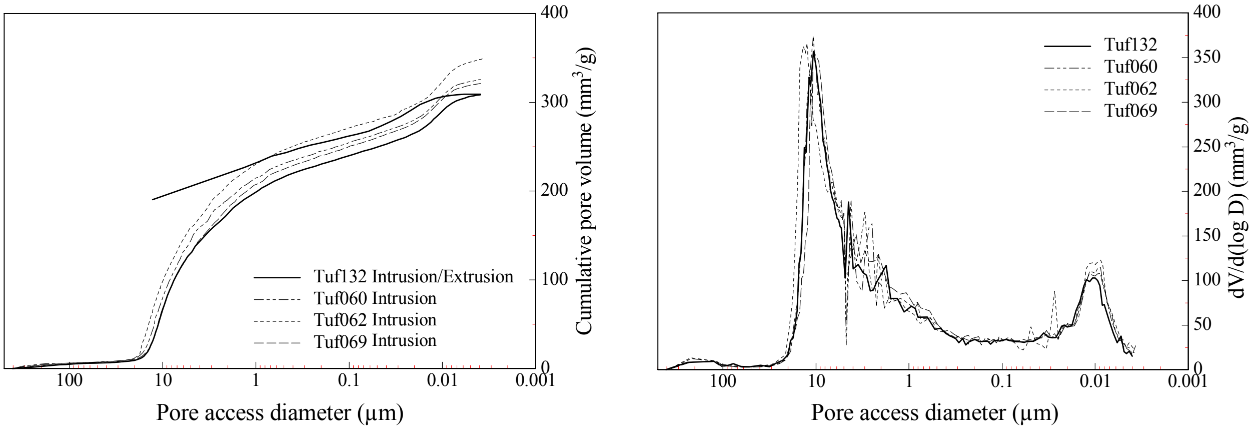

c. Vuillecin limestone

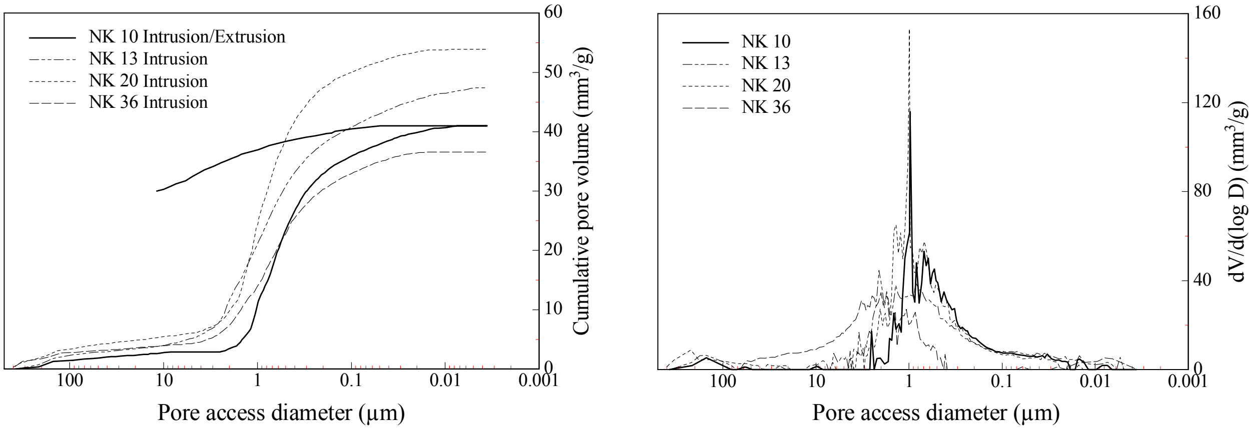

Fig. 14 – Cumulative pore volume curves and pore access diameter distributions of the chalk and the two limestones – solid line: example curves for a cycle mercury intrusion/withdrawal; dashed line: example curves for a mercury injection without withdrawal.

Table 3 – Statistical data from the mercury porosimetry (index Hg); Comparison with the water porosimetry (index W) and the helium pycnometry (index He).

		Font. sandstone	**"Grès à Meules" sandstone**	**Mons chalk**	**Tuffeau limestone**	**Vuillecin limestone**
Number of samples		15	14	20	15	13
Specific pore volume, porosity, density						
Hg	$V^*_{p,Hg}$ (mm^{3}g^{-1})	53.2	96.0	250.3	325.9	47.4
	Min[$V^*_{p,Hg}$] (mm^3 g^{-1})	47.7	92.1	235.3	308.7	36.6
	Max[$V^*_{p,Hg}$] (mm^3 g^{-1})	57.4	101.0	264.1	349.1	53.9
	$\sigma_{R,V^*_{p,Hg}}$ (%)	5.3	3.5	3.0	3.5	11.4
	N_{Hg} (%)	12.30	20.16	40.50	45.08	11.29
	Min[N_{Hg}] (%)	11.14	19.27	38.97	43.85	8.96
	Max[N_{Hg}] (%)	13.19	21.13	41.96	40.70	12.65
	$\sigma_{R,N_{Hg}}$ (%)	5.0	3.5	1.8	1.7	10.3
	$d_{M,Hg}$	2.64	2.62	2.71	2.52	2.69
	Min[$d_{M,Hg}$]	2.60	2.58	2.70	2.48	2.68
	Max[$d_{M,Hg}$]	2.67	2.66	2.74	2.54	2.70
	$\sigma_{R,d_{M,Hg}}$ (%)	0.8	1.1	0.4	0.8	0.4
	$d_{B,Hg}$	2.31	2.10	1.62	1.38	2.39
	Min[$d_{B,Hg}$]	2.30	2.08	1.66	1.34	2.35
	Max[$d_{B,Hg}$]	2.34	2.11	1.59	1.42	2.45
	$\sigma_{R,d_{B,Hg}}$ (%)	0.5	0.4	1.3	1.8	1.3
W	$V^*_{p,W}$ (mm^3 g^{-1})	50.3	98.9	252.2	334.4	48.2
	N_W (%)	11.73	20.97	40.68	46.00	11.51
	$d_{M,W}$	2.64	2.66	2.72	2.55	2.71
He	$d_{M,He}$	2.64	2.65	2.71	2.54	2.71
Specific surface area						
Hg	S_{Hg} (m^2 g^{-1})	$13\ 10^{-3}$	2.66	1.80	21.88	1.10
	Min[S_{Hg}] (m^2 g^{-1})	$11\ 10^{-3}$	0.36	1.53	20.40	0.60
	Max[S_{Hg}] (m^2 g^{-1})	$14\ 10^{-3}$	3.32	2.10	24.81	1.73
	$\sigma_{R,S_{Hg}}$ (%)	7.7	31.0	8.3	3.8	30.9
Pore access size						
Hg	D_{50} (µm)	31.40	7.23	0.80	3.23	0.84
	Min[D_{50}] (µm)	29.70	5.38	0.65	2.59	0.67
	Max[D_{50}] (µm)	33.85	9.41	0.88	3.92	1.09
	$\sigma_{R,D_{50}}$ (%)	11.8	13.9	9.5	13.0	13.8
	D_{AV} (µm)	18.16	0.23	0.54	0.05	0.19
	Min[D_{AV}] (µm)	15.72	0.11	0.46	0.05	0.12
	Max[D_{AV}] (µm)	21.82	1.12	0.62	0.06	0.29
	$\sigma_{R,D_{AV}}$ (%)	10.1	128.9	9.4	4.3	27.1
	D_H (µm)	39.25	12.58	1.18	17.52	2.25
	Min[D_H] (µm)	38.01	11.88	1.38	14.79	1.59
	Max[D_H] (µm)	42.75	13.62	0.97	21.39	3.65
	σ_{R,D_H} (%)	5.5	4.3	11.3	13.5	30.7

2.2.3.3. Specific surface area

It can be noted that S_{Hg} of the Fontainebleau sandstone is very low (10^{-2} m²g^{-1}), while S_{Hg} of the tuffeau limestone is very high (23 m²g^{-1}), and that $\sigma_{R,Hg}$ is significantly high for the "Grès à Meules" sandstone and the Vuillecin limestone (Table 3).

The specific surface area is quite dependent on the mineral content of each material, which is explained in the next section (§ 2.2.4.).

Remark:

Mercury porosimetry is based on a cylindrical pore model. Pores in the geomaterials have all kinds of shapes except regular cylindrical shapes. Despite the large application of this model during the calculation of the specific surface area, the mercury porosimetry displayed S_{Hg} values, which are in strong accordance with those of S_{BET} obtained by the gas adsorption (§2.3.3.1.). Thus, it can be asserted that, assuming the pores are cylindrical, calculating area from geometrical relationships is as valid as computing the theoretical surface area on the basis of the work required to immerse a surface in mercury. As shown below, the two computations are identical.

- Theory based on the required work:

The work required for immersing an area dS of a solid into mercury:

$$dW = \gamma \cos\theta \, dS$$

with γ being the surface tension of mercury and θ its contact angle with the solid surface.

For an incremented volume dV_p of mercury forced into a pore under pressure P, the precedent relation becomes:

$$-PdV_p = \gamma \cos\theta \, dS \quad (14)$$

- Cylindrical pore geometry:

According to Washburn, the minimum pressure P necessary for mercury to invade a cylinder with diameter D is given by Relation *11*. The circumference of the cylinder is equal to πD, and the cross section S' to πD²/4. If dS' is the cylinder's walled area, which is covered by mercury along a length dh (corresponding to a volume dV_p), this area is expressed by:

$$dS' = \pi D dh = \frac{4S' dh}{D} = \frac{4dV_p}{D}$$

Thus, replacing D by its expression (Relation *11*) leads to establish the relation:

$$-PdV_p = \gamma \cos\theta \, dS' \quad (14bis)$$

It can be concluded from Relations *14* and *14bis* that dS = dS'. Hence, Washburn's model must be convenient for the calculation of the specific surface area. The results of the specific surface area calculations from mercury porosimetry must depend only on the limits of the method itself (pore access diameter, 4 nm diameter limit…). These limits were reported in detail in §2.3.3.1. during a comparison between mercury porosimetry and the gas adsorption method.

2.2.3.4. D_{50}, D_{AV} and D_H

For all materials, D_{AV}, the average pore access diameter, is smaller than D_{50}, the median pore access diameter (Fig. 15). The difference between the two diameters varies from one material to another. In fact, D_{AV}, calculated from the ratio of the specific total pore volume divided to the specific surface area (Appendix D, Relation *8D*), strongly depends on the number of smallest pore accesses. These accesses mainly contribute to the value of the specific surface area and only slightly contribute to that of the specific total pore volume. D_{50} is the smallest diameter, for which half of the total pore volume has been filled by mercury, and is more directly linked to the pore volume distribution. D_{AV} is as closer to D_{50} as the pore access diameter distribution is narrow and unimodal. This is the case of the chalk and the Fontainebleau sandstone (Fig. 15).

It was seen that better predictions of the transport properties can be obtained using D_{50} during the application of models (in particular the Kozeny-Carman model; §3.2.5.).

Concerning the variations in the three parameters, two important remarks can be made:

- the D_{50} and D_{AV} relative standard deviations are often close to or more than 10%; they are particularly high for the “Grès à Meules” sandstone and the Vuillecin limestone;
- the D_H relative standard deviations -- high for the limestones and the chalk -- are noticeably low for the two sandstones.

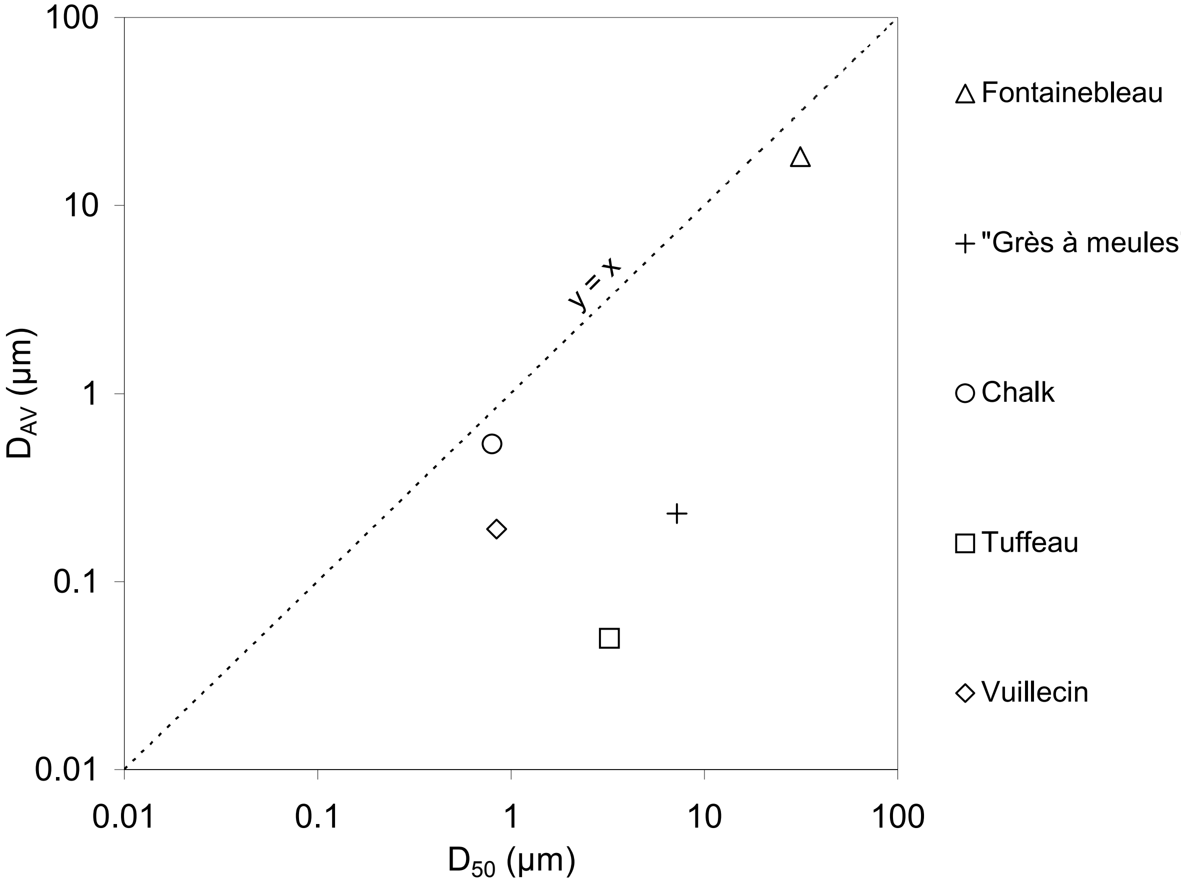

Fig. 15 – Comparison between D_{50} and D_{AV}: a point on the y=x curve would mean that the material contains a perfect unimodal pore access diameter distribution.

2.2.4. Correlation with the petrographical analysis

2.2.4.1. Fontainebleau sandstone

The petrograghical analysis led us to conclude that the porous network of the Fontainebleau sandstone is made of inter-granular macropores connected by smaller channels (Table 1, §1.3.). Thus, the mercury porosimetry results are to be understood under the assumption that the measured diameters belong to the pore accesses. The further correlation between the mercury porosimetry and the image analysis (§2.4.3.3.) made it possible to quantify the mean pore-to-throat-size ratio and to confirm that the difference between the pore size and the pore access diameter is significant in the Fontainebleau sandstone. The results of the mercury porosimetry have shown that the diameters of these pore accesses slightly vary.

Some pores are accessible by large diameters (400 to 40 µm), which were recorded at the beginning of the mercury injection (Fig. 13a). These pores represent a volume of less than 5% of the total pore volume; they are macropores located at the borders of the cylindrical sample. The range of pore access diameters related to these kinds of pores varies from one sample to another and induces relative standard deviations $\sigma_{R,D_{50}}$ and $\sigma_{R,D_{AV}}$ over 10%.

Micropores at the detrital grain/overgrowth interfaces and micro-channels in strongly cemented zones were observed on thin sections and by SEM. The mercury porosimetry made it possible to quantify the part of this microporosity, which represents 4% of the total porosity and which corresponds to pore access diameters from 15 µm to 0.2 µm (Table 4). This proves that the sandstone is mainly macroporous as the petrographical analysis concluded.

The very low value of the specific surface area (13 10^{-3} m^2g^{-1}) is in accordance with the smooth faces of the quartz grains observed on SEM and thin section images.

To conclude, the homogeneity of the porous structure of the Fontainebleau sandstone is confirmed by mercury porosimetry, despite variations in D_{50} and D_{AV}. These variations are mainly due to sample border artefacts as shown above. Hence, variations in the quartz overgrowth revealed by petrographical analysis have very little influence on the mercury porosimetry parameters (for sample volumes of 1-2 cm^3). That means that, during the diagenesis, silicification has engendered randomly distributed cemented zones.

Table 4 – Microporosity ($N_{Micro,Hg}$) and macroporosity ($N_{Macro,Hg}$) in the Fontainebleau sandstone: absolute values (%) and values normalized to the total porosity (% of N_{Hg}).

	%	% of N_{Hg}
$N_{Micro,Hg}$ (D < 15 µm)	0.5	4.1
$N_{Macro,Hg}$ (D > 15 µm)	11.8	95.9
N_{Hg}	12.3	100.0

2.2.4.2. “Grès à Meules” sandstone

Under pressure, mercury fills the main part of the pore volume of this rock for pore access diameters of about 10 µm. Some smaller volumes are filled for diameters within the range of 5 µm to 4 nm (Fig. 13b). This wide pore access diameter distribution can be explained by the presence of clay mineral concentrations, which was revealed by XRD analysis (illite, kaolinite and chlorite).

MATTHEWS et al. (1996) injected a synthetic amorphous gel composed of Al_2O_3, $2SiO_2$ in Fontainebleau sandstone samples. They showed that various artificial clay concentrations induce a change in the shape of the mercury porosimetry curves and an enlargement in the pore size distribution, without significantly changing the overall porosity of the rock.

For the "Grès à Meules" sandstone, which has a relatively constant porosity from one sample to another, the clay minerals induce a significant enlargement in the pore access diameter distribution. Moreover, some remarkable differences exist between the samples: for instance, no mercury penetrated the sample S2GM28 for diameters less than 0.1 µm, whereas it penetrated the sample S1GM3 up to a 4-nm diameter (Fig. 13b). This is due to various concentrations of clay minerals from one sample to another. Indeed, S2GM28 must have a lower content of clay minerals than S1GM3. Variations in the clay concentrations also explain the high relative standard deviations (σ_R) of the specific surface area (31%), and of D_{AV} (128%), which was calculated using S_{HG} (see Appendix D, Relation *6D*).

Aside from these variations from sample to sample, the hydraulic diameter D_H is almost constant ($\sigma_{R,D_H} = 4\%$). That means that there is a given constant diameter, from which the main part of the pore volume can access. As shown by the petrographical analysis, the clay minerals, which rim the grains, induce a trend towards identical sizes of the accesses of the inter-granular pores. The intruded volumes of mercury recorded for pore access diameters from 5 µm to 4 nm correspond to inter-particle pores in clay mineral aggregates.

The clay minerals (mainly illite and kaolinite) which fill or partially fill the throats of this sandstone have a strong influence on the mercury porosimetry measurements. Mercury porosimetry shows that they strongly contribute to variations in the pore access diameter distribution. These clay concentrations vary on the scale of a small sample (1-2 cm^3), which induces large variations in the specific surface area without significantly changing the porosity.

2.2.4.3. Mons chalk

The mercury porosimetry curves show that the chalk is microporous and that the pore access diameters are spread over a narrow range of about 1 µm (Fig. 14a). Very small volumes of injected mercury were recorded for diameters above 15 µm. No mercury was injected into the samples for diameters below 40 nm.

The low standard deviations of most of the parameters (Table 3) prove the homogeneity of the material on the small sample scale. An almost constant total porosity was already recorded for the scale of bigger core samples (§2.1.). The D_{50} and D_{AV} relative standard deviations were about 10%. Let us note that for this sandstone, D_H was less variable. These variations are negligible in comparison with those of the Vuillecin limestone.

The mercury porosimetry confirmed the observation made by the petrographical analysis: the porous structure of the Mons chalk consists of a homogeneous microporous network. Some macropores, revealed on thin sections or by SEM (Table 1), are isolated and represent a small part of the pore volume: they do not influence the mercury porosimetry parameters.

2.2.4.4. Tuffeau limestone

The curves show a wide range of pore access diameters in this limestone (Fig. 14b). Four domains could be distinguished on the mercury porosimetry curves (Fig. 16). The calculation of the mercury porosimetry parameters for each domain (Table 5), i.e. each pore access diameter range, led us to quantitatively characterize the porous structure of each domain with regard to the mineralogy of the material (with the help of the petrographical analysis).

Domain I: Pore access diameters above 20 µm

Domain I represents a small part of the porous network (6% of the total pore volume). The observation made on thin sections and by SEM led us to associate Domain I to macropores, which are directly accessible by mercury and located between big grains (quartz, K-feldspars, micas, glauconite, bioclasts), and disturbed packs of opal-CT spherules. These macropores induce a negligible part of the total specific surface area (3 10^{-3} m² g^{-1}, i.e. 10^{-2} %).

Domain II: Pore access diameters from 20 to 5 µm

This domain is characterized by a small range of pore access diameters of about 10 µm. This specific pore class is characteristic of the tuffeau limestone. This class of pores represents an important part of the pore volume – 35% of the total pore volume – and concerns a small specific surface area (52 10^{-3} m² g^{-1}, i.e. 0.2% of the total pore area). Domain II was associated with the opal-CT spherules, which were observed in high quantity on thin sections. More precisely, Domain II was associated with the pores between the packed spherules themselves and between the spherules and the neighbouring mineral phases.

Domain III: Pore access diameters from 5 to 0.02 µm

Domain III is spread over a very large diameter range and is not characterized by a particular dominant class of pore accesses. Nevertheless, its specific pore volume (144 mm³ g^{-1}) represents the highest part of the total specific pore volume of the rock (44%). This class of pore accesses concerns a non-negligible part of the specific surface area (12%).

Some specific mineral phases could be linked to this domain:

- The opal-CT spherules, which have a lamellar structure, often contain pores and pore accesses with diameters below 1 µm (Image board D, Fig. D).
- Microporous areas of micritic calcite also contribute to the porous volume of this domain.
- Some clay mineral concentrations (mainly illite) at the grain borders reduce the pore and pore access sizes, thus inducing diameters which belong to this domain.

Domain IV: Pore access diameters from 20 to 4 nm

In this domain, the pore access diameter distribution is characterized by a maximum at 10 nm. Although its pore volume represents only 14% of the total porous volume, its porous structure is responsible for the high specific surface area of the material (86% of the total specific surface area). Domain IV could be linked to mineral phases, which contain nanometric pores, namely:

- clay minerals like smectites (interlayer spaces and spaces between the fine particles),
- exfoliated muscovite (interlayer micropores),
- glauconite grains (intra-granular micropores).

This analysis has shown the complexity of the porous structure of the tuffeau limestone. It also pointed out the role of the different mineral phases in the porous structure.

To summarize, a large part of the pore volume of this limestone is due to micropores around and inside the opal-CT spherules and micropores between the calcite crystals of the micrite areas. The mineral heterogeneity is mainly responsible for the wide pore size distribution. The high specific surface area (23 m² g^{-1}) is mainly due to the presence of smectite aggregates and glauconite grains. Despite the mineral variety, variations in the mercury porosimetry parameters are low from one sample to another. This means that the arrangement of the different minerals remains relatively homogeneous at the scale of the samples.

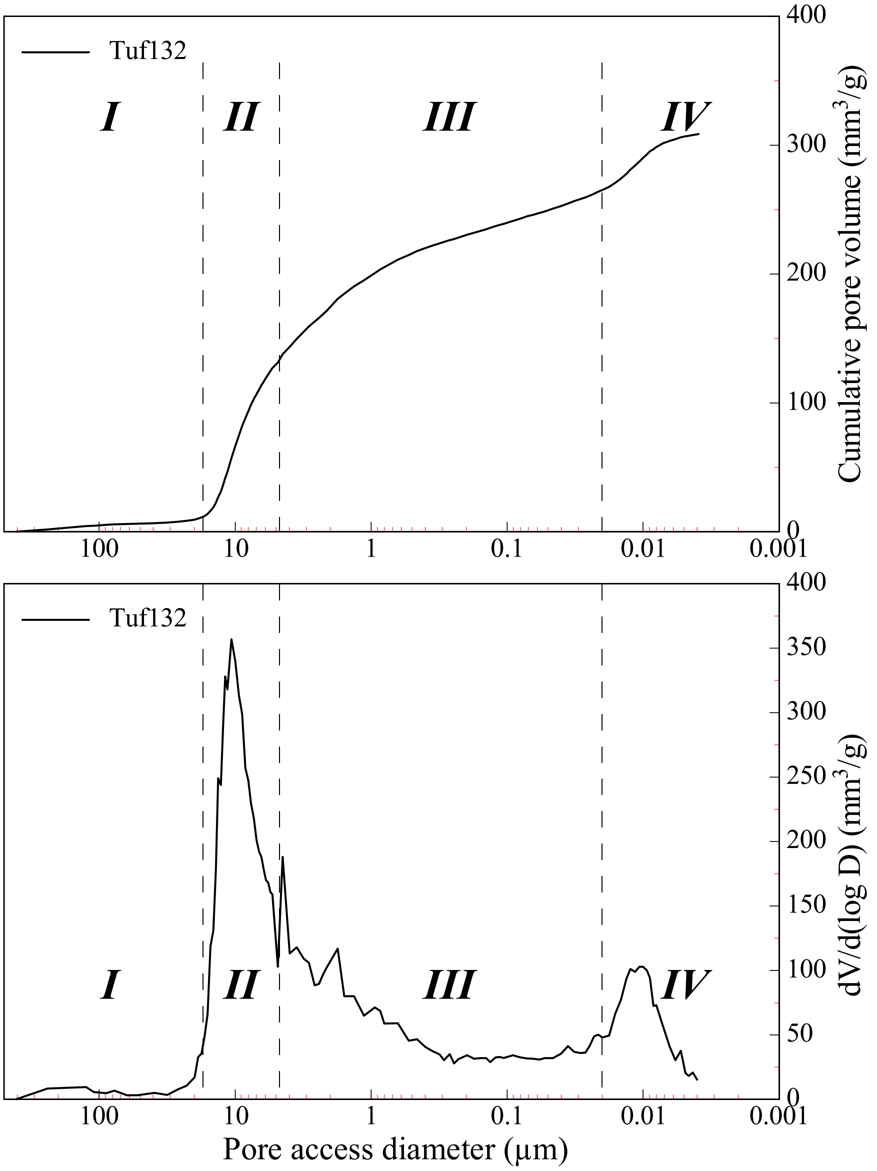

Fig. 16 – Division of the four typical domains (I, II, III, IV), which characterize the tuffeau limestone, shown as an example with the Tuf132 sample.

Table 5 – Mercury porosimetry parameters averaged on 15 samples of the tuffeau limestone for the four diameter domains defined in Figure 16.

Parameter	Domain I D>20 µm	Domain II 20>D> 5 µm	Domain III 5>D>0.02 µm	Domain IV 0.02>D>0.004 µm	Entire diameter spectrum
$V_{P,Hg}$ (mm^3 g^{-1})	20.2	114.6	143.8	47.1	325.9
N_{Hg} (%)	2.78	15.85	19.90	6.50	45.08
S_{Hg} (m^2 g^{-1})	3 10^{-3}	52 10^{-3}	2.77	19.57	22.88
D_{50} (µm)	25.4	9.5	1.0	10.1 10^{-3}	3.2

2.2.4.5. Vuillecin limestone

The large range of pore access diameters displayed by the mercury porosimetry distribution curves (Fig. 14c) was linked to the wide range of pores observed on the thin sections and by SEM. The mercury porosimetry curves shows the presence of micropore accesses within the range of very small diameters from 0.1 µm to 4 nm (this lower limit is variable according to the sample).

Diameters recorded from 300-200 to 5 µm correspond to accesses to numerous moldic and residual macropores, which are situated either where the dissolved bioclasts once were or inside the sparitic areas. The pore access diameters, from 5 µm to 0.1 µm, must concern the micrite areas. The smallest diameters recorded from 0.1 µm to 4 nm must belong to the throats located in stromgly cemented areas of sparites or of microsparites.

The strong deviations in the mercury porosimetry parameters, in particular D_H and S_{Hg} (Table 3), are due to amounts of the micritic and sparitic areas and of the bioclasts, which differ from one sample to another. For example:

- Only some micrite calcite areas, and simultaneously numerous sparite calcite areas or bioclasts means a lower specific surface area, and vice versa.
- A high degree of cementation means smaller throats and influences the hydraulic diameter.

To conclude, the mercury porosimetry results confirms that the Vuillecin limestone is the most heterogeneous of the five materials. Indeed, zones of various mineral and pore structures, heterogeneously distributed inside the rock, induce high variations in the calculated mercury porosimetry parameters.

2.2.5. Trapped mercury porosity

The mean trapped mercury porosity ($N_{TR,Hg}$) and its percentage of the total porosity ($N^*_{TR,Hg}$) are given in Table 6. One example of the mercury withdrawal curve of each rock is shown in Figures 12 and 13.

2.2.5.1. Fontainebleau sandstone and Mons chalk

In the Fontainebleau sandstone, the withdrawal curve overlaps the injection curve (Fig. 13a, sample Ftt1) for diameters from 4 nm (400 MPa) to 10 µm (0.1 MPa): mercury withdrawals only from the microporosity, which constitutes a small part of the total porosity (mercury remained trapped in 96% of the porous volume). On the contrary, the mercury mainly withdrew from the chalk samples: mercury remained trapped in about 30% of the total porous volume (Fig. 14a). Moreover, the narrow hysteresis observed shows that mercury withdrew from pores with sizes similar to those of the pore accesses.

2.2.5.2. “Grès à Meules” sandstone, tuffeau and Vuillecin limestones

Mercury was trapped in about 70% to 80% of the pore volume of these materials (Table 6). The high levels of trapped porosity, which were recorded for the rocks, are due to non-random heterogeneities. In the Vuillecin limestone, juxtaposed areas characterized by different pore and pore access sizes, allowed mercury to be trapped in zones with large pores, i.e. in sparitic areas and in dissolved bioclasts. Because of the various classes of throat diameters in the tuffeau limestone and the “Grès à Meules” sandstone, the non-random heterogeneities induced the trapping of mercury, where the pores were largest and where they could be accessed by small throats. Hence, mercury remained trapped mainly in the macropores and in the residual pores between the opal-CT spherules themselves and between the spherules and the neighbouring mineral phases of the tuffeau limestone. In the “Grès à Meules” sandstone, the mercury may logically be trapped in the numerous macropores of the coarse grain layers.

Thus, like the pore-to-throat-size ratio, non-random heterogeneities also govern the amount of mercury that is able to be trapped inside a rock.

2.2.5.3. Comparison with the trapped water porosity

There are significant differences between the values of trapped porosity obtained from the two techniques (Table 6). For all the materials, the trapped mercury porosity is from two to four times higher than the trapped water porosity.

No direct correlation could be made between the trapped mercury porosity and the trapped water porosity, due to the different trapping processes between the two techniques. Nevertheless, it seems that the ratio $N_{TR,Hg}/N_{TR,W}$ depends on the type of rock: $N_{TR,Hg}/N_{TR,W}$ is equal to 4 for the chalk and the tuffeau limestone and to 2 for the Fontainebleau and "Grès à Meules" sandstones.

Table 6 – Mean trapped mercury porosity ($N_{TR,Hg}$, and $N^*_{TR,Hg}$ as a percentage of the total porosity); comparison with the mean trapped water porosity (Table 2).

Material	Fontainebleau sandstone	"Grès à Meules" sandstone	Mons chalk	Tuffeau limestone	Vuillecin limestone
$N_{TR,Hg}$ (%)	11.75	15.79	12.10	30.02	8.59
$N^*_{TR,Hg}$ (%)	95.5	78.3	29.9	66.6	76.1
N_{Hg} (%)	12.30	20.16	40.50	45.08	11.29
$N_{TR,W}$ (%)	5.47	6.96	3.24	7.68	3.46
$N^*_{TR,W}$ (%)	43.9	32.8	7.4	16.6	29.4
N_W (%)	12.45	21.21	43.67	46.31	11.77
$N_{TR,Hg}/N_{TR,W}$	2.2	2.4	4.0	4.0	2.6

On the one hand, the pores and throats have sizes of the same order in the chalk (for almost only one class of pores) and in the tuffeau limestone (for each class of pores), as seen above. On the other hand, the pores are quite larger than the throats inside the Fontainebleau sandstone (macropores connected by small throats) and the "Grès à Meules" sandstone (due to clays which fill the throats).

These characteristics, and the results of the determination of the trapped mercury and water porosity, led us to conclude that the process of mercury trapping must be more sensible to the pore-to-throat-size ratio ($R_{P/T}$) than the water trapping. That means that $N_{TR,Hg}/N_{TR,W}$ inversely varies in relation to $R_{P/T}$, which leads to the following postulate:

$$R_{P/T} = \lambda \frac{N_{TR,W}}{N_{TR,Hg}} \qquad (15)$$

Determination of λ

Values of the factor λ were calculated using the coefficient $R_{P/T}$, which was determined during the BSE image analysis (§2.4.3.3.) of the Fontainebleau sandstone and the chalk (Table 7). The value of λ was found about 8 for both rocks, showing the validity of Relation *15* for these rocks. It would be hazardous for the same relation with the same value of λ to be valid for the other rocks ("Grès à Meules" sandstone, tuffeau and Vuillecin limestones), given their characteristics: a wide range of pore and pore access sizes, mineral heterogeneity...

Table 7 – Factor λ calculated for the Fontainebleau sandstone and the chalk.

	$R_{P/T}$	$N_{TR,W}/N_{TR,Hg}$	λ
Font. sandstone	3.6	0.45	7.9
Mons chalk	2.2	0.27	8.1

2.2.6. Summary

A close relationship was established between the porous structure and the mineralogy by combining the petrographical analysis with the mercury porosimetry.

The mercury porosimetry made it possible to better appreciate the homogeneity of the five rocks. The Vuillecin limestone distinguishes itself from the rocks due to very large variations in the parameters of its porous structure (porosity, pore size, specific surface area).

Up to this point, this study has given information about the role of the clay minerals in a porous medium. These minerals ensure the cohesion of the material (as in the “Grès à Meules” sandstone) and control the sizes of the accesses to the primary pores. The inter-granular spaces in clay mineral concentrations also induce a wide distribution of the void sizes in a material. In a larger grain structure, the small clay particles are mainly responsible for non-random heterogeneities, which can induce the trapping of mercury or air.

2.3. Gas adsorption

2.3.1. Theory

2.3.1.1. Definitions

The adsorption of a gas on a solid occurs when the molecule concentration of the gas becomes higher on the solid surface than inside the gas phase (MICHOT L., 1990). There are two distinguished processes: physical adsorption and chemical adsorption.

Physical adsorption

Physical adsorption is due to the Van der Waal’s interactions. Physical adsorption often results in a multi-layer molecular adsorption, which characterizes the phenomenon.

Chemical adsorption

Chemical adsorption is due to the ionic and covalent chemical bonds between the solid surface and the gas molecules. Chemical adsorption results in a molecular mono-layer adsorption characteristic of this phenomenon.

At the equilibrium, which is rapidly reached, the amount of adsorbed gas depends on the temperature, the partial vapour pressure, the gas chemical composition and the chemical-physical state of the solid surface.

The use of non-polarized and chemically inert gases like nitrogen, argon or krypton, makes it possible to only consider the physical adsorption.

Adsorption isotherm

The representation of the adsorbed gas amount versus the equilibrating pressure at a constant temperature is called the “adsorption isotherm”. After IUPAC, the most part of the isotherms, which result from physical adsorption, can be summarized in six types of curves (Fig. 17).

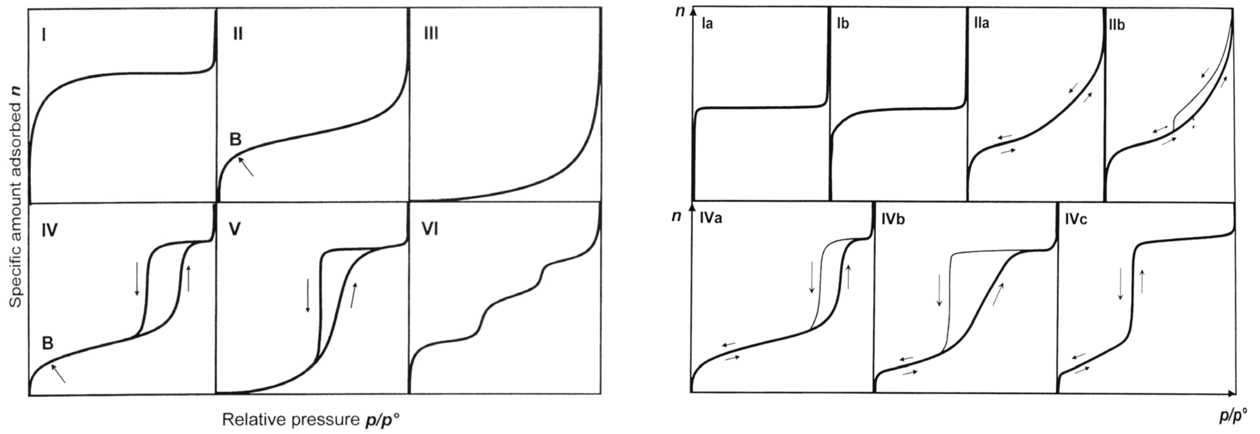

Fig. 17 – The six types of physical adsorption isotherms (on left) and the updated under-classification (on right), after IUPAC (Rouquerol F.et al. 1999).

2.3.1.2. The BET theory

Langmuir I. (1918) developed an adsorption theory where the homogeneous surface of a solid was regarded as an array of adsorption sites. A state of dynamic equilibrium was postulated in which the rate of molecules coming from the gas phase and sorbing onto bare sites was equal to the rate of molecules evaporating from the occupied sites (Gregg S.J. & Sing K.S.W., 1982). From this hypothesis, Langmuir established the following equation:

$$V_a = \frac{V_m bP}{1 + bP} \quad (16)$$

in which V_a is the volume of gas adsorbed at pressure P, V_m the volume of gas adsorbed when the entire surface is covered by a molecular mono-layer and b is an empirical constant.

Relation *16* can be rearranged to the linear form:

$$\frac{P}{V_a} = \frac{1}{V_m b} + \frac{P}{V_m} \quad (17)$$

This theory is more applicable to chemical adsorption than to physical adsorption, because chemical adsorption leads to the creation of a molecular mono-layer on the solid (Paul A. Webb & Clyde Orr, 1996).

Brunauer, Emmett & Teller (1938) developed a theory applicable to the multi-layer conformations, which led them to establish the following relation:

$$V_a = \frac{V_m c_o P}{(P_0 - P)\left[1 + (c_o - 1)\frac{P}{P_0}\right]} \quad (18)$$

after some simplification hypotheses (Fripiat et al., 1971):

- The solid surface is homogeneous: all the surface sites are identically accessible and have equivalent energies.
- There are no lateral bonds between the adsorbed molecules.
- The molecules can be adsorbed onto the next layer before the preceding one is fulfilled.
- From the second layer, the adsorption energy is equal to the liquefaction energy of the gas.

In Relation *18*, c_o is a constant and P_0 is the pressure reference.

Indeed, the experimental data are usually used with the following linear BET equation:

$$\frac{P}{V_a(P_0 - P)} = \frac{1}{V_m c_o} + \frac{c_o - 1}{V_m c_o}\left(\frac{P}{P_0}\right) \quad (19)$$

Plotting $P/[V_a(P_o\text{-}P)]$ versus P/P_o yields a straight line with intercept $1/V_m c_o$ and slope $(c_o\text{-}1)/V_m c_o$, from which the values of c_o and V_m are obtained.

2.3.1.3. Determination of the specific surface area

Despite its strict application conditions, the BET model is still used as a standard procedure for surface area determination. The BET surface area calculation can be generally applied to isotherms of types Ib, IIa, IIb, IVa, IVb, IVc, and VI (Fig. 17). The range of linearity of the BET plot is limited to low pressures, which rarely extend $P/P_0 = 0.35$ (ROUQUEROL F. et al., 1999).

The specific surface area ($m^2\ g^{-1}$) is calculated from the mono-layer capacity (expressed as the volume of gas V_m in m^3 at a standard pressure and temperature) according to the relation:

$$S_{BET} = \frac{\bar{a}\ V_m \mathcal{N}}{V_M\ w_S} \quad (20)$$

in which, $\bar{a}$ is the floor-space of one adsorbed gas molecule (m^2), V_M the molecular gas volume ($m^3\ mol^{-1}$), w_S the weight of the dried sample (g), and $\mathcal{N}$ the Avogadro's constant (mol^{-1}).

2.3.2. Experimental device and analysis conditions

The experimental device is represented in Figure 18. The apparatus ASAP 2010 (Micromeritics) performed the measurements using nitrogen (N_2) for analyzing the materials, except the Fontainebleau sandstone for which krypton (Kr) was required. Before the analysis, each sample was degassed at 80°C for 24 hours.

Samples of the same type (comparable volume and weight) were used for gas adsorption and mercury porosimetry. However, the stem of the gas absorption burettes had a diameter of about 7 mm. Thus, before the gas adsorption measurements, each sample was broken into smaller pieces, which created new adsorption surfaces. For the Fontainebleau sandstone, this surface increase was not negligible: breaking the sandstone meant that the precarious cohesion of the quartz grains particularly induced a lot of small particles, which in turn enhanced the total specific surface area. In order to minimize this effect, the samples of the Fontainebleau sandstone were cut (and not broken) into peaces with required sizes.

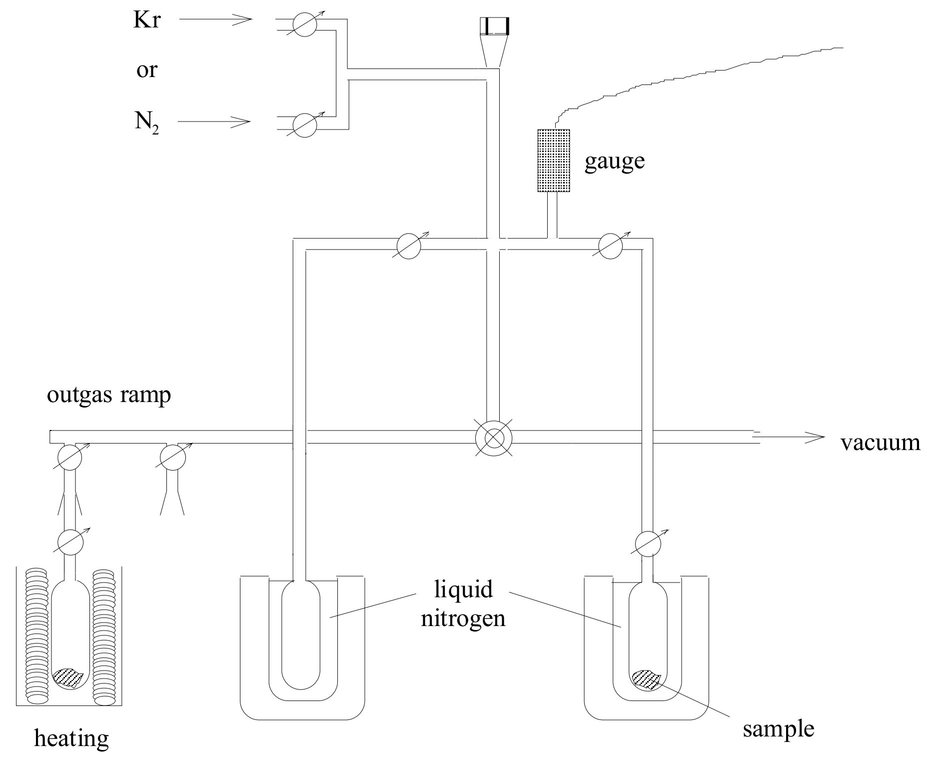

Fig. 18 – Diagram of the gas adsorption device.

2.3.3. Results and discussion

The exploitation of the isotherms obtained from the measurements (Appendix F) led us to calculate mean specific surface areas, whose values are summarized in Table 8. For the Fontainebleau sandstone, the measurement and the use of Kr did not allow for the whole isotherm (P/P_0 from 0 to 1) to be formed. The isotherms of the other materials are of Type II, and more precisely of Type IIa for the chalk and IIb for the others: the BET method can be applied.

Three of the rocks have values of S_{BET} between 1 and 3 m² g^{-1}; by comparison, the “Grès à Meules” sandstone has the higher specific surface area (about 3 m² g^{-1}). The Fontainebleau sandstone and the tuffeau limestone distinguish from these three rocks by their very low (0.01 m² g^{-1}) and very high (23 m² g^{-1}) specific surface areas, respectively.

2.3.3.1. Coincidence between S_{BET} and S_{HG}

Compared to the mercury porosimetry data (Table 8), S_{BET} is always slightly higher than S_{Hg}, which can be explained in the following way:

- High pressures applied to mercury could induce the deformation of the rock in some local places and limit the access to several micropores.
- The outgassing conditions of the two methods were different. Before the mercury intrusion, the samples were degassed under 2 10^{-2} Torr for about 15 min, at room temperature, whereas the gas adsorption measurements required an outgassing of 24 hours under 10^{-3} - 10^{-4} Torr, at 80°C. Thus, during the mercury porosimetry, some molecules of water could remain at the surface of the thin micropores.
- The lower limit of the accessible pores corresponds to an access diameter of 4 nm for mercury porosimetry and 1 nm for gas adsorption. A value deficit in the specific surface area measured by mercury porosimetry is always possible for materials like the tuffeau limestone and the “Grès à Meules” sandstone. Both rocks contain tiny pores in clay mineral concentrations.

Table 8 – Averaged, minimum and maximum values and relative standard deviation of the specific surface area from the gas adsorption measurements and from the mercury porosimetry.

Material	Fontainebleau sandstone	"Grès à Meules" sandstone	Mons Chalk	Tuffeau limestone	Vuillecin limestone
Number of samples	5	5	5	5	5
Adsorbat	Kr	N_2	N_2	N_2	N_2
Molecule floor-space (m²)	$21.0\ 10^{-20}$	$16.2\ 10^{-20}$	$16.2\ 10^{-20}$	$16.2\ 10^{-20}$	$16.2\ 10^{-20}$
S_{BET} (m² g^{-1})	$15\ 10^{-3}$	2.86	1.93	23.08	1.43
Min[S_{BET}] (m² g^{-1})	$13\ 10^{-3}$	2.10	1.85	19.77	1.01
Max[S_{BET}] (m² g^{-1})	$16\ 10^{-3}$	3.62	2.00	25.89	1.75
$\sigma_{R,S_{BET}}$ (%)	8.2	16.9	2.8	8.4	17.0
S_{Hg} (m² g^{-1})	$13\ 10^{-3}$	2.66	1.80	21.88	1.10
Min[S_{Hg}] (m² g^{-1})	$11\ 10^{-3}$	0.36	1.53	20.40	0.60
Max[S_{Hg}] (m² g^{-1})	$14\ 10^{-3}$	3.32	2.10	24.81	1.73
$\sigma_{R,S_{Hg}}$ (%)	7.7	31.0	8.3	3.8	30.9

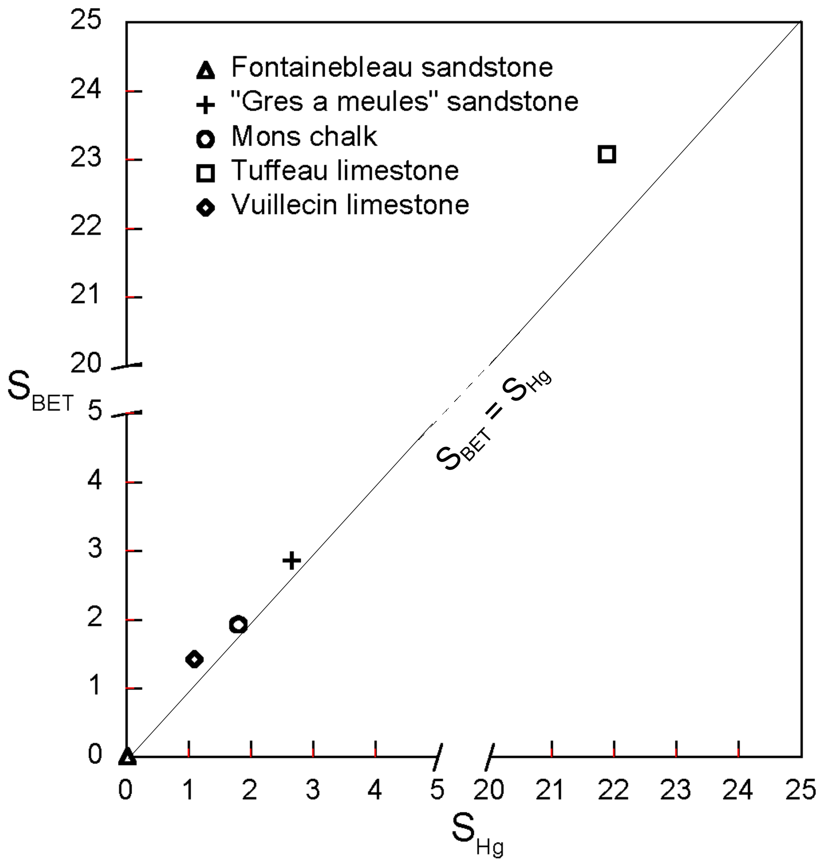

Fig. 19 – Gas adsorption specific surface area (S_{BET}) versus the mercury porosimetry specific surface area (S_{Hg}).

Despite higher values, the gas adsorption specific surface areas correlate with those of the mercury porosimetry with a factor close to 1 (Fig 19). Concerning the “Grès à meules” sandstone and the tuffeau limestone, both methods displayed comparable mean specific surface areas (S_{BET} about 2.9 m² g^{-1} and S_{Hg} about 2.7 m² g^{-1} for the “Grès à meules” sandstone; S_{BET} about 23 m² g^{-1} and S_{Hg} about 22 m² g^{-1} for the tuffeau limestone). It can be concluded that only a very small part of the porous network of these rocks was not invaded by mercury.

2.3.3.2. Relationship between S_{BET} and the pore and throat sizes

The different S_{BET} values found from one rock to another can be explained by the fact that the specific surface area is inversely proportional to the mean pore and throat sizes in a rock. Thus, the higher S_{BET} of the chalk (1.9 m² g^{-1}) compared to the Fontainebleau sandstone (0.013 m² g^{-1}) is due to the chalk’s smaller pores and throats. Nevertheless, the inverse relation is not linear for all rocks, because the specific surface area also varies according to other factors such as, the grain shape, the roughness of the grain surfaces, and the mineral content.

2.3.3.3. Influence of the mineral structure on the specific surface area

The best way to explain the S_{BET} differences between the rocks is to consider their mineral framework. Hence, clay mineral concentrations are responsible for high specific surface areas like in the “Grès à Meules” sandstone (kaolinite and filiform illite) and particularly in the tuffeau limestone (smectite). In the tuffeau limestone, the rough surface of opal-CT spherules also contributes to the very high S_{BET}. The very low S_{BET} of the Fontainebleau sandstone can be explained considering that the rock is made of macro-sized quartz grains with smooth surfaces. High variations in the S_{BET} values were recorded from sample to sample for the “Grès à Meules” sandstone and the Vuillecin limestone. These high variations are in accordance with the results of S_{Hg} obtained by mercury porosimetry (note that the gas adsorption and mercury porosimetry samples were of comparable volumes and weights). Such variations in these rocks are linked to changes in their mineral structures (changes in the clay mineral concentration or in the crystal size), as explained above in §2.2.4.2. and §2.2.4.5.

2.4. Image analysis

The main aim of the image analysis was to quantify the pore-to-throat-size ratio of the Fontainebleau sandstone and the chalk. It was also of interest to determine structural parameters such as the surface porosity, the pore size distribution, the specific surface area and the pore shape factor.

2.4.1. Image acquisition and analysis procedure

As shown in Figure 20, samples were taken from cylindrical cores of the materials. Two transversal (parallel to the cylinder’s axis) and two horizontal (perpendicular to the axis) slices were taken from the Fontainebleau sandstone. Only one horizontal slice was taken from the chalk; one slice was enough given the chalk’s small pore sizes. Each slice was degassed and then impregnated with a mixture made of a SpeciFix resin and a SpeciFix-20 curing agent (7:1). After 20 hours at room temperature, the resin was polymerized (solid) on the inside and outside of the sample. Then, the sliced surface was smoothly polished with control under the optical microscope. Back-Scattered Electron (BSE) images[1] were captured from the polished surfaces using a Scanning Electron Microscope JXA-8900 RL JEOL. The images were treated (binarization, correction or erosion/dilation cycles), and the structural parameters of interest were measured, using the software Image C 2.5a (IMTRONIC GmbH).

---

[1] In spite of big pores, the BSE method was also required for capturing the images of the Fontainebleau sandstone rather than the optical microscopy, since the BSE method provided better contrast between the resin and the material at the grain boundaries.

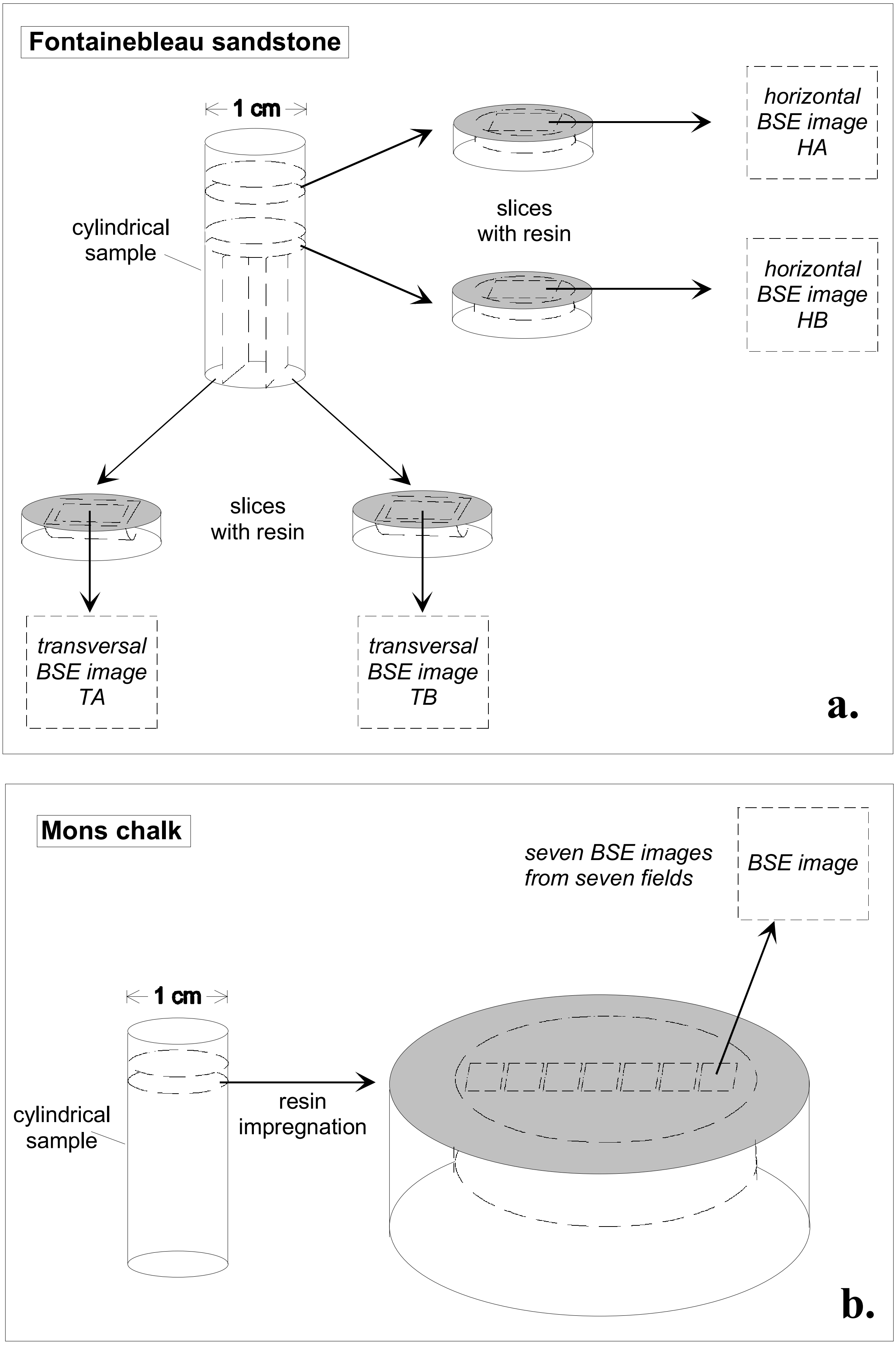

Fig. 20 – Diagram of the BSE image acquisition from polished surfaces (dark grey) of samples of the Fontainebleau sandstone (a.) and the Mons chalk (b.).

Capturing and treating the images required specific procedures (exposed below) depending on the rock.

Fontainebleau sandstone

In BSE imaging, a narrow beam of mono-energetic electrons was focused on a tiny area of the surface (a dwell point which corresponds to a pixel on the image). The amount of detected back-scattered electrons from the elastic collisions was translated into a grey level (0 to 255). The beam was then moved and the process was repeated pixel by pixel on the scanned surface. Four images were captured with a pixel resolution of 3x3 μm^2.

On these images, the pores, which were filled with the polymer (low atomic weights), and the mineral framework (quartz: high atomic weights of Si and O compared to those of C and H) were well contrasted in two grey levels: black and white, respectively. The grey level histogram of each image showed two narrow distinct peaks, which made the choice of the binarization threshold be evident. Some sparse black pixels, identified as artefacts by optical microscopy, were suppressed using an appropriate tool from the image treatment software.

Mons chalk

A previous preparation test pointed out two difficulties:

- Large domains in the centre of the slice remained unfilled with the SpeciFix resin.
- Chalk is fragile and the polishing phase led to the degradation of the surface (the calcite crystals were easily wiped off of the surface).

In the same vein, the chalk's skeleton was hardened using a silane mixture made of methyltrimethoxysilane (provided by Dow Corning; ref.: Z-6070), which provided chemical bonds with the inorganic calcite particle surfaces, and aminoethylaminopropyltrimethoxysilan (Dow Corning; ref.: Z-6020), which improved the chemical bonds. The silanes were dissolved in mixed methanol and distilled water. Each sample of the chalk was progressively imbibed with the liquid mixture at atmospheric pressure. In an oven at 60°C, the silane mixture changed into a thin solid polymer layer at the surface of the calcite micro-crystals, protecting them against the destructive effects of the polishing. The SpeciFix resin impregnation was still carried out to strengthen the sample's borders and to provide a cylindrical form, necessary for the automatic mechanical polishing and for the BSE image scanning. Under the electron microscope, the imaging field was set at a magnification of x1500. Seven images were captured with a pixel resolution of 0.02x0.02 μm^2.

For the chalk, the threshold value was difficult to fix, so two different procedures were used for comparison:

Binarization 1 – For each image, a visual appreciation was made during testing, which led the operator to set one threshold value. This made it possible to select the foreground of the image during the binarization.

Binarization 2 – According to the analysis of the grey level histograms, a mean threshold value was set and applied to the binarization of all the images.

Finally, the images were treated by an erosion/dilation cycle in order to suppress the isolated pixels.

2.4.2. Measured parameters

First, the binarization gave black 2-D images of the pores (designed as objects). Their mean Feret diameter D_F and shape factor f were calculated from their surface and circumference. A second method consisted in analyzing the entire image by statistical linear analysis. Two parameters were so determined: the mean internal line (MIL) and the specific surface area.

Expressed in pixels, the parameters were given using the μm unit after calibrating each image. The definition of these parameters is given below.

Surface

Each object has a surface s, which is the sum of the contained pixels.

Circumference

The circumference c of an object is defined as:

$$c = \frac{\pi}{4}(\text{Pro } 0 + \text{Pro } 45 + \text{Pro } 90 + \text{Pro } 135) \quad (21)$$

In the precedent relation, Pro α is the length of the projection of the object on a straight horizontal reference in the directions α (0°, 45°, 90° and 135°).

Surface porosity

The surface porosity is the number of black pixels that belong to the porous medium divided by the total number of pixels (black and white) contained in the image.

Mean Feret diameter DF

A Feret diameter of a 2-D object is the length of the segment of an oriented line that crosses its barycentre and its circumference. The mean Feret diameter of an object is calculated from its Feret diameters determined for angles from 0° to 180° with an incremented angle of five degrees.

Shape factor f

The shape factor f of an object is calculated from its surface and circumference according to the relation:

$$f = 4\pi \frac{s}{c^2} \quad (22)$$

Examples of f values obtained for some specific shapes according to Relation *22* are given in Table 9.

Table 9 – Shape factor for some simple pore shapes.

Object	Straight line	Disc	Square	Equilateral triangle
f	0	1	0.78	0.60

Mean internal line (MIL)

By spaced linear scanning, the image is reduced to white or black segments (internal lines) that belong to either the mineral medium or the porous medium, respectively (Fig. 21). For each medium, the length of each line is recorded and the total number of internal lines is counted. The mean internal line length (μm) of a medium is the ratio of its total internal line length divided by the total number of its internal lines.

Specific surface area S_{IA}

After scanning along a total length l, the value of the inner surface density is calculated as double (the two extremities of a line) the total internal line number of the porous medium divided by the length l. The specific surface area S_{IA} is determined dividing the precedent value by the known bulk density of the sample.

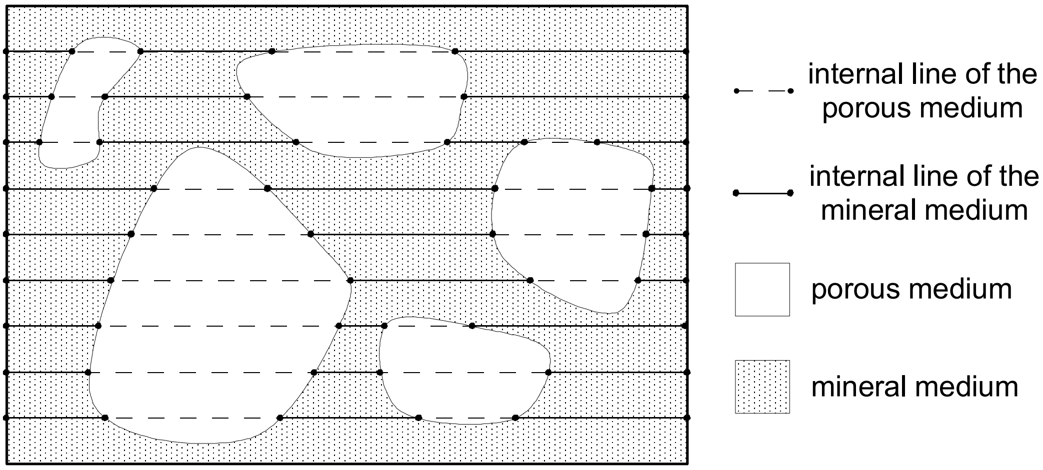

Fig. 21 – Principle of the linear analysis and determination of the internal lines.

2.4.3. Results and discussion

2.4.3.1. Fontainebleau sandstone

All the original and analyzed images, with their corresponding porosity and mean Feret diameter are reported in Appendix G. The parameters of each image are summarized in Table 10. The values from the four BSE images of the sandstone were averaged, leading to a mean surface porosity of 13.5%. This value is comparable to that of the total mercury porosity and water porosity (12.3% and 12.5%, respectively).

The mean Feret diameter D_F is about 110 µm, which is much higher than the median pore access diameter D_{50} (30 µm) quantified by mercury porosimetry. The pore size distribution histogram (Fig. 22) shows a maximum for the Feret diameters between 40 and 60 µm, which is in agreement with the petrographical observations (§1.2.2.1.). However, it could be noticed that the distribution is spread across a large range of diameters: a lot of big pores have diameters ranging from 60 to 300 µm. These results clearly show that mercury porosimetry do not give a direct estimation of the pore diameters but rather the pore access diameters. The interpretation of these results, along with the correlation between the image analysis and the mercury porosimetry and the calculation of the pore-to-throat-size ratio, was discussed further in section 2.4.3.3.

The MIL of the porous medium (57 µm) fits with D_{50} measured by mercury porosimetry. Indeed, the MIL calculation includes the lengths of the constrictions of the porous network, which explains that the MIL and D_{50} have comparable values.

Table 10 – Image analysis parameters of the Fontainebleau sandstone.

	Transversal A	Transversal B	Horizontal A	Horizontal B	Average	σ
Surface porosity (%)	13.97	13.88	13.69	12.58	13.53	0.56
D_F (µm)	118.7	112.5	107.7	109.3	112.1	4.2
Shape factor *f*	0.49	0.49	0.49	0.54	0.50	0.02
MIL of the mineral medium (µm)	349.5	361.7	322.9	357.4	347.9	15.1
MIL of the porous medium (µm)	59.6	61.1	54.2	54.3	57.3	3.1
S_{IA} ($m^2\ g^{-1}$)	$4\ 10^{-3}$	$4\ 10^{-3}$	$4\ 10^{-3}$	$4\ 10^{-3}$	$4\ 10^{-3}$	0

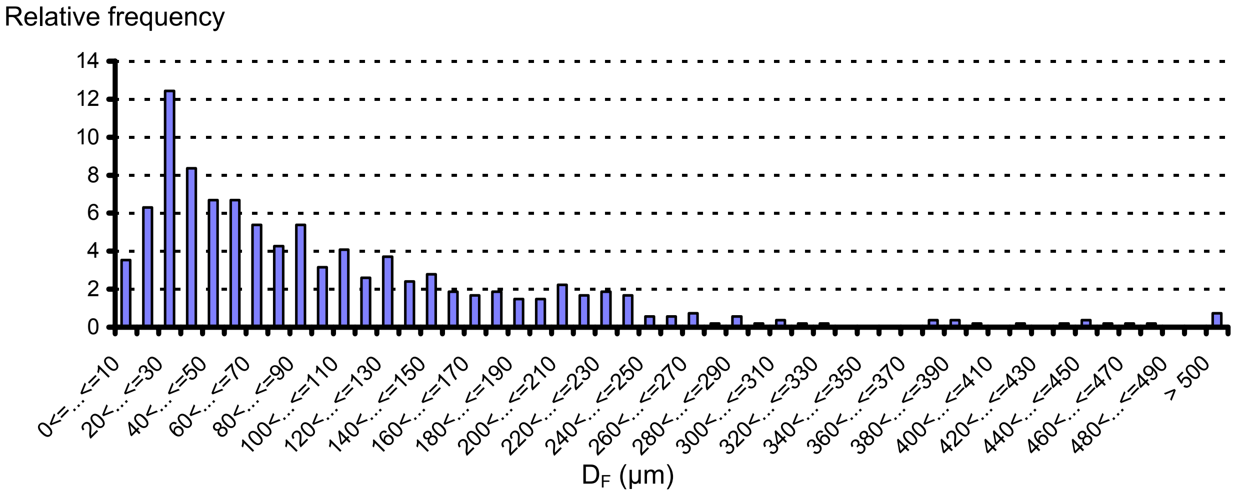

Fig. 22 – Distribution histogram of the mean Feret diameter D_F in the Fontainebleau sandstone.

Compared to those of simple shapes (Table 9), the value of 0.5 of the mean shape factor indicates that the pores must have shapes with sharp angles, which is in accordance with the petrographical analysis observation (a polyhedral structure of the inter-granular pore spaces and triangular shapes were often observed for smaller pores; see §1.2.2.1.).

The specific surface area S_{IA} (4 10^{-3} m² g^{-1}) is very low in comparison with the values from the gas adsorption and mercury porosimetry (15 10^{-3} and 13 10^{-3} m² g^{-1}, respectively). In fact, a stereological analysis (calculation of 3-D parameters using 2-D random cross section images of volumic objects) assumes that the material is quite isotropic in all directions. The isotropy of the Fontainebleau sandstone must be not sufficient enough to adequately determine the specific surface area by image analysis. The very low value of the S_{IA} can be also explained considering that a lot of grain boundaries are not represented on the BSE images.

Small deviations in the porosity and D_F can be observed from the comparison of the BSE images (Table 10). Thus, each image was found to be representative of the porosity of this sandstone. However, when one image (Horizontal A) is subdivided into four partial images (Fig. 23), the porosity calculated for each partial image varies significantly: from 11% (partial image 4) to 17% (partial image 2). The D_F and MIL of the porous medium are higher in partial image 2 than in partial image 4 (Table 11), suggesting that the pores are bigger in the first image. In comparison with partial image 4, numerous black areas with more complex shapes can be observed in partial image 2. These areas represent the interconnection of several pores. Moreover, the MIL of the mineral medium in partial image 4 is about 25% smaller than in partial image 2. This deviation means that the grains must be less agglomerated in partial image 2 than in partial image 4.

It can be concluded that the grains are more compacted in partial image 4, inducing a decrease in the 2-D pore sizes and in the amount of apparent 2-D interconnections (they can also be 3-D interconnected, however).

The discrepancies between these two images were explained by variations in the porous structure from a zone of intense silicification to a zone that is poorly silicified. Indeed, the petrographical analysis revealed the existence of zones of various silicification levels, which were directly linked to various quartz overgrowths. However, the influence of these changes in the mineral structure on the porous structure parameters could not be determined. The image analysis made it possible to correlate the increase in the amount of quartz overgrowths with a decrease in the porosity and pore size.

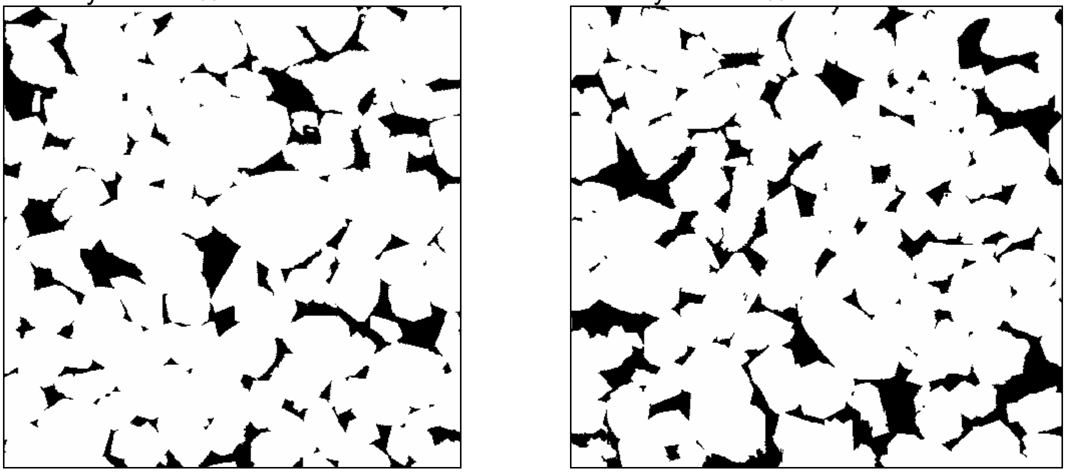

Partial image 1

Porosity = 12.67%

Partial image 2

Porosity = 17.03%

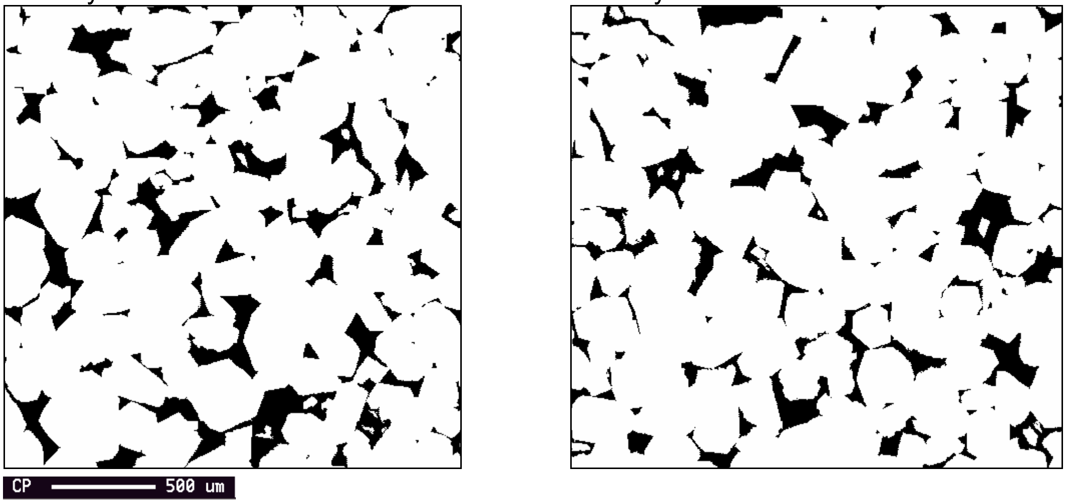

Partial image 3

Porosity = 13.82%

Partial image 4

Porosity = 11.09%

Fig. 23 – Subdivision of one BSE image of the Fontainebleau sandstone (Horizontal slice A with a mean porosity of 13.69%).

Table 11 – Image analysis parameters from the partial images 2 and 4 of the Fontainebleau sandstone.

	Partial image 2	Partial image 4
Surface porosity (%)	17.03	11.09
D_F (µm)	122.4	86.7
Shape factor f	0.51	0.52
MIL of the mineral medium (µm)	281.6	371.7
MIL of the porous medium (µm)	62.09	51.04
S_{IA} (m² g^{-1})	4 10^{-3}	4 10^{-3}

2.4.3.2. Mons chalk

All the original and analyzed images are reported in Appendix G. For a given image (Table 12), the surface porosity significantly varies between the two binarization procedures (deviation of 1 to 7%). That means that the choice of the binarization threshold must have a strong influence on the 2-D porosity values. However, it has a lower influence on the Feret diameter.

From one captured image to another, significant variations in the porosity were recorded whatever the binarization procedure (porosity from 35% to 49%). These variations are linked to heterogeneities in the porous or mineral structure at the scale of one analyzed image: indeed, the presence of macro-sized calcite shells (skeletons of bio-organisms) is responsible for the low porosity, like in the BSE image 5; the macropores enhance the surface porosity, like in the BSE image 7 (Appendix G).

The analytical results obtained from each procedure were averaged from the seven images (Table 13). Despite two different types of binarizations, these procedures displayed comparable statistical average values of the porosity (about 40%), which are in accordance with methods such as mercury and water porosimetry. This result proves that the threshold was adequately chosen and that seven images were sufficient for providing accurate and representative statistics.

The histogram in Figure 24 shows a narrow mean Feret diameter distribution with low frequencies in the biggest diameters, which is opposite to the Fontainebleau sandstone (Fig. 22). A maximum frequency was recorded at 0.8-0.9-µm diameters, proving that the chalk contains mainly micropores. However, some pores can reach diameters bigger than 15 µm (at diameters of about 15 µm and above, the pore are considered macropores).

The linear analysis of the chalk images led to a MIL value of the porous medium of 1.2 µm. This value is slightly higher than that of D_{50} obtained by mercury porosimetry, and is quite similar to that of the hydraulic diameter D_H. As explained for the Fontainebleau sandstone, the MIL is comparable to D_{50} and D_H, because it includes the length of the throats of the porous network. The MIL of the mineral medium was found to be about 1.8 µm. This value is almost equal to the 2-µm-size of most of the calcite crystals that were observed by petrographical analysis.

The image analysis displayed a very low specific surface area (0.8 m² g^{-1}) compared to the mercury porosimetry and the gas adsorption (1.8 m² g^{-1}). The reasons behind this low value are the same for the Fontainebleau sandstone (as pointed out in the previous section): the quite different measurement techniques and the insufficient isotropy of the chalk.

Table 12 – 2-D porosity and DF of the Mons chalk from binarizations 1 and 2.

Image no	1	2	3	4	5	6	7
	Binarization 1						
Surface porosity (%)	35.64	38.34	37.72	39.06	35.33	48.82	49.59
D_F (µm)	1.87	1.86	1.77	1.73	1.98	1.99	1.61
	Binarization 2						
Surface porosity (%)	37.36	39.33	40.35	42.62	34.78	41.85	47.06
D_F (µm)	1.96	1.78	1.78	1.68	1.97	2.08	1.63

Table 13 – Average image analysis results of the Mons chalk according to binarizations 1 and 2.

	Binarization 1	Binarization 2
Surface porosity (%)	40.64	40.48
D_F (µm)	1.83	1.84
Shape factor f	0.65	0.65
MIL of the mineral medium (µm)	1.81	1.76
MIL of the porous medium (µm)	1.24	1.20
S_{IA} (m^2g^{-1})	0.81	0.83

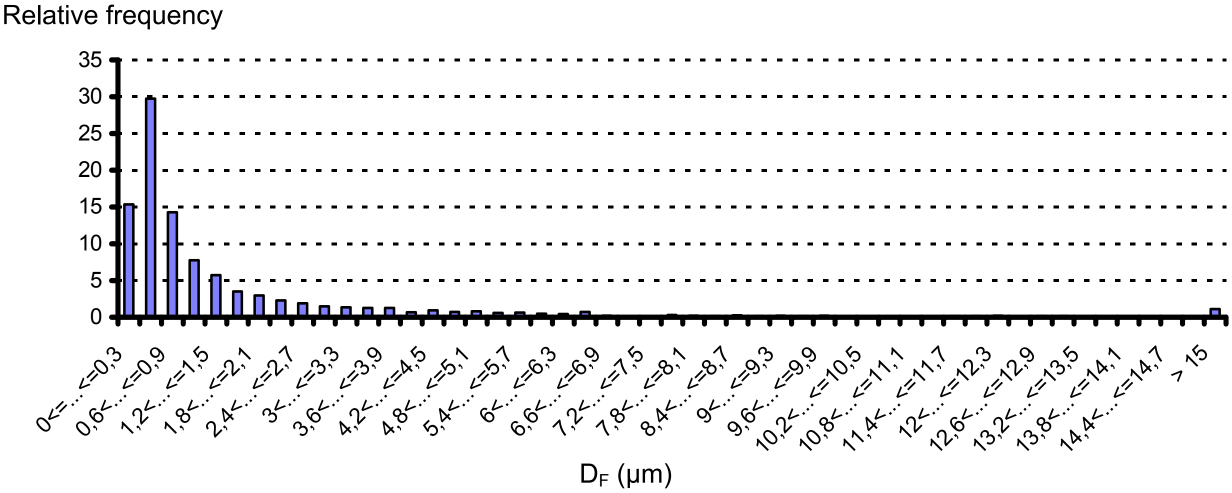

Fig. 24 – Distribution histogram of the mean Feret diameters from the Mons chalk BSE images.

2.4.3.3. Mean pore-to-throat-size ratio $R_{P/T}$ – Relationship with the trapped porosity

The pore-to-throat-size ratio was defined as the mean Feret diameter D_F (image analysis) divided by the mean pore access diameter D_{50} (mercury porosimetry):

$$R_{P/T} = \frac{D_F}{D_{50}} \quad (23)$$

The factor $R_{P/T}$ of the Fontainebleau sandstone is almost double that of the chalk (Table 14). That means that, in contrary to the chalk, there is a strong difference between the pore sizes and their corresponding throat sizes in the sandstone.

The different values of $R_{P/T}$ justify the discrepancy between the percentages of trapped porosity of the two rocks: the sandstone has higher percentages of trapped water and mercury porosity (Table 14). As a matter of fact, the mechanisms of air and mercury trapping are governed by $R_{P/T}$: the higher the ratio $R_{P/T}$, the higher the percentage of trapped water and mercury porosity. However, the ratio $R_{P/T}$ has a stronger influence on the mercury trapping than on the air trapping. In fact, the trapped-water-to-trapped-mercury porosity percentage ratio is proportional to $R_{P/T}$ in a factor λ (Relation *15*). The factor λ was found to be about 8 for both rocks, as seen in section 2.2.5.3.

Table 14 – Pore-to-throat-size ratios $R_{P/T}$ of the Fontainebleau sandstone and the Mons chalk: the higher the ratio, the higher the trapped water ($N^*_{TR,W}$) and mercury ($N^*_{TR,Hg}$) porosity percentage.

	D_F (µm)	D_{50} (µm)	$R_{P/T}$	$N^*_{TR,W}$	$N^*_{TR,Hg}$
Fontainebleau sandstone	112.1	31.4	3.6	43.9	95.5
Mons chalk	1.8	0.8	2.2	7.4	29.9

2.5. X-ray computed tomography

Developed in the medical field, X-ray computed tomography (CT) makes it possible to create 2-D or 3-D reconstructions of the internal structure of an object. Geologists have largely implemented this technique into their studies (WELLINGTON S.L. & VINEGAR H.J., 1987; FABRE D. et al., 1989; RAYNAUD S. et al., 1989; SWENNEN R. et al., 1990; ORSI T.H. et al., 1994; KLOBES P. et al., 1996; GERAUD Y. et al., 1999; HELLMUTH K.-H. et al., 1999). These studies have clearly demonstrated the power of CT with respect to classical petrography for porous structure analyses. Applied to this study of the sedimentary rocks, CT was useful for the assessment of their isotropy. The aim of the CT analysis was also the volumic analysis of the structure of the rocks, which was useful for interpreting the variations in the fluid transport properties (capillary water imbibition and gas permeability; Chapter 3).

2.5.1. Principle

2.5.1.1. Computed tomography (2-D CT)

During a CT measurement, a collimated X-ray beam (pencil) penetrates the investigated sample. Like in the case of the classical radiography, it is attenuated in proportion to the length and to the bulk density of the absorbing material (ILLERHAUS B. et al., 1996) – thus, in proportion to the atomic number. After an additional collimation (or filtering by light materials) in order to suppress scattered radiation, the intensity of the signal is measured, digitized and stored in a computer together with the position coordinates. The planned spatial resolution requires a repetition of the measurement, step by step. Next, the sample is turned to a small incremented angle and analyzed again (Fig. 25). After a 180°-rotation, the measurement is complete. The energy of the radiation should be high enough to penetrate the sample in every direction. If it is not, image artefacts would result. The collected data are treated by a computer in order to obtain the linear X-ray absorption coefficient. From this data set, the local bulk densities are calculated by filtered back-projection. The resulting image, called tomography image, gives a cross-sectional view of the sample. Each element (pixel) of the image contains the calculated bulk density of a volumous element (voxel). The density values are usually represented in the image by grey levels in 256 steps (with up to 4096 possible). Black is equivalent to air while white is set to the highest occurring bulk density.

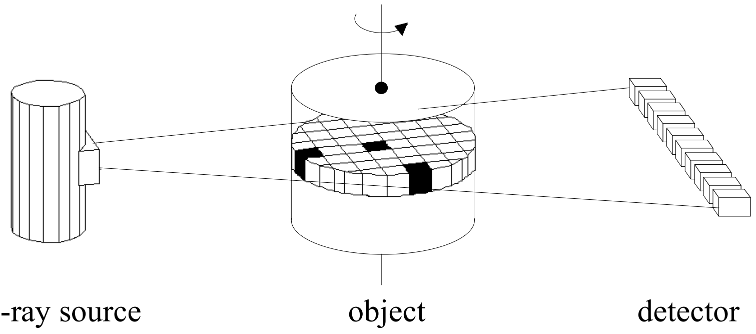

Fig. 25 – Principle of the X-ray computed tomography (2-D CT).

2.5.1.2. Three dimensional computed tomography (3-D CT)

During a 3-D CT measurement, the sample is fully submitted to X-rays as in usual radiography. This leads to sets of 2-D images (Fig. 26). After a full turn, a volumetric image can be calculated, e.g. using the Feldkamp algorithm (Feldkamp et al., 1984). Here, a collimation in front of the detector is no longer possible: the scattered radiation will influence the image and reduce the density resolution. The great advantage of the 3-D CT is that, after one turn, the entire object is investigated; this drastically reduces the measuring time. Furthermore, the active volume of a detection cell within a 2-D image is smaller than for one-dimensional line arrays.

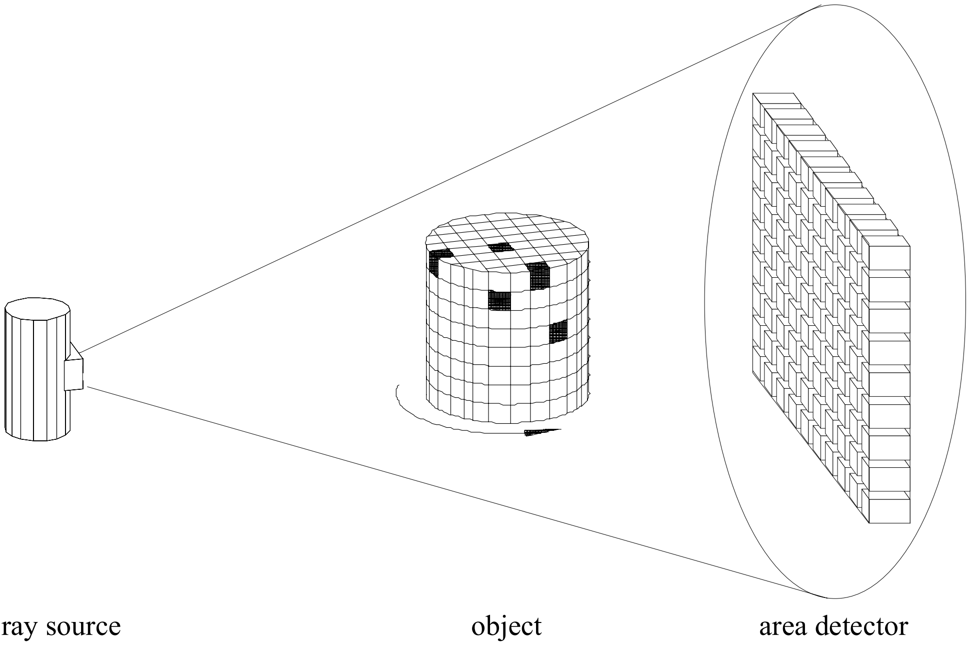

Fig. 26 – Principle of the cone beam 3-D CT.

2.5.1.3. Physical principles of the X-ray attenuation

For monochromatic X-ray sources, the relationship between the incident and attenuated intensities of the X-rays (I_0 and I_A, respectively) and χ the thickness of the object is expressed by Lambert-Beer's law, where μ is the linear attenuation coefficient:

$$\frac{I_A}{I_0} = \exp(-\mu\chi) \qquad (24)$$

Linear attenuation is known to depend predominantly on two processes, namely photoelectric absorption and Compton scattering (M. VAN GEET et al., 2000). This may be expressed as:

$$\mu = d_B\left(b_1 + b_2\frac{Z_e^{3.8}}{E^{3.2}}\right) \qquad (25)$$

where d_B is the bulk density of the material, Z_e the effective bulk atomic number[1] of the material, E the X-ray energy, and b_1 and b_2 the energy-dependent coefficients.

---

[1] For mixtures of atoms, the effective atomic number is given by $Z_e = (\Sigma f_i Z_i^{3.8})^{1/3.8}$, with f_i as the fraction of the total number of electrons contributed by the i^{th} element and Z_i its atomic number.

The first term in Relation *25* (dBB1) stands for Compton scattering, which is a predominant effect at X-ray energies above 100 kV. The second term accounts for the photoelectric absorption, whose effect is predominant at energies below 100 kV (JACOBS P. et al., 1995).

2.5.2. Experimental

The 3-D CT measurements of the sedimentary rocks were made using a microfocus tomograph for an incident X-ray of 200 kV (0.2 mA) and using a 2-mm Cu filter. The apparatus displayed measurements data with a resolution of 24.0x24.0x24.0 µm³ as its voxel size. This resolution was one disadvantage to the method for analyzing the selected rocks (most of them contain tiny pores with sizes quite below this resolution). Thus, the results were interpreted in terms of material compactness or porosity, rather than in terms of pores. For the "Grès à Meules" sandstone and the tuffeau limestone, various atomic numbers of different components also played a role in the X-ray linear attenuation. Therefore, even if the photoelectric absorption was not the major effect, the result interpretation for these two materials was made keeping in mind their different mineral compositions.

Tomography images

After the measurement, the reconstruction using the algorithm resulted in cross-sectional views, i.e. 2-D tomography images, of the cylindrical samples of each rock. The images were analyzed with regard to the observation direction: parallel or perpendicular to the cylinder's axis (Fig. 27).

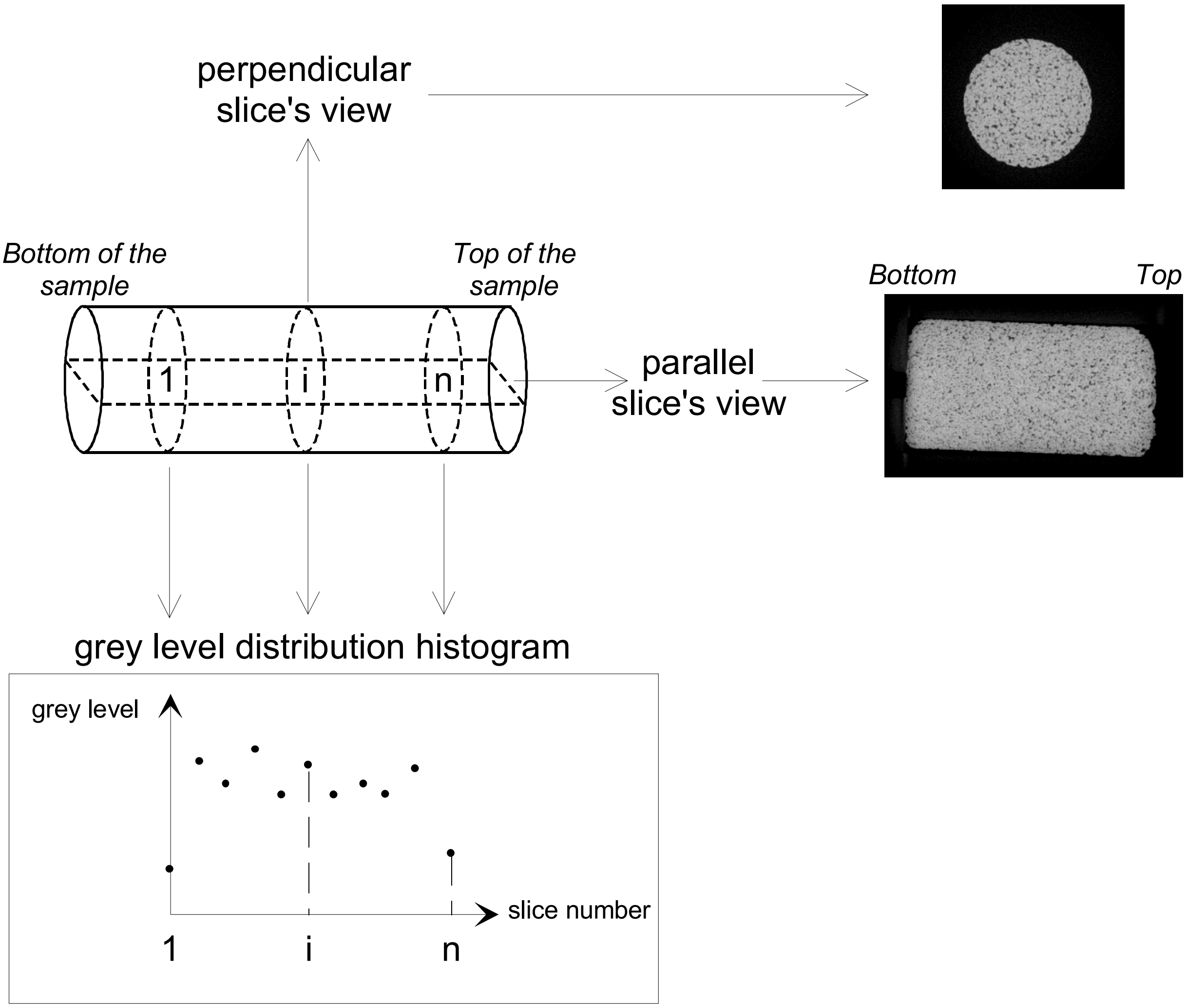

Fig. 27 – Diagram of the CT images and histogram setting.

Density histograms

The variations in the grey levels, i.e. in the bulk density, were analyzed following a given direction in the cylindrical sample (Fig. 27).

Each circular slice (perpendicular slice) has a thickness of one voxel. The grey levels of all the voxels included in each slice were averaged. Then, the mean grey level values were plotted versus the slice number (i.e. the slice location), which gave the density histogram of the sample.

2.5.3. Results and discussion

Fontainebleau sandstone

On the tomography images (Fig. 28), the macropores (in black or dull grey) are clearly apparent. They are randomly distributed throughout the material. Since the material is only composed of quartz, the random distribution supposes a relatively homogeneous porous structure. It can be observed that numerous larger macropores (in black) are always isolated in zones made of smaller pores, which have sizes that reach the limit of the method resolution. This observation partially explains the high value of the trapped porosity measured by water porosimetry (§2.1.2.). The second cause for a high trapped porosity is the significant difference between the size of these pores and the size of their accesses.

The grey level distribution histogram of Figure 28 confirms that the bulk density remains constant along the sample from one slice to another. This also confirms that the zones of high silification level, revealed by petrographical analysis, are distributed throughout the rock with a constant spatial periodicity and have no influence on the bulk density distribution.

These observations have led us to propose two conclusions concerning the interpretation of the mercury porosimetry data:

- Sparse large pores mean local non-random heterogeneities, which induce the trapping of mercury during withdrawal; they are responsible for the very high amount of trapped mercury (§2.2.5.).
- The variations in the quartz overgrowths are linked to strongly silicified areas, which are randomly distributed. These areas do not significantly influence the porosity and the mean density of 2-cm^3 samples. However, they induce variations in the mean pore sizes from one 2-cm^3 sample to another (see the mercury porosimetry results, §2.2.3.).

A pore size analysis from the CT measurement was possible for this material. It was realized by thresholding the grey levels of all the voxels contained in the analyzed volume. The threshold value was set by choosing the grey level that corresponds to air. Thresholding led us to the selection of voxels (set in black) that correspond to the porosity. That in turn led to the 2-D representation of the pores (Fig. 29). Thus, the pore diameters were determined using the inscribed sphere (spherical pore model). They were plotted versus their frequency (Fig. 30).

The histogram presents a maximum at 50-60 µm. The calculated mean pore diameter is 116.9 µm. The CT image analysis led to a mean pore diameter value that is quite in accordance with that of D_F (112 µm) obtained by the BSE image analysis (Table 10, §2.4.3.1.). Due to the resolution limit of the CT measurement, some micropores were not taken into account during the CT pore size analysis. Hence, the good agreement between the two techniques confirms that the microporosity of the sandstone is negligible. Moreover, the pore diameter distribution from the CT image analysis (Fig. 30) is quite similar to that provided by the BSE image analysis (Fig. 21, §2.4.3.1.), which improves the pore size homogeneity. The difference between the two methods is that the CT image analysis displayed volumic information for the full sample while the BSE image analysis concerned only some 2-D slices inside the sample. The conclusion is that the porous structure of this rock is homogeneous enough for the analytical results to be reproduced using these different methods.

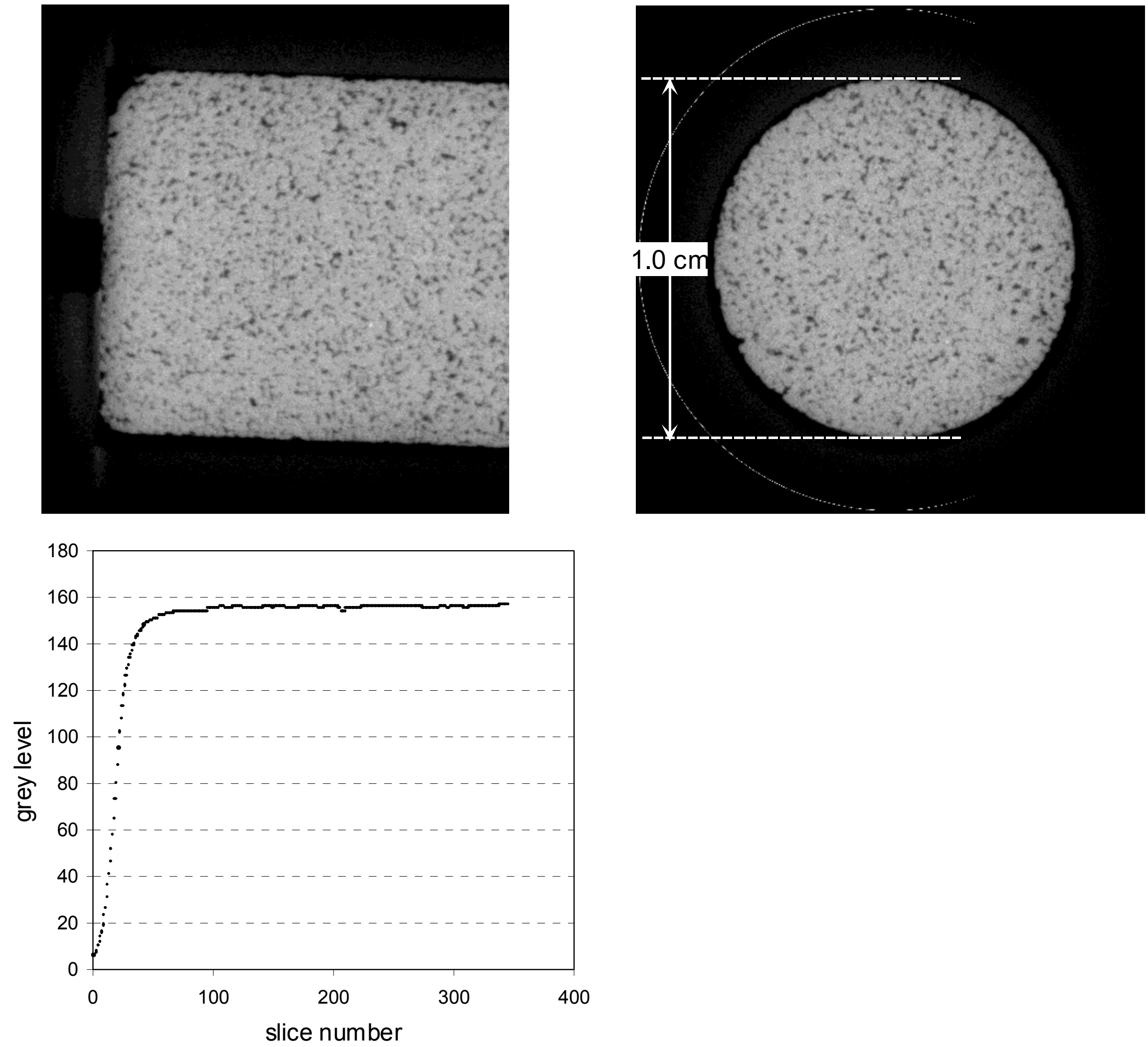

Fig. 28 – Examples of tomography images parallel (top left) and perpendicular (top right) to the axis of a Fontainebleau sandstone cylindrical sample, and grey level distribution histogram obtained for a given length of the sample.

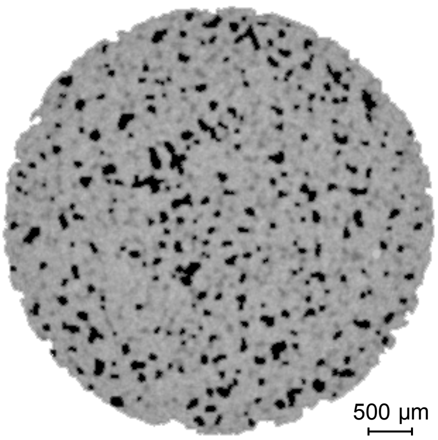

Fig. 29 – 2-D representation of the pores (in black) from the CT image analysis of the Fontainebleau sandstone.

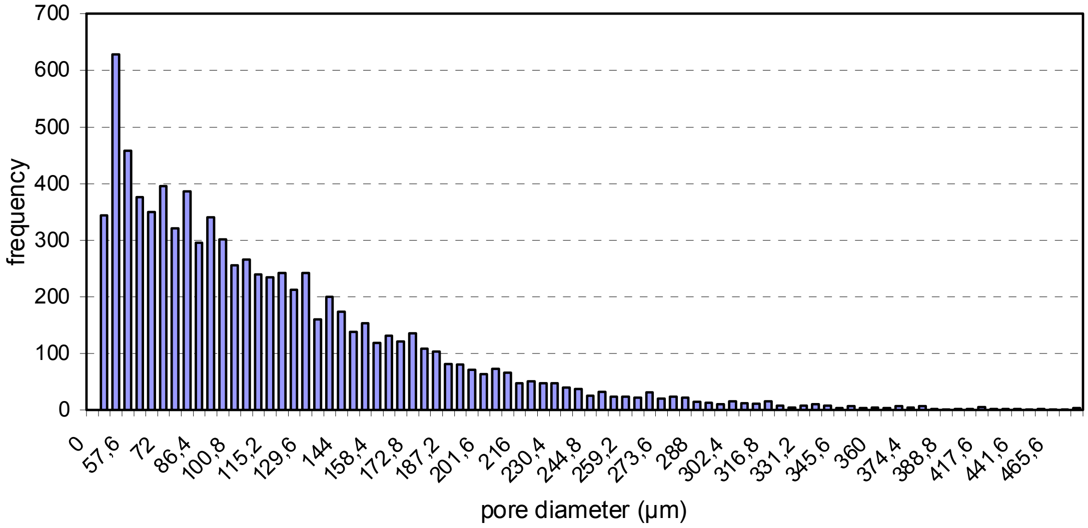

Fig. 30 – Pore diameter distribution provided by the CT image analysis of the Fontainebleau sandstone.

“Grès à Meules” sandstone

The “Grès à Meules” sandstone sample was drilled from the block in a direction parallel to the stratification (the axis of the cylindrical sample was parallel to the stratification planes). Zones of higher grey levels (brighter zones) can be observed on the two CT images (Fig. 31). The spatial distribution of these zones shows a layered structure. Layers, which contain lots of white spots, alternate with layers of lower-intermediate grey levels. Some black spots due to macropores can be also observed: their distribution follows the layered structure of the rock.

Histogram a. of Figure 31 represents the mean grey level variations (i.e. bulk density variations) from one perpendicular slice to another. It shows no significant variations in the density following the direction parallel to the stratification planes.

Histogram b. was realized by averaging the grey levels of each parallel slice. A periodical variation in the grey levels, clearly observed in Histogram b. (Fig. 31), reflects the presence of the stratification. This variation underlines noticeable changes in the mineral structure and the porous network between the brighter layers and the intermediate grey level layers.

On the one hand, the brighter layers are the location of coarser grains: larger sizes of the quartz and feldspar grains (or even big tabular crystals of muscovite) have induced white spots on the tomography images. In these layers, clay minerals are in low content and rim the grain borders. On the other hand, the layers of lower-intermediate grey levels contain smaller grains and inter-granular spaces. These fine grain layers also contain higher concentrations of clay minerals, which fill the inter-granular spaces, inducing a higher percentage of microporosity and intermediate bulk density values.

Thus, the CT-measurement of the “Grès à Meules” sandstone made it possible to point out the coarse/fine grained alternated layers that make up the structure of the rock. This kind of structure does not induce significant variations in the measurement data collected by techniques such as mercury porosimetry, water porosimetry or gas adsorption at the scale of laboratory samples. However, it is linked to various porosity structures at a lower scale, e.g. smaller throat sizes in the zones where the clay minerals are abundant and bigger pores linked to the layers of coarser grains. Hence, this anisotropic structure can induce anisotropy in the fluid transport properties.

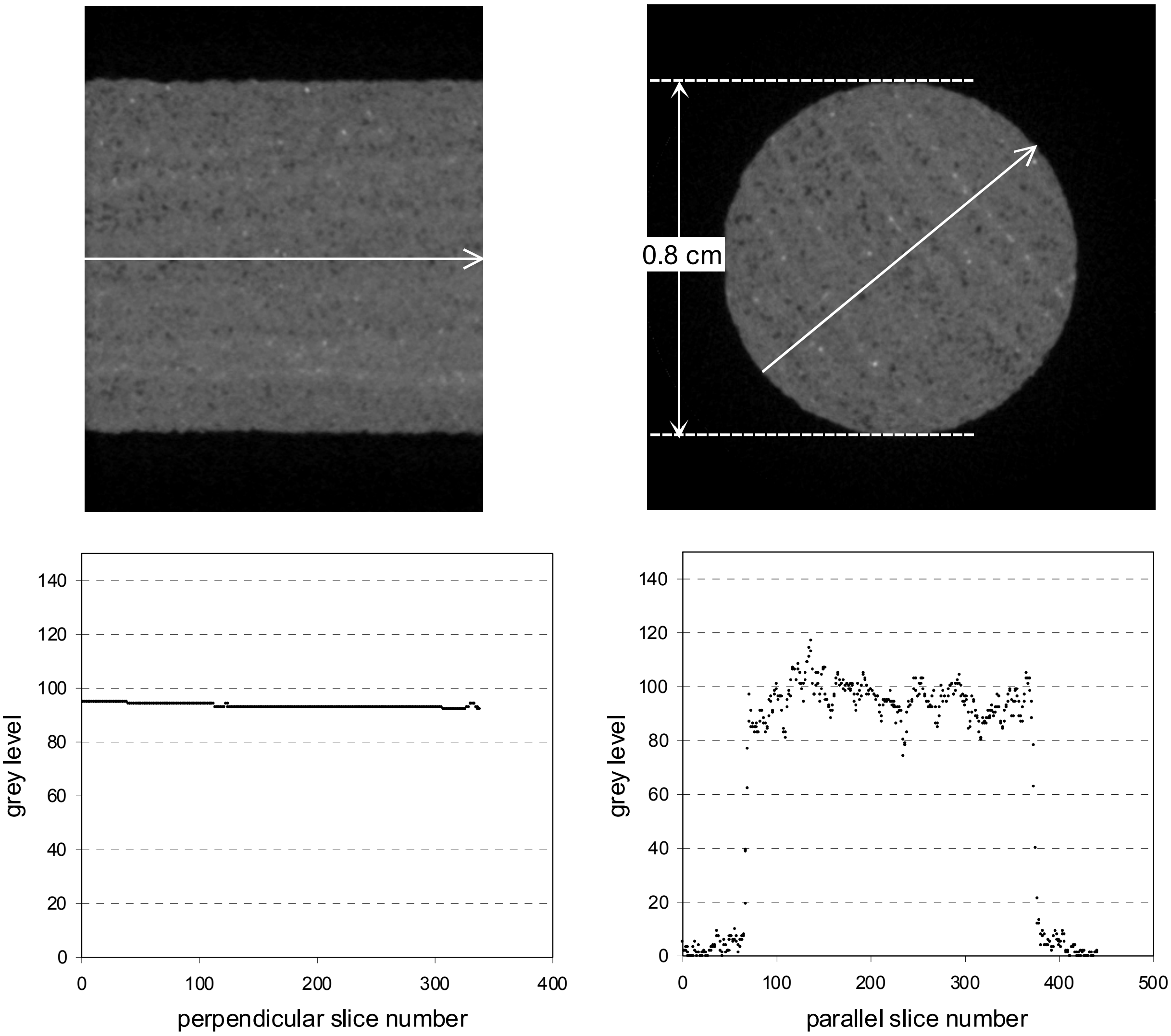

Histogram a.

Histogram b.

Fig. 31 – Tomography images and grey level distribution histograms for a sample of the "Grès à Meules" sandstone; the white arrowed line on each image shows the analysis direction for the corresponding histogram.

Mons chalk

An adequate setting of the brightness and the contrast of the images made it possible to observe variations in the grey levels, which correspond, however, to very small variations in the bulk density and in the porous structure (considering that the material is only made of calcite).

Some brighter spots can be observed on the CT images (Fig. 32). Isolated in a homogeneous matrix, they correspond to the macro-sized calcite shells, which were identified by petrographical analysis. The brighter linear zone observed on the right image was identified as a fracture cemented by calcite crystals that are very close to one another. The histogram of Figure 32 shows a slight variation in the density, delimiting two parts of the sample: a higher density at the bottom than at the top. However, the density deviation is very small, showing the homogeneous structure of the material.

Thus, the CT analysis confirmed that the major part of the chalk is made of a homogeneous microporous matrix. Sparse zones of higher compactness were occasionally observed, but they have no influence on the global porous structure of the material.

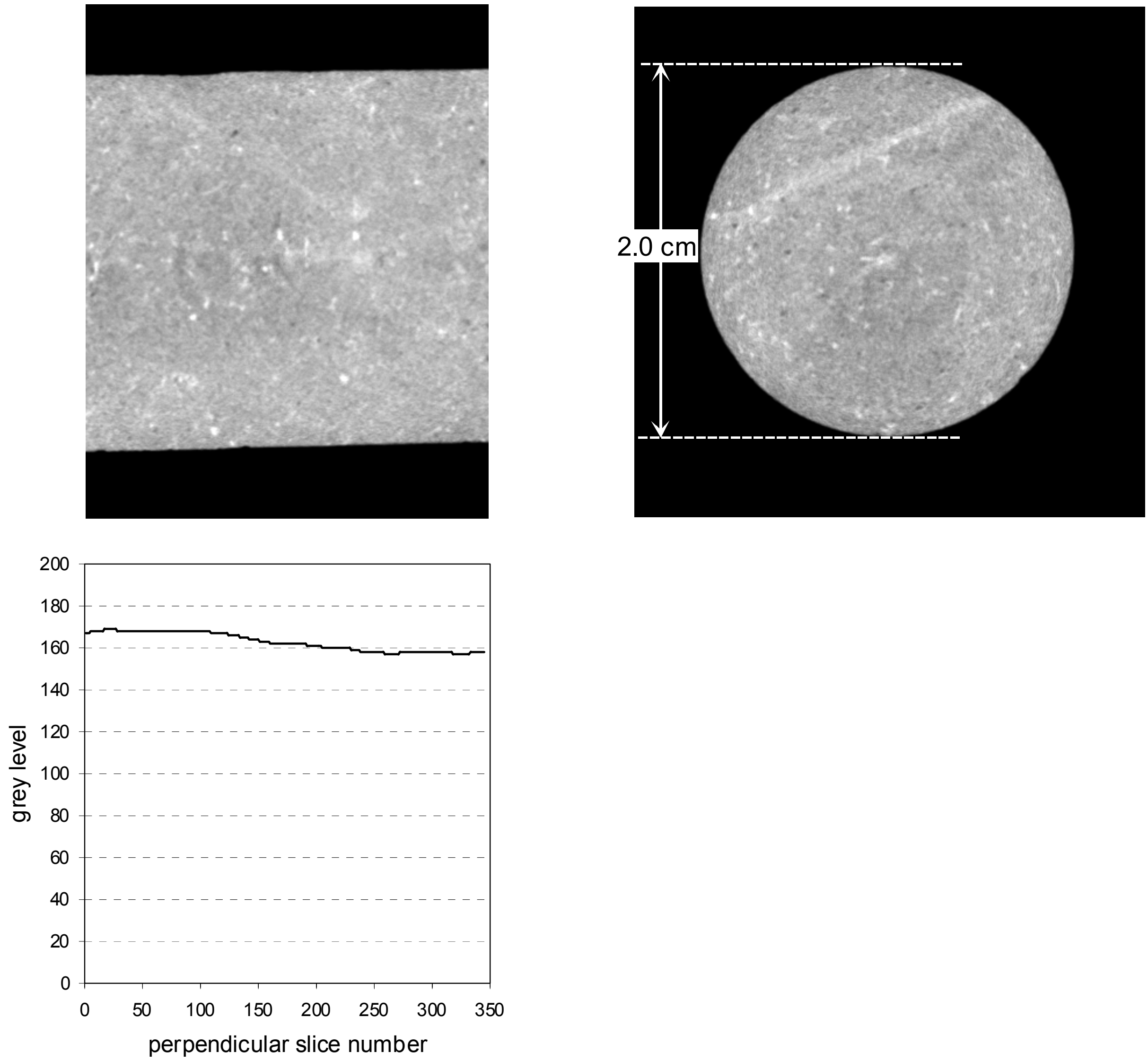

Fig. 32 – Tomography images and grey level distribution histogram of the Mons chalk; the right image shows an old fracture that has been newly cemented (linear zone which is made of white spots).

Tuffeau limestone

The CT-images are characterized by a succession of brighter and darker spot zones randomly distributed throughout the rock (Fig. 33). Some macropores can also be observed. These variations in the grey levels (from white to black) in the images denote a structure complexity of the material at the scale of one slice. This complexity has been already noted by petrographical analysis. However, the random distribution of the zones of various grey levels led us to suppose that the mean bulk density may be constant from slice to slice. That was clearly confirmed while establishing the density histogram represented in Figure 33.

Quartz grains and feldspars of macroscopic sizes were associated with the brighter zones. Next to these zones, various grey intensities in the matrix were linked to the various porosity structures and the various mineral contents. Unfortunately, the low resolution did not allow for a correlation to be made with the different porous structures previously identified by petrographical analysis.

Nevertheless, the random spatial distribution revealed by the CT analysis explains the small deviations in the parameters of the porous structure, which were measured using methods such as water porosimetry and mercury porosimetry.

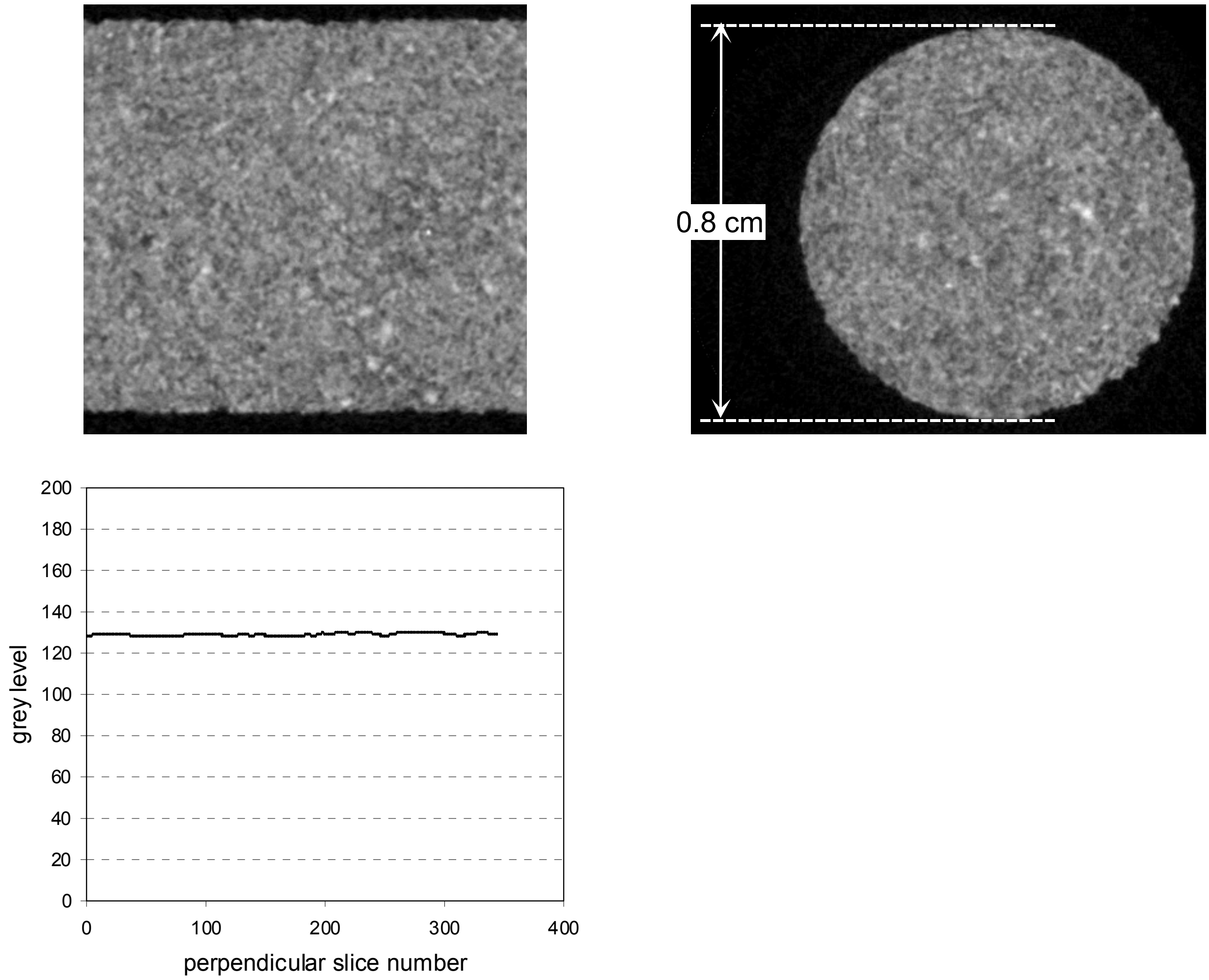

Fig. 33 – Tomography images of the tuffeau limestone, showing the complexity of this limestone's structure; macropores (black spots) as well as macro-sized grain clusters (white spots) can be observed - Histogram of the grey level distribution along the axis of the cylindrical sample of this rock.

Vuillecin limestone

The CT images (Fig. 34) show large variations in the grey levels, which means a heterogeneous spatial distribution of the bulk density and changes in the porous structure of the Vuillecin limestone. Numerous macropores (in black) can be observed. They are isolated, and surrounded by wide white and grey areas.

With reference to the petrographical analysis, the white areas were linked to microporous micrite zones and to some allochems for the brighter ones. The grey zones were associated with calcisparite areas, which often contain either macropores or big micropores.

Despite the seemingly material heterogeneity revealed by the CT images, the mean bulk density remains about constant from one slice to the other, as shown by the grey level distribution histogram of Figure 34. The SEM analysis and the thin section observations have revealed that the porosity of this material mainly consist in micropores. The predominance of microporous areas, also noted from the observation of the CT images, explains that the mean density measured from one slice to another remains almost constant.

Thus, the CT analysis pointed out the heterogeneous structure of this limestone and led us to suppose that irregularities in the fluid transport properties may certainly occur (see Chapter 3).

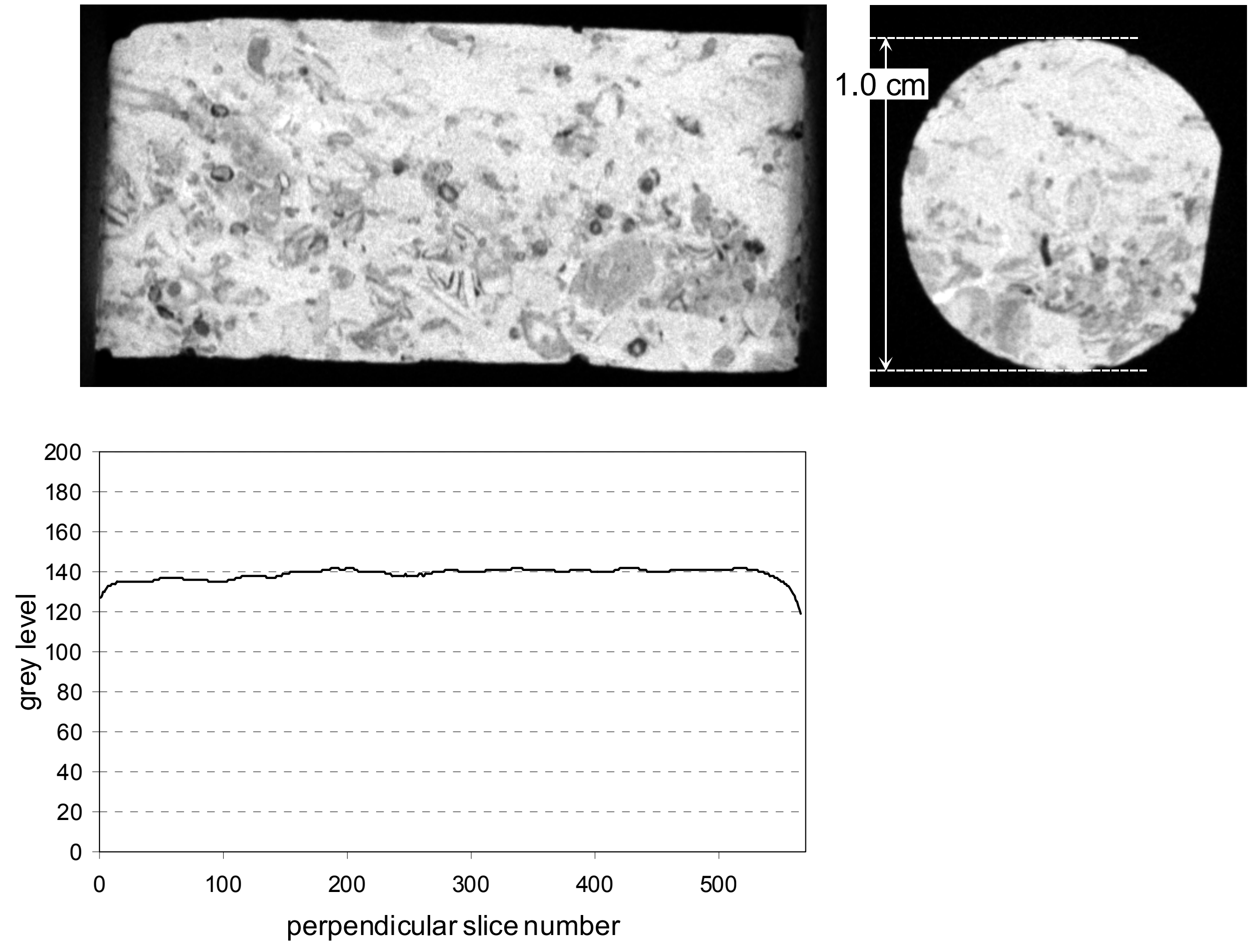

Fig. 34 – Tomography images, showing the heterogeneous structure of the Vuillecin limestone; and grey level distribution histogram of this limestone.

2.6. X-ray absorption/refraction characterization

This method is based on the effects of X-ray absorption and refraction. Many techniques in the fields of sciences use the well-known effects of X-ray absorption. The effect of X-ray refraction is the basis of unconventional small angle X-ray scattering techniques (SAXS). These techniques have recently been developed in response to industry demands for the improved non-destructive characterization of composites, ceramics and other heterogeneous materials.

Applied in this study, this method helped in characterizing the sedimentary rocks mainly by simultaneously analyzing the three important microstructure parameters: porosity, specific surface area and pore size. The interest was to establish the correlation between these parameters and to study their spatial distributions in the rocks using “topographic images”.

2.6.1. Physics and instrumental

Each sample was scanned across a narrow incident monochromatic Mo-K_{α} X-ray beam (40 KeV, 20 mA). The transmitted X-ray beam with no angle deviation contained the absorbed intensity information, which was detected after reflection using a scattering foil (Fig. 35). The refracted X-ray beam was detected at the known angle θ (the straight primary beam was omitted by a beam stop).

The porosity and the inner surface of the sample were determined from the X-ray absorption measurement and the X-ray refraction analysis, respectively.

2.6.1.1. X-ray absorption: porosity measurement

For X-ray absorption in a material, the relationship in intensity between the incident and attenuated X-rays (respectively, I_0 and I_A) and χ, the thickness of the sample, is expressed by Lambert-Beer's law (Relation *24*, §2.5.1.3.).

The porosity $N_{X\text{-}AR}$ of a material is determined by comparing the parameter μ (attenuation coefficient of the porous sample) with that of the solid skeleton of material μ_0. The porosity is given by the relation:

$$N_{X\text{-}AR} = 1 - (\mu/\mu_0) \quad (26)$$

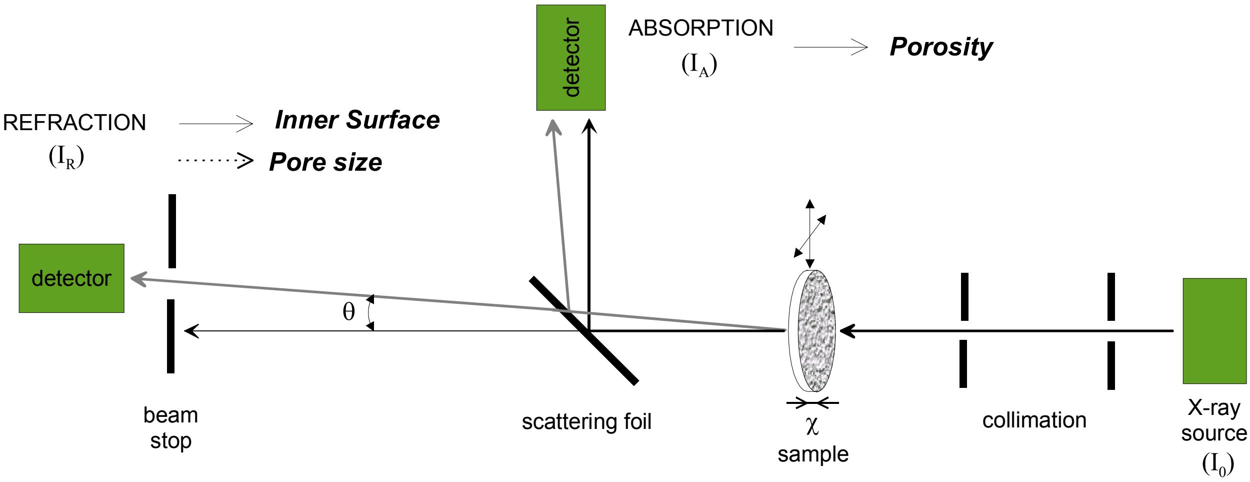

Fig. 35 – Principle of X-ray absorption and refraction measurements (K.-W. HARBICH et al. 2001).

2.6.1.2. X-ray refraction: specific surface area and pore size determination

The physics of X-ray refraction is quite similar to the refraction of light by optical lenses and prisms (HENTSCHEL M.P. et al., 1987; K.-W. HARBICH and HENTSCHEL M.P., 2002). However, the difference is the very small angle of deflection. For a porous material, the refraction effect is essentially due to the difference in the refractive index between the pores (filled with air or gas) and the solid framework, thus occurring at the grain/pore interfaces.

For the quantitative X-ray refraction analysis, the measurements are usually made at a constant angle θ (of a few minutes), and at a fixed wavelength. Under these conditions, the relative intensity difference between refraction and absorption (I_R - I_A) only depends on the inner surface density Σ (surface per volume unit; μm^{-1}), the X-ray path length χ (μm) across the sample and the transmitted intensity I_A (HENTSCHEL M.P. et al., 1994; K.-W. HARBICH et al., 2001). This is expressed by the relation:

$$I_R - I_A = c_0 \Sigma \chi I_A \quad (27)$$

with c_0, the apparatus constant.

A refraction coefficient $C_{X\text{-}AR}$ (μm^{-1}) is defined as:

$$C_{X-AR} = c_0 \Sigma \quad (28)$$

The apparatus constant c_0 is determined after calibration using a synthetic homogeneous certified reference material of known inner surface density.

At each step of the sample scanning, the refraction value of $C_{X\text{-}AR}$ is determined from the measured intensities I_R and I_A, using the following relation:

$$C_{X\text{-}AR} = \frac{1}{\chi}\left(\frac{I_R}{I_A} - 1\right) \quad (29)$$

Values of Σ of the sample are determined from the measured refraction values of $C_{X\text{-}AR}$ following Relation *28*. The specific surface area $S_{X\text{-}AR}$ ($m^2\ g^{-1}$) of the analyzed zone of the sample is deduced from Σ (expressed in μm^{-1}), the known mineral density $d_{M,W}$ ($g\ cm^{-3}$) and the porosity $N_{X\text{-}AR}$ (expressed as a ratio) using the relation:

$$S_{X\text{-}AR} = \frac{\Sigma}{d_{M,W}\left(1 - N_{X-AR}\right)} \quad (30)$$

For the analyses of this study, the calculation of the pore diameters required the application of a pore model. The calculation was made using the general volume (V)-surface (S) relation:

$$D = \frac{aV_p}{S} \quad (31)$$

in which *a* is a constant depending on the model, V_p and S the pore volume and the pore surface area, respectively.

In Relation *31*, V_p was replaced by the product of the porosity $N_{X\text{-}AR}$ with the analyzed volume sample and S was expressed by the product of the inner surface density Σ with the analyzed volume. The value of *a* was set equal to 6, which led us to determine the diameters of theoretical spherical pores $D_{X\text{-}AR}$ (expressed in μm) using the relation:

$$D_{X\text{-}AR} = \frac{6N_{X-AR}}{\Sigma} \quad (32)$$

2.6.2. Topographic images and frequency histograms

Each rock's sample (1 cm in diameter and about 1 mm in thickness) was scanned and the software made the calculation of the microstructural parameters of the analyzed zone for each incremental displacement. The values were translated in grey levels (black for the minimum value, white for the maximum). At the end of the scanning, images in grey levels were established. On each image, one pixel contains information (the mean porosity, the mean specific surface area and the mean pore size) about the subjacent elementary volume ($50x500x\chi$-μm^3 voxel): the image is called topographic image, or topography.

In Figures 36 through 38, the images on the left-hand side show the local porosity distribution. The middle images represent typical examples of X-ray refraction scanning topographies of the rocks: they show the distribution of the specific surface area within the scanned samples. The images on the right-hand side represent typical spatial distributions of the pore diameter in the rock's samples: they are the combination of the right-hand and middle images after the application of Relation *32*.

Frequency histograms of the parameters were established considering the whole analyzed zone of each rock's sample, except the sample borders (and in particular the black zone, which can be seen in the lower left-hand side of two images of the Fontainebleau sandstone in Figure 36; this was attributed to a measurement artefact).

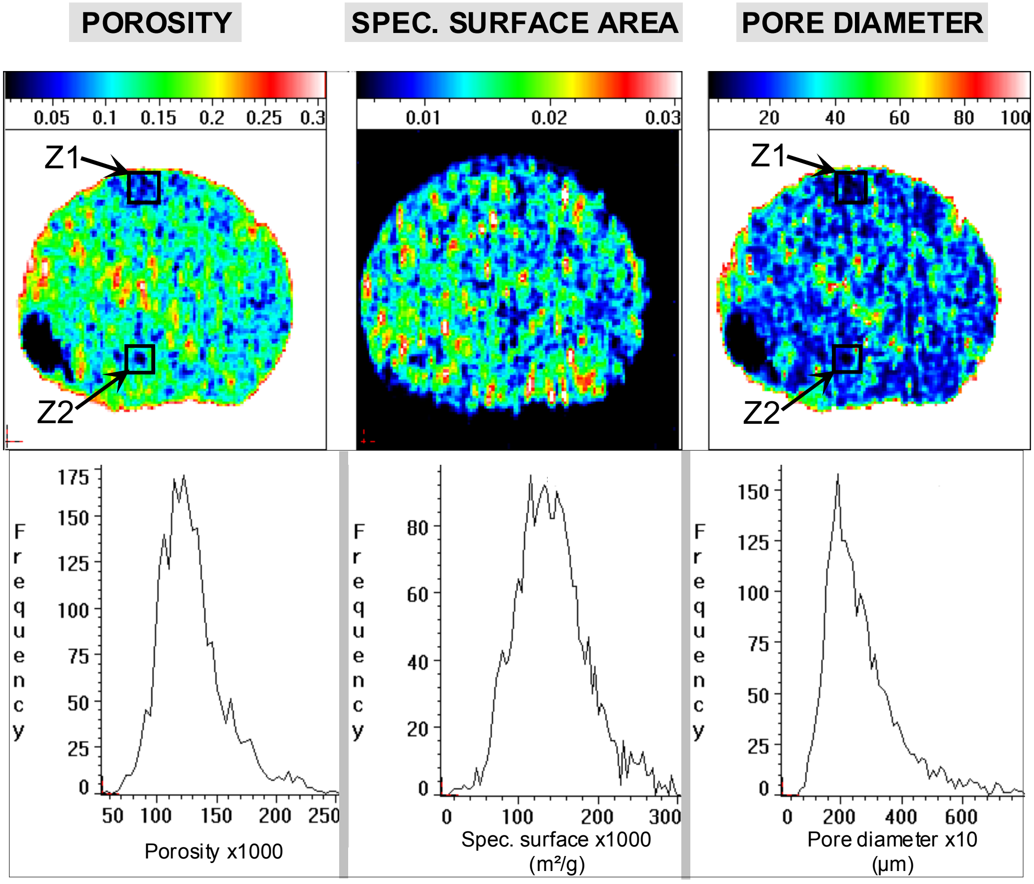

Fig. 36 – Typical topographic images and frequency histograms from the X-ray absorption/refraction characterization of a Fontainebleau sandstone sample.

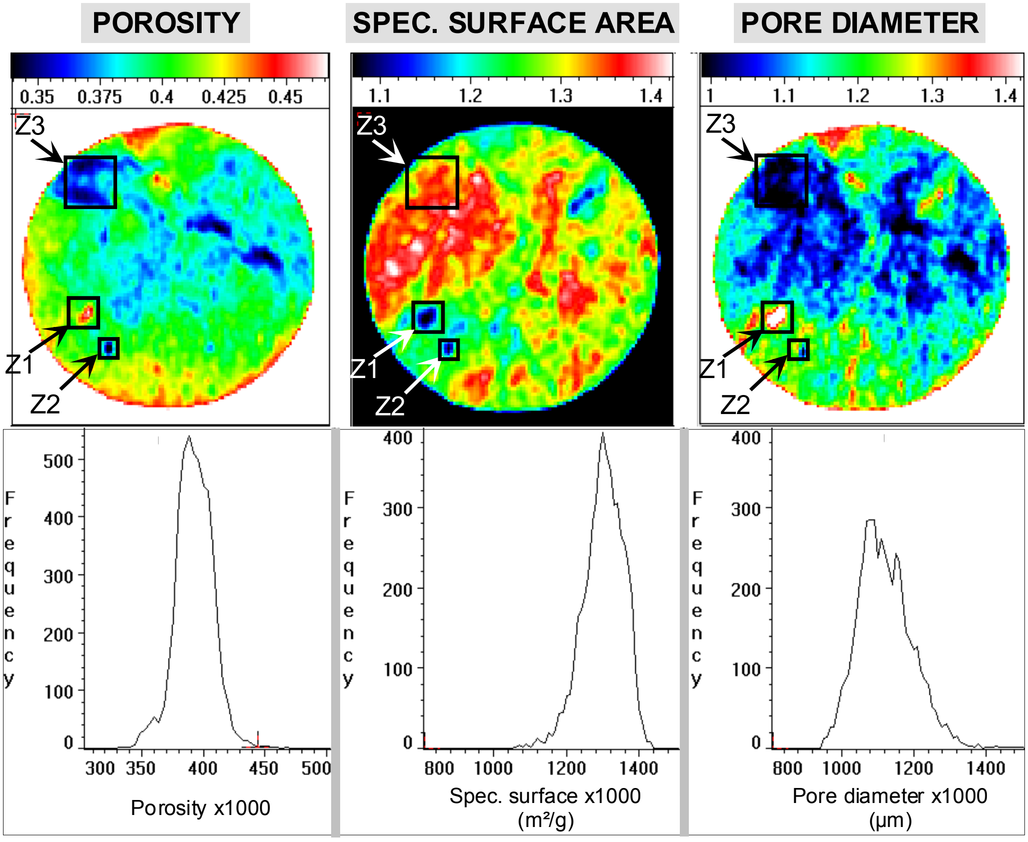

Fig. 37 – X-ray absorption/refraction typical topographic images and frequency histograms of the Mons chalk.

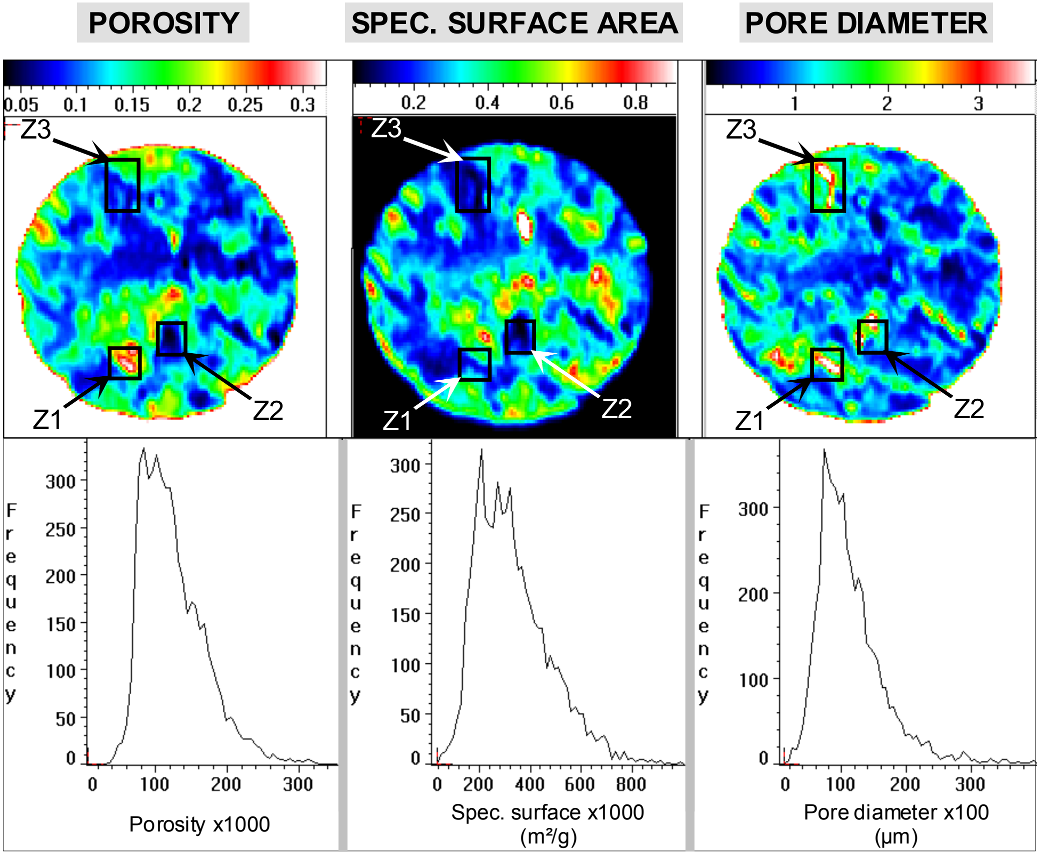

Fig. 38 – Typical topographic images and frequency histograms obtained from the Vuillecin limestone X-ray absorption/refraction characterization.

Fontainebleau sandstone

The various zones (in white and red and in dull-blue and black) that can be observed on each topographic image of this sandstone (Fig. 36) denote variations in the measured structure parameters. These zones are randomly distributed throughout the sample. The histogram on the left-hand side shows a maximum porosity frequency of about 12%. The porosity varies from 5% (dull blue zones) to more than 30% (red and white zones). Large deviations can be also observed for the specific surface area and the pore size: the specific surface area varies from 0.006 to 0.03 $m^2 g^{-1}$, and the pore diameter from 8 to 60 µm. Keeping in mind the results of the petrographical analysis (§1.2.2.1.), the zones of high porosity (in red and white) could be linked to areas of big macropores. In contrast, the low porosity zones were found to be due to strong cementation. Thus, the quartz overgrowths play a role in the variations observed. However, it is important to consider that for the Fontainebleau sandstone, contrary to the chalk and the Vuillecin limestone, the elementary voxel size and the mean pore and grain sizes are of the same order, which partially explains the wide range of measured porosity and specific surface areas. Two remarks can be made from a global observation of the three images:

- The local zones with high (in white and red) or low (in dull-blue) porosity do not correspond to the high and low specific surface areas, respectively.
- The zones with small pores correspond to the lowly porous areas (like Z1 and Z2 in Figure 36) and, in the same way, the areas of big pores correspond to the highly porous zones.

In conclusion, the accumulation of quartz overgrowths (strongly cemented areas) in the Fontainebleau sandstone simultaneously induces a lower porosity and smaller inter-granular spaces. The X-ray absorption/refraction analysis made it possible to show that the quartz overgrowth variations do not correlate with the variations in the specific surface area. This result means that the silicification in the Fontainebleau sandstone does not significantly change the density of the open inter-granular spaces[1] but only induces a reduction in their sizes.

Mons chalk

The topographic image on the left-hand side of Figure 37 shows the relative homogeneous distribution of the porosity in the sample of the Mons chalk (with the exception of the sample's borders). The main part of the sample is moderately porous (zones in green). Only some small special zones are highly porous (in red and white) or lowly porous (in dull blue). On the contrary, the specific surface area and pore size topographies show more heterogeneous spatial distributions of these parameters. The wide zones in red and white on the middle image of Figure 37 correspond to the maximum values of the specific surface area. These zones generally coincide with zones of smaller pores (in blue or black on the right-hand image). The frequency histograms show variations from about 35% to 45% in the porosity (similar deviations of the porosity were previously observed by BSE image analysis, §2.4.3.2.), from 1.1 to 1.4 m² g^{-1} in the specific surface area, and deviations from 0.8 to 1.4 µm in the pore size. However, these variations are low in comparison to those of the Vuillecin limestone exposed below. To illustrate the interpretation of these results, three zones were particularly considered:

- Zone Z1: this zone presents larger pores, a higher local porosity and corresponds to the lower values of the specific surface area. This zone was linked to foraminifera's cells.
- Zone Z2: this zone of minimum porosity is the location of the lower specific surface areas (like Z1). It was linked to bioclasts.
- Zone Z3: like Zone Z2, this zone shows the minimum porosity values, but its specific surface area reaches the maximum. It could be interpreted as the location of tightly packed micritic crystals surrounded by very small canals, which enhance the specific surface area and reduce the mean pore size in this zone.

Thus, a few foraminifera's cells (or macropores) enhance the porosity to the maximum, and the bioclasts are the cause of the low porosity areas. These macropores and bioclasts induce local variations in the specific surface area and the pore size. However, the specific surface area topography does not allow for a distinction to be made between the macropores and bioclasts, as seen throughout the examples of the zones Z1 and Z2. The crystal tightening plays also an important role in the variations in the specific surface area and the pore size. It is mainly responsible for the relatively heterogeneous distribution of these two parameters revealed by the X-ray absorption/refraction analysis. The topographic images made it possible to show that no relation may exist between the variations in the local porosity and the deviations in the local specific surface area. In fact, the degree of compactness inside the chalk does not have the same effect on the porosity and the specific surface area: the closer the particles, the finer and more numerous the canals. The porous volume is slightly changed, however. An indrease in the number of canals more significantly enhances the specific surface area than the porosity. This result remains all the more coherent considering that the analysis of the pore size by X-ray refraction always takes into account the pore diameters as well as the canal (throat) diameters.

To conclude, the X-ray absorption/refraction analysis made it possible to detect small variations in the values of the porous structure parameters of the chalk. The sensibility of the X-ray refraction analysis permitted us to show that the presence of macropores and of macro-sized shells is the cause of localized changes in the structure parameters. The analysis has also shown that the degree of compactness of the crystals, which varies throughout the chalk, is a factor responsible for the changes in the specific surface area and the pore size, without having any obvious influence on the porosity.

---

[1] When two grains are not embedded in each other, the inter-granular space remains open and accessible to a fluid. In the studied Fontainebleau sandstone, the silicification (the accumulation of quartz overgrowths) must not be so intense as to totally join together most of the grains and eliminate the interspaces between them.

The pore size was calculated on the basis of a model that correlates the data of the specific surface area and of the porosity (Relation *32*). Because the porosity remains generally constant in the chalk, the variations in the pore sizes observed on the right-hand topography generally reflect the variations in the specific surface area. Hence, the zones of smaller pore sizes correspond to higher values of the specific surface area and must be due to higher degrees of compaction.

Vuillecin limestone

The topographies of this limestone clearly show heterogeneities in the distribution of the porosity, the specific surface area and the pore size (Fig. 38). Compared to the chalk, the porosity values are distributed within a larger range, from 5% to 30%, as observed in the porosity frequency histogram in Figure 38. The same remark could be made for the specific surface area and the pore size: the frequency histograms show variations in the specific surface area from 0.08 to 0.8 $m^2 g^{-1}$ and in the local mean pore diameter from 0.2 to more than 3 µm.

Local variations in the porosity are induced by the presence of macropores (like for zone Z1 of Figure 38) or allochems (zone Z2).

The results led us to expose two major differences that distinguish the Vuillecin limestone from the chalk:

- Larger variations in all of the parameters of the limestone;
- The spatial distribution of the limestone's porosity coincides with that of the specific surface area for large zones of the sample (blue zones on the corresponding topographies), which was not found to be the case for the chalk. Nevertheless, an inverse relation between the variations in the specific surface area and the variations in the pore size still exists in the limestone: a minimum specific surface area often means a maximum mean pore size (like for the zones Z2 and Z3).

These discrepancies between the chalk and the limestone are explained by a difference in the size of the calcite crystals that constitute the two rocks: the Vuillecin limestone contains crystals which more significantly vary in size. Indeed, as already proved by petrographical analysis (see §1.2.2.5.), the calcite fragments in the Vuillecin limestone can be macroscopic (bioclasts, intraclasts) or microscopic (calcimicrite cement).

On the one hand, the zones of maximum porosity in the sample of the Vuillecin limestone were linked to macropores, which are generally surrounded by macroscopic fragment agglomerates. In these zones the specific surface area is at the minimum and the pore sizes at the maximum (like for zone Z1). On the other hand, it was seen by petrographical analysis that the difference between the calcisparite and calcimicrite zones in this limestone induces various porosity structures (in particular various pore sizes). Therefore, the data of X-ray absorption/refraction depend on whether the analysis location was in a sparite zone or a micrite zone.

Beside the various sizes of the fragments that characterize the Vuillecin limestone, large variations in the degree of cementation are also responsible for the local deviations measured. In general, a large amount of cement induces a high skeletal density; this means a minimum porosity and a minimum specific surface area. This is the case for the blue zones on the left-hand and middle topographies of the Vuillecin limestone in Figure 38. Moreover, the large range of pore access sizes recorded by mercury porosimetry (§2.2.4.5.) confirms the hypothesis on the various degree of cementation within this limestone.

Thus, the variations in the quantity of cement is the main petrophysical characteristic of the Vuillecin limestone, which governs the local absorption and refraction properties of this rock. Such cement amounts were not observed in the chalk.

2.6.3. Microstructure parameter averages – Comparison with other methods

As for the frequency histograms, the mean porosity, the mean specific surface area and the mean pore diameter were calculated by averaging the values of the three parameters for a limited spatial area of the sample, omitting the sample borders. The mean values obtained for all the material samples are summarized in Table 15.

2.6.3.1. Porosity and specific surface area

As seen in Table 15, the mean values of the porosity measured by X-ray absorption ($N_{X\text{-}AR}$) are in agreement with those already obtained by other methods like mercury porosimetry (N_{Hg}) for all the samples of the three materials. This seems to assure that the tested samples were representative of the materials.

Concerning the specific surface area, the agreement between $S_{X\text{-}AR}$ and S_{Hg} is not valid for all the materials:

- $S_{X\text{-}AR}$ is similar to S_{Hg} for the Fontainebleau sandstone.
- There is a slight deviation between $S_{X\text{-}AR}$ and S_{Hg} of the chalk.
- An outstandingly large deviation can be observed for the Vuillecin limestone, for which $S_{X\text{-}AR}$ is almost three times smaller than S_{Hg}.

The cause of the different values for the specific surface area of the limestone can not only be due to the material's porous structure heterogeneity: three samples of the material displayed similar values of $S_{X\text{-}AR}$, which remain even quite below the minimum value obtained by mercury porosimetry.

These results are explained considering the physics of the method and the limit of the X-ray refraction analysis. For void sizes below 0.1 µm, the refraction effect is no longer the only major phenomenon that occurs; the diffraction effect also plays a role in the deflection of the X-ray beam. Up to now, it was seen that the sandstone contains only macropores. On the other hand, the porous structure of the chalk mainly consists of micropores whose diameters are about 1 or 2 µm. A small portion of the micropores can have diameters below the limit value of 0.1 µm (the minimum diameter recorded by mercury porosimetry was about 0.02 µm). For this portion of micropores, the diffraction effect could occur and induced a slight underestimation of the specific surface area. In the Vuillecin limestone, numerous pores have diameters below 0.1 µm (see the results of the petrographical analysis and mercury porosimetry). These small pores count for a large part of the specific surface area of this material. They induced an underestimation of the transmitted X-ray intensity and of the specific surface area, which were recorded during the X-ray refraction analysis.

2.6.3.2. Pore size

The X-ray refraction analysis led to $D_{X\text{-}AR}$ values, which are comparable to the D_{50} values of mercury porosimetry (Table 15). For both parameters, however, the values are smaller than those of D_F from the BSE image analysis. As already explained, the smaller mean pore sizes recorded by mercury porosimetry are mainly due to the physical limits of this technique: mercury is forced into the pores and the measured diameters correspond to the pores' entry (throats) and not to the pores themselves. For the X-ray refraction analysis, the mean pore size was calculated using the value of the specific surface area. Thus, the explanation for lower $D_{X\text{-}AR}$, in comparison with D_F, is that the estimation of D_F does not take the throat size into account and the calculation of $D_{X\text{-}AR}$ does.

Thus, both the X-ray refraction analysis and mercury porosimetry depend not only on the pore sizes but also (and even more, so) on the throat sizes. The smaller mean diameters recorded using these methods, compared to the BSE image analysis, remain all the more understood assuming that the studied sedimentary rocks contain pores that are interconnected by numerous throats, which have various lengths and diameters (according to the rock).

Table 15 – Mean values of the porosity ($N_{X\text{-}AR}$), the specific surface area ($S_{X\text{-}AR}$) and the pore diameter ($D_{X\text{-}AR}$) obtained from the X-ray absorption/refraction characterization of samples of the Fontainebleau sandstone, the Mons chalk and the Vuillecin limestone; comparison with the mercury porosimetry (N_{Hg}, S_{Hg}, and D_{50}) and the BSE image analysis (surface porosity, S_{IA}, D_F).

	X-ray absorption/refraction characterization			
	Sample number	Mean porosity $N_{X\text{-}AR}$ (%)	Mean spec. surf. area $S_{X\text{-}AR}$ (m^2 g^{-1})	Mean pore size $D_{X\text{-}AR}$ (µm)
Fontainebleau sandstone	1	12.80	$14\ 10^{-3}$	25
Mons chalk	1	40.54	1.2	1.3
	2	40.80	1.3	1.1
Vuillecin limestone	1	11.79	0.3	0.9
	2	12.00	0.4	0.7
	3	11.91	0.4	0.8
	Mercury porosimetry			
		N_{Hg} (%)	S_{Hg} (m^2 g^{-1})	D_{50} (µm)
Fontainebleau sandstone		12.30	$13\ 10^{-3}$	31
Mons chalk		40.50	1.8	0.8
Vuillecin limestone		11.29	1.1	0.8
	BSE image analysis			
		Surface porosity	S_{IA} (m^2 g^{-1})	D_F (µm)
Fontainebleau sandstone		13.53	$4\ 10^{-3}$	112.1
Mons chalk		40.64	0.8	1.8
Vuillecin limestone		/	/	/

Despite the different specific surface areas measured in the Vuillecin limestone ($S_{X\text{-}AR} << S_{Hg}$), comparable values of D_{50} and $D_{X\text{-}AR}$ were recorded. This can be explained considering that D_{50} was not calculated using the specific surface area. The $D_{X\text{-}AR}$ was re-calculated using Relation 31 with a = 4 (cylindrical pore model). Using this new calculation method, D_{AV} and $D_{X\text{-}AR}$ remain similar for the Fontainebleau sandstone and the chalk (Table 16), however, D_{AV} is three times smaller than $D_{X\text{-}AR}$ for the limestone. This result is more coherent with S_{Hg} as it is three times higher than $S_{X\text{-}AR}$ in this rock. This shows that, although all the mercury porosimetry diameters were calculated using Washburn's relation, D_{50} depends less on the cylindrical pore model than D_{AV}. It also shows that the mean diameters calculated using the specific surface area and the cylindrical pore model is particularly representative of the sizes of the smaller pores, and even the throats inside the sedimentary rocks. Thus, the fact that the same D_{50} and $D_{X\text{-}AR}$ (spherical model) were recorded in the Vuillecin limestone has no real meaning concerning the porous structure of this rock.

Table 16 – Comparison of the mean pore diameters determined by X-ray absorption/refraction ($D_{X\text{-}AR}$) and mercury porosimetry (D_{AV}) using a cylindrical pore model.

	Fontainebleau sandstone	Mons chalk	Vuillecin limestone
$D_{X\text{-}AR}$ (cylinders)	17	0.8	0.6
D_{AV}	18	0.7	0.2

2.6.4. Summary of the X-ray adsorption/refraction characterization

The X-ray absorption/refraction analysis made it possible to simultaneously analyze the porosity, the specific surface area and the pore size in the sedimentary rocks (mercury porosimetry is the only method that also allows for these parameters to be simultaneously determined). The X-ray absorption/refraction analysis made it also possible to represent the spatial distributions of these three parameters. The advantage of this technique is that the spatial variations in these parameters are independent from any models and can be directly interpreted. It was shown that, for the Vuillecin limestone, the values of the specific surface area and the pore size measured by X-ray absorption/refraction significantly differed from those of common techniques like mercury porosimetry due to the presence of very small pores and throats in this rock. This made it possible to appreciate the limits of the method and the problems that can occur during the analysis of sedimentary rocks: more investigations must be made on improving the physical aspects of the method for pore sizes below 0.1 µm.

Using the X-ray absorption/refraction characterization, the spatial variations in the porous structure parameters of the sedimentary rocks were linked to the characteristics of their mineral structures. The variations in the parameters (mainly the specific surface area and the pore size) were mainly due to heterogeneities in the arrangement of the crystals and in the sizes of the crystals (in particular in the Vuillecin limestone). The interest of the X-ray absorption/refraction characterization was particularly the study of the relationship between the porosity and the specific surface area in the sedimentary rocks. It was concluded that, in the sedimentary rocks, the relation porosity-specific surface area is generally not direct: for instance, when the porosity in a rock is similar from one zone to another, the specific surface area can highly vary. The main reason for a “complex” relation is that factors like the quantity of cement or the degree of compactness in the sedimentary rocks influence the porosity and the specific surface area in different ways.

3. Fluid transport properties – Determination and prediction

The purpose of this part of the study was the analysis of fluid transport properties: water imbibition kinetics and gas permeability. The transport property data were interpreted with regard to the pore and mineral structures of the rocks. The applications of porous network models using the data previously obtained in this study were helpful for the understanding of the fluid transport properties. They made it also possible to appreciate in which limits a particular porous network model is applicable to a more or less homogeneous sedimentary rock.

3.1. Capillary water imbibition kinetics

3.1.1. Theory

The theory of the capillary water imbibition under atmospheric conditions is based on the hydrodynamic principles and the capillary pressure expression. POISEUILLE (1842) has established a theory, which expresses the flow of a fluid in a cylindrical tube (Fig. 39). Considering a fluid velocity u, the flow Q in the tube of cross section s is written as:

$$Q = \int u \, ds \quad (33)$$

Under a differential pressure ΔP, the fluid velocity u is a function of the radius r (R: radius of the tube; η: fluid viscosity; L: length of the tube):

$$u(r) = \frac{\Delta P}{4\eta L}\left(R^2 - r^2\right) \quad (34)$$

Replacing the velocity by its expression in Relation 33 and integrating it leads to Poiseuille's law, which expresses the fluid flow as a function of the radius R, the differential pressure ΔP and the length L of the cylinder:

$$Q = \frac{\pi R^4 \Delta P}{8\eta L} \quad (35)$$

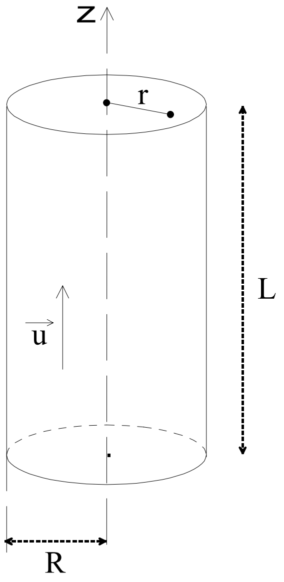

Fig. 39 – Model of a cylindrical vertical tube.

WASHBURN (1921) has developed this theory in order to express the kinetics of water migration by capillary imbibition for cylindrical pores.

In the case of the capillary water absorption in a vertical cylindrical pore, the water flow is governed by the capillary pressure and the gravity. Thus, the differential pressure is:

$$\Delta P = \frac{2\gamma\cos\theta}{R} - \rho g L \qquad \textit{(36)}$$

where ρ is the water density, γ the surface tension of water, θ the contact angle between water and the tube and g the gravity acceleration.

If the effect of gravity is considered negligible in a short vertical tube, replacing ΔP in Relation 35 gives the following expression of the water flow (for water at 20°C, $\cos\theta \approx 1$, $\gamma = 72.2\ 10^{-3}$ N m^{-1}, $\eta = 1.002\ \pi\ 10^{-3}$ Pa s):

$$Q = \frac{\gamma \pi R^3}{4\eta L} \qquad \textit{(37)}$$

The flow Q can also be written as a volume variation with time:

$$Q = \frac{dV}{dt} = \frac{\pi R^2\, dL}{dt} \qquad \textit{(38)}$$

The combination of Relations *37* and *38* leads to:

$$\frac{dL}{dt} = \frac{\gamma R}{4\eta L} \qquad \textit{(39)}$$

After the integration of Relation *39*, the height of water L is expressed as a function of the square root of time (considering a height of water L = 0 at the time t = 0):

$$L = B\sqrt{t} \qquad (40)$$

$$\text{with } B = \sqrt{\frac{\gamma R}{2\eta}} \qquad \textit{(41)}$$

The volume V of water, which invades the cylindrical pore at time t is $V = \pi R^2 L = R^2 B\sqrt{t}$.

Thus, the weight of water absorbed (weight increase, δw, of the imbibed sample) per surface unit also varies with the square root of time (the water density $\rho = 1$ g cm^{-3}):

$$\frac{\delta w}{s} = A\sqrt{t} \qquad \textit{(42)}$$

$$\text{with } A = \pi R^{5/2}\sqrt{\frac{\gamma}{2\eta}} \qquad \textit{(43)}$$

Relations *40* and *42* express Washburn's theory for the kinetics of the water capillary absorption.

3.1.2. Experimental

The cores (diameter of 4 cm, length from 4 to 8 cm), tested by water porosimetry (total and free water porosity) were used again for water absorption kinetics measurements. The procedure followed for the determination of the water absorption coefficients was the one recommended in the European Norm EN 1925:1999. A sample is preliminary dried in an oven at 60°C until a stable weight. Then, it is placed in an air-tight container to prevent evaporation and at a stable temperature (25°C) – the temperature variations can modify the surface tension and the viscosity of water and influence the absorption kinetics (MERTZ J.D., 1991; MENG B., 1993). During the experiment, a constant volume of distilled water (5 mm in depth) permits the imbibition from the bottom of the sample (Fig. 40). The length of the part of the sample invaded by water, also called the height of the wet fringe (L), and the weight increase of the sample (δw) are measured during the experiment. Curves are established by plotting L and δw/s (where s is the sample's cross section area) with the square root of time (see the example curves in Figure 41a.). These curves are called "capillarity curves".

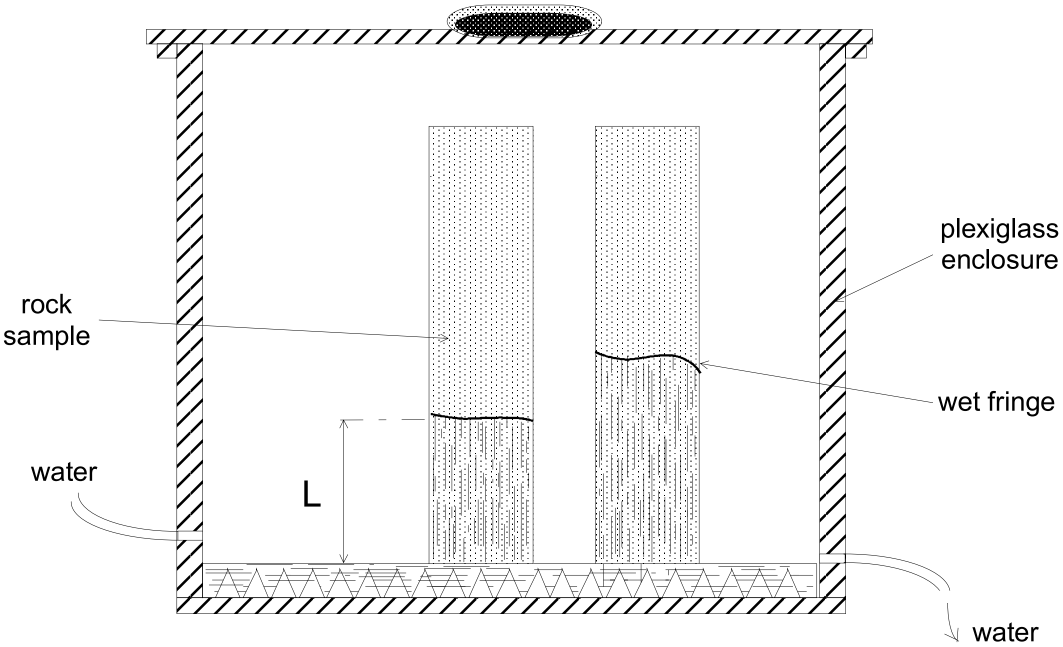

Fig. 40 – Diagram of the capillary water imbibition kinetics device.

3.1.3. Influence of porous structure heterogeneities on the capillarity curves

3.1.3.1. Theoretical capillarity curves for homogeneous porous media

For a homogeneous sample, the representation of the height of the wet fringe with the square root of time is theoretically linear (Fig. 41a.) in accordance with Relation *40*. The slope of the line is B (cm $h^{-1/2}$).

The representation of the weight increase per surface unit with the square root of time shows two parts, corresponding to different mechanisms:

- The first straight line corresponds to the process of water absorption in the capillary pore network, i.e. to the water imbibition of the free porosity. According to Relation *42*, A (g cm^{-2} $h^{-1/2}$) is the slope of this line.
- The second linear part corresponds to a slower imbibition process: the bigger pores are progressively filled by the dissolution and diffusion of trapped air in water (BOUSQUIE P, 1979; MERZ J.D., 1991). This phenomenon is governed by the FICK's laws.

3.1.3.2. Theoretical capillarity curves for heterogeneous porous media

For a sample with a heterogeneous porous network, noticeable changes occur in the slope of the curves (Fig. 41b. and 41c.). Such changes denote the presence of various porous structures, for example, relevant variations in the pore or throat mean size within the sample.

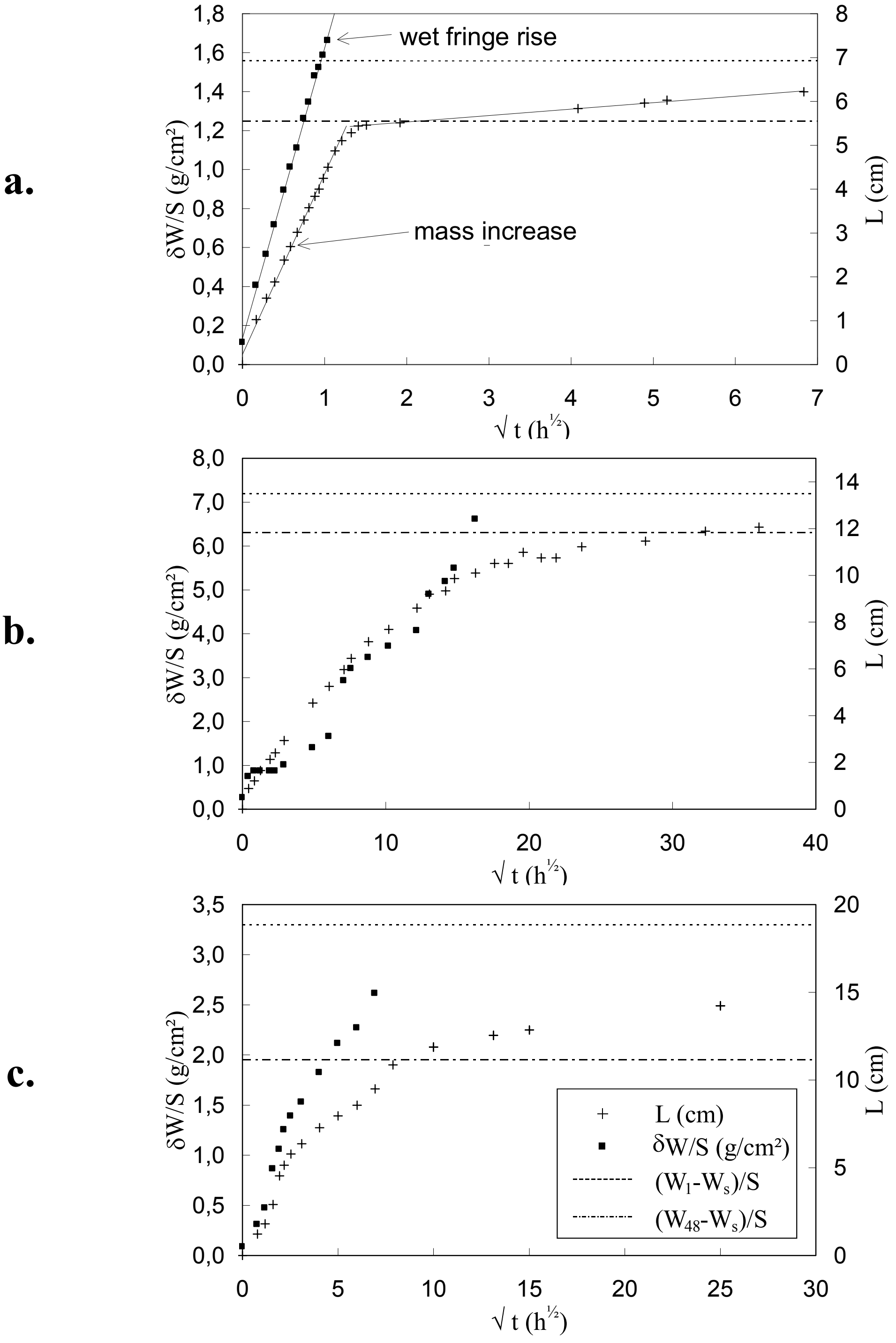

Fig. 41 – Examples of capillarity curves (HAMMECKER C., 1993). a.: Homogeneous porous network (Hontoria limestone). b.: layered porous structure (Darney sandstone). c.: Plurimodal porous network (Gueberschwihr sandstone).

3.1.4. Interpretation of the curves and the parameter values

The primary data of capillary water imbibition kinetics are reported in Appendix H (capillarity curves and analytical results), and the analytical average results are summarized in Table 17.

Typical capillarity curves were obtained for four of the rocks (Fontainebleau and "Grès à Meules" sandstones, Mons chalk and tuffeau limestone). These curves correspond to the imbibition kinetics within homogeneous porous networks and show regular weight increases and wet fringe rises. At the end of the first part of the imbibition, the volume of voids imbibed corresponds to the free porous volume (water free porosity, N_{48}). These results denote a high connectivity of the porous network of these rocks. Moreover, relatively low standard deviations of A and B coefficients (Table 17) mean a relative invariability of the porous structure (mean pore and pore access sizes, connectivity…) from one sample to another, i.e. at the scale of the block. Concerning the fifth rock, the Vuillecin limestone, changes in the slope of the capillarity curves (weight increase as well as water fringe migration) can be observed for many samples (Appendix H). The A and B coefficients of this limestone are quite lower than those of the other rocks. They greatly vary from one sample to another: that means a low connectivity of the porous network of the Vuillecin limestone and high variations in its porous structure.

Differences in the A and B values can be observed between the five rocks, meaning different pore structure characteristics. Considering the B values and the capillarity curves, a classification was proposed:

1. The Fontainebleau sandstone: very fast wet fringe rise and almost all the free porosity is imbibed after less than half an hour.
2. The Mons chalk, the tuffeau limestone and the "Grès à Meules" sandstone: slower wet fringe rises (the free porous volume was filled after 2-4 hours, the chalk being filled the fastest by water).
3. The Vuillecin limestone: very slow wet fringe rise for 30 to 100 hours.

Table 17 – Experimental mean coefficients A and B and their standard deviations for the five sedimentary rocks.

	Fontainebleau sandstone	"Grès à Meules" sandstone	Mons chalk	Tuffeau limestone	Vuillecin limestone
Number of samples	4	4	11	7	9
A_{exp} (g cm^{-2} h$^{-1/2}$)	0.98	0.49	2.92	1.90	0.06
σ_A (g cm^{-2} h$^{-1/2}$)	0.04	0.04	0.08	0.46	0.01
$\sigma_{R,A}$ (%)	4.1	8.2	2.7	24.2	16.7
B_{exp} (cm h$^{-1/2}$)	14.53	3.86	8.21	5.52	0.67
σ_B (cm h$^{-1/2}$)	0.55	0.30	0.45	0.22	0.12
$\sigma_{R,B}$ (%)	3.8	7.8	5.5	4.0	17.9

Fontainebleau Sandstone

The free porosity, previously observed on thin sections, constitutes a continuous porous network, allowing for continuous water flow throughout the rock (trapped porosity is linked to sparse macropores). The free porous volume is mainly represented by the volume of the throats and a little by the dihedral parts of the bigger pores and some small pores. The homogeneous spatial distribution and the almost constant size of these flow paths (remember the relatively small range of diameters measured by mercury porosimetry) explain the regular weight increase. The very fast wet fringe rise is due to the large mean size of the throats (around 30 µm).

Locally, water rises slower at the wider part of the big sparse macropores. However, slightly smaller parallel throats allow for such pores to be bypassed (Fig. 42a). Such parallel paths are located inside areas in which the grain arrangement is more compact and inside areas with higher amounts of quartz overgrowths. Because they are randomly distributed inside the rock, highly cemented zones (very small throats) do not induce variations in the water imbibition properties inside a core. Thus, the water migration in this rock could be simply described by a bypass model (Fig. 42b).

“Grès à Meules” Sandstone

The B and A coefficients of the “Grès à Meules” sandstone are four and two times lower than those of the Fontainebleau sandstone, which is mainly due to the presence of clay minerals in the “Grès à Meules” sandstone. In this sandstone, the microporosity linked to the clay minerals (illite, kaolinite) makes preferential continuous and regular flow paths (Fig. 43a). Thus, three complementary effects of the clays during water imbibition can be pointed out:

1. The clays reduce the size of the pores and throats, globally inducing a slower water rise (lower B value).
2. The clays are responsible for a constant mean size of the throats of the main part of the porous network, ensuring a regular weight increase (mercury porosimetry revealed a main pore access diameter class with diameters of around 10 µm).
3. The clays rim the pore walls, allowing for water to continuously flow throughout the porous network of the coarse grain layers (Mode 1).

Despite the layered structure (linked to changes in the porous network characteristics; see the results of the computed tomography analysis, §2.5.3.2.), no variations in the water imbibition kinetics were recorded for analyses following the direction perpendicular to the stratification planes. This is in contradiction with common capillary imbibition results, which are obtained for such bedded geomaterials (MERTZ, 1991). There should be two reasons for this. First, the thickness of the layers is too low to induce measurable variations at the scale of the core sample. Second, the concentration of clay minerals is quite lower in the coarse grain layers, but high enough to ensure the continuity and regularity of the water flow (Fig. 43a).

Contrary to the Fontainebleau sandstone, the bypass model was found to be not applicable to this sandstone. An adequate model was proposed. Its diagram is represented in Figure 43b.

Mons Chalk

The free porous volume of the chalk constitutes the main part of its total porous volume. The pore access size is of the same order as the pore size (as seen by BSE-image analysis combined with mercury porosimetry); thus, water rises with almost the same velocity whether in the pores or in the throats. The water flow paths are regular in size and well interconnected (Fig. 44a). Because of the high free porosity, the flow paths are numerous per surface unit. These characteristics are the cause of the regular weight increase and wet fringe rise, and of the high value of A. The small mean size of the pores and pore accesses (1-2 µm) must be the main reason for the low wet fringe rise. These results show that the sparse macropores observed on thin sections do not influence the water imbibition kinetics. Thus, the water imbibition within this rock could be simply described by a tubular model (Fig. 44b).

Tuffeau Limestone

Considering the various porosity structures (observed by petrographical analysis) and the various pore access classes (revealed by mercury porosimetry) inside this limestone, quite regular weight increases and wet fringe rises can be surprising. As a matter of fact, the random homogeneous distribution of these different structures globally allows for a regular capillary rise within this rock.

The class of pores linked to the pore access diameters of about 10 µm measured in the tuffeau limestone constitutes preferential flow paths for the water imbibition. This class of pores represents a large part of the porous network. It was identified as the pores located between the opal-CT spherules, and between the spherules and the neighbouring minerals (see §2.2.4.4.). Since the spherules are homogeneously distributed throughout the rock, these porous spaces constitute regular and continuous flow paths. Moreover, these spherules have a lamellar structure, which induces a high micro-roughness; this facilitates the water rise (Fig. 45a and b). The high value of A is mainly due to the high free porosity (as for the chalk). Because they are concentrated inside sparse areas, the clay minerals such as smectite and glauconite do not induce a slow capillary water rising inside this limestone, as illite and kaolinite do inside the "Grès à Meules" sandstone. These clay minerals induce rough surfaces of some sparse macropores and occasionally contribute to the water rise (Mode 1).

Vuillecin Limestone

Contrary to the samples VUI1 and 3, the samples VUI 6 and 7 show strong changes in the slope of the weight increase and wet fringe rise curves. The capillarity curves of the other samples (VUI 2, 4, 8 and 9) also do not really follow a linear trend. These results can be explained by different distributions of the diverse porous areas, and particularly by the distribution of the microporous micrite areas, which constitute preferential paths for the water migration:

- In VUI1 and 3, there must be numerous contiguous micrite areas that constitute a continuous microporous network throughout the core, inducing a regular wet fringe rise and weight increase.
- In the other samples, a lower amount of micritic cement leads to a more or less discontinuous microporous network. Large zones of bioclasts (calcite shells) or large sparitic areas with groups of macropores connected by tight canals are intercalated (Fig. 46a). The water rise is interrupted (in fact, it is an extremely slow water flow) at the wider part of the macropores and in zones of sparite shells containing close calcite crystals. The bypass of macropores occurs through rare, thin and complex "parallel" flow paths.

Thus, a bypass model with a thin and tortuous parallel canal was found to well describe the water migration in this limestone (Fig. 46b).

In all samples, lots of micrite and sparite areas are highly cemented and constitute a labyrinth of very small and complex canals (high tortuosity), which explains the very slow wet fringe rise and the very low value of B. The low values of A are mainly due to the low porosity and to the small amount of tiny canals. The high relative standard deviations of A and B recorded from one sample to another show the porous network's heterogeneity at the scale of the block, previously pointed out at the scale of smaller samples, by petrographical analysis, mercury porosimetry and computed tomography.

The sampling direction for the samples VUI1 to 4 is parallel to that of the stratification planes inside the block, and perpendicular for the samples VUI5 to 9. High variations in the slopes of the curves can be often observed for the sample set VUI5 to 9. In fact, accumulated bioclasts, which are flow barriers for the water migration, mainly have long shapes with large diameters that are sub-parallel to the bedding stratification.

Legend of Figures 42 to 46

→ : water flow

→ : gas flow

D_A : pore access diameter

■ : clay mineral concentrations

Fontainebleau sandstone

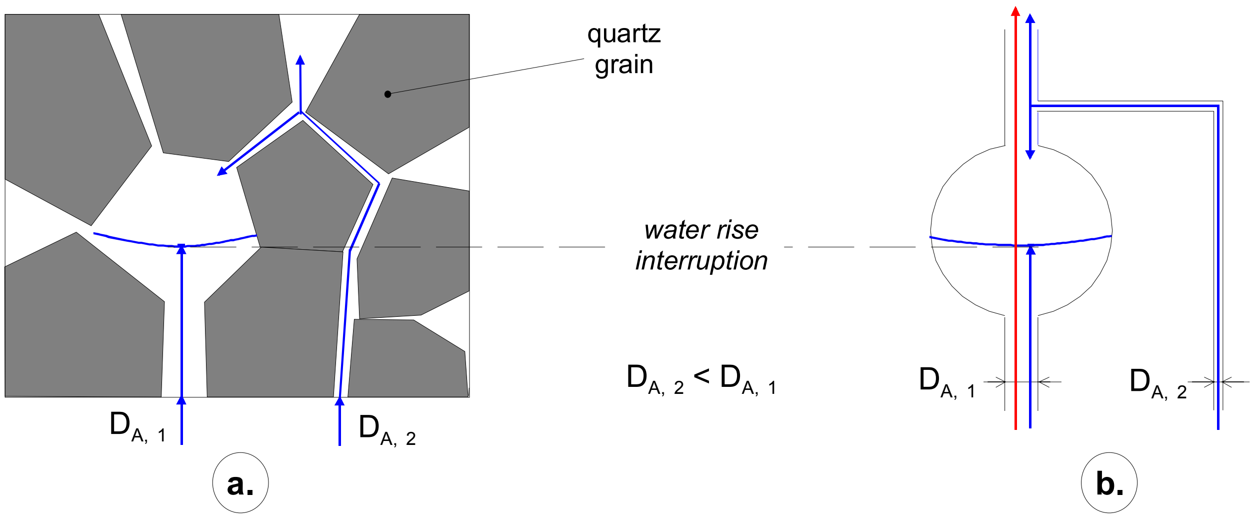

Fig. 42 – a. Diagram of the water migration paths (arrowed bold-line) within the Fontainebleau sandstone; b. Model proposed for describing the water capillary imbibition and the gas flow.

“Grès à Meules” sandstone

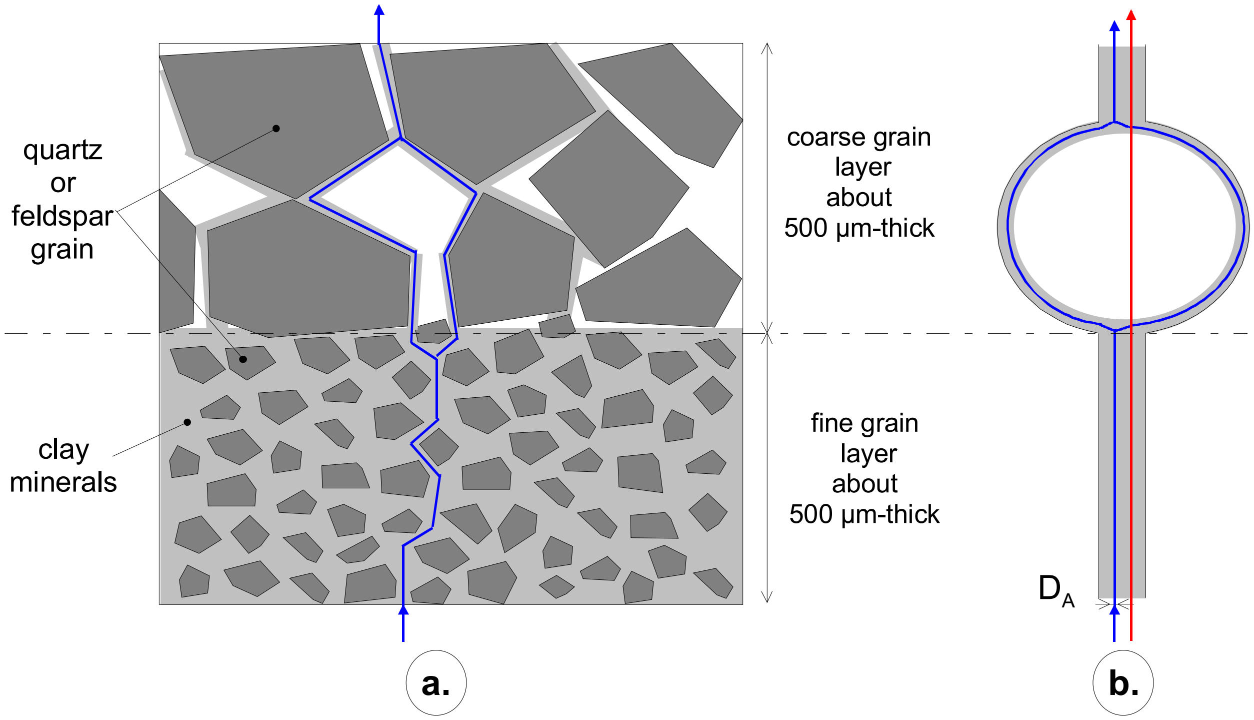

Fig. 43 – a. Diagram of the water migration paths (arrowed bold-line) within the “Grès à Meules” sandstone; b. Corresponding model proposed for water capillary imbibition and gas flow.

Mons chalk

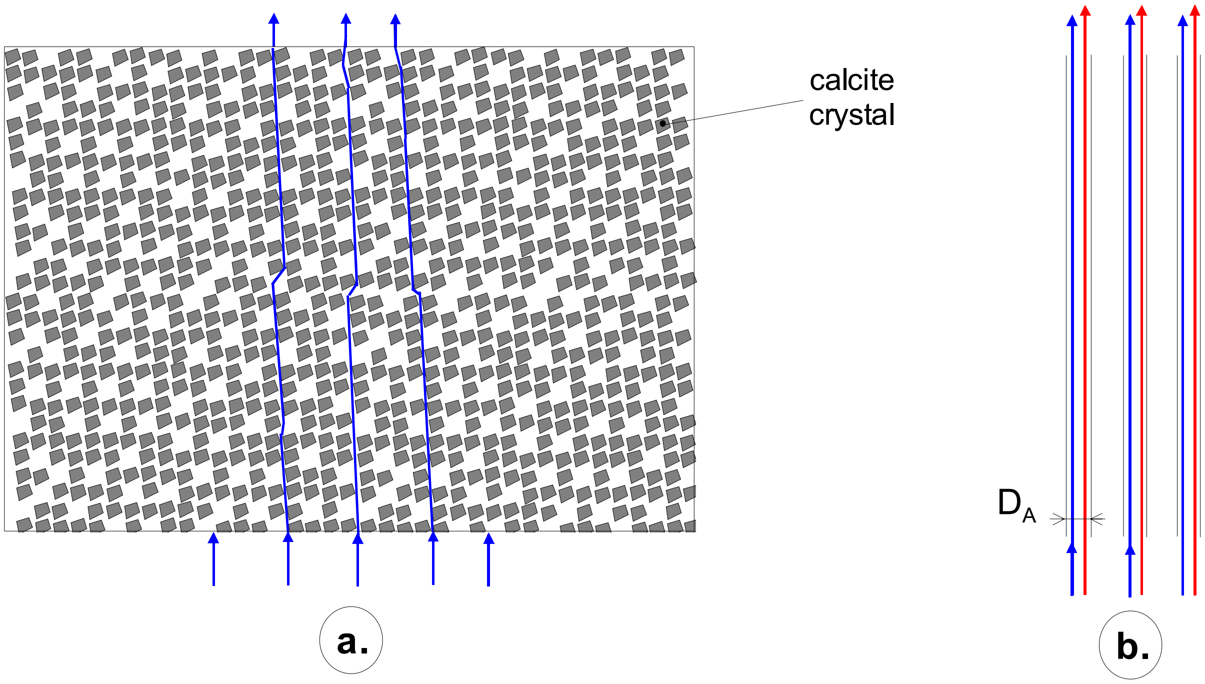

Fig. 44 – a. Diagram of the water migration paths (arrowed bold-line) within the Mons chalk; b. Corresponding tubular model proposed for water capillary imbibition and gas flow.

Tuffeau limestone

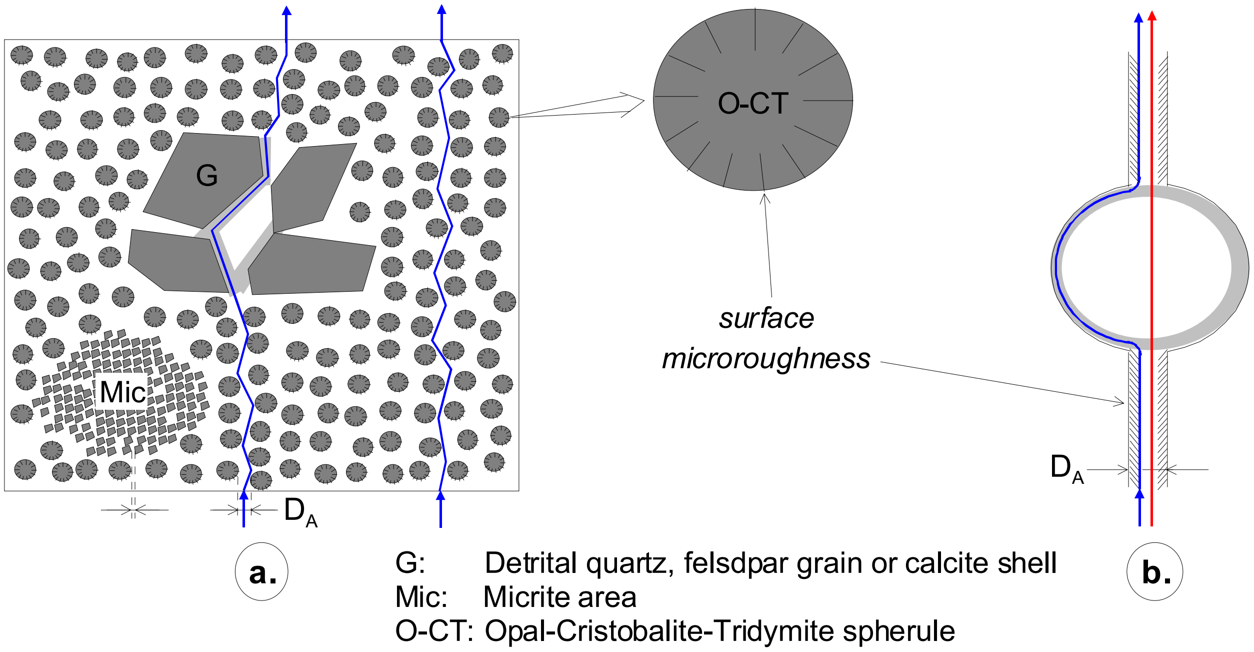

Fig. 45 – a. Diagram of the water migration paths (arrowed bold-line) within the tuffeau limestone; b. Model proposed for the water capillary imbibition and the gas flow.

Vuillecin limestone

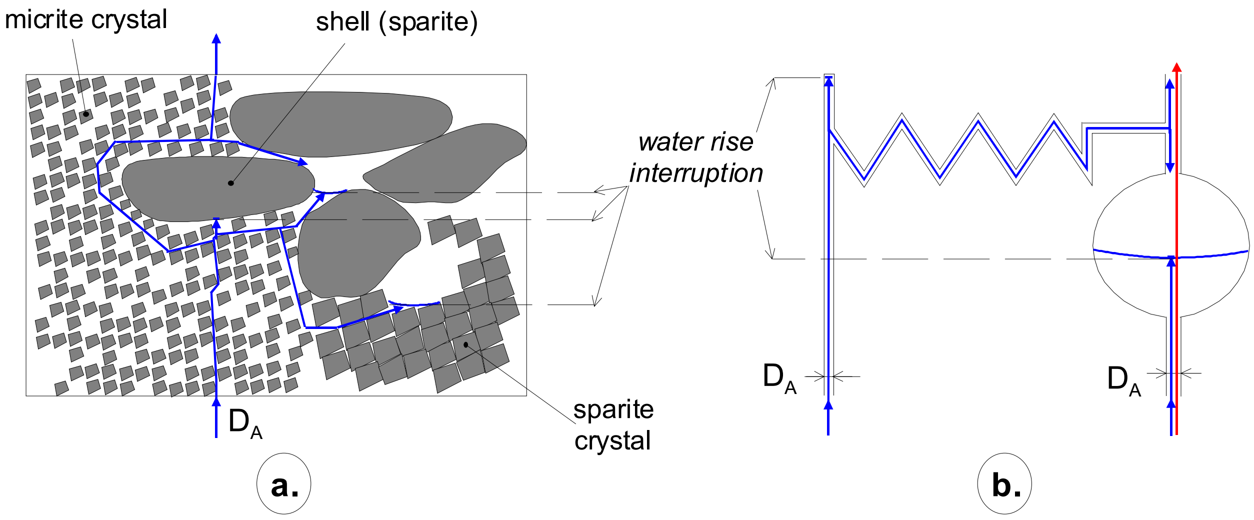

Fig. 46 – a. Diagram of the water migration paths (arrowed bold-line) within the Vuillecin limestone; b. Corresponding model proposed for both the water capillary imbibition and the gas permeability.

3.1.5. Relationships between the A and B experimental values (A_{exp} and B_{exp}) and structure parameters

3.1.5.1. Relation between B_{exp} and D_H

No relation can be pointed out between B_{exp} and D_{50}, the median pore access diameter determined by mercury porosimetry. However, as shown in Figure 47, there is a linear relation between B_{exp} and D_H, except for the chalk. The larger the hydraulic diameter, the higher the coefficient B is; this is in agreement with Relation *41*.

D_H is the greatest access diameter from which mercury begins to fill the main part of the porous network (Appendix D). This diameter governs the water rise velocity in the chalk, mainly because of the small difference between the pore size and the throat size – the porous network of the chalk is not "complex" and can be assimilated to linear tubes (Fig. 44b). In the other rocks, the lowest throat diameters govern the water rise velocity. These diameters must be:

- those of small parallel flow paths (smaller throats) which govern the water rise velocity in the Fontainebleau sandstone (Fig. 42a) and in the Vuillecin limestone (Fig. 46a) due to the bypass phenomenon.
- those linked to a micro-roughness at the throat borders due to the clay minerals in the "Grès à Meules" sandstone (Fig. 43a) or to the lamellar structure of the opal-CT spherules in the tuffeau limestone (Fig. 45a).

3.1.5.2. Relation between A_{exp} and S_{48}

A linear correlation can be established between A_{exp} and S_{48} for three rocks (Fontainebleau sandstone, chalk and tuffeau limestone), which shows that the coefficient A increases with the amount of free porosity (Fig. 48). The same correlation is not valid for the "Grès à Meules" sandstone and the Vuillecin limestone for which A is too low to follow the trend given by the samples of the other three rocks. The same remark can be made for the sample TUF6; the interpretation for this particular case is exposed in the next section (§3.1.5.3.).

In the coarse grain layers of the "Grès à Meules" sandstone, the clay minerals allow water to flow through (Fig. 43a and 43b). Their lower concentration compared to the fine grain layers means a smaller delivery of water inside the coarse grain layers without changing the mean water rise velocity. In other words, clays allow for the free porosity to be fulfilled in fine grain layers, but induce a low volume of water that can continuously flow throughout the coarse grain layers. The consequence is that the amount of free porosity is not directly linked to A, but more depends on the distribution of the clay minerals.

The same discrepancy between the amount of free porosity and the delivery of water also exists for the Vuillecin limestone, due to the fact that in lots of places water must flow through a few thin "parallel" paths (in micrite or even sparite zones, which are often highly cemented) to rise further up in the sample (Fig. 46a).

3.1.5.3. Relationship A – B – N_{48}

Calculating Ax100/N_{48} for each rock sample and plotting the results versus B (Fig. 49) made it possible to show that the free porosity is a correlation factor between B and A, since a linear relation between Ax100/N_{48} and B in a factor 1 exists whatever rocks.

It can be noted that the sample TUF6 is plotted apart from the other tuffeau limestone samples, i.e. apart from the linear trend followed by the other samples (Fig. 48 and Fig. 49). This can be linked to the fact that the sample TUF6 displayed a low coefficient A (1.14 g cm^{-2} $h^{-1/2}$) and a high mineral density (2.67 g cm^{-3}) in comparison with the other samples (2 g cm^{-2} $h^{-1/2}$ and 2.65 g cm^{-3}, respectively).

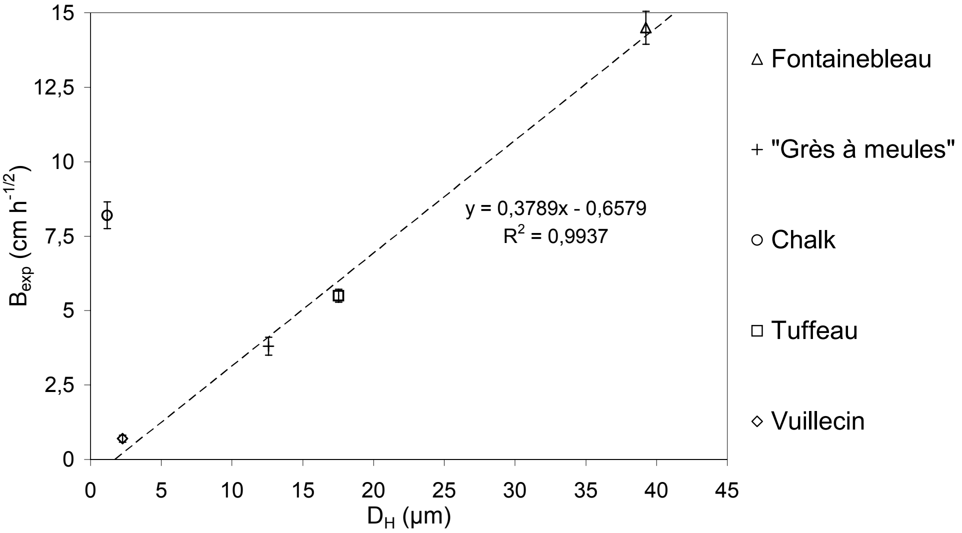

Fig. 47 – Diagram of the mean B_{exp} *versus the hydraulic diameter* D_H*.*

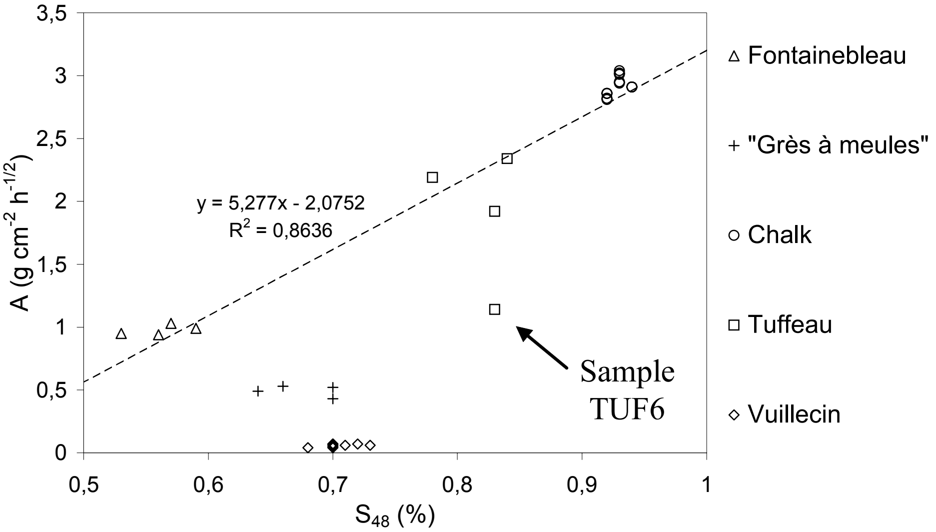

Fig. 48 – Diagram of A versus Hirschwald's coefficient S_{48} *considering all the samples.*

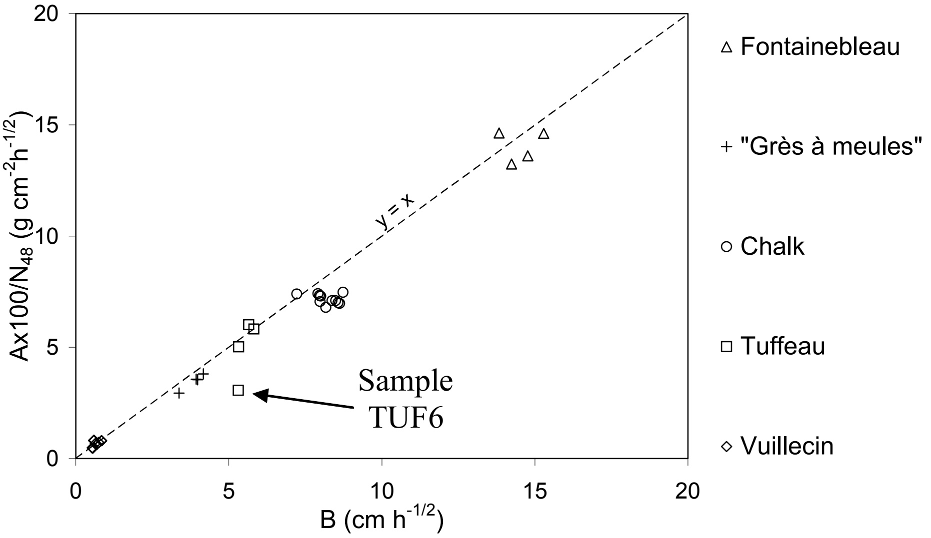

Fig. 49 – Diagram of Ax100/N_{48} *versus B considering all the rocks samples.*

Let us consider that the mineral density d_M of the sample can be written as:

$$d_M = \frac{\sum_k d_{M,k} V_k}{V} \quad (44)$$

with $d_{M,\,k}$ as the mineral density of the mineral phase, or component k, V_k the volume occupied by this phase and V the total volume of the sample.

The opal-CT spherules have the lowest mineral density in comparison with the other components of the limestone (Table 18). According to Relation *44*, the higher mineral density in the sample TUF6 can be explained by a lower volume occupied by the opal-CT spherules. The volume difference is dropped for the clay minerals, the quartz and/or feldspar grains. The higher bulk density (1.42 g cm^{-3}) in the sample TUF6 is then explained by a higher volume occupied by the quartz grains, which are not microporous. As seen above, the opal-CT spherules play a predominant role in the water imbibition kinetics. TUF6 contain a lower quantity of spherules compared to the other samples and numerous quartz or feldspar grains, inducing a less homogeneous flow path distribution and especially a lower quantity of flow paths in this sample. These structure characteristics of the sample TUF6 explain its lower value of A. However, the opal-CT spherules are numerous enough to allow for the water rise velocity inside TUF6 to be similar to that inside the other samples (similar values of B).

Table 18 – Mineral density for the tuffeau limestone components.

Components of the tuffeau limestone	Opal-CT spherules			Quartz/ Feldspar	Clay minerals	calcite
	Opal	Cristobalite	Tridymite			
Mineral density d_M (g cm^{-3})	2.01 - 2.16	2.33	2.26	2.65	2 – 3	2.71

3.1.6. Prediction of the coefficient B

3.1.6.1. The cylindrical pore model

Theoretical coefficients B_{cyl} were calculated on the basis of the Washburn cylindrical pore model (Relation *41*) using the D_H hydraulic diameter since it was concluded above that the pore access size mainly governs the water imbibition.

The values of B_{cyl} are 6 to 30 times higher than B_{exp} (Table 19), except for the Chalk. The small difference for the chalk shows that the cylindrical pore model is valid for this rock and confirms that the flow paths in the chalk can be simplified by regular linear tubes (Fig. 44b).

Similar theoretical values of B_{cyl} were obtained for the chalk and the Vuillecin limestone. However, the experimental data have shown that the capillary water imbibition properties of the Vuillecin limestone differ from those of the chalk: the limestone B_{exp} is quite lower due to the heterogeneity of the porous structure of this rock, as explained in §3.1.4.5.

As for many previous applications of the cylindrical pore model (SZEKELY J. et al., 1971; DULLIEN F.A.L., 1979; LEVINE S. et al., 1980), these results confirm that, although the model can describe the capillarity behaviour, there is often an incompatibility between the dimensions (pore or pore access size) of the simulated porous network and the real geometry of the pores. To try to solve this problem, other pore geometries must be envisaged.

Table 19 – Coefficient B_{cyl}, calculated using the cylindrical pore model and D_H, compared to the experimental B_{exp}.

Material	Fontainebleau sandstone	“Grès à Meules” sandstone	Mons chalk	Tuffeau limestone	Vuillecin limestone
D_H (µm)	39.3	12.6	1.2	17.5	2.2
B_{cyl} (cm $h^{-1/2}$)	90.4	51.2	12.8	60.3	21.4
B_{exp} (cm $h^{-1/2}$)	14.5	3.8	8.2	5.5	0.7

3.1.6.2. The model of spherical pores

Theory review

The problem of the B-pore size correlation led some authors (MERZ J.D. et al., 1988; HAMMECKER C. et al., 1989 and 1993; HAMMECKER C., 1993) to think about flow paths, which would be tubes built with a succession of hollow spheres (Fig. 50). The authors have developed a model of spherical pores for the simulation of capillary imbibition in sedimentary rocks (details of the theory were reported in Appendix I).

The model is described by only two parameters D and D_A, which can be assimilated as the pore diameter and the pore access diameter, respectively. D_A can be well-determined by mercury porosimetry (D_{50}), however D cannot be precisely determined for all rocks, even by image analysis.

An alternative method for estimating these parameters is to assimilate the rock structure as packed spherical grains. The theoretical diameter of the grains D_S is determined with the following relation (LOWELL S. and SHIELDS J.E., 1984):

$$D_S = \frac{6}{d_B S_i} \qquad (45)$$

using bulk density (d_B) and specific surface area (S_i) experimental data.

The porous structure is reduced to spheres of diameters D and D_A, which fill the cavities between the spherical grains and the entry to these cavities, respectively. D and D_A, pore structure parameters of the model, are calculated from D_S using geometrical relations (Appendix I). Three packing patterns are considered: cubic, tetrahedral and octahedral. The values of the parameters of each sedimentary rock of this study are given in Table 21.

The authors (HAMMECKER C., 1993; HAMMECKER et al., 1993) have calculated B coefficients for an imbibition over a 5 cm-height L using the model of spherical pores and according to each packing pattern. They plotted the values versus different values of the specific surface area and came to the following empirical relation:

$$B = \frac{a}{\sqrt{d_B S_i}} \qquad (46)$$

with the condition $0.1 < S_i < 50$ m² g^{-1}. The model constant a depends on the grain packing pattern:

- Octahedral: a = 9.882
- Tetrahedral: a = 23.07
- Cubic: a = 28.91

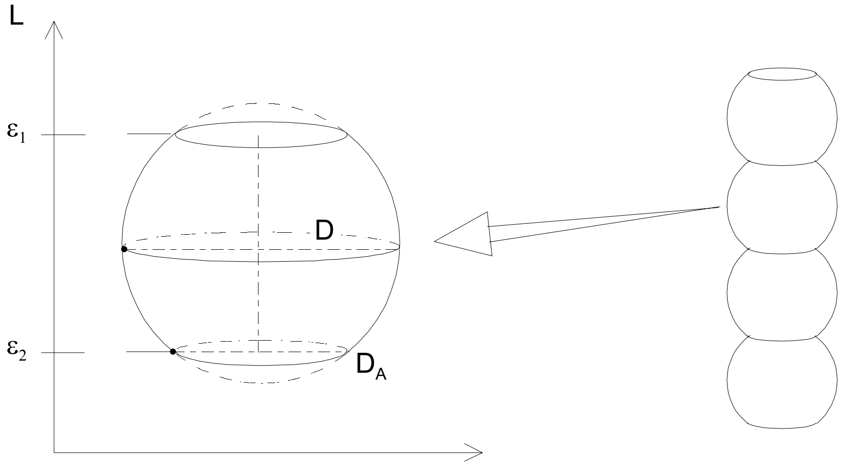

Fig. 50 – Diagram of the spherical pore model.

Application of the model

During the calculation of the mean grain sizes D_S of the sedimentary rocks according to Relation *45*, the experimental data were those of $d_{B,Hg}$ and S_{BET} obtained in this study (Table 20). The mean grain sizes of the Fontainebleau sandstone and the chalk are quite in agreement with the sizes of the grains observed on thin sections and SEM images (the great variety of grain sizes in the other rocks did not allow for evaluations to be made). The values of the model parameters D and D_A are reported in Table 21. It can be noted that D_A is either near or quite lower than D_{50}. In fact, the granular model, which uses BET surface area data, takes the finer pores more into consideration. The calculated B values, determined for the five rocks according to each packing pattern, are reported in Table 22. When B_{octa}, B_{tetra} and B_{cubic} are compared to B_{exp}, it can be noted that the octahedral packing pattern allows for the better estimations of B to be made (although the cubic packing pattern seems to be more adapted to the tuffeau limestone). Thus, only the octahedral packing pattern can be retained for the rest of the interpretation. The diagram of Figure 51 represents the value of B obtained from the cylindrical pore model (B_{cyl}) and the one obtained from the spherical pore model ($B_{sph} = B_{octa}$, calculated with the octahedral packing) divided by the experimental value. It clearly shows the better efficiency of the spherical pore model for the B estimations. B_{sph} is quite near B_{exp} for the chalk (due to the "simplicity" of the rock's porous network) and for the tuffeau limestone and the "Grès à Meules" sandstone; however, B is still over-estimated for the other two rocks.

These features are explained by the fact that the use of the specific surface area as the basis of the spherical intergranular pore model allows for the smaller throats, and in particular, the surface roughness in the rocks to be taken into account. For instance:

- The amount of specific surface area in the Vuillecin limestone is mainly due to the numerous micrite and microsparite areas, which are made of small calcite crystals and which contain small pores and throats. These areas are preferential flow paths for water migration, as already seen (§3.1.4.5.). In the Fontainebleau sandstone, it is the smaller throats that govern the water imbibition kinetics. However, in both rocks various levels of cementation also play a role in the water migration, without significantly changing the specific surface area. Thus, the model does not describe such a phenomenon, which explains that the B values were found to be still over-estimated.
- In the "Grès à Meules" sandstone, the clay minerals take a prominent part in the specific surface area. Clay minerals and opal-CT spherules in the tuffeau are responsible for the high specific surface area. In both rocks, these minerals are linked to a surface roughness that governs the water migration.

Table 20 – Mean grain size of each rock calculated from the specific surface area and the bulk density.

Rock	S_{BET} (m² g^{-1})	$d_{B,Hg}$ (g cm^{-3})	D_S (µm)
Fontainebleau sandstone	0.013	2.33	198.1
“Grès à Meules” sandstone	2.86	2.10	1.0
Mons chalk	1.93	1.62	1.9
Tuffeau limestone	23.08	1.37	0.2
Vuillecin limestone	1.43	2.39	1.8

Table 21 – Model parameters D and D_A according to the grain packing pattern; comparison of D_A with D_{50} (all values are in µm).

Rock	Granular packing model						Mercury poro.
	Octahedral		Tetrahedral		Cubic		
	D	D_A	D	D_A	D	D_A	D_{50}
Fontainebleau sandstone	82.0	30.6	44.9	30.6	140.1	82.0	31.4
“Grès à Meules” sandstone	0.4	0.2	0.2	0.1	0.7	0.4	7.2
Mons chalk	0.8	0.3	0.4	0.3	1.4	0.8	0.8
Tuffeau limestone	0.2	$8\ 10^{-2}$	4 10-2	$3\ 10^{-2}$	0.1	$8\ 10^{-2}$	3.2
Vuillecin limestone	0.7	0.3	0.4	0.3	1.2	0.7	0.8

Table 22 – Coefficient B calculated using the spherical pore model according to the type of packing (Bocta, Btetra and Bcubic), and using the cylindrical pore model (B_{cyl}). Comparison with the experimental data (B_{exp}).

Rock	B_{octa}	B_{tetra}	B_{cubic}	B_{cyl}	B_{exp}
Fontainebleau	56.8	132.6	166.1	90.4	14.5
“Grès à Meules”	4.0	9.4	11.8	51.2	3.8
Mons chalk	5.6	13.0	16.3	15.8	8.2
Tuffeau	2.2	4.1	5.1	60.3	5.5
Vuillecin	5.3	12.5	15.6	21.4	0.7

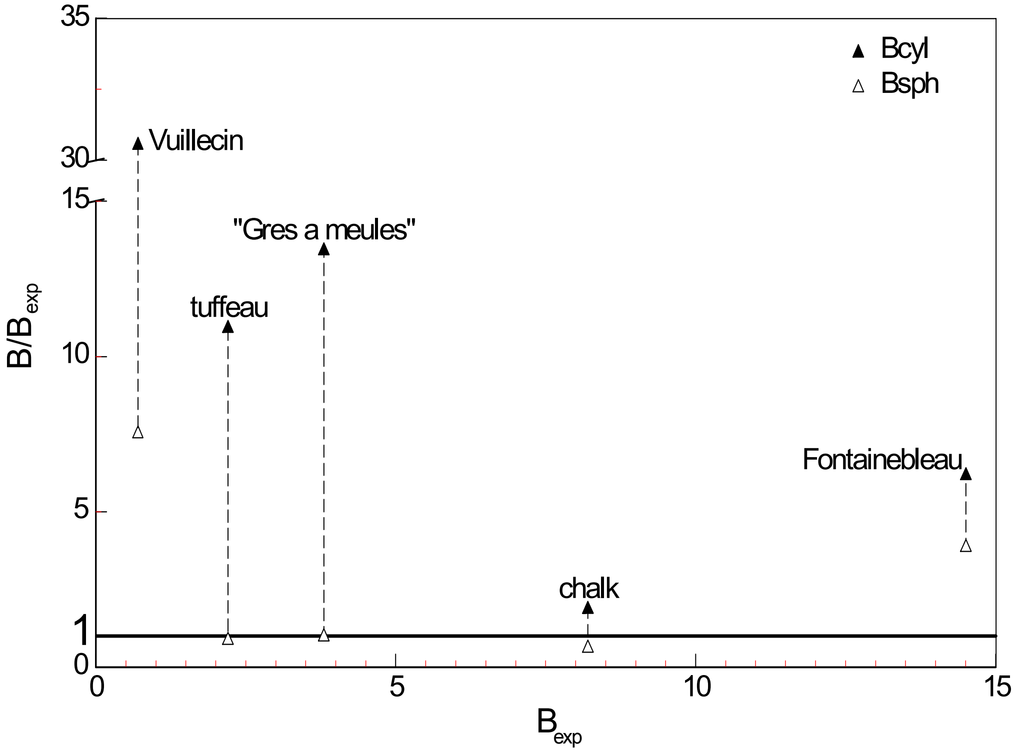

Fig. 51 – Diagram of B/B$_{exp}$ plotted versus B$_{exp}$ for the cylindrical and spherical pore models.

3.2. Gas permeability

3.2.1. Darcy’s law

Considering a fluid of viscosity η flowing through a tube (length: L, cross section area: s) during a time unit under differential pressure ΔP, the flow Q is written as:

$$Q = \frac{s\,\Delta P\,K}{\eta L} \quad (47)$$

where K represents the permeability of the tube. The permeability units commonly used are the Darcy (D) and the milli-Darcy (mD). A milli-Darcy is equivalent to 0.9869 10^{-15} m^2.

Darcy’s law (Relation *47*) is valid for viscous compressible fluids in the case of laminar flow. According to the hydrodynamic theory, the limit between laminar flow and turbulent flow is expressed by Reynolds’ number (KOSAKA N., 1995):

$$Re = \frac{\rho u \sqrt{K}}{\eta N} \quad (48)$$

with N the total porosity (%), ρ and η the fluid density and viscosity, u the average flow velocity ($u = \frac{K\,\Delta P}{\eta L}$).

In the case of laminar flow, Reynolds’ number is inferior to 1 (GUÉGUEN & PALCIAUSKAS, 1992), which leads to the following inequality:

$$\frac{\rho K^{3/2}\,\Delta P}{\eta^2 N L} << 1 \quad (49)$$

3.2.2. Experimental device

Each core of the rocks (the one used for water porosimetry and capillary water imbibition kinetics) was previously dried and put in a Hassler cell (Fig. 52). The fluid pressure was measured at the top (Pf_1) and at the bottom (Pf_2) of the core. The nitrogen outflow Q was measured using a flowmeter (density $\rho_{N_2} = 2.293$ kg m^{-3}; viscosity $\eta_{N_2} = 17.6\ 10^{-6}$ Pa s). The gas outflow at the lateral core borders was avoided using a confinement pressure Pc slightly higher than the fluid pressure. The application of Darcy's law (Relation *47*) allowed us to experimentally determine the permeability K_A of the sample after the relation:

$$K_A = \frac{\eta_{N_2}\ L\,Q}{s\ \Delta P} \qquad (50)$$

in which L is the length of the core, ΔP the differential pressure (Pf_1 - Pf_2) and s the cross section area of the core.

Reynolds' number (Relation *48*) was determined in order to control that the flow was laminar.

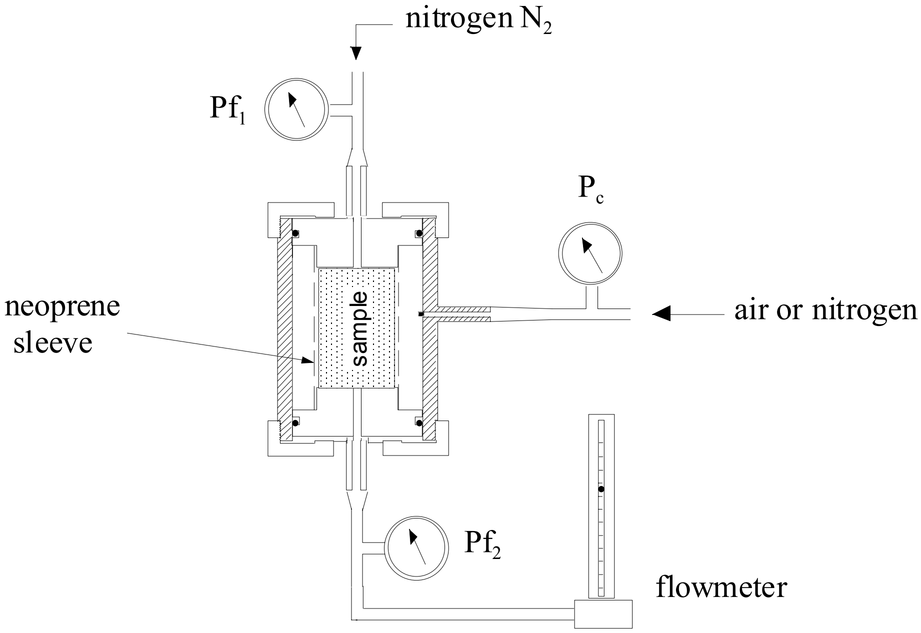

Fig. 52 – Diagram of a permeameter (HAMMECKER C., 1993). Pc: confinement pressure; Pf_1 and Pf_2: fluid pressure at the top and at the bottom of the sample, respectively.

3.2.3. Discussion about the measured permeability values

The permeability measured for each sample is noted K_A*. The mean permeability K_A and its absolute (σ_{K_A}) and relative (σ_{R,K_A}) standard deviations were calculated for each rock. The mean permeabilities show that the Fontainebleau sandstone is highly permeable, while the chalk and the Vuillecin limestone have quite lower permeabilities (Table 23). The other rocks have intermediate mean permeabilities. The permeabilities K_A* are variable within each rock, inducing high σ_{R,K_A} values, except in the case of the Fontainebleau sandstone, mainly because of its very high permeability.

Fontainebleau sandstone

In the case of laminar flow, the throats and the central part of the pores are the main flow paths for gas inside this sandstone (Fig. 42b). Thus, the macropores do not really influence the gas flow in this sandstone – on the contrary, it was seen that they play a major role in the water imbibition ability. It is in fact the size of the throats that govern the gas flow. The low permeability variations express a constant mean size of the throats in the block.

"Grès à Meules" sandstone

The sketch in Figure 43b describes the gas flow throughout the fine and coarse grain layers of this rock. Opposite from the major role in the water imbibition, the clays located in the coarse grain layers play a minor role in the gas flow. In comparison with the Fontainebleau sandstone, the lower permeability is directly linked to tighter throats due to clay concentrations. It can be noted that the permeability of the sample SGM4, which was carried out from the block in a direction perpendicular to the stratification planes, does not differ from the one of the other samples. That means that the presence of the stratification does not induce significant permeability anisotropy.

This isotropy can be explained considering that this sandstone sampled in quarry underwent a slighter burial diagenesis (low compaction by pressure solution process[1]) in comparison with equivalent "Grès à Meules" sandstones extracted by borehole, under a thick sedimentary cover, and already studied (Sizun J.-P. and Jeannette D., 1994). In the latter, under a given lithostatic pressure, the phenomenon of solution at grain contacts was more intense in the fine grain layers than in the coarse grain layers (due to the small grain sizes and the presence of numerous clay minerals at grain contacts inside the fine grain layers). This induced throat sizes that are quite smaller in the first type of layers than in the second, and then permeability anisotropy. Inside the "Grès à Meules" of this study, the compaction by pressure solution must have been not significant enough to induce remarkable permeability anisotropy.

Mons chalk

The fluid flow paths are the same either for water capillary imbibition or for mono-phase fluid flow (Fig. 44b). Despite a high porosity (40%), the permeability values are only about 10 mD – for comparison, the tuffeau limestone (porosity about 45%) is almost 50 times more permeable. The low permeability in the chalk can be directly linked to the very small size of the pore accesses (about 1 µm) inside this rock.

---

[1] Seven main factors, which influence the phenomena of pressure solution, were proposed by Houseknecht (1986):

- Shape and size of the grains;
- Clay mineral content;
- Composition maturity;
- Presence of cement;
- Salinity of interstice fluids;
- Temperature;
- Burial depth (pressure).

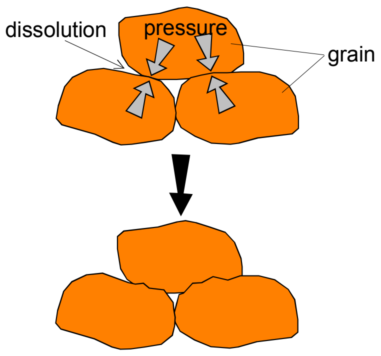

Diagram of the pressure solution phenomenon

Table 23 – Experimental nitrogen permeability (K_A) of each sample (// or ⊥: analysis direction parallel or perpendicular to the stratification planes, respectively); mean measured permeability of each rock (K_A) and its absolute (σ_{K_A}) and relative (σ_{R,K_A}) standard deviations.*

Rock	Samples	K_A* (mD)	K_A (mD)	σ_{K_A} (mD)	σ_{R,K_A} (%)
Fontainebleau sandstone	Font1	2114.5	2159.3	83.9	3.9
	Font2	2269.3			
	Font3	2203.6			
	Font4	2049.5			
“Grès à Meules” sandstone	SGM1 //	86.4	122.4	38.9	31.8
	SGM2 //	117.3			
	SGM3 //	187.0			
	SGM4 ⊥	98.7			
Mons chalk	MS1	10.5	12.5	2.2	17.6
	MS2	9.3			
	MS3	10.0			
	MS4	12.1			
	MS5	13.7			
	MS7	15.9			
	MS8	12.8			
	MS9	12.4			
Tuffeau limestone	TUF1	572.5	479.2	99.5	20.8
	TUF2	646.2			
	TUF3	438.0			
	TUF4	519.8			
	TUF5	433.7			
	TUF6	326.0			
	TUF7	418.0			
Vuillecin limestone	VUI1 //	21.7	9.6	5.6	58.3
	VUI2 //	13.2			
	VUI3 //	14.4			
	VUI4 //	10.4			
	VUI5 ⊥	4.2			
	VUI6 ⊥	5.3			
	VUI7 ⊥	6.5			
	VUI8 ⊥	4.0			
	VUI9 ⊥	6.6			

Tuffeau limestone

Nitrogen can flow throughout the residual interspaces between the opal-CT spherules themselves and between opal-CT spherules and neighbouring minerals, which make together a continuous and well-interconnected porous network. This allows for an excellent flow within the sample since the spherules are homogeneously distributed. In this case, clay minerals do not play a role in the gas flow (Fig. 45b).

The interspaces delimited by the spherules are connected by pore access diameters from about 15 to 5 µm, as concluded from the interpretation of the mercury porosimetry results. This explains why the limestone permeability (500 mD) is 50 times higher than that of the chalk (10 mD).

Vuillecin limestone

Like the chalk, this limestone has a low permeability (10 mD). Nitrogen can preferentially flow throughout the pores between the calcite crystals of the cement and the central part of numerous macropores (Fig. 46b). However, it is the presence of highly cemented areas of microsparite crystals (bioclasts or cement) that reduces the flow ability. The low permeability can also be linked to the presence of small throats inside this limestone (mean pore access of about 1 µm in diameter, like in the Mons chalk), and to a low connectivity and a high tortuosity.

Considering the analysis direction, the permeability is lower in the direction perpendicular to the bedding stratification. As for water imbibition, the discrepancy is explained by the fact that the bioclasts have elongated shapes with the biggest diameters sub-parallel to the bedding.

3.2.4. Relationships between K_A and pore structure parameters

3.2.4.1. Relation between K_A and D_H

When no simple relation can be established between the permeability of the rocks and their total porosity (Fig. 53), the left-hand diagram in Figure 54 shows that K_A increases exponentially in relation to the hydraulic diameter D_H. The right-hand diagram shows a quite linear correlation between $\mathrm{Log}K_A$ and $\mathrm{Log}D_H$, proving that the permeability of the rocks depends on the throat size.

3.2.4.2. Empirical relationship permeability–porosity–hydraulic diameter

Using regressions on a database of 202 samples of sandstone from 14 facies ranging in age from Ordovician to Tertiary, Pittman E.D. (1992) developed an empirical relationship between air permeability, porosity and hydraulic diameter. These sandstones varied in composition and texture, including clayey sandstones and clean but tightly cemented sandstones. The multiple regression yielded the following equation with a correlation factor of 0.900:

$$\mathrm{Log}D_H = 0.137 + 0.479\,\mathrm{Log}K - 0.143\,\mathrm{Log}N \qquad \text{(51)}$$

This equation was applied in this study to calculate the permeabilities (K_{PI} in mD) of the five sedimentary rocks, using D_H (µm) from the mercury porosimetry and N_{Hg} (%) representing the total mercury porosity.

The calculated permeabilities K_{PI} (Table 24) are of the same order as the experimental ones (K_A). Relation *51* was originally established for sandstones, but these comparable results of the permeability show that this relationship between permeability, porosity and hydraulic diameter is applicable for the two studied sandstones, the two limestones and the chalk. This shows that the hydraulic diameter and the porosity are critical factors that govern the permeability of the five rocks.

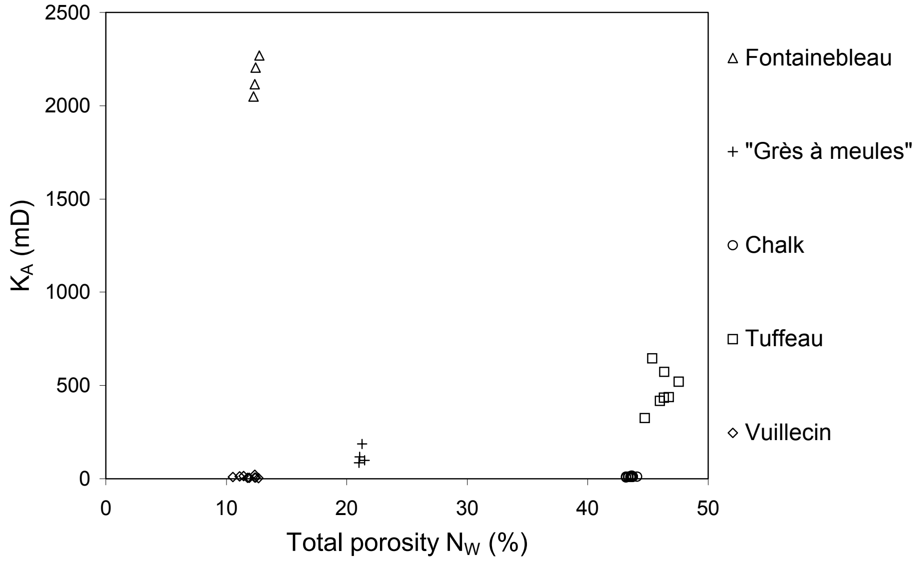

Fig. 53 – Permeability K_A versus the total water porosity N_W.*

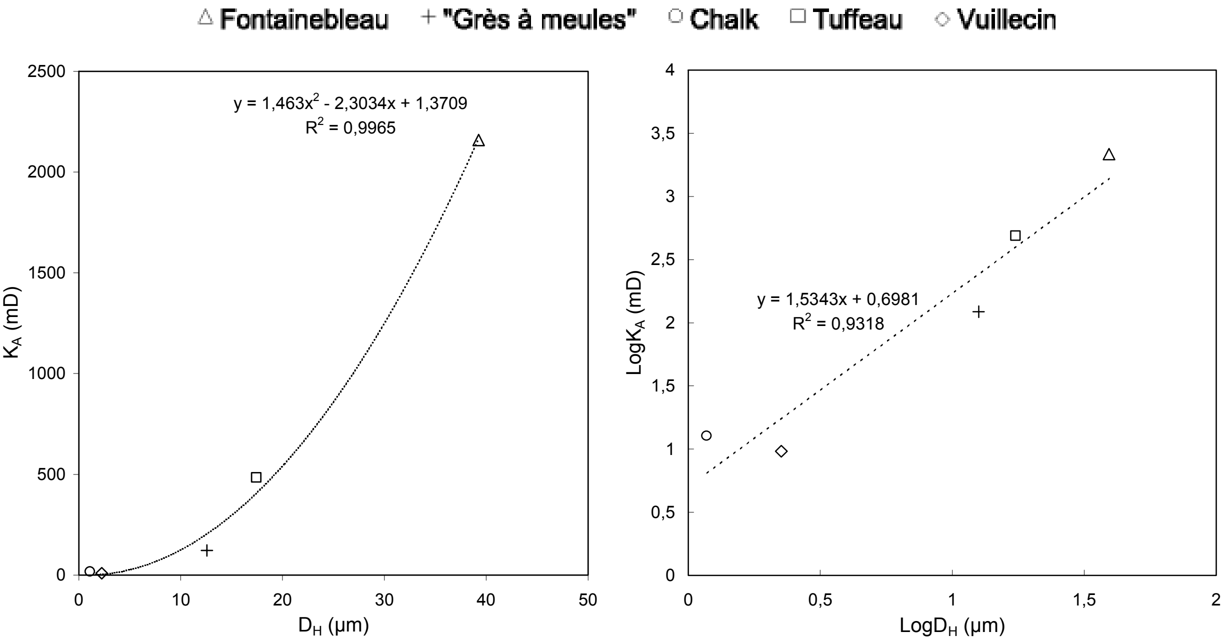

Fig. 54 – Permeability (K_A) versus the hydraulic diameter (D_H) for a normal and a Log-Log representation.

Table 24 – Permeabilities K_{PI} calculated using D_H and N_{Hg}, and Pittman's empirical equation (Relation 51). Comparison with the experimental data (K_A).

	D_H (µm)	N_{Hg} (%)	K_{PI} (mD)	K_A (mD)
Fontainebleau sandstone	39.2	12.30	2327	2159
"Grès à meules" sandstone	12.6	20.16	251	122
Mons chalk	1.2	40.50	2	12
Tuffeau limestone	17.5	45.08	636	479
Vuillecin limestone	2.2	11.29	6	10

3.2.5. Prediction of the gas permeability using pore models

3.2.5.1. Presentation of the models

Darcy-Poiseuille's model (DP): straight tubes

One simple method for calculating the permeability from a combination of porous structure parameters (porosity and pore size) is to assume that the flow is occurring through straight cylindrical channels of diameter D (Fig. 55). The porosity N arising from these channels is calculated by equating the flow as expressed by Darcy's law (Relation *47*) with that given by the Poiseuille's equation (Relation *35*), leading to (LOWELL S. and SHIELDS J.E., 1991):

$$K_{DP} = \frac{N\,D^2}{32} \qquad (52)$$

Kozeny-Carman's model (KC): tortuous tubes

The porous network of a sample is represented by tortuous tubes (Fig. 55). Each tube has a constant section along its whole length. The formalism, developed by SCHEIDDEGER (1974), determines the permeability through the relation:

$$K_{KC} = \frac{cN^3}{T^2 S_0^2 (1-N)^2} \qquad (53)$$

with:

N: total porosity of the sample (ratio)

S_0: specific surface area divided by the specific volume of the solid phase

T^2: tortuosity, $T^2 = (Le/L)^2$ where Le is the effective flow path and L the sample length

c: geometrical constant depending on the pore shape (c = 1/2 for circular section pores, c = 1/3 for plane cracks.

The model is valid considering the following hypotheses (DAVID C., 1991):

- Only the connected porosity is considered.
- The pore spatial distribution must be homogeneous.
- The pore size distribution must be relatively unimodal.
- The porosity must not be too high.
- The analogy with the flow in the capillary tubes must be acceptable.

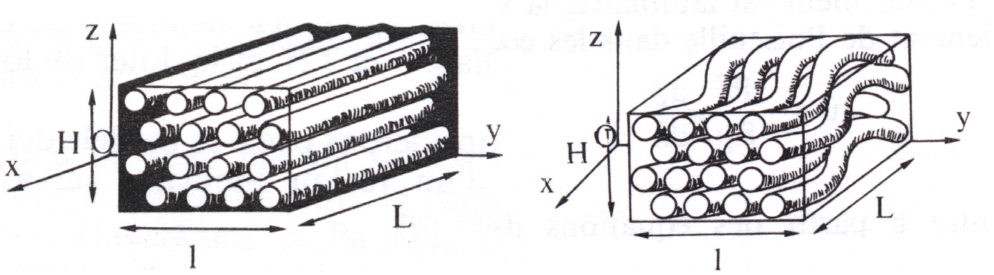

Fig. 55 – Model of straight (left) or tortuous (right) tubes (PANTALONI, 1988).

Marshall's model (M): elemental volumes

This model (MARSHALL, 1958) makes it possible to calculate theoretical permeabilities from the mercury porosimetry data. The model is based on the following hypotheses:

- All the pore access sizes determined by mercury porosimetry are represented on each section along the core sample.
- The total pore volume is divided into n identical elemental volumes ΔV_p. The gas flows through the different existing pores and throats of these elemental volumes (Fig. 56).
- The permeability is controlled by the smaller pore necks (throats).

Under these hypotheses, the permeability K_M is expressed by the relation:

$$K_M = \frac{N_{Hg}^2 \sum_i (2i-1) D_i^2}{32 n^2} \qquad (54)$$

with i = 1,…,n; N_{Hg} is the mercury total porosity (%); and D_i, the pore access diameter corresponding to the i^th elemental volume ΔV_p invaded by mercury.

The limits of the model come from the mercury porosimetry:

- the model supposes that pores can be assimilated to cylinders (Washburn's cylindrical pore model);
- only the access diameters from 400 µm to 4 nm are considered.

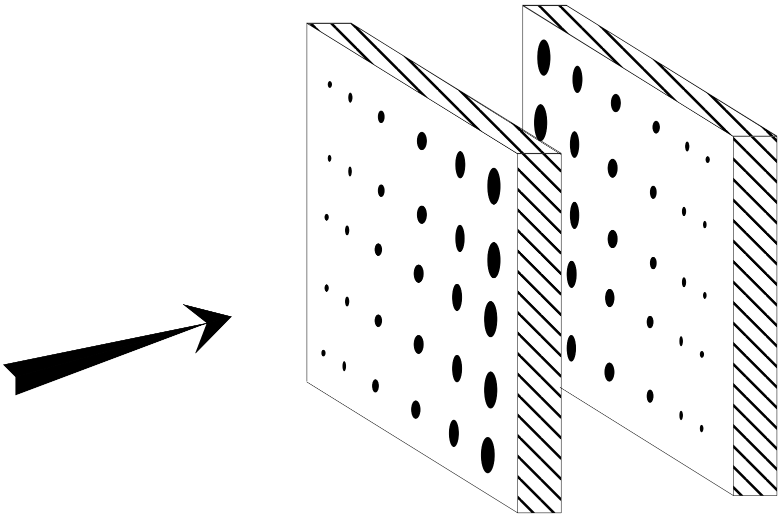

Fig. 56 – Diagram of the connected elemental volumes, Marshall's model (PAVONE, 1982).

The PORE-COR model (PC)

The chief data source of the **Pore**-fluids property **Cor**relator is mercury porosimetry.

The void space within a porous material is regarded as a network of cubic pores connected by cylindrical throats. The PORE-COR network comprises a three-dimensional cubic unit cell (Fig. 57) containing 1000 nodes on a regular 10x10x10 matrix (MATTHEWS G.P. et al., 1995a; SCHOELKOPF J. et al., 2000). The throats are randomly positioned within the unit cell. The range of the throat diameter distribution is set to the limits of the experimental mercury intrusion curve, calculated from the pressure range of the curves by means of Washburn's equation (Relation *11*, § 2.2.1.1.). A cubic pore is then assigned to each node that has at least one throat connected to it;

the pore size is at least equal to the diameter of the largest throat that reaches this node. The number of throats connected to one pore is the coordination number, which expresses the connectivity (MATTHEWS G.P. et al., 1996). The random positioning of the throats introduces a degree of randomness into the pore sizes (MATTHEWS G.P. et al., 1995b). Finally, the row spacing of the matrix is set so that the total porosity of the simulated network is equal to that of the experimental sample – increasing the pore row spacing lengthens the throats, increases the unit cell size and reduces the porosity. It has been shown in many publications that the model reproduces the experimental mercury intrusion curve and the pore-throat size correlation (SPEARING M.C. and MATTHEWS G.P., 1991), porosity and connectivity (MATTHEWS G.P. and SPEARING M.C., 1992), and permeability (MATTHEWS G.P. et al., 1993)[1].

The PORE-COR model was interesting for this study in that it makes it possible to calculate absolute nitrogen permeabilities (K_{PC}) using the unit cell. Considering a unit cell, Darcy's law (Relation *57*) may be written:

$$Q_{cell} = \frac{K_{PC} s_{cell} \delta P_{cell}}{\mu l_{cell}} \qquad (55)$$

where $\delta P_{cell}/l_{cell}$ is the pressure gradient across the length l_{cell} of the cell, s_{cell} the cross sectional area, and μ the viscosity of nitrogen.

The fluid flowing through a tube (radius r_{tube}) takes up a parabolic velocity profile, with a maximum flow rate down the centre of the tube. If the flow at the walls is assumed to be zero, integration over the velocity profile yields the Poiseuillian equation:

$$Q_{tube} = -\frac{\pi r_{tube}^4 \delta P_{tube}}{8\mu l_{tube}} \qquad (56)$$

The Poiseuillian flow for each pore-throat-pore arc is calculated using parameterized Navier Stokes relationships for a laminar flow in square and cylindrical tube cross-sections (MATTHEWS et al., 1993). The permeability of the whole unit cell is determined by calculating the total flow capacity of the network. It is assumed that the Poiseuillian flow occurs across the whole cell in the -z direction, i.e. from the top to the bottom side of the unit cell, then:

$$Q_{tube} = -\frac{\pi\Omega\left(r_{tube,z}^4\right)_{cell}\delta P_{cell}}{8\mu l_{cell}} = -\frac{\pi\Omega\,\delta P_{cell}}{8\mu\beta}\left(\frac{r_{tube,z}^4}{l_{tube,z}}\right)_{cell} \qquad (57)$$

in which Ω is an averaging operator over the whole unit cell, operating on the flow capacities of the individual radii $r_{tube,z}$ of all the tubes lying parallel to the z axis (Ω is parameterized so that Relation *57* is satisfied); β is the number of tubes in the z direction in the unit cell ($l_{cell} = \beta l_{tube,z}$); $\left(r_{tube,z}^4 / l_{tube,z}\right)_{cell}$ is averaged on the whole unit cell.

By considering tubes in the ±x and ±y directions as well and comparing with Relation *55*, it follows that (MATTHEWS G.P. et al., 1995b):

$$K_{PC} = \frac{\pi}{8\beta}\Omega\left(\frac{r_{tube}^4}{l_{tube}}\right)_{cell}\frac{l_{cell}}{s_{cell}} \qquad (58)$$

---

[1] for more information about the model, see: http://www.pore-cor.com/about.htm

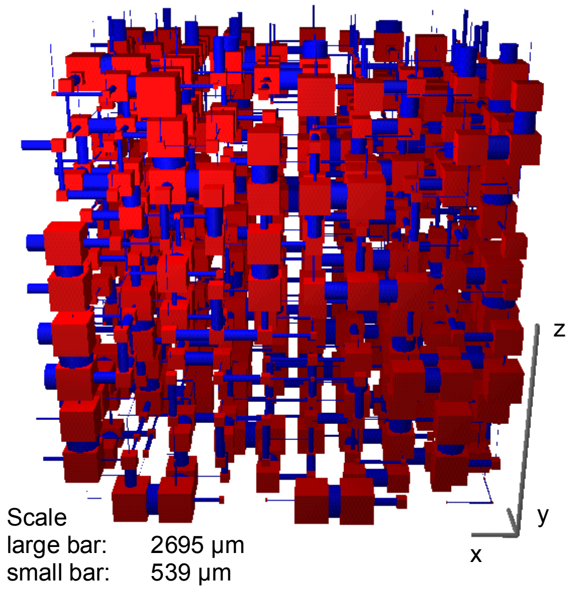

Fig. 57 – Representation of a PORE-COR unit cell (sample of the Fontainebleau sandstone).

3.2.5.2. Applications and discussion

The KDP permeability was calculated using mercury porosimetry N_{Hg} and D_{50}.

The Kozeny-Carman's equation (Relation *53*) was applied using N_{Hg} and S_{BET}, and the tortuosity was determined from the mercury porosimetry data by (CARLOS A., 1998; CARNIGLIA S.C., 1986):

$$T = 2.23 - 1.13 V_{Hg} d_{B,Hg} \qquad (59)$$

with V_{Hg} the total specific pore volume, and $d_{B,Hg}$ the bulk density.

The application of Marshall's model required the mercury injection curve data provided in this study (§2.2.). The K_{DP}, K_{KC} or K_M calculations were made for several samples. The mean values of these parameters are given in Table 25. The application of the PORE-COR model was made using raw mercury saturation versus pore access diameter data. Problems in the application (errata during the software calculation) made us choose only two or three adequate samples of each rock. The results of the simulations are reported in Appendix J. The average permeability was all the more calculated from these two or three permeability values (Table 25).

The table shows that the permeability was often underestimated. Debye-Poiseuille's (DP) and Marshall's (M) relations led to permeabilities of the same order as the experimental values. The PORE-COR (PC) and Kozeny-Carman (KC) models, however, often quite underestimated the permeability. Indeed, as seen in Figure 58, two groups of points, G1 and G2, show that using PC and KC led to very low permeabilities for the Vuillecin limestone, on the one hand, and for the "Grès à Meules" sandstone and the tuffeau limestone, on the other hand.

These results can be explained considering two features of the models:

- The KC model uses the specific surface area data: the permeability of the "Grès à Meules" sandstone and the tuffeau limestone were underestimated due to the presence of clay minerals, which enhance the specific surface area of these rocks. In the Vuillecin limestone, many bioclast shells, with rough surfaces, and many sparse strongly cemented areas take a large part in the specific surface area, without really influencing the permeability.

- The PC model, which requires the pore access size distributions from mercury porosimetry, takes all pore accesses, in particular the smallest, into account during the calculation of the permeability (Relation *58*). Underestimations occurred for the “Grès à Meules” sandstone and for the tuffeau and Vuillecin limestones, due to large ranges of pore access diameters and the presence of numerous small diameters. In fact, the estimation of the permeability of such rocks must be made taking only the biggest well-represented throats into account.

Table 25 – Permeability of the rocks calculated using the four pore models.

	Debye-Poiseuille	Kozeny-Carman	Marshall	PORE-COR	Experimental mean value
	K_{DP} (mD)	K_{KC} (mD)	K_M (mD)	K_{PC} (mD)	K_A (mD)
Fontainebleau sandstone	3642	472	705	3018	2159
“Grès à Meules” sandstone	297	0.05	276	32	122
Mons chalk	6.9	1.4	2.2	4	12
Tuffeau limestone	138	0.02	120	$2\ 10^{-2}$	479
Vuillecin limestone	3.2	0.05	6.8	$1\ 10^{-1}$	10

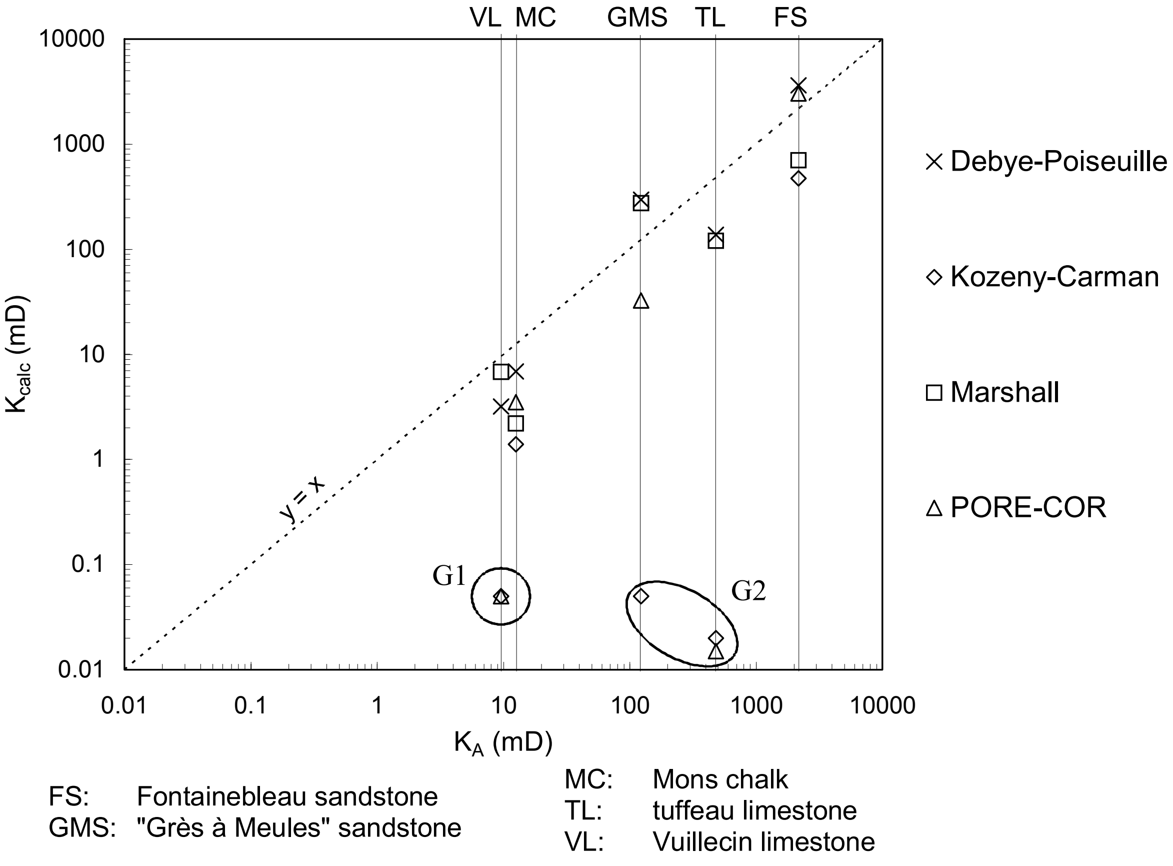

Fig. 58 – Permeability Kcalc calculated using the four pore models versus the experimental permeability K_A.

3.3. Conclusions about the fluid transport properties

This research about the fluid transport properties of the sedimentary rocks made it possible to identify the main flow paths and the role of the different mineral components in these properties. Sketches were composed (Fig. 42a to 46a). They illustrate how water invades each rock through capillary imbibition or how gas flows within the rocks with regards to their mineral and porous structures. Using the sketches, models of porous structure were proposed (Fig. 42b to 46b). These models qualitatively describe the different fluid transport properties of the rocks.

The application of pore models led us to conclude that the fluid transport properties of homogeneous rocks such as the Fontainebleau sandstone and the chalk can be well predicted. Nevertheless, acceptable predictions can be obtained for more heterogeneous rocks as long as some mineral components (e.g. clay minerals) or other petrographical characteristics of the rock are taken into account or omitted either for gas permeability or water capillary imbibition. In this study, it was possible to identify the mineral components or the petrographical characteristics that have a leading role in the fluid transport properties.

On the one hand, the models, which are not based on the use of the specific surface area, generally display the best estimations of the permeability of the sedimentary rocks. The models, which use the specific surface area data, give a good estimation of the water capillary imbibition properties. In fact, the water transport properties of a rock with various porosity structures strongly depend on its finer porous structures within the rock (smaller well represented throats, microroughness…); on the contrary the gas transport properties depend on coarser porous structures. That is quantitatively expressed by a strong relation between the gas permeability and D_H, and a relationship of A and B mainly to smaller pore access diameters ($D_A < D_{50}$).

4. Conclusions

4.1. Summary of the characteristics of the sedimentary rocks

The main characteristics of the rocks obtained from the measurements and their interpretation are summarized in Table 26.

Fontainebleau sandstone

This rock is well sorted and macroporous. Its porous structure is homogeneous. This sandstone is highly permeable and its porous network allows a high capillary water imbibition. Various amounts of quartz overgrowths induce local changes in the mineral and porous structure, which have nevertheless very low influence on the porosity or on the fluid transport properties of the rock.

"Grès à Meules" sandstone

This sandstone shows a characteristic layered structure. It contains high concentrations of clay minerals and is mainly microporous. Its porous network is moderately homogeneous at the scale of laboratory samples and allows a slight gas permeability and capillary water imbibition, which strongly depend on the clayey concentrations.

Mons chalk

The chalk, which is well sorted, has a homogeneous microporous network. It is low-permeable but its porous structure makes the rock has well capillary water imbibition abilities (fast wet fringe migration and weight increase velocity, high saturation degree).

Tuffeau limestone

This limestone is mainly microporous. Its porous network is characterized by various structures of porosity (differences in pore and throat sizes due to several types of minerals). These structures are randomly distributed inside the rock, leading to a moderate homogeneity of its porous structure, considering a 50x50x50 cm^3 block, as well as 1 or 2 cm^3 samples. Clays and opal-CT spherules are the minerals that have the major influence on the porous structure of this limestone. Its fluid transport properties (moderate permeability and good capillary water imbibition capacity) are mainly due to the presence and the distribution of the opal-CT spherules.

Vuillecin limestone

The Vuillecin limestone is poorly sorted. This rock is essentially microporous and shows high variations in most of its characteristics and properties due to various levels of cementation. This limestone is as lowly permeable as the chalk, but this limestone shows very low capillary water imbibition capacity, mainly due to the high tortuosity and the low connectivity of its porous network.

4.2. Advantages of the simultaneous application of several measurement techniques

All the rocks selected for this study were already one or more times analyzed, however with the simultaneous use of a few techniques. This study required the simultaneous application of many measurement techniques (commonly used: mercury porosimetry, gas adsorption…; or less commonly used: X-ray refraction), providing a more precise qualitative and quantitative characterization of the porous structure of the rocks in comparison with the analyses already made up to the date of this study. When the techniques are compared (Table 3, §2.2.3.; Table 8, §2.3.3.; Table 15, §2.6.3.), a good repeatability of the measurements with an acceptable level of confidence can be concluded.

Table 26 – Summary of the main characteristics of the rocks. ●●●●: very fast imbibition; ●●●: fast imbibition; ●●: moderate imbibition velocity; ○: very slow imbibition; MP: macropore; µP: micropore; Q: quartz.

Rock name	Rock type	Main mineral structure characteristics		Main porous structure characteristics				Fluid transport properties	
		Mineral comp.	Textural characteristics	Pore class	Porosity	Pore access size	Sp. Surf. Area	Capillary water imbibition	Gas permeability (mD)
Font. sandstone	Quartz-arenite	Quartz	Well sorted 200 µm-euhedral Q grains Q overgrowths in various amounts	MP (polygonal shape)	12%	31 µm	10^{-2} m²g^{-1}	●●●● Imbibition throughout the throats and the smallest pores	2160 Gas flow throughout the throats and the MP
“Grès à meules” sandstone	Feldspathic sublith-arenite	Quartz Feldspar Clays	Clays rim grain borders Layered structure (coarse/fine grains)	MP µP	20%	7 µm	3 m²g^{-1}	●● Imbibition throughout particle interspaces linked to clays	120 Gas flow throughout throats and MP between the Q grains
Mons chalk	Mudstone or biomicrite	Calcite	Well sorted 2 µm-euhedral calcite crystals Low cementation	µP	40%	0.8 µm	2 m²g^{-1}	●●● Gas flow or water imbibition throughout crystal interspaces	10
Tuffeau limestone	Siliceous bio-clcarenite	Calcite Quartz Clays	Clays rim Q grains Rough Opal-CT-spherules	MP µP	45%	3 µm	22 m²g^{-1}	●● Gas flow or water imbibition throughout interspaces linked to opal-CT spherules	480
Vuillecin limestone	Packstone or biosparite	Calcite	Poorly sorted Areas of bioclasts sparite and micrite Variable cementation	MP (elongated shape) µP	11%	0.8 µm	1 m²g^{-1}	○ Imbibition throughout crystal interspaces in micrite areas	10 Gas flow throughout crystal interspaces and MP

The values of the characteristics like porosity, density, permeability and the specific surface area are comparable with those reported in the bibliography. In this study, the assessment of the variations of these characteristics through statistical analyses done at different scales, made it possible to estimate the homogeneity of the rocks.

The advantage of numerous comparisons and/or combinations between the techniques made it possible to achieve a better understanding of the influence of the structure of each rock on its fluid transport properties (and variations in its structure on its properties). This advantage is more apparent when considering the general relations that could be established (§4.4. and §4.5.).

The structure (porous and mineral) of the Vuillecin limestone, which was poorly known before, was qualitatively and quantitatively characterized. Contrary to most previous investigations, this study succeeded in analyzing the whole porous network of the tuffeau limestone and the “Grès à Meules” sandstone. This allowed for a more complete characterization of these rocks to be made and permitted us to explain the role of the smaller pores and pore accesses, which are due to clay mineral concentrations.

This study of the tuffeau limestone from Marigny-Brizay provided data until 4 nm in pore access size and a mean porosity of about 45% measured by mercury porosimetry, as well as by water porosimetry. For comparison, a previous study of the tuffeau from Touraine did not provide any data for the small pore accesses with sizes below 25 nm. The mean porosity measured by mercury porosimetry was about 39%, whereas the mean total water porosity was about 44% (DESSANDIER D et al., 1996). In this present study, the distribution of the pore accesses of the whole porous network permitted us to classify the different porosity structures of the tuffeau limestone in domains. It also permitted us to determine the role of the different minerals of this limestone in its porous structure (in the porous volume, the porosity, the pore access size and the specific surface area) and in its transport properties – in particular the role of clay minerals like smectite and glauconite. These clay minerals are responsible for the high specific surface area of the limestone and induce a wide range of very small pore sizes. Although these minerals have a strong influence on the porous structure of the limestone, they play a minor role in its fluid transport properties, which are mainly due to the opal-CT spherules.

The mercury porosimetry analysis of the “Grès à Meules” sandstone displayed its whole pore access diameter distribution, which helped to precisely understand the role of clay minerals inside its porous structure and in its fluid transport properties. It was shown that the role of these minerals varies according to the type of layers (coarse or fine grain layer). Various clay mineral concentrations from one laboratory sample to another are the cause of variations in the specific surface area of this sandstone and of variable pore access size distributions (§2.2.4.2.). Various clay mineral concentrations also induce different properties inside a sample itself (when considering either a coarse grain layer or a fine grain layer). In fact, many relations exist between the mineral framework of a rock and its porous structure, as exposed below in a general view.

4.3. Relations between the mineralogy of a rock and its porous structure

Many relationships between the mineral skeleton and the porous structure of the rocks could be established from the results of the characterization of the rocks (Fig. 59). These relations explain the differences in the values of the porous structure parameters of the rocks.

- **The bigger the grains, the larger the pores and throats** – Macrometric quartz grains surround macropores and macrometric throats in the Fontainebleau sandstone. In the Mons chalk, micrometric calcite crystals induce micropores ands micrometric throats. This dependence between grain size and pore and throat size explains why the Vuillecin limestone, whose mineral framework is made of crystals variable in size (from macrometric to micrometric), contains pores and throats with sizes distributed on a large range of diameters. In the same way, it also explains the large throat size distribution of the “Grès à meules” sandstone (presence of clays between the macrometric grains) and the tuffeau limestone (several minerals variable in type and size).

- **Influence of the type of minerals** – The different minerals found in the sedimentary rocks have specific shapes and sizes, which govern porous structure characteristics like pore and throat size and specific surface area. Hence, detrital quartz and feldspars are often macrometric rounded or polygonal grains, which surround macropores (quartz grains and quartz overgrowths in the Fontainebleau sandstone). Calcite crystals often induce micropores like in the Mons chalk and the Vuillecin limestone. In some rocks, clay mineral concentrations (kaolinite, illite, smectite…) govern the distribution of the sizes of the pores and throats. The clay minerals induce very small pore access sizes generally in the range of diameters from 500 nm to a few nanometres for kaolinite and illite, and from 20 to 1 or 2 nm for smectite. Concentrations of clays strongly enhance the specific surface area in a rock (refer to the “Grès à meules” sandstone and the tuffeau limestone).
- **The grain compactness** – In some of the studied rocks, changes in the grain compactness are mainly linked to various levels of cementation from one area to the other. These changes induce variations in the porous structure (mainly in the pore and throat size and in the porosity), and therefore, play a role in the porous structure homogeneity of a rock according to the distribution of the areas with a high or low degree of cementation. In the Fontainebleau sandstone, the amount of quartz overgrowth varies according to the location in the rock. These variations induce some changes in the characteristics of the rock from one area to the other (several areas of strong cementation have sizes that can reach 1 mm in diameter). The relative homogeneity of this sandstone at the scale of laboratory samples (2 cm^3 samples or bigger) is understandable considering the random and periodic distribution of overgrowth. In the case of the Vuillecin limestone, various levels of calcitic cementation induce pores and throat sizes that drastically vary even at the scale of laboratory samples. In the Mons chalk, the very low variations in the compactness and in the porous structure can be linked to the fact that there is no significant cementation inside the rock.
- **The grain roughness influences the specific surface area** – The rough surfaces of opal-CT spherules in the tuffeau limestone play an important role in the specific surface area of this rock. The smooth surfaces of the quartz grains explain the low specific surface area of the Fontainebleau sandstone.
- **The grain “sorting”** (see the definition in § 1.1.1.) – The “sorting” is linked to the grain size. There is a relation between the “sorting” and the porous structure homogeneity of a sedimentary rock. For instance, the Fontainebleau sandstone and the Mons chalk, which are well “sorted”, have the most homogeneous porous structures, while the Vuillecin limestone, which is poorly “sorted”, has a porous structure with the lowest degree of homogeneity. In fact, this relation between the “sorting” and the homogeneity of the rock is a consequence of the close dependence of the pore and throat sizes on the grain size.

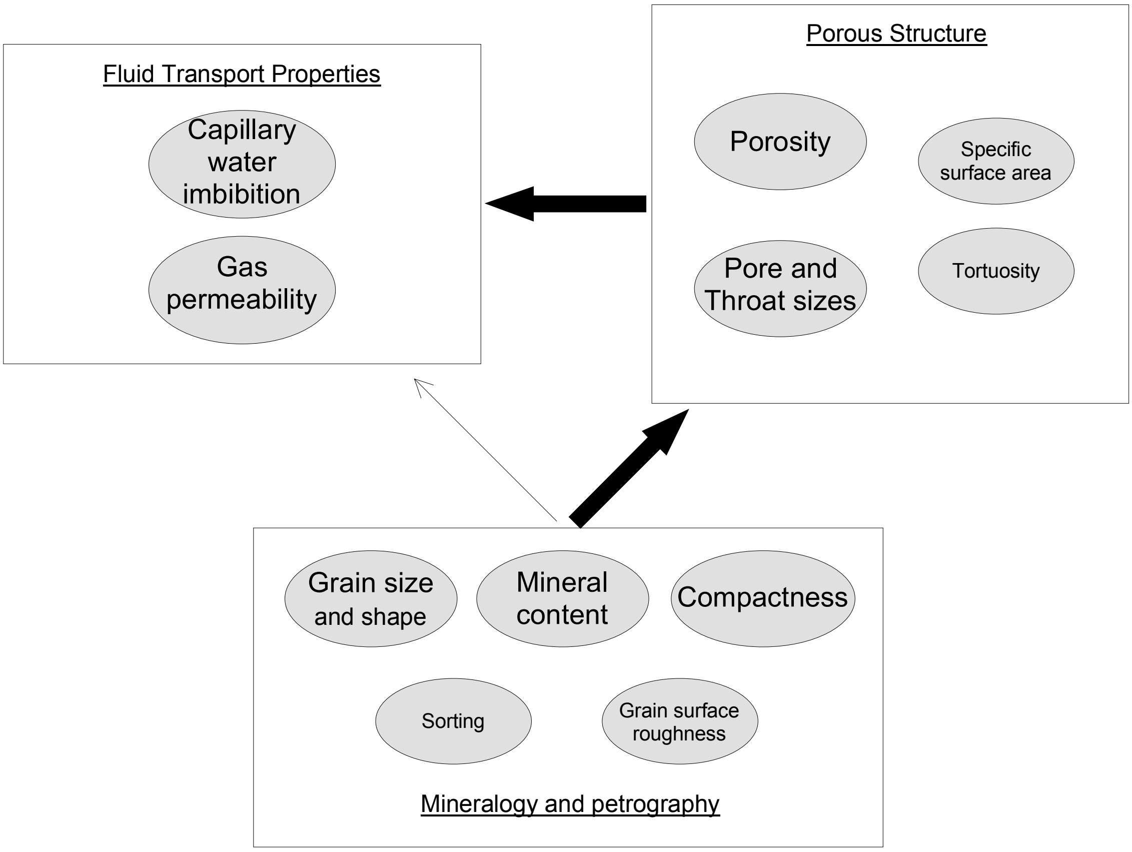

Fig. 59 – Diagram of the relations between the mineralogy and petrography, the porous structure, and the fluid transport properties in a sedimentary rock.

4.4. Relations between the fluid transport properties of a rock and its mineralogy and porous structure

The fluid transport properties of the studied rocks are summarized in Table 26. It appears that preferential flow paths within a rock are different either for gas permeability or for capillary water imbibition, except in the chalk and the tuffeau limestone due to the homogeneity of the porous and mineral structure in the first rock, and to the emphasized role of the opal-CT spherules in the second.

One conclusion made from the analytical measurements of this study is that both the permeability and the capillary water imbibition in a rock strongly depend on the throat size. Another conclusion is that many other porous structure features and mineralogical characteristics have also an influence on the fluid transport properties as indicated below and as summarized in Fig. 59.

4.4.1. Influence of porous structure parameters on the capillary water imbibition

- **Pore and throat size** – The pore and throat sizes govern the water flow intensity: the bigger the pores and the throats, the higher the volume able to flow within a rock is. The mean flow velocity depends on the sizes of the pores, but mainly the sizes of the throats: the bigger the pores and throats, the faster the imbibition is. Moreover, the difference between the size of the pores and that of the throats governs the quantity of trapped air during a water imbibition (Mode 2 of the air trapping mechanisms, §2.1.1.5.). This dependence explains the very fast imbibition in the macroporous Fontainebleau sandstone and the slower imbibition in the microporous chalk. Moreover, changes in the pore and throat sizes in the Vuillecin limestone induce changes in the capillary water imbibition properties within this rock.

- **Porosity** – The porosity mainly influences the volume of water able to flow. Hence, the high porosity of the chalk allows a significant water flow (high weight increase coefficient A of capillary water imbibition kinetics, §3.1.4.). On the contrary, a lower porosity reduces the water flow intensity (lower value of A), like in the Fontainebleau sandstone and in the Vuillecin limestone.
- **Tortuosity** – The tortuosity of the porous network of a rock has an influence on the mean velocity of the water migration within this rock. For instance, the high tortuosity in the Vuillecin limestone is one of the causes of the very slow water imbibition in this rock. The low tortuosity in the chalk explains the fast imbibition, although the pores and throats of this rock are micrometric.
- **Role of the connectivity** – The connectivity is already known to have a certain influence on the capillary water imbibition in a rock: a high connectivity facilitates a regular water flow migration (David C., 1991; Hammecker C., 1993; PÅl-Eric Øren and Stig Bakke, 2002). However, this influence is linked to the porous structure homogeneity of the rock. For instance, the low connectivity in the Vuillecin limestone drastically reduces the water flow abilities mainly because of the presence of strongly cemented areas and of many macropores in which the water migration is almost interrupted. The low connectivity and the porous structure heterogeneity mean rare parallel flow paths, which allow water to bypass these areas and macropores. Hence, the capillary water imbibition in this limestone has a “1-D character”, as defined by Benavente D et al. (2002), as opposed to the “3-D character” of the imbibition in the other studied rocks. Moreover, in spite of various porosity structures, the capillary water imbibition inside the tuffeau limestone is high, fast and regular. The homogeneous spatial distribution of these structures and the high amount of pore inter-connections is one reason for the good capillary water imbibition capacity of this limestone – the second reason is the emphasized role of the opal-CT spherules (see §4.3.3.).

4.4.2. Dependence of the permeability on porous structure features

- **Throat size** – This feature is the most important one on which the gas permeability of a rock depends: the higher the throat sizes, the higher the gas permeability is. Unlike the case of the capillary water imbibition, the pore sizes do not significantly influence the permeability. The permeability differences between the rocks are mainly explained by their different mean throat size (see §3.2.3.).
- **Influence of the porosity** – The Vuillecin limestone, which is four times less porous than the chalk, has the same permeability as the chalk. This result excludes the possibility of a direct permeability-porosity correlation. This fact was already noted in many previous studies (Dana E. and Skoczylas F., 1999; Singh M. and Mohanty K., 2000; Pape Hansgeorg et al., 2000). In this study, the use of both the porosity and the throat size for permeability calculations led to theoretical permeability values in accordance with the experimental ones for all the rocks (Pittman’s empirical relation 51, §3.2.4.2.; Debye-Poiseuille’s model, Relation 52, §3.2.5.1.). The good results obtained using these relations suggest that the throat size must be coupled with the porosity for better determination of the permeability of the sedimentary rocks, and that, at constant throat size, a porosity diminution decreases the permeability but only in a slight way.

4.4.3. Relationship of the fluid transport properties of a rock to its mineralogy

- **Grain roughness** – Rough grain surfaces play a role in the capillary water imbibition properties. This roughness allows a fast and continuous water migration, as in the case of the "Grès à meules" sandstone (due to the presence of clays at grain borders) and of the tuffeau limestone (due to rough opal-CT spherules and also to the presence of clays). However, the micro-roughness enhances the quantity of trapped air in macropores during a water imbibition (Mode 1 of the air trapping mechanisms, §2.1.1.5.) and decrease the water saturation according to the amount of macropores.
- **Mineral content** – The porous structure of the rocks depends on their mineralogy, as seen above (§4.2.), but some specific minerals contained in a rock have a very strong influence on its fluid transport properties. The result is a relation between the mineral content and the fluid transport properties:
  i) Presence of clay minerals: clays generally decrease the permeability, mainly because they reduce the size of the throats. They influence the capillary water imbibition in a rock according to their concentrations and location inside the rock. The "Grès à meules" sandstone and the tuffeau limestone are good examples for this. High concentrations in the fine grain layers of the sandstone decrease the water flow velocity. However, low concentrations of clays in the coarse grain layers of the sandstone are sufficient to insure the water flow continuity. But these concentrations reduce the flow intensity and facilitate the trapping of air in the bigger pores during the imbibition (Mode 1 of the air trapping mechanisms, §2.1.1.5.). When clays are concentrated in sparse areas in a rock, like in the tuffeau limestone, they have only a slight influence on the capillary water imbibition properties.
  ii) The influence of opal CT-spherules: numerous in the tuffeau limestone, the spherules explain the fluid transport properties of this limestone. They induce a regular, intense and fast imbibition in this rock, because they have rough surfaces and are homogeneously distributed inside the rock. The interspaces between the spherules and between the spherules and their neighbouring minerals are big enough to allow high gas permeability within this rock.

4.4.4. Consequences for the prediction of the fluid transport properties

With reference to the last section, the factors that influence either the permeability or the capillary water imbibition in a rock are summarized in Table 27.

Table 27 – Summary of the structure parameters, on which the permeability and the capillary water imbibition depend.

	Gas permeability	Capillary water imbibition
Depending structure Parameters	Porosity Throat size	Porosity Pore size Throat size Tortuosity Connectivity Roughness

It can be seen that the permeability mainly depends on the throat size and the porosity. Other characteristics that influence the permeability were given in the literature such as the grain size or the burial depth (SCHÖN J.H., 1996). As a matter of fact, the grain size and the burial depth are closely related to the throat size and/or the porosity. As seen above, the grain size almost determines the width of the pores and throats. The porosity and the throat size vary according to the burial depth (SCHÖN J.H., 1996). Thus, only two accurate parameters which govern the permeability of the sedimentary rocks can be retained: porosity and throat size[1]. The consequence is that precise predictions of the permeability of the studied rocks can be obtained with models using only the mean throat size and the porosity (see the results of the model applications §3.2.5.).

The capillary water imbibition strongly depends on many factors (Table 27), making it more difficult to predict the capillary water imbibition properties as opposed to the case of the permeability. For instance, the application of a pore model based only on the throat size led to inaccurate predictions of B coefficients (see §3.1.6.). However, it was shown that three of these factors are sufficient for good predictions of the coefficient B of the studied rocks: pore size, throat size and specific surface area (refer to the application of the granular model, §3.1.5.2.).

We have identified the porous structure parameters that must be considered for predicting models. The application of pore structure models also helped us to determine the best type of models that must be applied to each rock. A schematic representation of these models is given in §3.1.4. They qualitatively described the fluid transport properties of the rocks:

- A **“bypass model”** can simplify the porous structure of the **Fontainebleau sandstone** (§3.1.4., Fig. 42). This model is based on the phenomenon of “bypass” (Mode 1 of the air trapping mechanisms) expressed by BOUSQUIE P. (1979). It consists of spherical pores directly or indirectly interconnected by tubular throats and can be used in order to predict the flow of gas or water within rocks like the Fontainebleau sandstone.

- A **“roughness model”** that consists of rough spherical pores to which rough tubular throats are connected (Fig. 43 and 45) can be applied to describe the permeability and the capillary water imbibition properties of the **“Grès à Meules” sandstone** and the **tuffeau limestone**. The diameters of the spheres and the tubes are given by the mean size of the pores and the pore accesses in the rocks, respectively (in the case of various classes of pore accesses the mean diameter corresponding to the main class is retained). The advantage of this model is the inclusion of the notion of roughness, which is quite important to explain the fluid transport properties of these rocks.

- A **tubular model** can be used to describe the fluid transport properties of the **Mons chalk** (Fig. 44). This model is made of a succession of tubes with diameters equal to the mean size of the pore accesses within the rock.

- A **“tortuous bypass model”** fits in with the porous structure of the **Vuillecin limestone**. This model is a modified “bypass model” (Fig. 46), which includes the notion of tortuosity, an important factor in this limestone. The throats within the rock are represented by tortuous cylindrical tubes.

---

[1] Some authors (BEAR J., 1988; BENAVENTE D. et al., 2002) mentioned that the permeability inversely varies with the tortuosity, but the examples of the Vuillecin limestone and the chalk made us not retain the tortuosity as a factor that can explain the permeabilities of the studied sedimentary rocks (the limestone is as permeable as the chalk in spite of the quite higher tortuosity of its porous network).

4.5. “Homogeneity” of the porous structure of the rocks: estimation and classification

4.5.1. Limits of homogeneity and classification of the rocks

Within a massif, changes in the structure of a rock are linked to its geological history (as exposed in §1.1.1.). We have taken samples from one specific layer of each rock’s massif (see sampling, §1.1.2.).

The porous structure homogeneity of the rocks could be estimated and a classification was made by analyzing and summarizing the results of the numerous parameters measured at different scales. The parameters which may be constant were identified according to the analysis scale. A parameter was arbitrarily considered as constant when its relative standard deviation was below or equal to 10%. Three scales of analysis were considered:

i) The 30x30x30-cm³ block – The homogeneity in the block of each rock was estimated from the results of the statistical analysis and the measurements of the 15-cm³ and 2-cm³ sample sets (results of the water porosimetry, the mercury porosimetry and the gas adsorption).
ii) One 2-cm³ sample – The assessment of the homogeneity of each rock within a 2-cm³ sample was made from the results of the techniques like the mercury porosimetry (pore access size distribution) and the X-ray tomography.
iii) One sample below 1 cm³ - The assessment of the variability of the structure parameters at this lower scale was made from the results of the techniques like the BSE image analysis and the X-ray absorption/refraction analysis.

The conclusions, relating to the constant parameters and the relative homogeneity degree of the rocks, are summarized in Figure 60. The rocks can be classified according to the homogeneity of their porous structure in the following way:

1. – Mons chalk – Most of the measured porous structure parameters of this rock have standard deviations below 10%, considering either the block or a 2-cm³ sample. That means a high homogeneity of the porous structure of the rock at these scales. For smaller samples (< 1 cm³) higher variations in all the parameters are linked to various arrangements of the 2-µm-sized calcite crystals. Only the specific surface area remain constant until a very small scale (refer to the X-ray refraction analysis, §2.6.6.2.)
2. – Fontainebleau sandstone – At the scale of the block, the porous structure of this material can be characterized as to be homogeneous, since many parameters such as density, porosity, pore volume, specific surface area, hydraulic diameter and pore size slightly vary. Within a small 2-cm³ sample, the homogeneity is less convincing: the density and the pore access diameter remain about constant but the other parameters (porosity, pore size, pore volume, specific surface area) are quite variable mainly due to various amounts of quartz overgrowth and the presence of strongly cemented areas (the mean size of these areas is about 1 mm).
3. – Tuffeau limestone – Like in the Fontainebleau sandstone, many parameters of this limestone are constant at the scale of the block. Studying a small 2-cm³ sample, this limestone is characterized by different juxtaposed porosity structures linked to the different minerals of this rock. These different structures particularly induce a wide range of pore and pore access sizes in this limestone. Due to these different porosity structures, all the structure parameters strongly vary at the scale of a 2-cm³ sample, except the density which is constant, as seen by X-ray computed

tomography. High variations in the density are evident considering a smaller scale (below 1 cm³).

4. – “Grès à meules” sandstone – Some parameters of this rock (density, porosity, pore volume and hydraulic diameter) slightly vary within the studied block. In contrast to the tuffeau limestone, the specific surface area strongly varies from one 2-cm³ sample to another because of various clay mineral concentrations. At a smaller scale, only the density remains constant (X-ray tomography). This rock is made of a succession of two types of layers, which differ from each other in their mineral and porous characteristics (the thickness of a layer is about 200 µm).
5. – Vuillecin limestone – High variations in all the parameters (except the density) were recorded whatever analysis scale. This limestone is the rock with the lowest degree of homogeneity and can be even considered as to be heterogeneous in comparison with the other rocks. This heterogeneity is due to a quite variable mineral structure (various grain sizes, different arrangements of the grains…). The heterogeneity of the mineral framework induces the existence of various areas with different porous structure characteristics. Some such areas can reach up to a few centimetres in diameter.

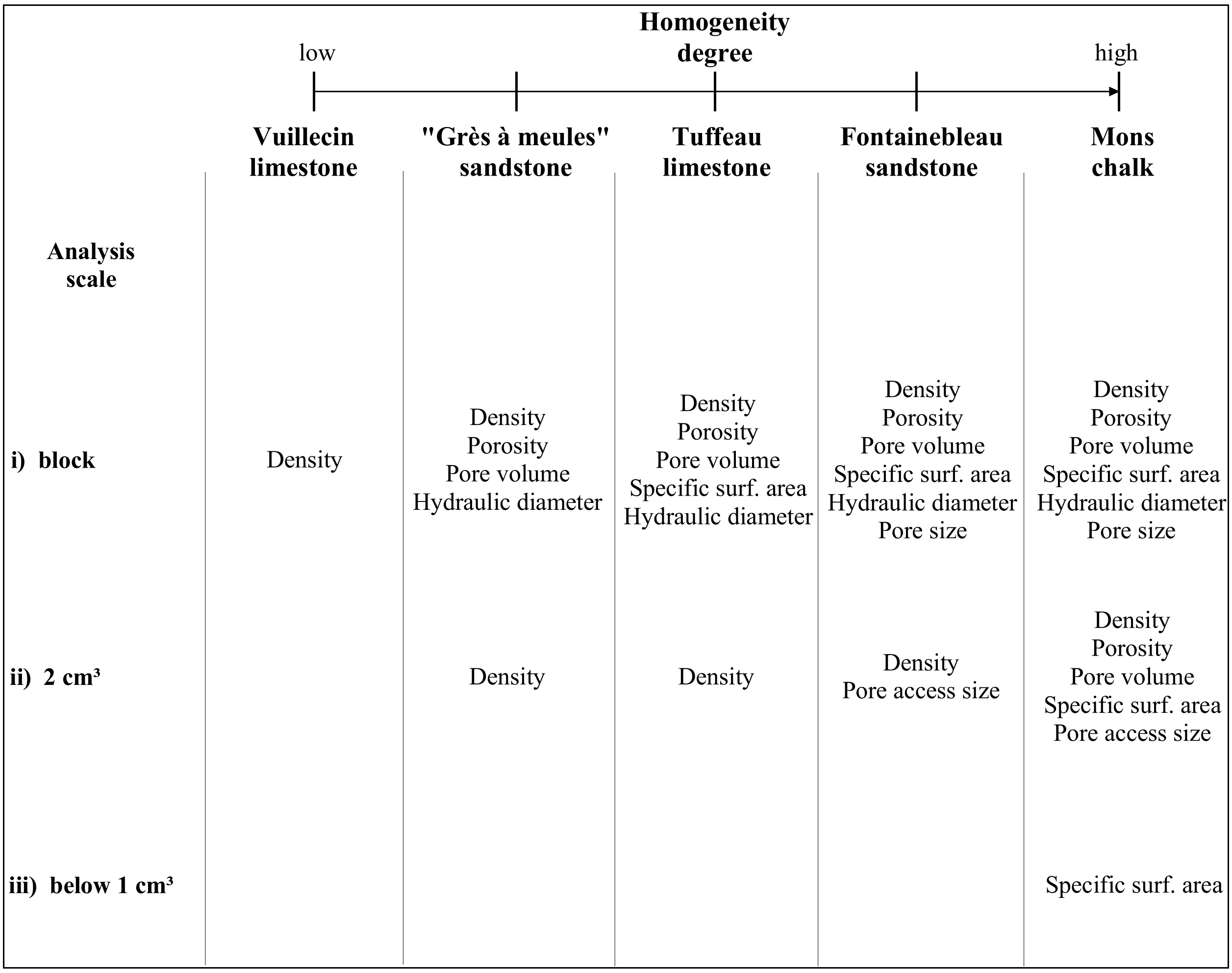

Analysis scale	Vuillecin limestone	"Grès à meules" sandstone	Tuffeau limestone	Fontainebleau sandstone	Mons chalk
i) block	Density	Density Porosity Pore volume Hydraulic diameter	Density Porosity Pore volume Specific surf. area Hydraulic diameter	Density Porosity Pore volume Specific surf. area Hydraulic diameter Pore size	Density Porosity Pore volume Specific surf. area Hydraulic diameter Pore size
ii) 2 cm³		Density	Density	Density Pore access size	Density Porosity Pore volume Specific surf. area Pore access size
iii) below 1 cm³					Specific surf. area

Fig. 60 – Relative situation of the rocks on a scale of homogeneity degree and structure parameters, which were found constant according to the analysis scale.

4.5.2. Comparison with porous CRMs

A comparison was made between the rocks and many synthetic porous Certified Reference Materials[1] in order to better situate the degree of the porous structure homogeneity of the sedimentary rocks.

Certified data of porous CRMs were compared with the data obtained in this study from the measurement of the sedimentary rocks (a certificate of a porous CRM is reported as example in Appendix K). The porous structure homogeneity of the sedimentary rocks could be qualitatively estimated in regard to any porous CRMs by comparing:

- the standard deviations of structure parameters like the specific pore volume, the mean pore size[2] and the specific surface area (determined either by mercury porosimetry or by gas adsorption);
- the variations in the mercury porosimetry curves.

Table 28 shows that the three structure parameters of the sedimentary rocks highly vary in comparison with those of the CRMs. Only the specific pore volume standard deviations of the sedimentary rocks are of the same order as those of the CRMs.

Moreover, the sedimentary rocks present higher variations in the mercury porosimetry curves. For example, Figure 61 shows the contrast between the curve interval of the Mons chalk (given by the extreme curves), which is the most homogeneous of the sedimentary rocks, and the curve uncertainty interval of CRM BAM-PM-120.

It can be concluded from all the comparisons that the porous structure homogeneity of the sedimentary rocks is low, in regard to that of any synthetic CRMs.

Indeed, many factors, such as the “sorting”, the mineral content, the burial depth, the atmospheric conditions, determined the structure of the sedimentary rocks during their diagenesis, as exposed in details in §1.1.1. These factors are responsible for the low homogeneity of the actual porous structure of the rocks, in regard to any synthetic CRMs. In other words, these factors determine the limit of homogeneity of the porous structure of the rocks.

The homogeneity of synthetic CRMs can be optimized by modifying the production procedures (temperature, pressure conditions) or the composition (component concentrations, mixing of minerals). Of course, this is not possible for the sedimentary rocks.

---

[1] Only a few examples of porous CRMs were cited in this report. The comparison was made using a wider range of porous CRMs found:

- in the Catalogue of CRMs provided by BAM (Federal Institute for Materials Research and Testing, Germany); more information is available on the websites of BAM: http://www.bam.de/index4.htm
- in international databases and catalogues (category porous CRMs) available online: http://isotc.iso.ch/livelink/livelink.exe

[2] For the homogeneity comparison, and in particular the comparison of the standard deviations, this quantity, measured either by mercury porosimetry or by gas adsorption, was considered as to be the mean pore diameter (as in the bibliography) of the CRMs cited in the table. However, it must be kept in mind that, using mercury porosimetry, this quantity is more representative of the mean pore access diameter than the mean pore diameter, particularly for the sedimentary rocks.

Table 28 – Comparison of the variations of quantitative characteristics of porous CRMs with those of the sedimentary rocks. σR*: relative standard deviation.*

Material	Measurement method	**Structure characteristics**					
		Specific pore volume		Mean pore (access) diameter		Specific surface area	
		Value (mm^3/g)	σ_R	Value (nm)	σ_R	Value (m^2g^{-1})	σ_R
CRMs							
BAM-PM-101	Gas adsorption for the determination of the three parameters					0.177 ± 0.04	2.2%
BAM-PM-102						5.41 ± 0.2	4.4%
BAM-PM-103		250 ± 8	3.2%	6.36 ± 0.16	2.5%	156.0 ± 7.2	4.6%
BAM-PM-104		210 ± 9	4.3%	10.62 ± 0.48	4.5%	79.8 ± 2.0	2.5%
BAM-PM-107		217 ± 4	1.8%	1.72 ± 0.06	3.5%		
BAM-PM-120	Mercury porosimetry for the three parameters	548.1 ± 13.1	2.4%	456.0 ± 11.8	2.6%		
BAM-PM-121		624.6 ± 13.4	2.1%	30.2 ± 0.4	1.3%		
BAM-PM-122		924.4 ± 17.2	1.8%	278.0 ± 7.4	2.7%		
Rocks							
Font. sandstone	Mercury porosimetry for the specific pore volume and the mean pore access diameter; Gas adsorption for the specific surface area	53.2 ± 2.8	5.3%	31404 ± 3706	11.8%	$15\ 10^{-3} \pm 10^{-3}$	8.2%
“Grès à meules” sandstone		96.0 ± 3.4	3.5%	7232 ± 1005	13.9%	2.86 ± 0.48	16.9%
Mons chalk		250.3 ± 7.5	3.0%	807 ± 77	9.5%	1.80 ± 0.15	8.3%
Tuffeau limestone		325.9 ± 11.4	3.5%	3234 ± 420	13.0%	23.08 ± 1.94	8.4%
Vuillecin limestone		47.4 ± 5.4	11.4%	845 ± 117	13.8%	1.43 ± 0.24	16.8%

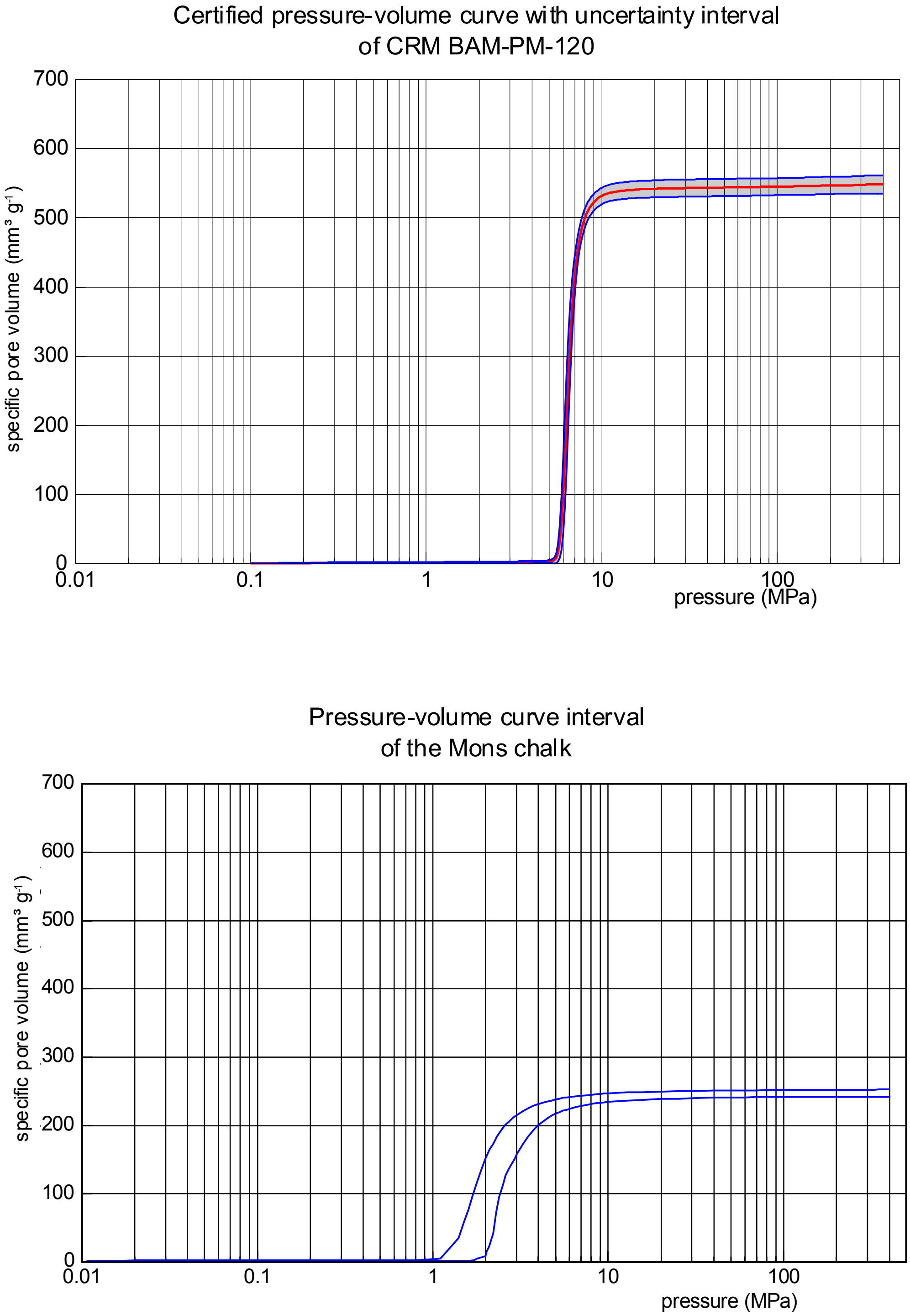
Certified pressure-volume curve with uncertainty interval of CRM BAM-PM-120

Pressure-volume curve interval of the Mons chalk

Fig. 61 – Mercury porosimetry curves comparison between CRM BAM-PM-120 and the Mons chalk.

4.6. What about “Reference Geomaterials”?

The conclusions made from the assessment of the homogeneity of the sedimentary rocks and the comparison with existing synthetic porous CRMs can be summarized in the following way:

i) A good repeatability of the results of the porous structure parameter values and deviations of the rocks was obtained: the values were often obtained with an acceptable level of confidence. However, the smaller the analyzed volumes, the higher the deviations of the measured porous structure parameters were.

ii) In comparison with any synthetic CRM, the sedimentary rocks has shown higher variations in all their porous structure parameters, when especially considering small sample’s volumes, i.e. when using measurement methods such as mercury porosimetry, gas adsorption, and so on.

It follows that the establishment of reference values for selected characteristics using some of the rocks seems to be even possible, particularly in the case of big samples (over 15 cm^3) measured using methods such as the water porosimetry or the water imbibition analysis. However, the delivery of such “Reference Geomaterials” (Geo-RMs) would mean a restraint range of possible applications that differs from that of the synthetic CRMs.

The synthetic CRMs are usually used for the calibration of measuring systems, the assessment of analytical procedures, the performance test of instruments, the definition of measurement scales, and also for inter-laboratory comparisons and for qualitative and quantitative analyses of materials (see “Definition and role of the reference materials”; §1.1.1.). Because of the too low degrees of the porous structure homogeneity of the sedimentary rocks, in regard to synthetic CRMs, the use of small samples of the rocks for the establishment of reference values, in the aim of the equipment calibration or the definition of measurement scales, would not be conceivable. However, a few “standardization” possibilities could be envisaged (Table 29) and summarized in the following way:

- The total specific pore volume of the rocks (except the Vuillecin limestone) is the only parameter, which was obtained with very low deviations (same range of low relative standard deviation as that of synthetics CRMs, as shown in Table 28) using water porosimetry or mercury porosimetry and 2-cm^3 samples. The eventual certification of this lone parameter could be used for performance tests in particular for the water total porosimetry technique. Actually, international norms exist for the procedure of this technique but no certified references are available concerning geomaterials analyzed using this technique.
- The low specific surface area of the Fontainebleau sandstone makes this rock applicable for controls of specific surface area measurements using gas adsorption or mercury porosimetry, in the range of very low values, since no certified references exists in this range.
- The variations in the mercury porosimetry curves of the sandstone and the chalk are high in comparison with any synthetic CRMs. That means that these materials cannot be retained as useful references in view of measurement control for mercury porosimetry, but added to other characteristics, the use of mercury porosimetry curves would be of other specific interest as exposed below.

In fact, it would be helpful to provide standard values of several characteristics of a rock (specific pore volume, specific surface area and pore access diameter distribution), using rocks such as in particular the Fontainebleau sandstone or the Mons chalk. The interest for this concerns the field of geomaterial research and can be summarized in two points (Fig. 62):

Table 29 – Standardizations possibilities and eventual application fields.

Characteristic	Rock	Technique	Application / Application field
Total specific pore volume	Fontainebleau sandstone Mons Chalk “Grès à meules” sandstone Tuffeau limestone	Water porosimetry Mercury porosimetry	Performance test Qualitative and quantitative analysis of rocks / Geomaterial research
Specific surface area	Fontainebleau sandstone Mons Chalk	Gas adsorption Mercury porosimetry	Measurement control Qualitative and quantitative analysis of rocks / Industry field Geomaterial research
Mercury porosimetry curve (cumulative pore volume curve, pore access diameter distribution)	Fontainebleau sandstone Mons Chalk	Mercury porosimetry	Qualitative and quantitative analysis of rocks / Geomaterial research

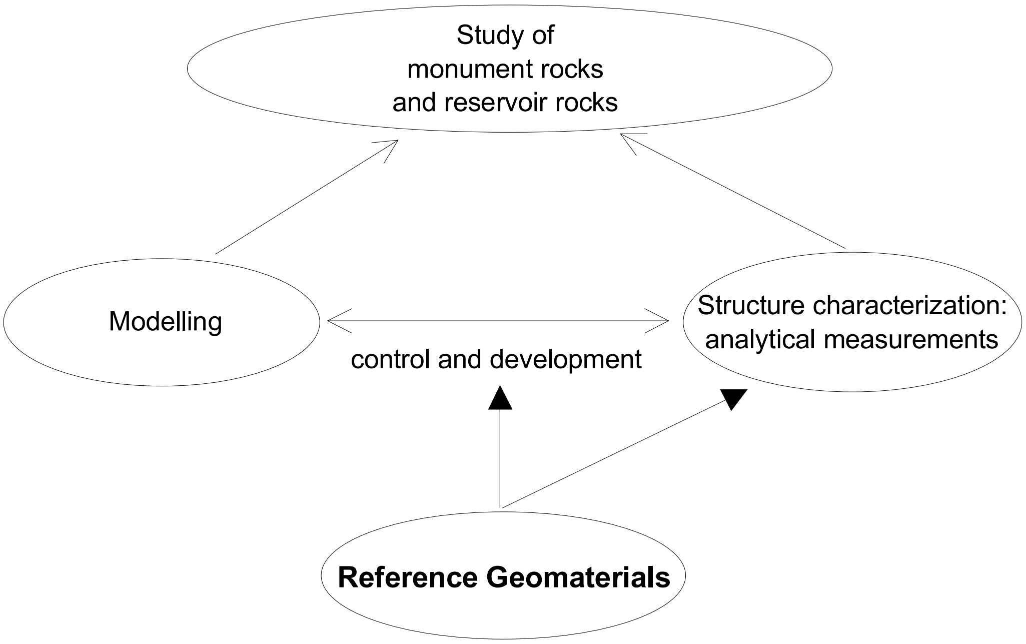

Fig. 62 – Eventual role of “Geo-RMs” in geomaterial research.

1. To assist and improve the qualitative and quantitative analyses of geomaterials (with equal or lower degree of homogeneity) – During this study, the Fontainebleau sandstone and the chalk were often used as “references” for the understanding and the interpretation of the measurement results of the other sedimentary rocks, allowing us to obtain a high precision in the characterization of the sedimentary rocks of this study, as well as to obtain new scientific results.
2. To test the efficiency or to develop relationships and pore structure models applied to geomaterials – Indeed, there’s already a great actual demand for rocks like the Fontainebleau sandstone, or the chalk (samples, measured characteristics…), which are often used for the development of porous network models. In this study, the X-ray refraction technique was applied to sedimentary rocks for the first time. The values of the structure parameters (mainly the specific surface area and the porous volume) of the Fontainebleau sandstone and the chalk, which were determined by mercury porosimetry and gas adsorption, could be used as “standard values” in order to assess both the efficiency and the limits of the method during its application to geomaterials (see §2.6.).

4.7. Summary and perspectives

This study managed to precisely determine and synthesize the characteristics of the selected rocks. General relationships between the mineral structure and the porous structure of a rock and its fluid transport properties were established. These relations remain however in a qualitative aspect for most of them. The precise characterization helped us to understand the fluid transport properties of the rocks. Concerning this last topic, our research led us to identify the main characteristics of the mineral and porous structure on which the fluid transport properties depend. Sketches were proposed for each rock. These sketches integer the relations established. They are schematic models that qualitatively describe the fluid transport properties of the rocks. As perspectives, the qualitative relationships and the sketches could be the basis for the test or the development of analytical expressions or new pore models. The porous structure characterization of the sedimentary rocks made it possible to give answers about the problem concerning the eventual establishment of “Geo-RMs”. A few porous structure parameters of some rocks could be considered in some eventual certifications for which the certified parameters would be given at certain levels of confidence. Such certifications would mainly concern big sample volumes measured using water porosimetry or capillary water imbibition kinetics as reference methods. The level of accuracy of most of the characteristic results of the sedimentary rocks was found to be low (lower than for synthetic CRMs), especially when considering small sample volumes, i.e. considering methods such as mercury porosimetry or gas adsorption. For this reason, “Geo-RMs” would have restraint applications, particularly in the field of industry, and their establishment would even be unconceivable. For materials such as the Fontainebleau sandstone and the Mons chalk, the level of accuracy was however found to be sufficient to arouse some interests and perspectives in the field of research about the structure and properties of geomaterials.

Some approaches to this study were missing. Pore diameters were not determined for some of the rocks and grain size measurements were not performed for any of the five sedimentary rocks. The analysis of these two parameters (using for example NMR microscopy for the pore size) would provide important additional information for the characterization of the structure of the rocks and would be useful to confirm or improve some relationships established in the study. Concerning the theme about reference materials, the problem of the rocks’ stability was not approached. Extracted rocks always undergo structure evolution the moment after their extraction. The evolution time and mechanisms depend on the rock. The structure of the rocks seemed to remain stable for about three years (time between the first and the last analysis of this study).

References

ALLEN T. (1997) – *Particle Size Measurement* – Chapman and Hall New York, 5th ed., Vol.2: Surface Area and Pore Size Determination.

Autopore III, Operator's Manual (1998) – Micromeritics Instrument Corporation, Part No. 942-42807-01, Appendix D-H.

BEAR J. (1988) – *Dynamics of Fluids in Porous Media* – Elsevier, New-York.

BENAVENTE D., LOCK P., ÁNGELES GARCÍA DEL CURA M. and ORDÓÑEZ S. (2002) – *Predicting the Capillary Imbibition of Porous Rocks from Microstructure – Transport in Porous Media,* 49, 59-76.

BOURBIÉ T., COUSSY O., ZINSZNER B. (1986) – *Acoustique des milieux poreux – Collection science et technologie du pétrole* – Institut Français du Pétrole, 27, p.11.

BOUSQUIÉ P. (1979) – *Texture et porosité de roches calcaires* – PhD thesis of Paris VI University.

BRUNAUER S., EMMETT P.H. and TELLER E. (1938) – *Adsorption of gases in multimolecular layers – J. Amer. Chem. Soc.* – 60, 309-318.

CARLOS A. LEÓN y LEÓN (1998) – *New perspectives in mercury porosimetry – Advances in Colloid and Interface Science* – 76-77, 341-372.

CARNIGLIA S.C. (1986) – *J. Catal. 102* – 401.

CHAUVE P. (1975) – *Jura – Guides géologiques* – Ed. Masson.

CHOQUETTE P.W. & PRAY L.C. (1970) – *Geological nomenclature and classification of porosity in sedimentary carbonates – Amer. Assoc. Petrol. Geol. Bull.* – 54, 2, 207-250.

COSTER L. and CHERMANT J.L. (1989) – *Précis d'analyse d'images* – CNRS Press, Paris, 560 pp.

DANA E. and SKOCZYLAS F. (1999) – *Gas relative permeability and pore structure of sandstones – Internat. J. of Rock Mechanics and Mining Sciences* – 36, 613-625.

DAVID C. (1991) – *La perméabilité et la conductivité électrique des roches dans la croûte: expériences en laboratoire et modèles théoriques* – PhD thesis of Louis Pasteur University, Strasbourg, 255 pp.

DESSANDIER D. and GABORIAU H. (1996) – *Facies, porous medium and fluid transfer properties of Tuffeau stones used in the cathedral Saint–Gatien of Tours* – Office "Bureau de recherches Géologique et minières", Orléans.

DESSANDIER D., GABORIAU H., LE BERRE P., RASPLUS L. and RAUTUREAU M. (1996) – *Etude des propriétés pétrophysiques du Tuffeau blanc de Touraine. Application à la durabilité des pierres en oeuvre (Petrophysical properties of the "Tuffeau blanc de Touraine". Application to the durability of building stones) – Chron. rech. min.* – n°524, pp. 3-13.

DULLIEN F.A.L. (1979) – *Porous media: fluid transport and pore structure* – Academic Press, San Diego Calif.

DULLIEN F.A.L., ZARCONE C., MACDONALD I.F., COLLINS A., BOCHARD R.D.E. (1983) – *The effects of the surface roughness on the capillary pressure curves and the heights of capillary rise in glass bead packs – Journal of colloid and interface* – 172, (2), 362-372.

DUNHAM R.J. (1962) – *Classification of carbonate rocks according to depositional texture - In*

Classification of carbonate rocks – Ham W.E. Ed., *Mem. Amer. Ass. Petrol. Geol.*, 1, 108-121.

EN 1925:1999 – *Natural stone test methods: determination of water absorption coefficients by capillarity* – Edition May 1999, 10 pp.

FABRE D., MAZEROLLE F. and RAYNAUD S. (1989) – *Caractérisation tomodensitométrique de la porosité et de la fissuration de roches sédimentaires – Rock at great depth* – Maury & Fourmaintraux Ed., 297-304.

FELDKAMP L.A., DAVIS L.C., and KRESS J.W. (1984) – *Practical Cone-Beam Algorithm – J. Opt. Soc. Amer.* – A1, 612-619.

FOLK R.L. (1962) – *Spectral subdivision of limestones types* – Ham W.E. Ed., *Mem. Amer. Ass. Petrol. Geol.*, 1, 62-84.

FRIPIAT J., CHZAUSSIDON J. & JELLI A. (1971) – *Chimie physique des phénomènes de surface* – Masson & Cie Ed., Paris.

GALL J.-C. (1971) – *Faunes et Paysages du Grès à Voltzia du nord des Vosges: Essai Paléoécologique sur le Buntsandstein supérieur – Mém. Serv. Carte géol. Als. Lorr.* – 34.

GALL J.-C., DURAND M. and MULLER E. (1977) – *Le Trias de part et d'autre du Rhin. Corrélations entre les marges et le centre du bassin germanique – Bull. B.R.G.M.* – 4, 3, 193-204.

GÉRAUD Y., TOURNIER B. and MAZEROLLE F. (1999) – *Detection of porosity and mineralogical variations in geological materials: radiological density measured by X-ray tomography – International symposium on imaging applications in geology, Geovision 99* – Liege, 6-7 may 1999, 109-112.

GREGG S.J. & SING K.S.W. (1982) – *Adsorption, Surface Area and Porosity* – 2nd Ed., New York.

GROLIER J., FERNANDEZ A., HUCHER M., RISS J. (1990) – *Les propriétés physiques des roches : Théories et modèles* – Masson Ed., 462 pp.

GUÉGUEN Y. & PALCIAUSKAS V. (1992) – *Introduction à la physique des roches* – Hermann ed., Paris, 299 p.

HAMMECKER C. (1993) – *Importance des transferts d'eau dans la dégradation des pierres en œuvre* – PhD thesis of Louis Pasteur University, Strasbourg, 254 pp.

HAMMECKER C., MERZ J.D., FISCHER C. (1989) – *Capillary imbibition in sandstone: a trial of modelisation according to petrographic data – E.U.G. V.* – Strasbourg.

HAMMECKER C., MERZ J.D., FISCHER C., JEANNETTE D. (1993) – *A geometrical model for numerical simulation of capillary imbibition in sedimentary rocks – Transport in Porous Media* – 12, 3.

HARBICH K.-W., HENTSCHEL M.P., SCHORS J. (2001) – *X-ray refraction characterization of non-metallic materials – NDT&E International* – 34, 297-302.

HARBICH K.-W. and HENTSCHEL M.P. (2002) – *Non-destructive Characterization of Monolithic Ceramics by X-ray Refraction – Key Engineering Materials* – Vols. 206-213, pp 673-676, Trans Tech Publications, Switzerland.

HELLMUTH K.-H., SIITARI-KAUPPI M., KLOBES P., MEYER K. and GOEBBELS J. (1999) – *Imaging and Analyzing Rock Porosity by Autoradiography and Hg-porosimetry/X-ray Computer tomography - Applications – Phys. Chem. Earth (A)* – Vol. 24, No. 7, pp. 569-573.

HENTSCHEL M.P., HOSEMANN R., LANGE A., UTHER B., BRÜCKNER R. (1987) – *Röntgen-Kleinwinkelbrechung an Metalldrähten, Glasfäden und hartelastischem Polypropylen – Acta Cryst. A34* – pp. 506-513.

HENTSCHEL M.P., HARBICH K.-W., LANGE A. (1994) – *Nondestructive evaluation of single fiber debonding in composites by X-ray refraction – NDT&E International* – 27, pp. 275-280.

ILLERHAUS B., GOEBBELS J., RIESENMEIER H. (1996) – *3D Computerized Tomography - Synergism between Technique and Art* – Copyright: Springer Verlag.

ISO Guide 30 (1992) – *Terms and Definitions used in Connection with Reference Materials*.

ISO Guide 31 (1981) – *Contents of Certificates of Reference Materials*.

ISO Guide 32 (1996) – *Calibration in Analytical Chemistry using Reference Materials*.

ISO Guide 33 (1989) – *Use of Certified Reference Materials*.

ISO Guide 34 (1996) – *Quality systems Guideline for Production of Reference Materials*.

ISO Guide 35 (1989) – *Certification of Reference Materials - General and Statistical Principles*.

JACOBS P., SEVENS E., KUNNEN M. (1995) – *Principles of computerized X-ray tomography and applications to building materials – The Science of the Total Environment* – 167, 161-170.

KATZ & THOMPSON (1987) – *Prediction of rock electrical conductivity from mercury injection measurements – Journal of Geophysical Research* – 92, B1, 599-607.

KLOBES P., RIESEMEIER H., MEYER K., GOEBBELS J. and HELLMUTH K.-H. (1996) – *Rock porosity determination by combination of X-ray computed tomography with mercury porosimetry – Fresenius J. Anal. Chem.* – 357, 543-547.

KOSAKA N. (1995) – *Etude expérimentale de l'interaction entre des solution naturelles et des roches poreuses : contrôle géochimique et pétrophysique* – PhD thesis of Louis Pasteur University, Strasbourg, 182 p.

LANGMUIR I. (1918) – *J. Am. Chem. Soc.* – 40, 1631.

LEVINE S., LOWNDES J. and REED P. (1980) – *Two phase fluid flow and hysteresis in a periodic capillary tube – J. Colloid Interface Sci.* – 77, 253-263.

LOWELL S. and SHIELDS J.E. (1991) – *Powder surface area and porosity* – 3rd ed., Chapman and Hall, New York.

MACHHOUR L., SIZUN J.-P., RICHARD J., GAVIGLIO P. & VANDYCKE S. (2002) – *Origin and variability of reservoir characteristics in the chalk deposit: example of Mons Basin (Belgium)– 64th EAGE Conference & Exhibition* – Florence, 27-30, May 2002.

MARSHALL T.J. (1958) – *A relation between permeability and size distribution of pores – J. Soil Sci.* – 9, 1-8.

MATTHEWS G.P. and SPEARING M.C. (1992) – *Measurement and Modelling of Diffusion, Porosity and Other Pore Level Characteristics of Sandstones – Marine and Petroleum Geol.* – 9, 146.

MATTHEWS G.P., MOSS A.K., SPEARING M.C. and VOLAND V. (1993) – *Network Calculation of Mercury Intrusion and Absolute Permeability in Sandstone and Other Porous Media – Powder Technology* – 76, 95.

MATTHEWS G.P., RIDGWAY C.J. and SPEARING M.C. (1995a) – *Void space modelling of mercury intrusion hysteresis in sandstone, paper coating, and other porous media – Journal of Colloid and Interface Science* – 171, 8-27.

MATTHEWS G.P., MOSS A.K., RIDGWAY C.J. (1995b) – *The effects of correlated networks on mercury intrusion simulations and permeabilities of sandstone and other porous media – Powder Technology* – 83, 61-77.

MATTHEWS G.P., RIDGWAY C.J. & SMALL J.S. (1996) – *Modelling of simulated clay precipitation within reservoir sandstones – Marine and Petrol. Geol.* – Vol. 13, No. 5, 581-589.

MENG B. (1993) – *Charakterisierung der Porenstruktur im Hinblick auf die Interpretation von Feuchtetransportsvorgängen – Aachener Beiträge zur Bauforschung* – Band 3.

MERTZ J.D. (1991) – *Structure de porosité et propriétés de transport dans les grès – Sci. Géol, Mém.* – 90, 129 pp.

MERTZ J.D., HAMMECKER C., FISCHER C. (1988) – *Recherche d'un modèle de réseau représentatif des remontés capillaires dans une roche – 12e Réunion des Sciences de la Terre* – Lille.

MEYER K., LORENZ P., RÖHL-KUHN B., KLOBES. P. (1994) – *Porous Solids and their Characterization – Cryst. Res. Tchnol.* – 29, 7, 903-930.

MICHOT L. (1990) – *Propriétés physicochimiques superficielles du talc et de la chlorite* – PhD thesis INPL, Nancy, 285 pp.

M. VAN GEET, R. SWENNEN, M. WEVERS (2000) – *Quantitative analysis of reservoir rocks by microfocus X-ray computerised tomography – J. of Sedimentary Geol.* – 132, 25-36.

NF B.10.513 (1991) – *Produits de carrières, pierres naturelles, essais de gel* – September 1991.

ORSI T.H., EDWARDS C.M., ANDERSON A.L. (1994) – *X-ray computed tomography: a non-destructive method for quantitative analysis of sediment cores – J. Sed. Res.* – A64, 690-693.

PÅL-ERIC ØREN and STIG BAKKE (2002) – *Process Based Reconstruction of Sandstones and Prediction of Transport Properties – Transport in Porous Media* – 46, 311-343.

PAPE HANSGEORG, BARTELS JÖRN, KÜHN MICHAEL, and CLAUSER CHRISTOPH (2000) – *Long-term performance of heat mining in hot aquifers: water-rock interaction and permeability changes – Proceedings World Geothermal Congress 2000* – Kyushu-Tohoku, Japan, May 28.

PANTALONI J. (1988) – *Ecoulement de fluide. Ecoulement en milieu poreux, Séminaire « procédés de séparation »* – 6-8 septembre, Paris, Comité français de l'électricité, 32 pp.

PAUL A. WEBB (2001) – *An Introduction to the Physical Characterization of Materials by Mercury Intrusion Porosimetry with Emphasis on Reduction and Presentation of Experimental Data* – Micromeritics Instrument Corporation, Norcross, Georgia.

PAUL A. WEBB and CLYDE ORR (1996) – *Analytical Methods in Fine Particle Technology* – Micromeritics Instrument Corporation.

PAULI J., SCHEYING G., MÜGGE C., ZSCHUNKE A., LORENZ P. (1997) – *Determination of the pore widths of highly porous materials with NMR microscopy* – Springer Verlag, *Fresenius J. Anal. Chem.* 357, 508-513.

PAVONE D. (1982) – *Pétrographie et pétrophysique d'un calcaire oolithique et d'entroquites* – Thèse Ecole des Mines, Paris, 199 pp.

PERRIAUX J. (1961) – *Contribution à la géologie des Vosges gréseuses – Mém. Serv. Carte Géol. Als. Lor.* – 18, 236 p.

PITTMAN E.D. (1972) – *Diagenesis of quartz in sandstones as revealed by scanning electron* *microscopy – J. Sedim. Petrol. –* 42, 3, 507-519.

PITTMAN E.D. (1992) – *Relationship of Porosity and Permeability to Various Parameters Derived from Mercury Injection-Capillary Pressure Curves for Sandstone – Am. Assoc. of Petrol. Geol. Bull. –* v. 76, 2, 191-198.

POISEUILLE J.L.M. (1842) – *Recherches expérimentales sur le mouvement des liquides dans les tubes de très petits diamètres – D.R. Acad. Sci. –* Paris, 15, 1167-1186.

RASPLUS L. (1987) – *Aspect et évolution géologique du Bassin Parisien – Bull. Géol. Bassin Parisien –* Hors-série n°6, 183-202.

RAYNAUD S., FABRE D., MAZEROLLE F., GERAUD Y., LATIERE H.J. (1989) – *Analysis of the internal structure of rocks and characterization of mechanical deformation by a non-destructive method: X-ray tomodensitometry – Tectonophysics –* 159, 149-159.

RILEM norm (May–June 1980) – *Essais recommandés pour mesurer l'altération des pierres et évaluer l'efficacité des méthodes de traitement – Matériau et construction –* no 75.

RITTER H.L., DRAKE L.C. (1945) – IEC Anal. Ed. 17, 782.

ROBASZINSKY F. et al. (1982) – *Le Turonien de la région–type: Saumurois et Touraine, stratigraphie, biozonations, sédimentologie – Bull. Soc. Nat. Elf Aquitaine –* Pau, 6, 1, 119-225.

ROBASZINSKY F. and CHRISTENSEN W.K. (1989) – *The Upper Campanian-Lower Maastrichtian chalks of the Mons basin, Belgium: a preliminary study of belemnites and foraminifera in the Harmignies and Ciply areas – Geology en Mijnbouw –* 68, 391-408.

ROUQUEROL F., ROUQUEROL J. and SING K. (1999) – *Adsorption by powders & porous solids: principles, methodology and applications –* Academic Press.

ROUSSET TOURNIER B. (2001) – *Transferts par capillarité et évaporation dans des roches : Roles des structures de porosité –* PhD thesis of Louis Pasteur University, Strasbourg, 203 pp.

SCHEIDEGGER A.E. (1974) – *The physics of flow through porous media –* 3rd edition, University of Toronto Press.

SCHOELKOPF J., RIDGWAY C.J., GANE P. A.C., MATTHEWS G.P. and SPIELMANN D.C. (2000) – *Measurement and network modelling of liquid permeation into compacted mineral blocks – Journal of Colloid and Interface Science –* 227, 119-131.

SCHÖN J.H. (1996) – *Physical properties of rocks: Fondamentals and principles of petrophysics – Handbook of geophysical exploration, Section I: seismic exploration –* vol. 18, p. 26.

SINGH M. and MOHANTY K. (2000) – *Permeability of spatially correlated porous media – Chemical Engineering Science –* 55, 5393-5403.

SITTLER C. (1965) – *Le Paléogène des fossés rhénan et rhodanien. Etudes sédimentologiques et paléoclimatiques – Mém. Serv. Carte Géol. Alsace-Lorraine –* 234 p.

SIZUN J–P. and JEANNETTE D. (1994) – *Transformations pétrographiques successives conduisant à la structuration des réservoirs du Buntsandstein : le forage géothermique EPS1 de Soultz-sous-Forêts (Alsace, France) – C. R. Acad. Sci. –* Paris, t. 320, Série II, p. 365-372.

SIZUN J–P. (1995) – *Modifications des structures de porosité de grès lors à des transformations pétrographiques dans la diagenèse et l'hydrothermalisme. Application au Trias de la marge ardéchoise et du fossé rhénan –* PhD thesis, Strasbourg, 244 p.

SIZUN J–P., RICHARD J., HENRY P., MACHHOUR L., GAVIGLIO P. & VANDYCKE S. (avril 2002) – *Influence des paléoenvironnements sur les propriétés pétrophysiques de la craie du basin de Mons (Belgique)* – 19ème RST, Nantes.

SPEARING M.C. and MATTHEWS G.P. (1991) – *Modelling Characteristic Properties of Sandstones – Transport in Porous Media* – 6, 71.

SWENNEN R., POOT B., MARCHAL G. (1990) – *Computerized tomography as a tool in reservoir characterization – Zbl. Geol. Paläont.* – Teil I, 1105-1124.

SZEKELY J., NEUMANN A.W. and CHUANG Y.K. (1971) – *The rate of capillary penetration and the applicability of Washburn equation – J. Colloid Interface Sci.* – 35, 273-283.

THIRY & BERTRAND–AYRAULT (1988) – *Le grès de Fontainebleau: genèse par écoulement de nappes phréatiques lors de l'entaille des vallées durant le Plio-quaternaire et phénomènes connexes – Bull. Inf. Géol. Bass.* – Paris, 25, 4, 25-40.

TSAKIROGLOU C.D. and PAYATAKES A.C. (1998) – *Mercury intrusion and retraction in model porous media – Advances in Colloid and Interface Science* – 75, 215-253.

TSAKIROGLOU C.D. and PAYATAKES A.C. (2000) – *Characterization of the pore structure of reservoir rocks with the aid of serial sectioning analysis, mercury porosimetry and network simulation – Advances in Water Resources* – Volume 23, Issue 7, June 2000, Pages 773-789.

VANDYCKE S., BERGERAT F. & DUPUIS CH. (1991) – *Meso-Cenozoic faulting and inferred palaeostresses in the Mons Basin, Belgium – Tectonophysics* – 192, 261-271.

WARDLAW N.C. and MCKELLAR M. (1981) – *Mercury Porosimetry and the Interpretation of Pore Geometry in Sedimentary Rocks and Artificial Models – Powder Technology* – 29, 127-143.

WASHBURN E. W. (1921) – *The dynamic of capillary flow – Phys. Rev.* – 17, 273.

WASHBURN E. W. (1921) – *Note on a Method of Determining the Distribution of Pore Sizes in a Porous Material – Proc. Nat. Acad. Sci. USA* – 7, 115-116.

WELLINGTON S.L. and VINEGAR H.J. (1987) – *X-ray computerized tomography – J. Petrol. Technol.* – 885-898.

ZSCHUNKE A. (Ed.) (2000) – *Reference Materials in Analytical Chemistry - A Guide for Selection and Use (With contributions by numerous experts)* – Springer Series in Material Science, Vol. 40, 222 pp.

Image board A

Fontainebleau Sandstone

Fig. A – Thin section view of the quartz grains and of the porosity (red): the detrital quartz grains (Qd) present, on their borders intensive overgrowths (Qa) which lead to the development of the polyhedral shape of the inter-granular residual macropores (MP). Small amounts of Iron and/or Manganese oxide-hydroxide may be trapped between detrital grains and authigenic overgrowths. These impurities locally inhibit the formation of the overgrowth and preserve a microporosity (µP) at grain-overgrowth interface.

Fig. B –Thin section observation of the trapped (blue) and free (red) porosity. The free porosity is mostly composed of small pores. The trapped porosity is located in the largest macropores especially in their central area. Iron and Manganese oxide (Ox) and organic materials concentrated in pore throats may contribute to air trapping in the macropores.

Fig. C – SEM global view showing the imbrication of the quartz grains with well developed crystal faces and "corner" shape pore spaces.

Fig. D – Strongly cemented area (CA) observed by SEM: macropores are reduced to residual triangular pores (RP) connected each over by very fine capillaries (FC).

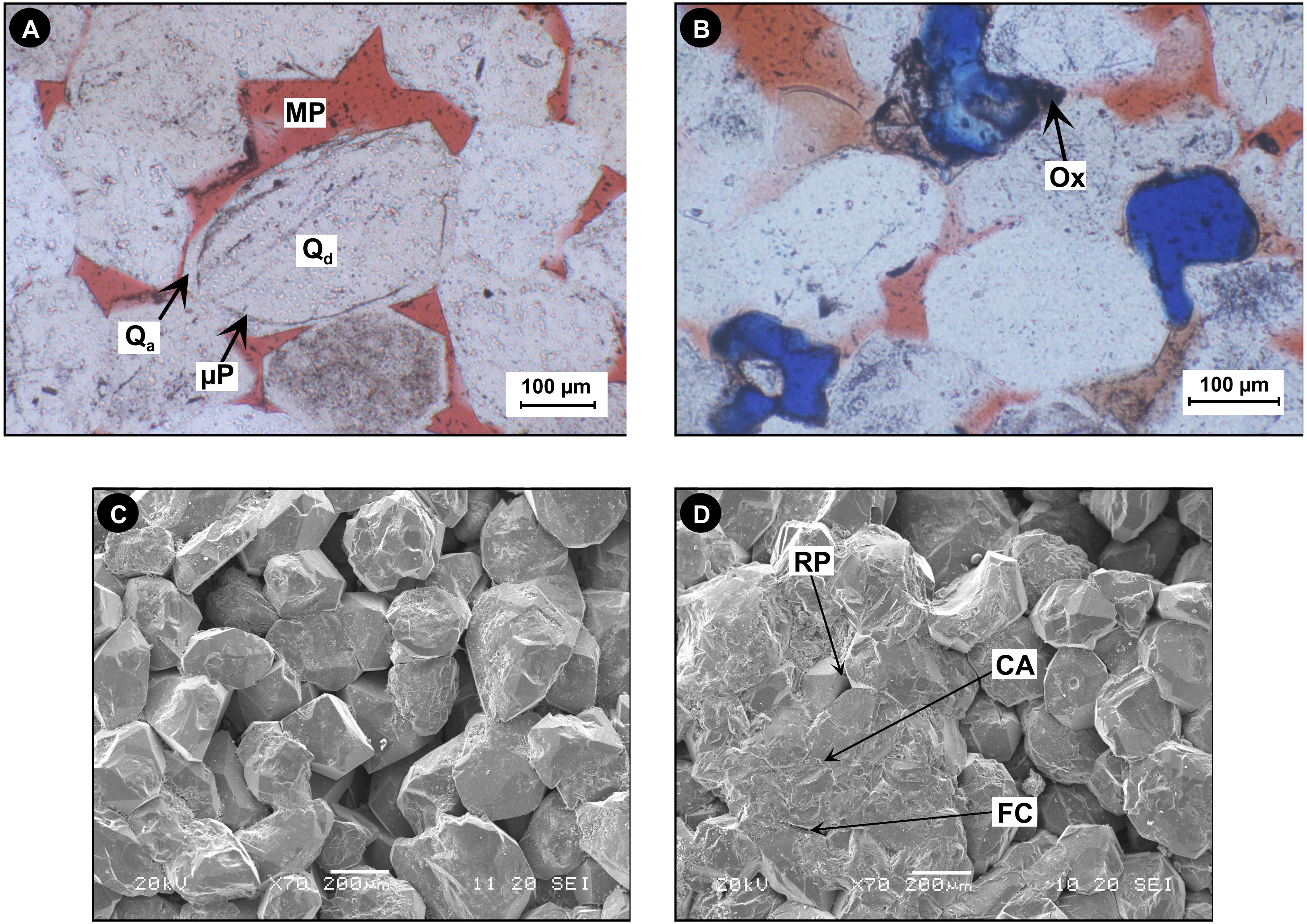
A
MP
Q_d
Q_a
µP
100 µm
B
Ox
100 µm
C
20kV X70 200µm 11 20 SEI
D
RP
CA
FC
20kV X70 200µm 10 20 SEI

IMAGE BOARD B

"GRES A MEULES" SANDSTONE

Fig. A – Thin section global view showing the petrographical heterogeneity of the sandstone (quartz: Q; feldspar: F; muscovite: M) and the distribution of trapped (blue) and free (red) porosity.

Fig. B – Thin section image showing Iron and Manganese oxide-hydroxide that line grain borders and fill a pore entry: this pore is occupied by trapped porosity (blue). Qd: detrital quartz grain; F: feldspar; Ox:Fe/Mn oxide-hydroxide.

Fig. C – SEM view of the rock: this sandstone is mainly composed of quartz (Q), feldspars (F) and clay minerals (CM). These clays, mainly illite, are located on grain surfaces or are clustered together in inter-granular pore spaces, forming microporous areas.

Fig. D – Detail of a clayey cluster by SEM. Q: quartz with overgrowth (euhedral shape); F: feldspar; FI: fibrous illite; FSI: flake shape illite.

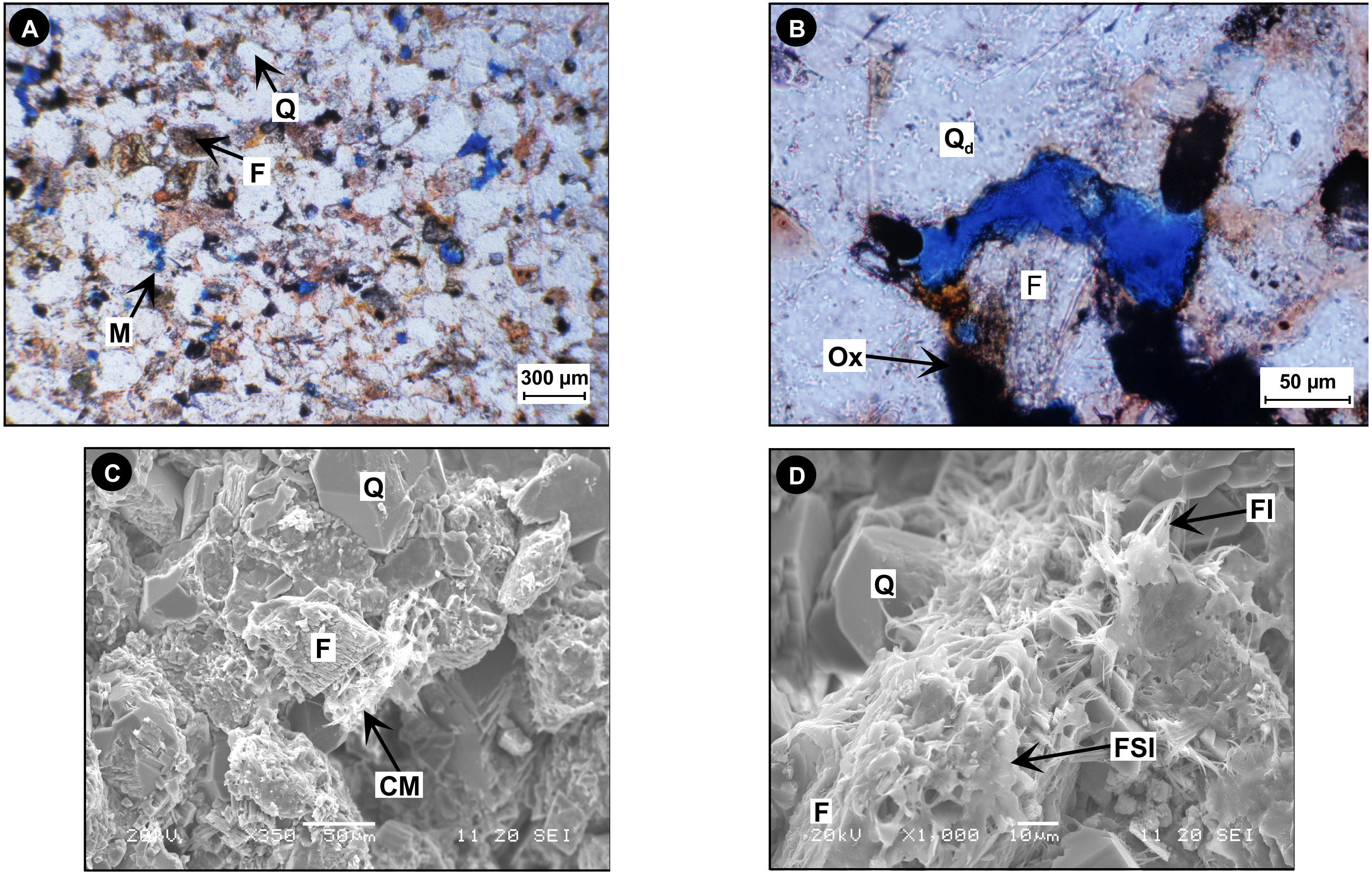
A
Q
F
M
300 µm
B
Q_d
F
Ox
50 µm
C
Q
F
CM
20kV X350 50µm 11 20 SEI
D
FI
Q
FSI
F
20kV X1,000 10µm 11 20 SEI

IMAGE BOARD C

MONS CHALK

Fig. A – Porosity (red) distribution in the Mons chalk observed on thin section: the material mainly contains microporosity (µP) located in the micritic matrix; some macropores (MP) are located in a few foraminifera cells.

Fig. B – Types of porosity in the Mons chalk observed on thin section: the most part of the pore network concerns a free porosity (red) associated to the microporous calcite matrix (µP); some macropores (MP) contains trapped porosity (blue).

Fig. C – SEM view of a macropore (MP); the low abundance of macropores makes them have a small contribution to the total porosity.

Fig. D – SEM observation of the microporous calcite matrix composed of calcimicrite crystals which delimit interparticular micropores (µP) of sizes, which mainly range from 1 to 5 µm.

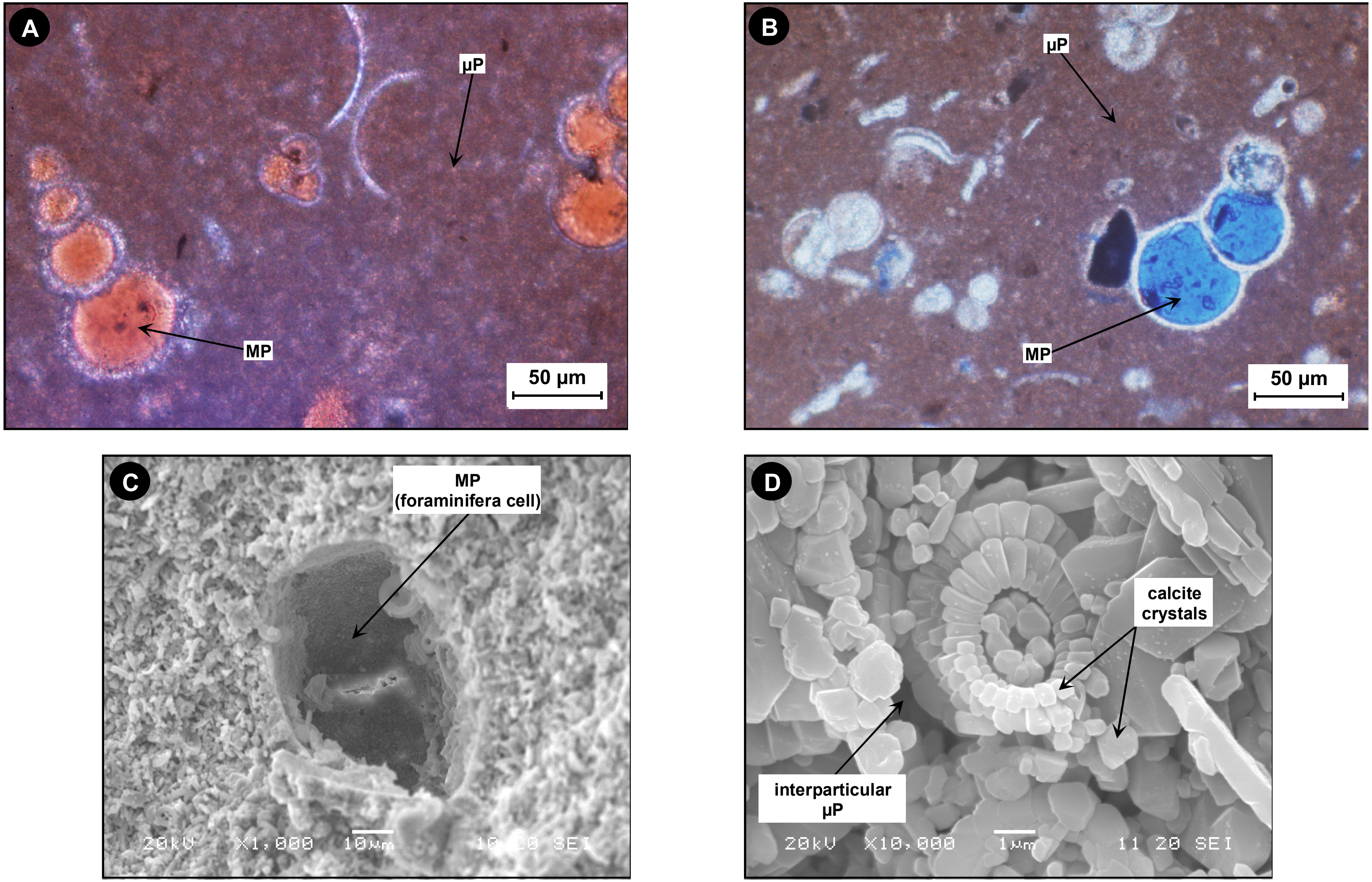
A
µP
MP
50 µm
B
µP
MP
50 µm
C
MP
(foraminifera cell)
20kV X1,000 10µm 10 20 SEI
D
calcite
crystals
interparticular
µP
20kV X10,000 1µm 11 20 SEI

IMAGE BOARD D

TUFFEAU LIMESTONE

Fig. A – Thin section global view showing the petrographical heterogeneity and the porosity complexity of this limestone. CAL: microporous micrite calcite cement; Q: quartz; OCT: opal-CT spherule; M: muscovite; GL: glauconite; MP: macropore.

Fig. B – Thin section image showing the juxtaposition of microporous zones and macropores. It also represents the distribution of trapped (blue) and free (red) porosity: the first one is located in the bigger macropores, and the second one is mainly associated to the microporous zones.

Fig. C – SEM global view showing different minerals made of the two main constituents of this material: calcite and quartz; the latter is in the form of quartz grains (Q) or opal-CT spherules. Note the important amount of opal-CT spherules which are a characteristic of the tuffeau limestone.

Fig. D – SEM view of an opal-CT spherule. Its own lamellar structure develops micropores of nanometer sizes and is partially responsible in the high specific surface area of this material.

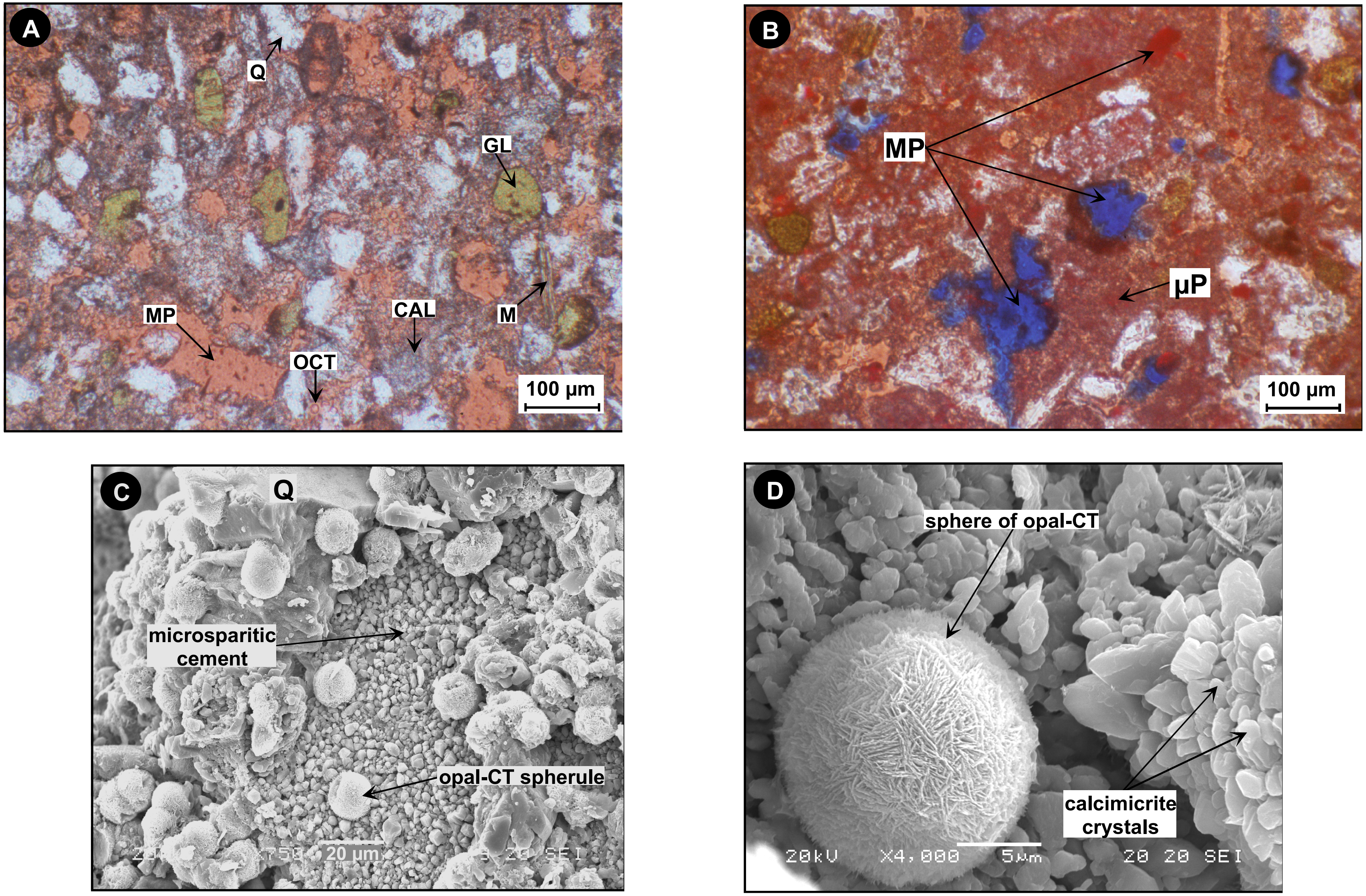
A
Q
GL
MP
CAL
M
OCT
100 µm
B
MP
µP
100 µm
C
Q
microsparitic cement
opal-CT spherule
x750
20 µm
SEI
D
sphere of opal-CT
calcimicrite crystals
20kV X4,000 5µm 20 20 SEI

Fig. E – SEM representation of a muscovite: microporosity is localized between the exfoliated crystal layers; the distance from one to the other reaches several tens nanometers.

Fig. F – SEM view that shows a clay mineral aggregate. Clays have a strong influence in the structure of the material, since they fill pores and throats; they are associated to micropores which size can reach several nanometers; these clay minerals (mainly smectite in this material) develop very high specific surface area.

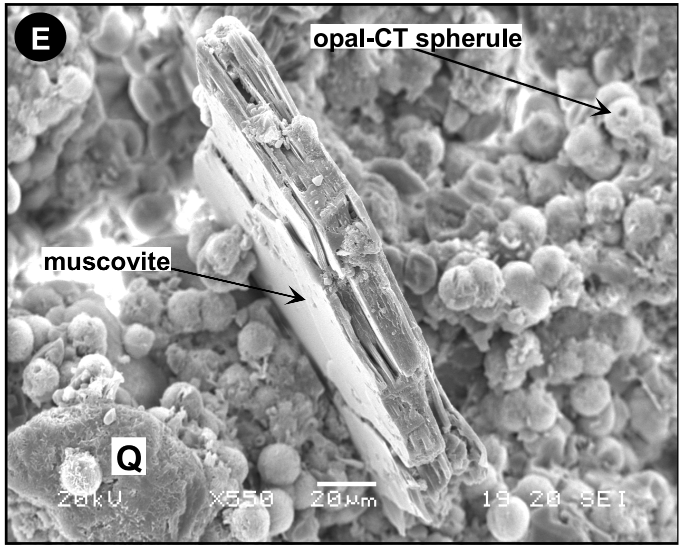
E
opal-CT spherule
muscovite
Q
20kV X550 20µm 19 20 SEI

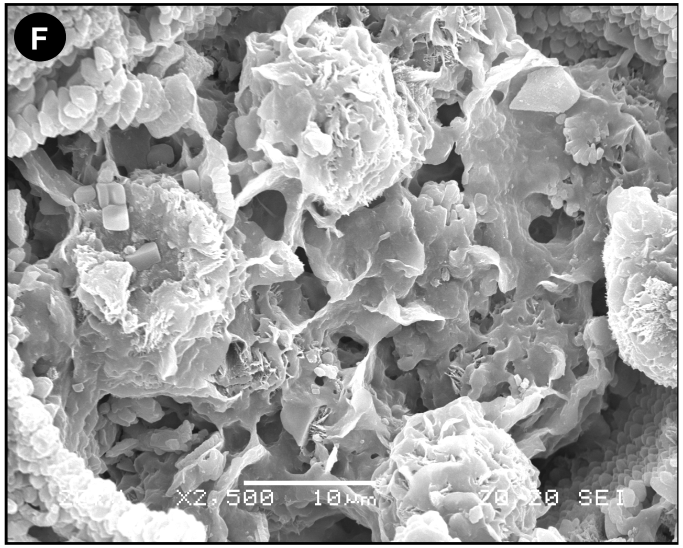
F
X2,500 10µm 20 20 SEI

IMAGE BOARD E

VUILLECIN LIMESTONE

Fig. A – Global view of a thin section showing the complexity of the structure of the limestone. The mineral structure consists in a juxtaposition of allochems – the allochem (All) shows on the figure is an oncholith made of a sparite nucleus and a microporous microcrystalline coating – surrounded by zones of sparite (Sp) or micrite (Mi) cement. This view shows the heterogeneity of the rock porous structure, which consists either in numerous primary and secondary isolated macropores (MP; the macropores shown are mouldic pore type) or micropores (µP) situated in micrite areas. These areas are better distinguished by SEM in Figures B, C and D.

Fig. B – SEM global view showing the different mineral and pore structures that composed the limestone: bioclasts (B) isolated by the cement made of rhomboedral sparite crystals (Sp), which delimit residual inter-granular macropores (MP); calcimicrite (Mi) areas, which are microporous (µP); some calcite mollusc shells (CS) delimit macropores (MP).

Fig. C – Detail by SEM of a sparitic area: macropores (MP) are delimited by sparitic calcite crystals (Sp).

Fig. D – Detail by SEM of a micritic area made of micrite crystals (Mi) that delimit micropores (µP).

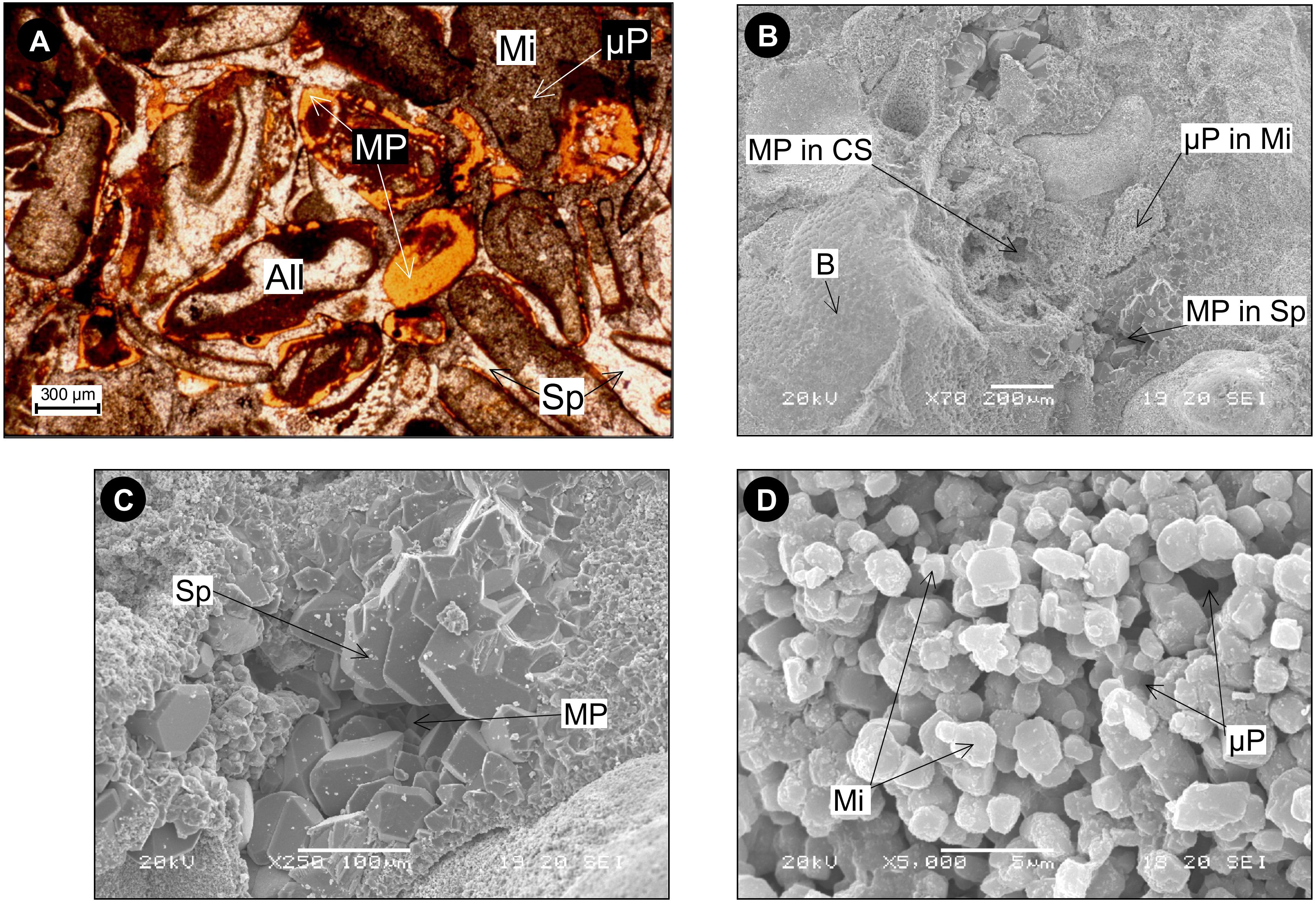
A
Mi
μP
MP
All
Sp
300 μm
B
MP in CS
μP in Mi
B
MP in Sp
20kV X70 200μm 19 20 SEI
C
Sp
MP
20kV X250 100μm 19 20 SEI
D
μP
Mi
20kV X5,000 5μm 18 20 SEI

Appendix A:
Geographical location of the quarry sites

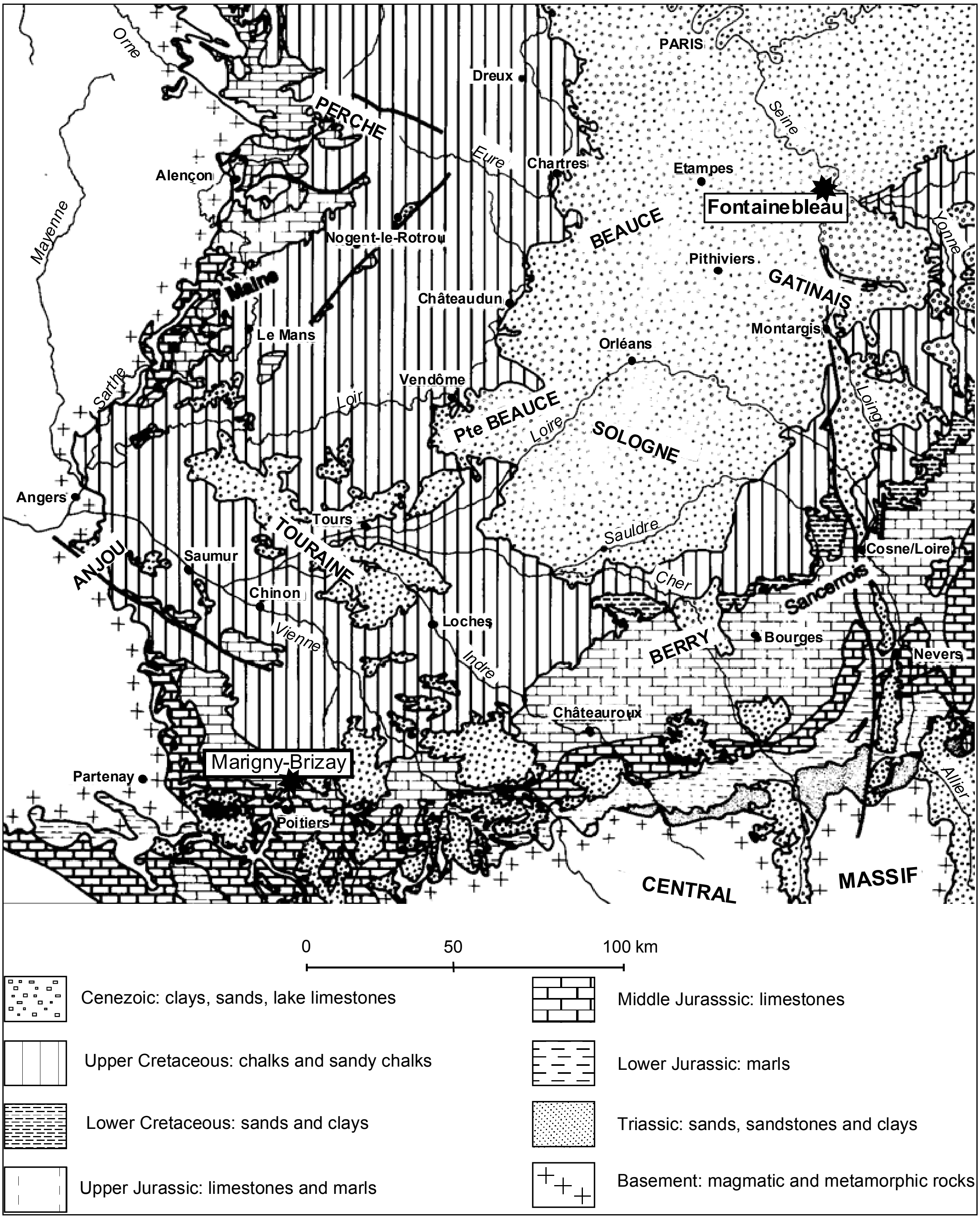

Fig. A – Geographical location of the Fontainebleau and Marigny-Brisay areas on the geological sketch map of the centre of France.

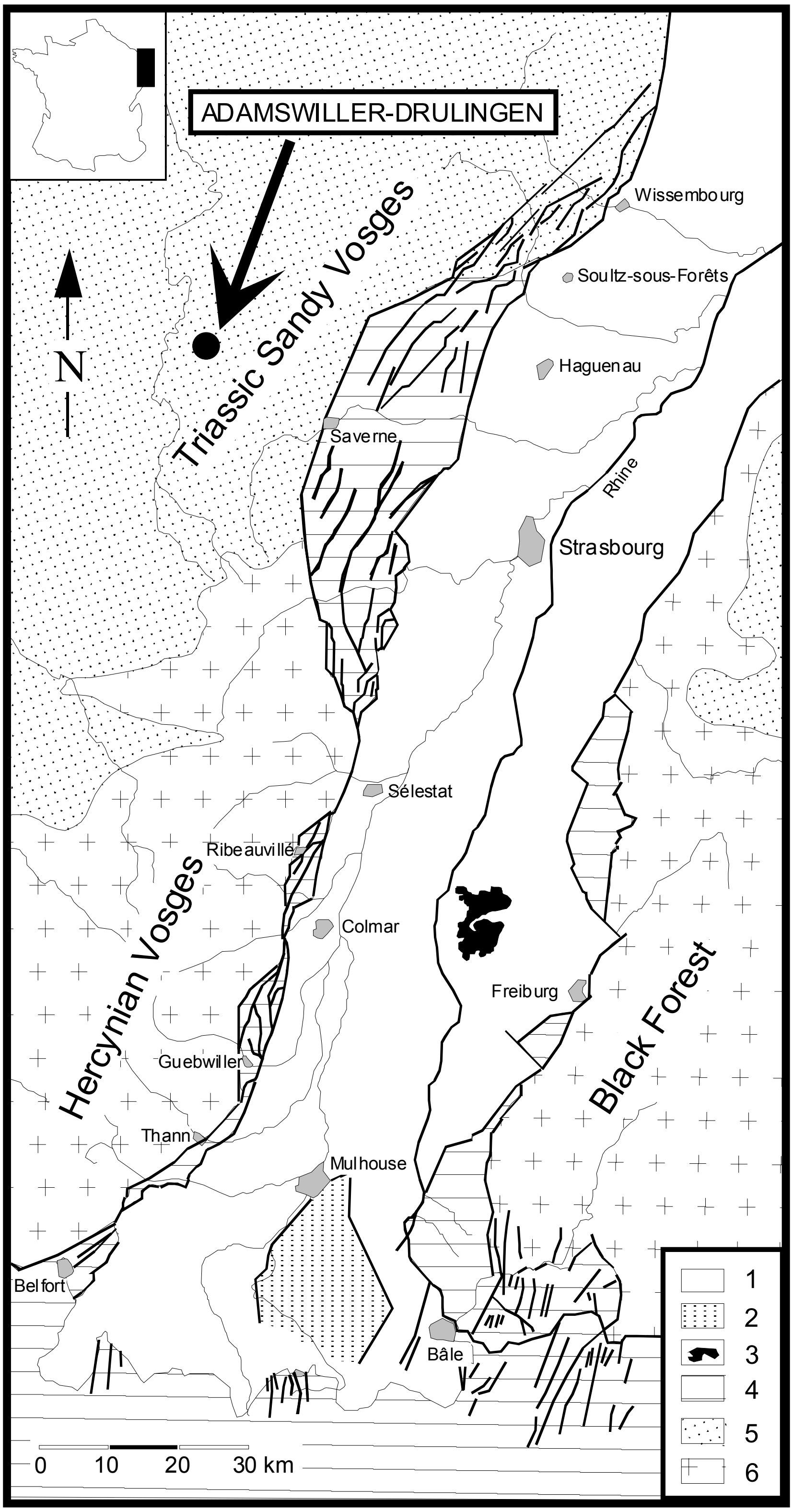

Fig. B – Geographical location of the Adamswiller-Drulingen area on the geological sketch map of the Rhine Grabben (after Sittler C., 1965 modified). 1. Paleozoîc basement of Vosges and Black Forest (crystalline rocks); 2. Triassic sedimentary cover; 3. Fault fields of Vosges and Black Forest foothills; 4. Kaisersthul (Neogene Volcanism); 5. Mulhouse Horst; 6. Rhine Graben and Alsace lowland (Holocene deposits).

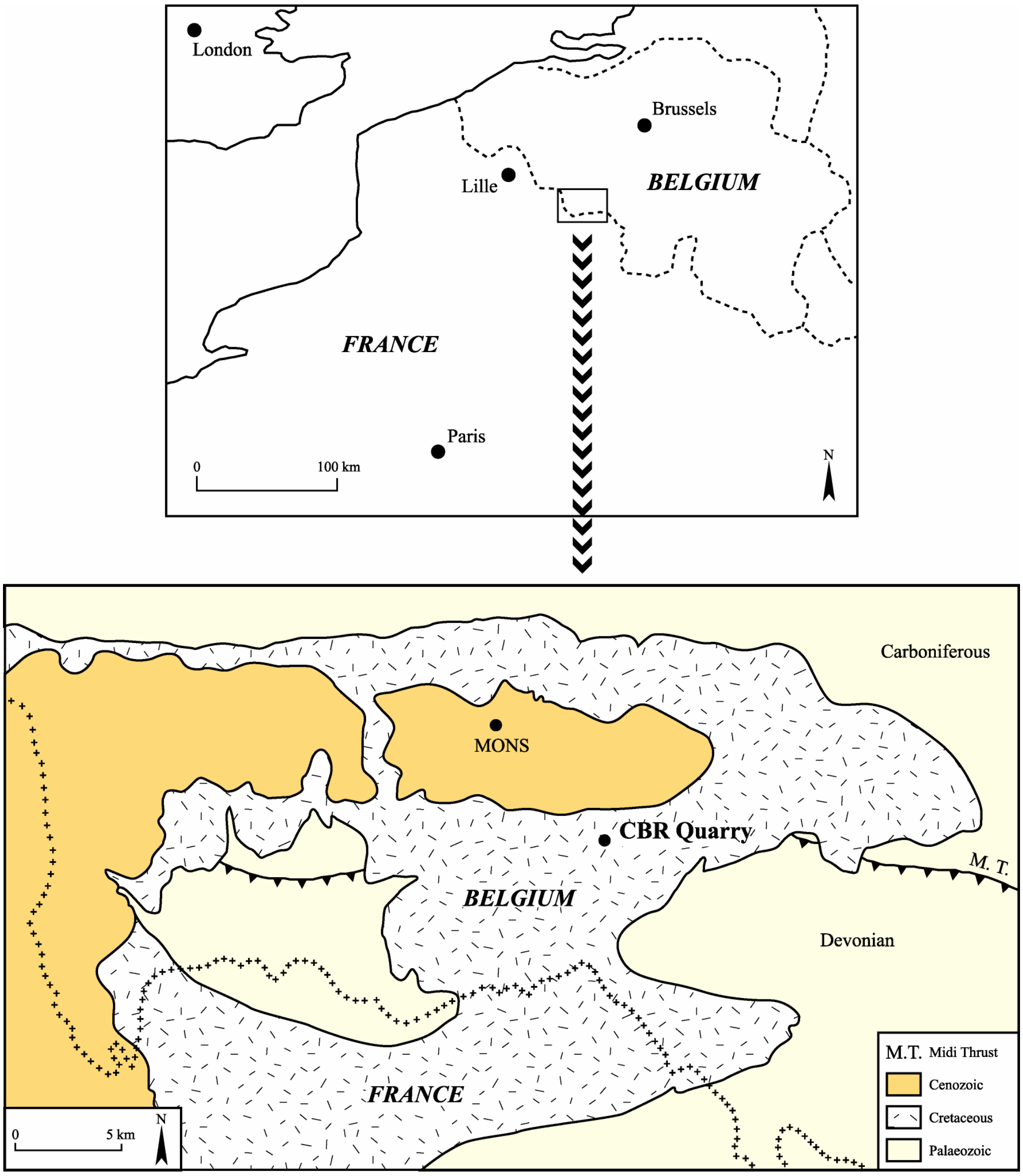

Fig. C – Geographical location of the CBR quarry on a geological sketch map of Mons Basin.

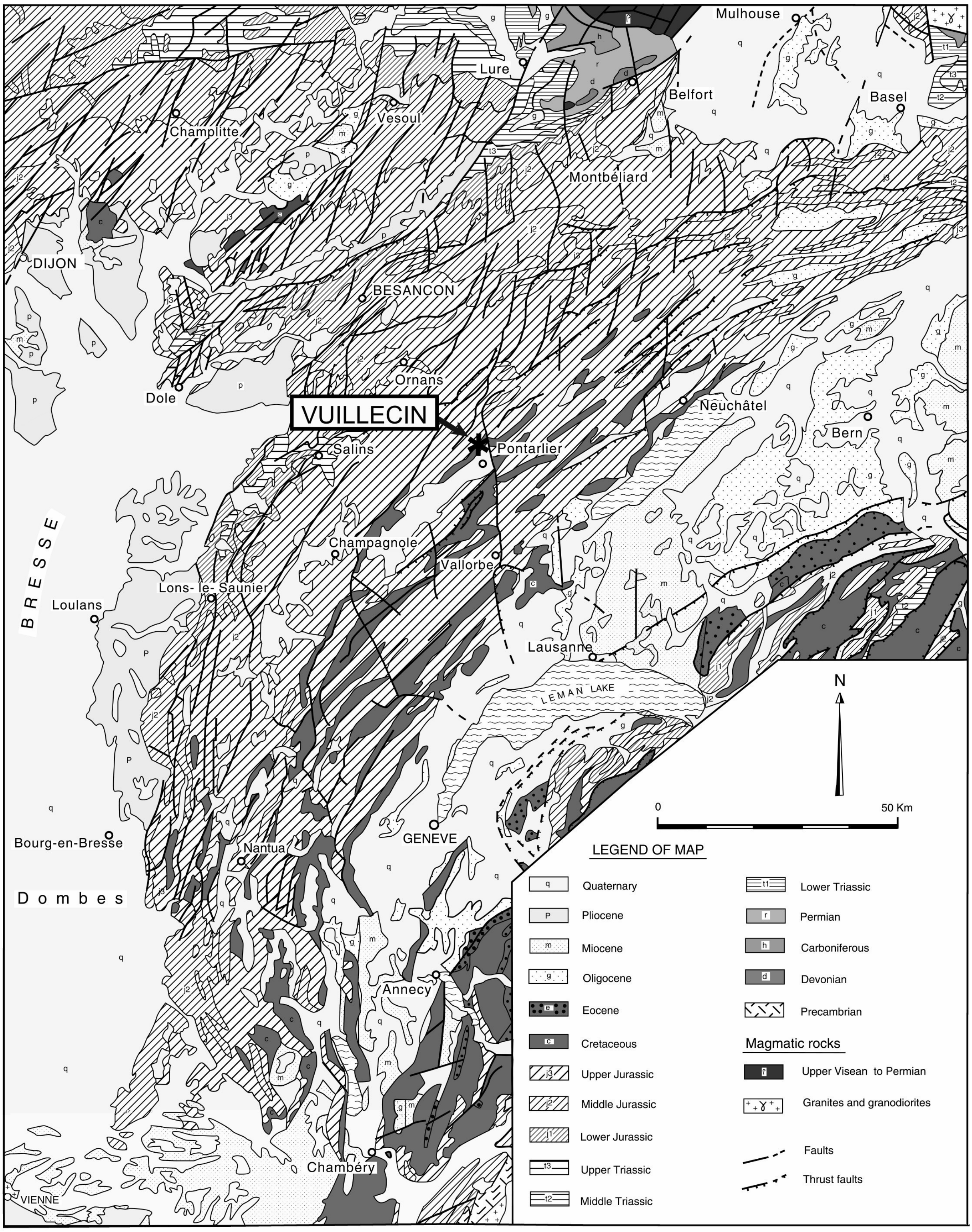

Fig. D – Geographical location of the Vuillecin area on a geological map of Jura Arc.

Appendix B:
Visualization of the porous structure using thin sections of a rock impregnated with a colored resin

Related bibliography: SIZUN J.-P., 1995

The simultaneous visualization of the pore and mineral structure of a rock allows for its porosity structures (pore distribution; localization of pores; total, free and trapped porosity) to be studied with regard to the different minerals. The porosity structures are analyzed on thin sections of the rock impregnated with a colored epoxy.

There are two different types of thin sections. The first one is made from rocks injected under vacuum and then, pressure. During this process all the interconnected pores larger than 0.1 µm are occupied. In the second type, samples are not degassed, the imbibable porosity is filled with red epoxy, and the porosity occupied by air is then filled by spreading blue epoxy on the cut surfaces.

The pore volume accessible to epoxy under vacuum and then under pressure, and the volume invaded by water under vacuum are nearly identical. However, during the double coloration process, the pore volume filled with epoxy by capillarity at atmospheric pressure depends on epoxy viscosity. As water viscosity is lower, the porosity volume invaded by red epoxy is smaller than the volume accessible to water.

These methods make it possible to determine the behavior of the different pore structures during imbibition together with their size and their location with regards to the different minerals. The anisotropy as well as the continuity of the porous network can also be studied.

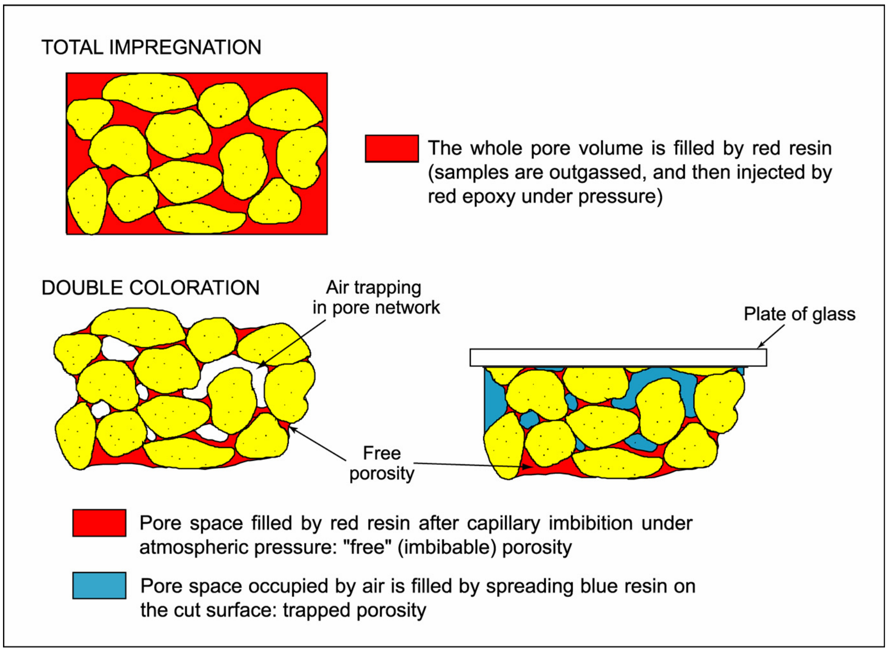

Visualization of the pore structure by total impregnation and double coloration.

Appendix C:
Water porosimetry data

The data exposed below are those of the total water and 48 hours porosity measurements (theories in §2.1.1.) of this study, which were made for sets of cylindrical samples with volumes of about 1-2 cm³ (w_S: dry sample weight; N_W: total water porosity; N_{48}: 48 hours, or free, porosity; $N_{TR,W}$: trapped water porosity; S_{48}: Hirschwald's coefficient).

Fontainebleau sandstone

Sample	w_S	N_W (%)	N_{48} (%)	$N_{TR.\,W}$ (%)	S_{48}
FONT1	161.11	12.37	6.91	5.46	0.56
FONT2	165.62	12.73	7.48	5.25	0.59
FONT3	160.46	12.44	7.04	5.40	0.57
FONT4	165.91	12.25	6.50	5.75	0.53
Average		12.45	6.98	5.47	0.56
σ		0.18	0.35	0.18	0.02
σ_R		1.4%	5.0%	3.3%	3.8%

"Grès à meules" sandstone

Sample	w_S	N_W (%)	N_{48} (%)	$N_{TR.\,W}$ (%)	S_{48}
SGM1	149.44	21.01	14.61	6.40	0.70
SGM2	148.51	21.08	14.69	6.39	0.70
SGM3	151.89	21.26	13.94	7.32	0.66
SGM4	149.62	21.48	13.75	7.73	0.64
Average		21.21	14.25	6.96	0.68
σ		0.18	0.41	0.58	0.03
σ_R		0.8%	2.9%	8.3%	3.8%

Mons chalk

Sample	w_S	N_W (%)	N_{48} (%)	$N_{TR.\,W}$ (%)	S_{48}
MS1	220.90	43.45	40.24	3.21	0.93
MS2	247.13	43.78	40.67	3.11	0.93
MS3	238.53	43.69	40.29	3.41	0.92
MS4	234.40	43.60	40.62	2.97	0.93
MS5	205.17	43.72	40.31	3.41	0.92
MS6	123.99	43.46	40.30	3.15	0.93
MS7	184.25	43.67	40.34	3.34	0.92
MS8	136.77	43.79	40.25	3.53	0.92
MS9	110.22	43.83	40.84	2.99	0.93
MS10	43.46	43.74	41.28	2.46	0.94
MS11	41.05	43.68	41.11	2.57	0.94
Average		43.67	40.57	3.10	0.93
σ		0.12	0.35	0.33	0.01
σ_R		0.3%	0.9%	10.5%	0.8%

Tuffeau limestone

Sample	w_S	N_W (%)	N_{48} (%)	$N_{TR.\ W}$ (%)	S_{48}
Tuf1	94.96	46.53	35.20	11.33	0.76
Tuf2	97.73	45.60	42.04	3.56	0.92
Tuf3	86.90	46.80	39.35	7.45	0.84
Tuf4	90.05	47.69	40.19	7.50	0.84
Tuf5	92.71	46.46	36.39	10.07	0.84
Tuf6	94.17	44.90	37.15	7.75	0.83
Tuf7	94.68	46.17	38.25	7.92	0.83
Average		46.31	38.37	7.94	0.84
σ		0.82	2.18	2.26	0.04
σ_R		1.8%	5.7%	28.4%	5.3%

Vuillecin limestone

Sample	w_S	N_W (%)	N_{48} (%)	$N_{TR.\ W}$ (%)	S_{48}
VUI1	161.49	12.37	8.67	3.70	0.70
VUI2	168.20	11.12	7.82	3.30	0.70
VUI3	165.83	11.43	8.31	3.12	0.73
VUI4	140.15	10.54	7.51	3.03	0.71
VUI5	164.50	11.89	8.36	3.53	0.70
VUI6	153.34	11.77	8.49	3.28	0.72
VUI7	161.24	12.37	8.66	3.71	0.70
VUI8	164.18	12.67	8.64	4.03	0.68
Average		11.77	8.31	3.46	0.71
σ		0.67	0.40	0.32	0.01
σ_R		5.7%	4.8%	9.2%	2.0%

Appendix D:
Mercury porosimetry data reduction

Total specific pore volume

At each equilibrium i under pressure P^i, the intruded volume of mercury V_p' is measured. When the pressure is increased to its maximum, the total volume of mercury injected into the sample corresponds to the total pore volume V_p^{tot} and to the total specific pore volume $V^*_{P,Hg}$, which is the total pore volume normalized to the sample weight (w_S).

Bulk density

The bulk volume V_B is the sum of the volumes of the solid matter and the voids. It is calculated as the internal volume of the penetrometer V_{PN} minus the volume of mercury inside it:

$$V_B = V_{PN} - \frac{w_{Hg+S+PN} - w_S - w_{PN}}{\rho_{Hg}} \quad \textit{(D1)}$$

with $w_{Hg+S+PN}$ the weight of the system mercury-sample-penetrometer, W_{PN} the weight of the penetrometer, w_S the dry sample weight, and ρ_{Hg} the density of mercury.

The bulk density of the sample is given by the ratio:

$$d_B = \frac{w_S}{V_B} \quad \textit{(D2)}$$

Apparent skeletal density

The skeletal volume is the solid volume of the sample. It is the difference between the bulk volume V_B and the total pore volume V_p^{tot}. The apparent skeletal density, also called mineral density ($d_{M,Hg}$), is given by the ratio:

$$d_{M,Hg} = \frac{w_S}{V_B - V_p^{tot}} \quad \textit{(D3)}$$

Total porosity

The total porosity N_{Hg} of a sample (expressed in %) is calculated as followed:

$$N_{Hg} = 100 \times V^*_{p,Hg} \times d_B \quad \textit{(D4)}$$

where d_B is the calculated bulk density of the sample, and $V^*_{p,Hg}$ the total specific pore volume.

Specific surface area

Between two equilibriums i and i-1 under pressure P^i and P^{i-1}, respectively, the incremental pore surface area δS is determined using the relation:

$$\delta S = \frac{4 \times \left(V_p^i - V_p^{i-1}\right)}{D} \quad \textit{(D5)}$$

in which $D = \frac{D^{i-1} + D^{i}}{2}$, D^{i-1} and D^{i} Washburn's diameters at P^{i-1} and P^{i}, respectively.

At the maximum pressure, the sum of the incremental areas divided by the sample weight gives the total specific surface area:

$$S_{Hg} = \frac{\sum \delta S}{w_S} \qquad (D6)$$

Median (D_{50}) and average (D_{AV}) pore diameter

Several methods are commonly used to calculate mean pore diameters from mercury porosimetry data (Paul A. WEBB, 2001). Two of them were retained for our study: the determination of the median pore diameter and the average pore diameter. The terminology is that proposed by Micromeritics Instrument Corporation (Autopore III, Operator's Manual, 1998).

The injection of 50% of the total volume of mercury occurs at the interpolated pressure P_{50}. According to Washburn's relation, P_{50} corresponds to a diameter D_{50}, called the median pore diameter:

$$D_{50} = \frac{-4\gamma \cos\theta}{P_{50}} \qquad (D7)$$

The average pore diameter D_{AV} is determined from the results of the total specific pore volume and the total specific surface area and using the relationship between the volume and the surface in a cylinder:

$$D_{AV} = \frac{4V^{*}_{p,Hg}}{S_{Hg}} \qquad (D8)$$

Hydraulic diameter D_H

It is determined from the cumulative intrusion volume versus pore access diameter curve. Various methods were proposed by some authors. These methods include the inflection point or the point of intersection of the tangents, either at the basis or at the top of the intrusion curve (DULLIEN F.A.L., 1979; KATZ & THOMPSON, 1987; MERTZ J.D., 1991; PITTMAN E.D., 1992; ROUSSET TOURNIER B., 2001).

For our study, the hydraulic diameter D_H was calculated from the equations of the secant tangents at the basis of the curve (Fig. A). In this case, the hydraulic (or threshold) diameter can be defined as the greatest access diameter from which mercury begins to fill the main part of the porous network (unimodal pore access distribution).

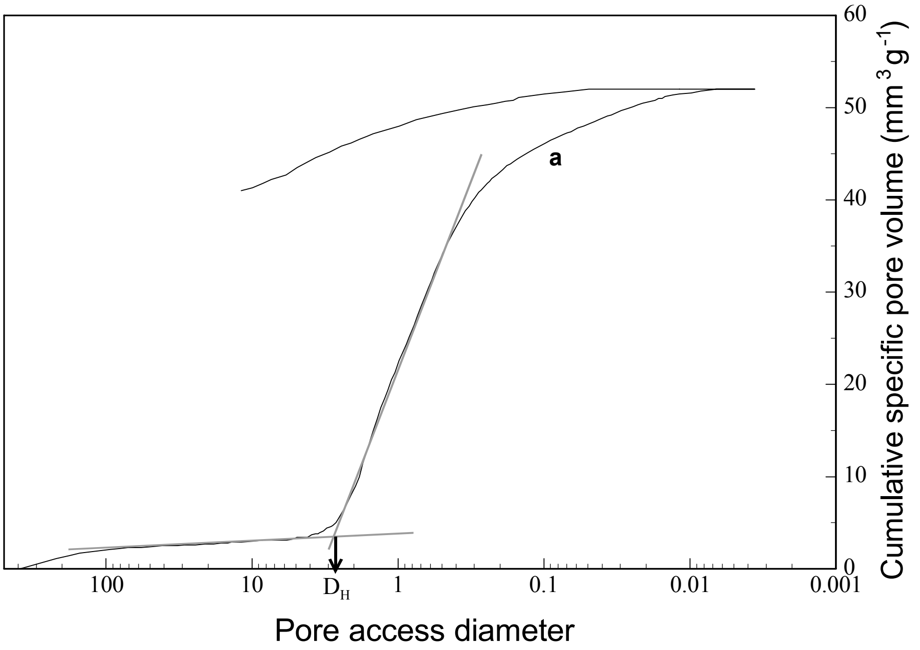

Fig. A – Graphical determination of the hydraulic diameter D_H from the mercury injection curve (a) of a Vuillecin limestone sample.

Appendix E:

Examples of mercury/solid surface contact angles

The following table summarizes values of contact angles for several natural minerals (CARLOS A. LEÓN y LEÓN, 1998):

Mineral	Contact angle (°)
Alkali borosilicate glass	153
Aluminium oxide	127.142
Calcite	146
Carbon	155.162
Cement	125
Clay minerals	139-147
Coal	142
Glass	135-140
Mica	126
Nickel	130
Oxide-type surfaces	140
Paraffin wax	149
Pyrite	146
Quartz	132-147
Steel	154
Titanium dioxide	141.160
Zinc oxide	141

Appendix F:
Gas adsorption isotherms and BET specific surface area reports

Fontainebleau sandstone

Sample FS7

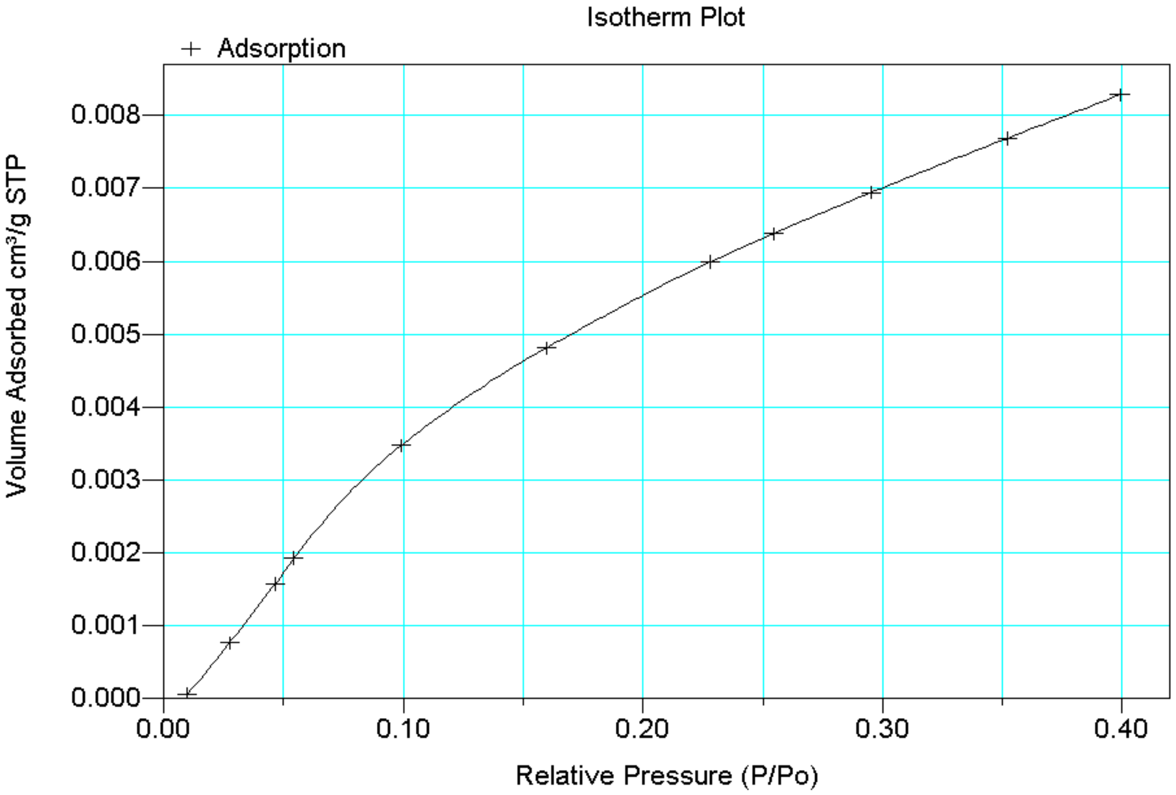

BET Surface Area Report

BET Surface Area : 0.0163 ± 0.0022 m^2/g
Slope : 130.411142 ± 8.798419
Y-Intercept : 20.309368 ± 1.767184
c_0 : 7.421.231
V_M : 0.006635 cm^3/g STP
Correlation Coefficient: 9.910189e-01

Molecular Cross-section: 0.2100 nm^2

Relative Pressure	Vol Adsorbed (cm^3/g STP)	1/ [VA*(Po/P - 1)]
0.054157633	0.0019	29.754.878
0.099086979	0.0035	31.683.153
0.159559749	0.0048	39.476.456
0.227970438	0.0060	49.315.479
0.254404015	0.0064	53.500.819
0.295207993	0.0069	60.324.009

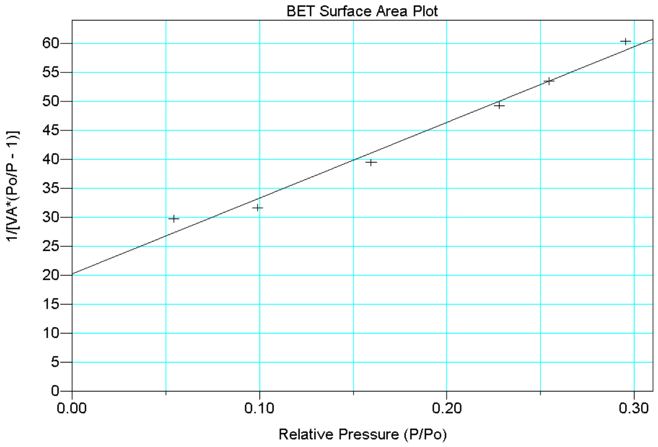

Sample FS9

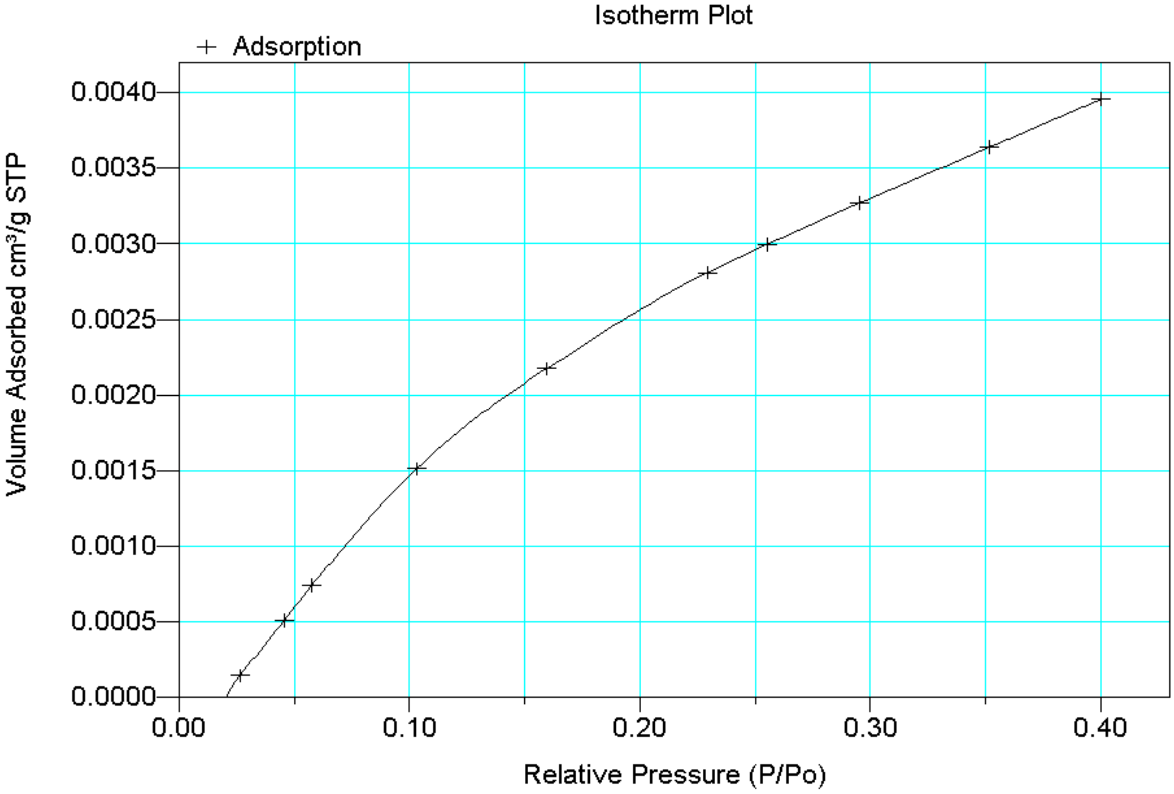

BET Surface Area Report

BET Surface Area : 0.0159 ± 0.0029 m²/g
Slope : 208.569269 ± 35.909087
Y-Intercept : 60.727743 ± 7.242846
c_0 : 4.434.497
V_M : 0.003713 cm³/g STP
Correlation Coefficient: 9.455158e-01

Molecular Cross-section: 0.2100 nm²

Relative Pressure	Vol Adsorbed (cm³/g STP)	1/ [VA*(Po/P - 1)]
0.057585595	0.0007	82.404.765
0.102949328	0.0015	75.871.725
0.159526424	0.0022	87.255.635
0.229177793	0.0028	105.811.890
0.255058203	0.0030	114.276.962
0.295221436	0.0033	128.071.307

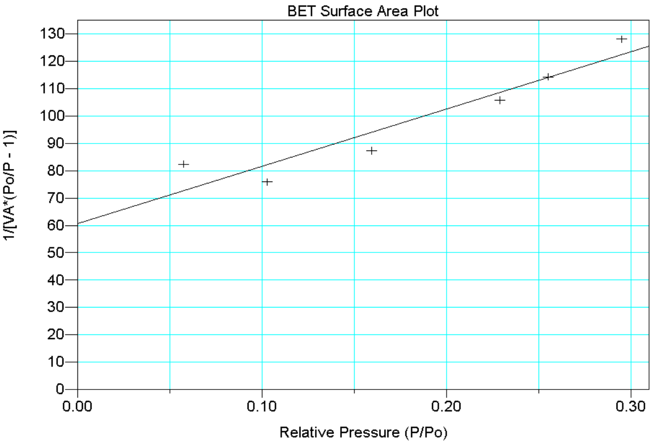

Sample FS102

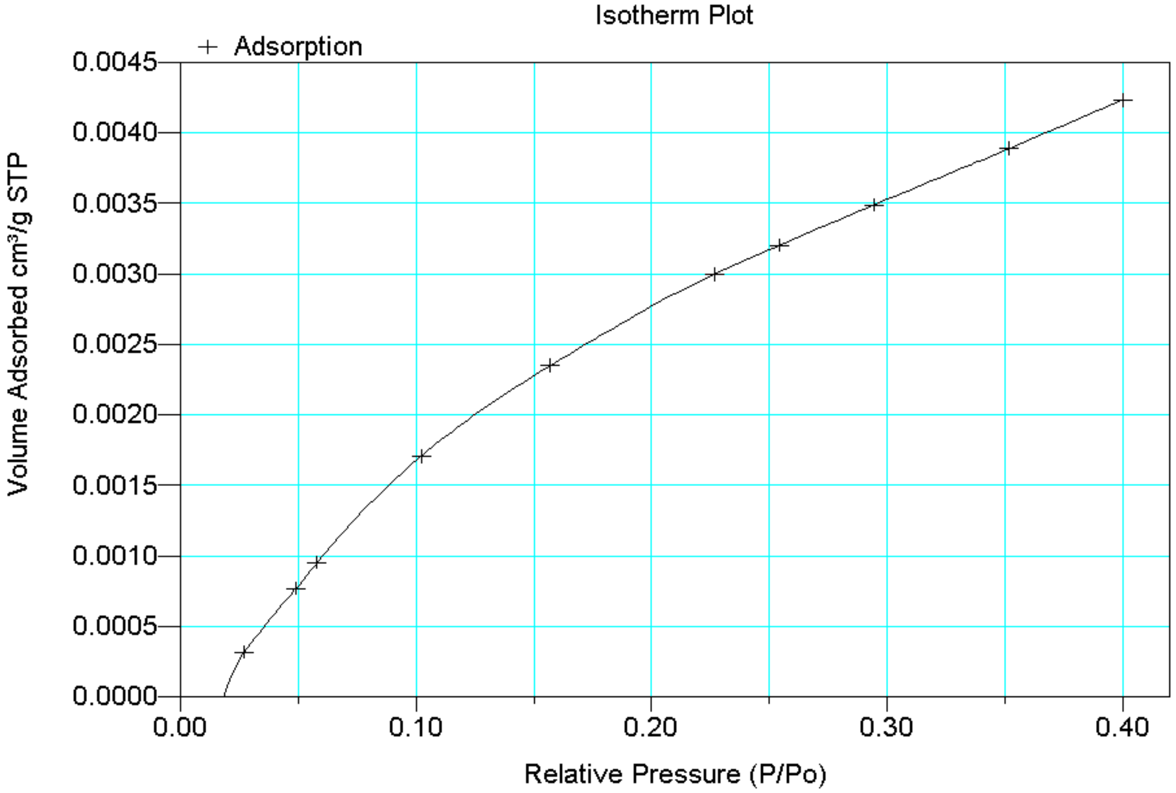

BET Surface Area Report

BET Surface Area : 0.0136 ± 0.0014 m²/g
Slope : 304.444696 ± 20.136976
Y-Intercept : 45.223319 ± 4.035946
c_0 : 6.316.830
V_M : 0.003501 cm³/g STP
Correlation Coefficient: 9.862607e-01

Molecular Cross-section: 0.2100 nm²

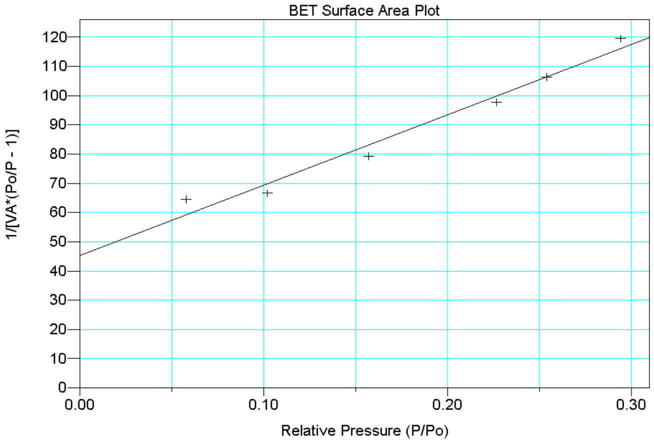

Relative Pressure	Vol Adsorbed (cm³/g STP)	1/ [VA*(Po/P - 1)]
0.057925960	0.0010	64.455.142
0.102113477	0.0017	66.601.347
0.157108817	0.0024	79.266.420
0.226609568	0.0030	97.731.853
0.254138447	0.0032	106.391.770
0.294306303	0.0035	119.507.698

Sample FS105

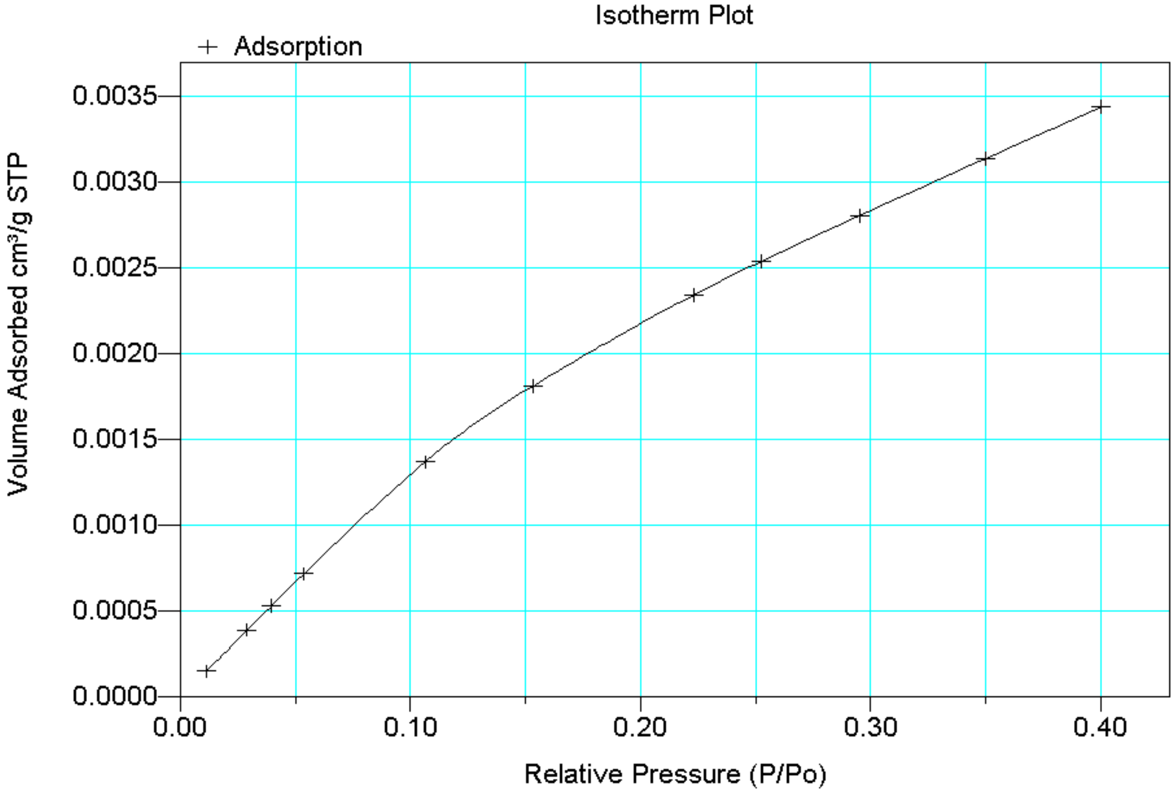

BET Surface Area Report

BET Surface Area : 0.0138 ± 0.0009 m²/g
Slope : 296.586915 ± 19.404604
Y-Intercept : 58.098097 ± 3.865207
c_0 : 6.104.933
V_M : 0.002819 cm³/g STP
Correlation Coefficient: 9.915472e-01

Molecular Cross-section: 0.2100 nm²

Relative Pressure	Vol Adsorbed (cm³/g STP)	1/ [VA*(Po/P - 1)]
0.053786442	0.0007	79.100.955
0.106204887	0.0014	86.708.255
0.153017458	0.0018	99.670.100
0.223090024	0.0023	122.487.372
0.252275220	0.0025	132.830.456
0.295062160	0.0028	149.124.445

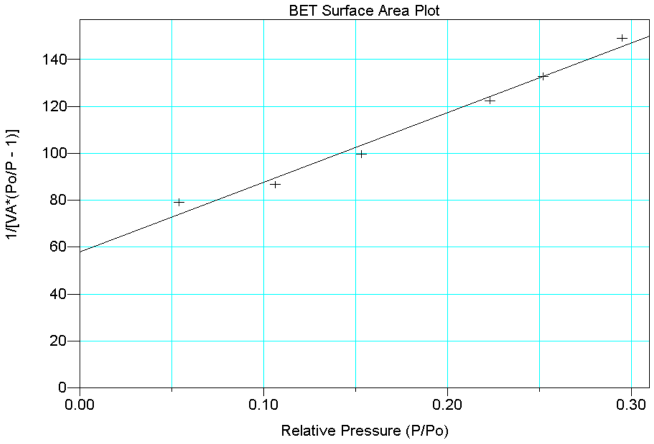

Sample FS107

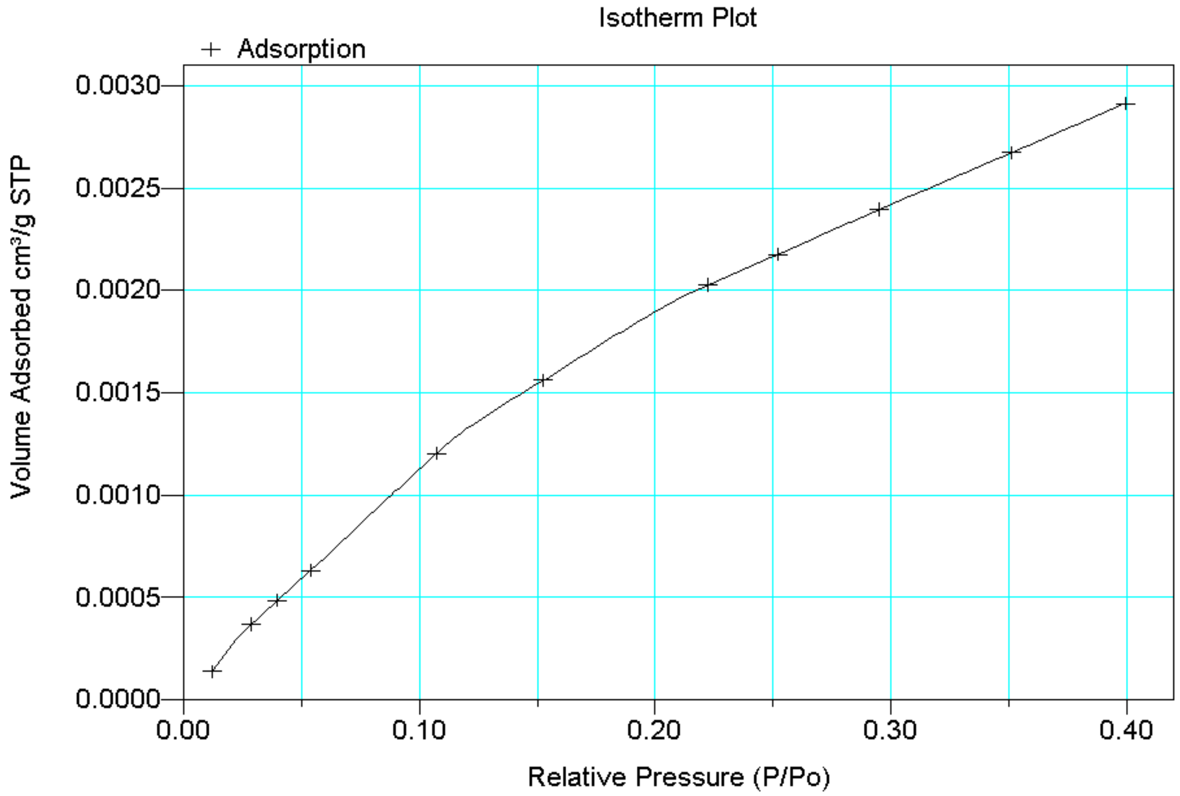

BET Surface Area Report

BET Surface Area : 0.0134 ± 0.0007 m^2/g
Slope : 357.544527 ± 23.202197
Y-Intercept : 64.772314 ± 4.618353
c_0 : 6.520.021
V_M : 0.002368 cm^3/g STP
Correlation Coefficient: 9.916827e-01

Molecular Cross-section: 0.2100 nm^2

Relative Pressure	Vol Adsorbed (cm^3/g STP)	1/ [VA*(Po/P - 1)]
0.053708897	0.0006	89.804.312
0.107271846	0.0012	99.840.428
0.152640847	0.0016	115.406.111
0.222445756	0.0020	141.165.383
0.252033594	0.0022	154.877.309
0.295002764	0.0024	174.798.142

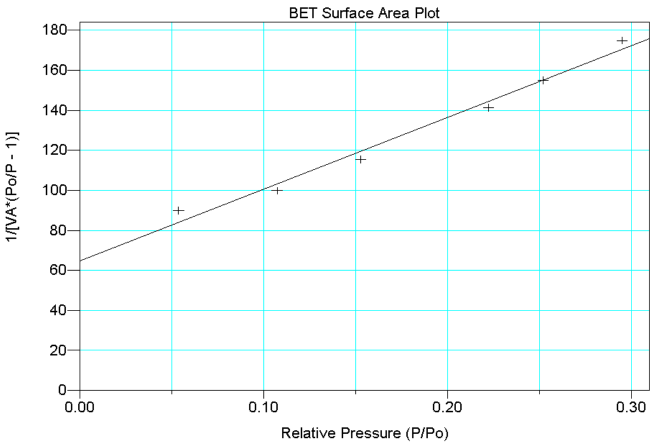

“Grès à Meules” sandstone

Sample GM01

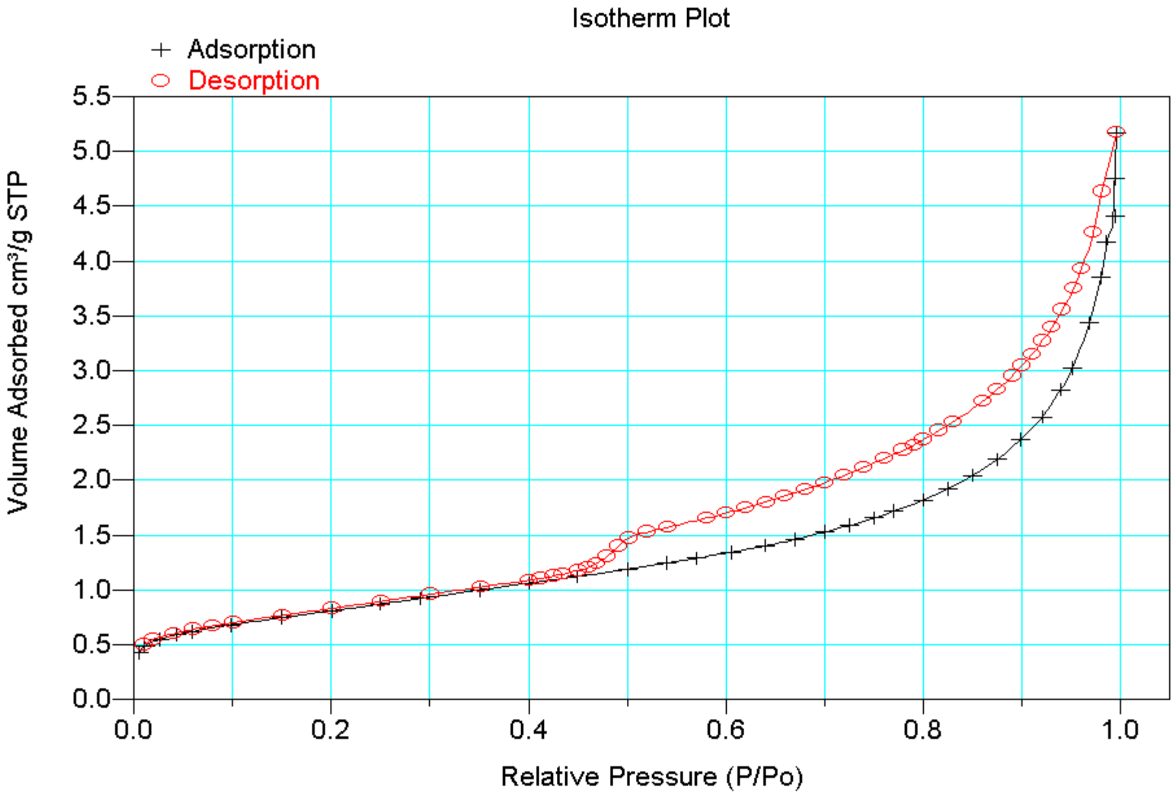

BET Surface Area Report

BET Surface Area : 2.9719 ± 0.0081 m²/g
Slope : 1.476681 ± 0.004056
Y-Intercept : 0.014297 ± 0.000780
c_0 : 104.289.473
V_M : 0.670701 cm³/g STP
Correlation Coefficient: 9.999849e-01

Molecular Cross-section: 0.1620 nm²

Relative Pressure	Vol Adsorbed (cm³/g STP)	1/ [VA*(Po/P - 1)]
0.059029178	0.6215	0.100938
0.098006888	0.6790	0.160025
0.149725941	0.7479	0.235453
0.200225871	0.8092	0.309379
0.249781233	0.8705	0.382475
0.289891839	0.9213	0.443093

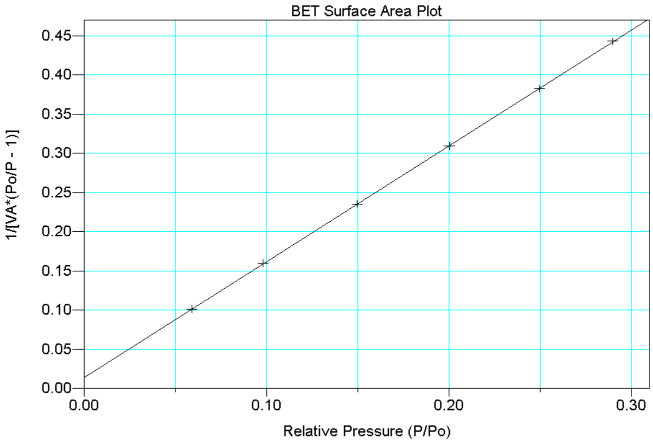

Sample GM02

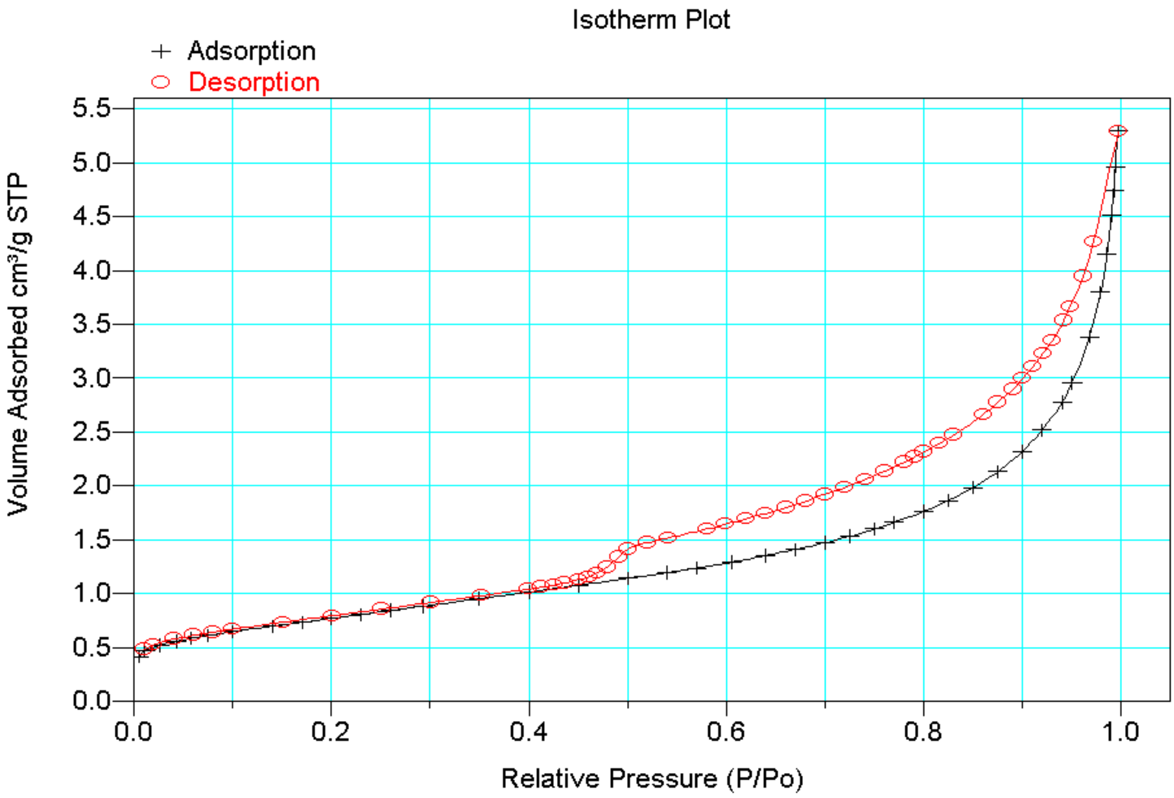

BET Surface Area Report

BET Surface Area : 2.8146 ± 0.0059 m²/g
Slope : 1.540533 ± 0.003229
Y-Intercept : 0.016587 ± 0.000603
c_0 : 93.878.241
V_M : 0.642211 cm³/g STP
Correlation Coefficient: 9.999846e-01

Molecular Cross-section: 0.1620 nm²

Relative Pressure	Vol Adsorbed (cm³/g STP)	1/ [VA*(Po/P - 1)]
0.058203335	0.5880	0.105109
0.074465110	0.6131	0.131222
0.099832079	0.6470	0.171421
0.139994284	0.6988	0.232936
0.170144831	0.7347	0.279069
0.199971644	0.7701	0.324588
0.229986718	0.8066	0.370294
0.260273724	0.8440	0.416873
0.292385303	0.8839	0.467476

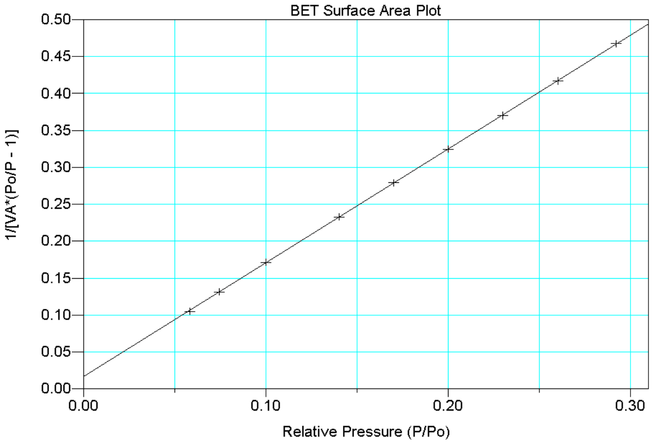

Sample GM03

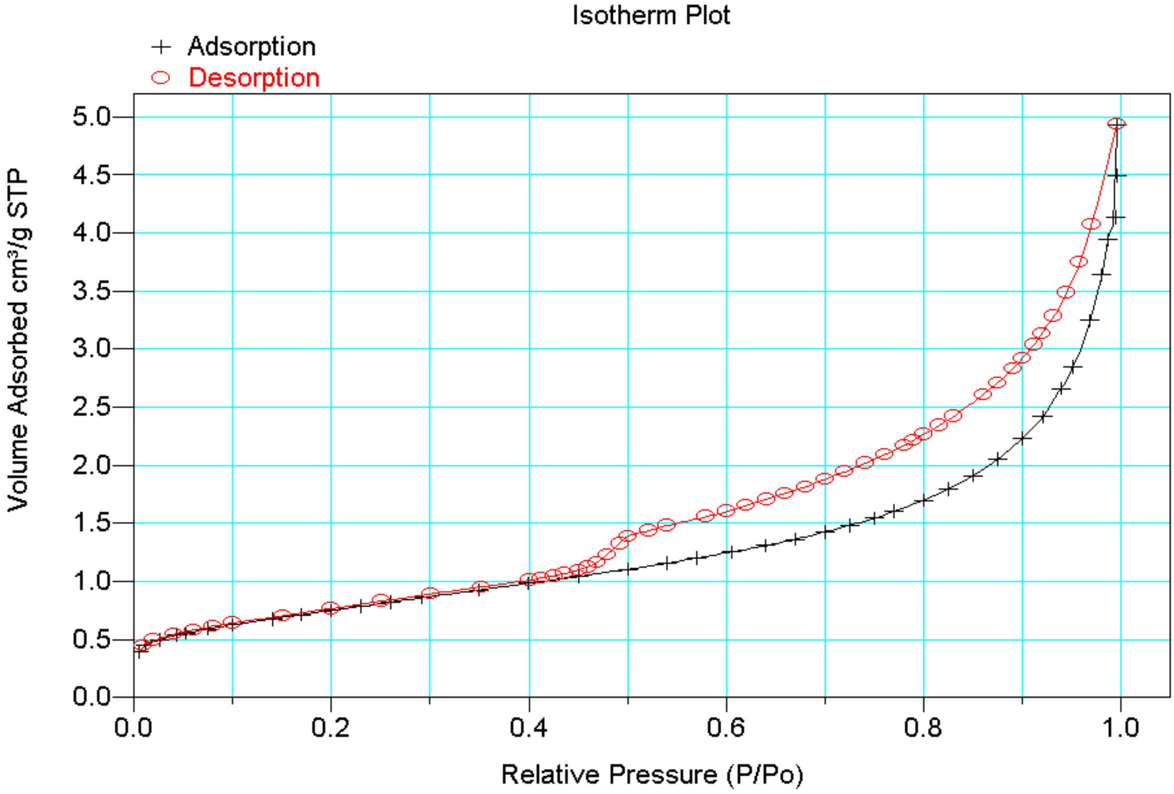

BET Surface Area Report

BET Surface Area : 2.1036 ± 0.0080 m^2/g
Slope : 1.649928 ± 0.004619
Y-Intercept : 0.018408 ± 0.000861
c_0 : 86.826.370
V_M : 0.625651 cm^3/g STP
Correlation Coefficient: 9.999701e-01

Molecular Cross-section: 0.1620 nm^2

Relative Pressure	Vol Adsorbed (cm³/g STP)	1/ [VA*(Po/P - 1)]
0.052062037	0.5548	0.098999
0.074325390	0.5900	0.136096
0.099763292	0.6261	0.176988
0.139995159	0.6761	0.240764
0.170000040	0.7120	0.287650
0.200093918	0.7476	0.334587
0.230193112	0.7850	0.380922
0.260091606	0.8206	0.428357
0.292068908	0.8585	0.480582

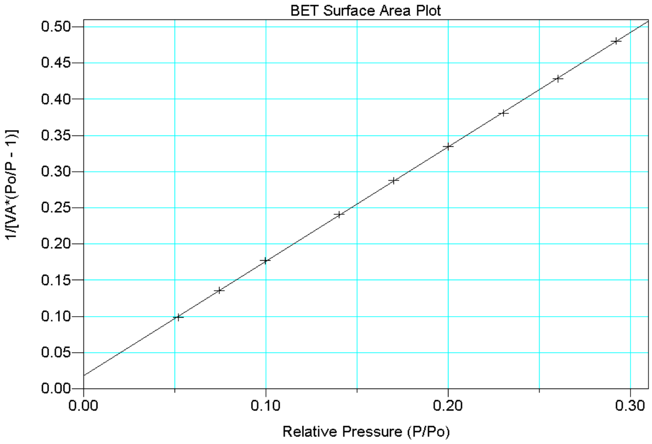

Sample GM04

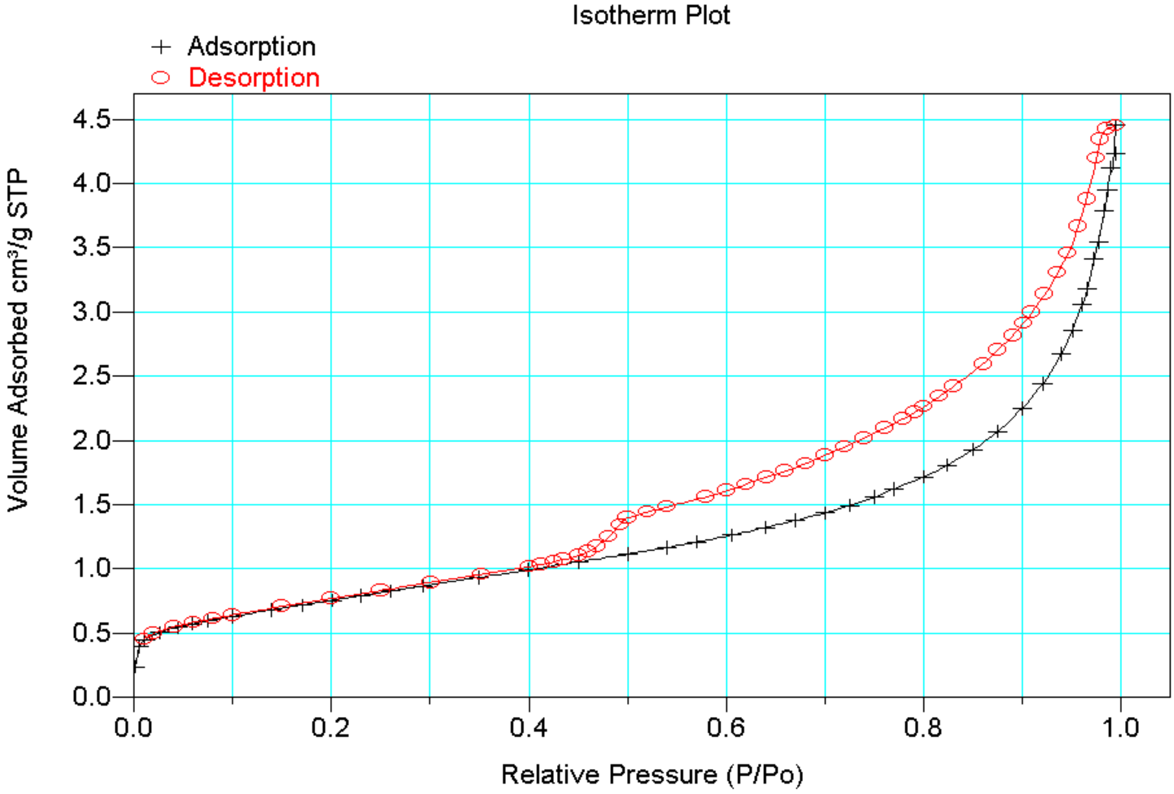

BET Surface Area Report

BET Surface Area : 2.7903 ± 0.0071 m²/g
Slope : 1.563953 ± 0.004014
Y-Intercept : 0.018842 ± 0.000749
c_0 : 84.004.402
V_M : 0.631794 cm³/g STP
Correlation Coefficient: 9.999769e-01

Molecular Cross-section: 0.1620 nm²

Relative Pressure	Vol Adsorbed (cm³/g STP)	1/ [VA*(Po/P - 1)]
0.059362248	0.5720	0.110332
0.074618043	0.5963	0.135218
0.100315555	0.6312	0.176655
0.139426348	0.6808	0.237962
0.170129132	0.7177	0.285640
0.200212637	0.7535	0.332245
0.230094208	0.7903	0.378156
0.260202580	0.8282	0.424670
0.292192956	0.8670	0.476158

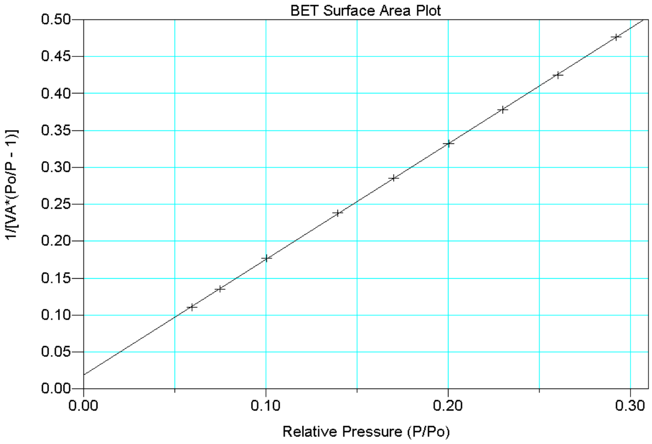

Sample GM05

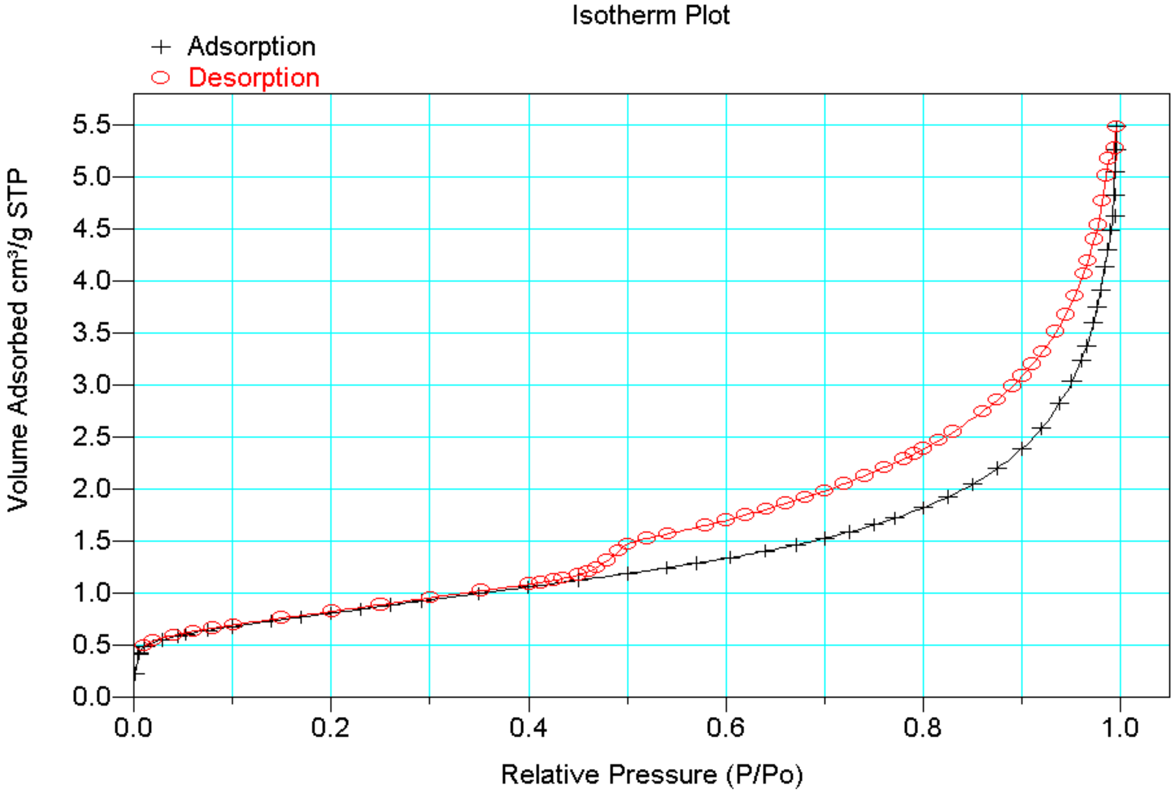

BET Surface Area Report

BET Surface Area : 3.6121 ± 0.0069 m²/g
Slope : 1.430326 ± 0.003458
Y-Intercept : 0.015331 ± 0.000645
c_0 : 96.842.340
V_M : 0.673556 cm³/g STP
Correlation Coefficient: 9.999806e-01

Molecular Cross-section: 0.1620 nm²

Relative Pressure	Vol Adsorbed (cm³/g STP)	1/ [VA*(Po/P - 1)]
0.051976783	0.6066	0.090383
0.074162828	0.6434	0.124494
0.099875207	0.6798	0.163225
0.139812414	0.7341	0.221400
0.169969919	0.7719	0.265296
0.200093300	0.8090	0.309194
0.230301748	0.8472	0.353164
0.260301967	0.8863	0.397057
0.292070814	0.9271	0.445030

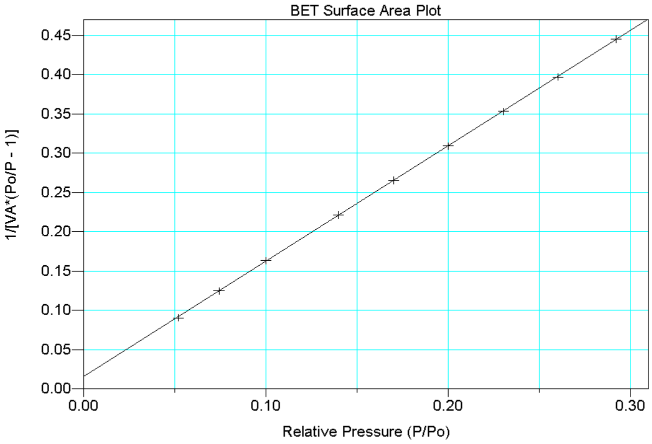

Mons chalk

Sample CM01

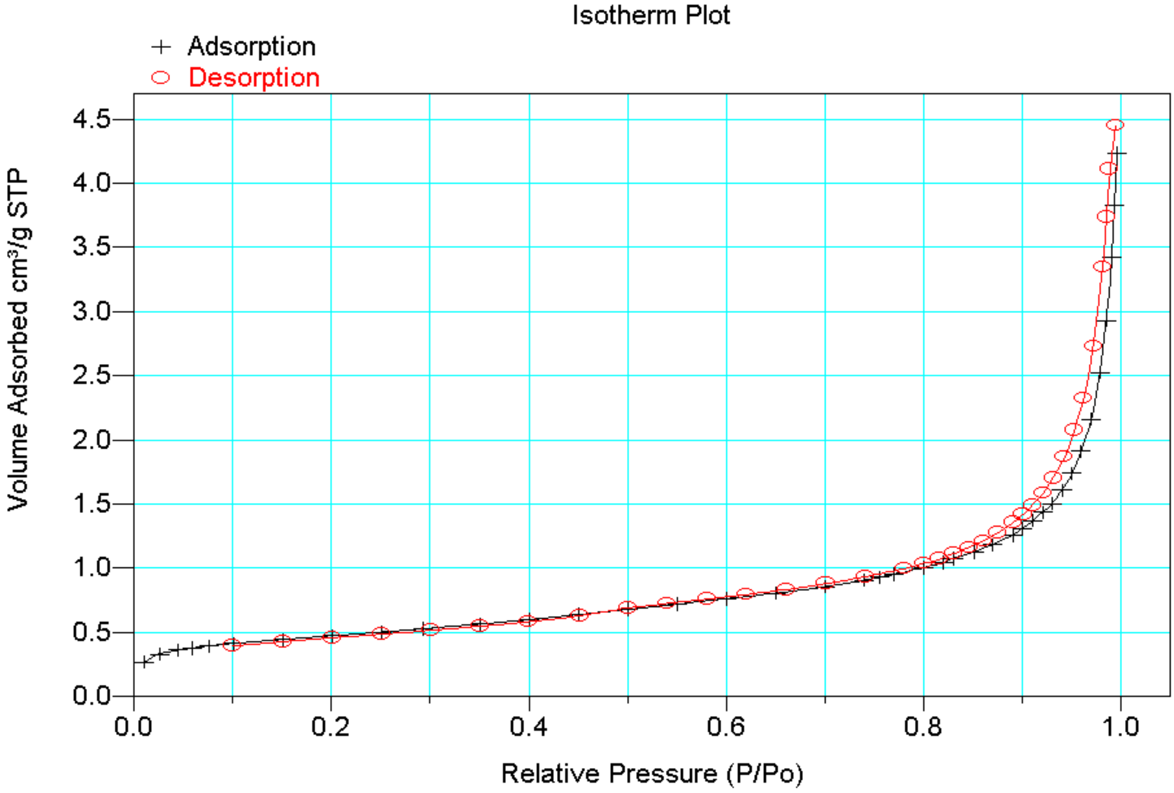

BET Surface Area Report

BET Surface Area : 1.855 ± 0.0131 m²/g
Slope : 2.633581 ± 0.020680
Y-Intercept : 0.006630 ± 0.003755
c_0 : 398.193.710
V_M : 0.378758 cm³/g STP
Correlation Coefficient: 9.998459e-01

Molecular Cross-section: 0.1620 nm²

Relative Pressure	Vol Adsorbed (cm³/g STP)	1/ [VA*(Po/P - 1)]
0.059465639	0.3779	0.167313
0.075900672	0.3943	0.208328
0.100437301	0.4135	0.269987
0.150367451	0.4439	0.398691
0.200570801	0.4741	0.529236
0.250769343	0.5025	0.666051
0.292684998	0.5283	0.783270

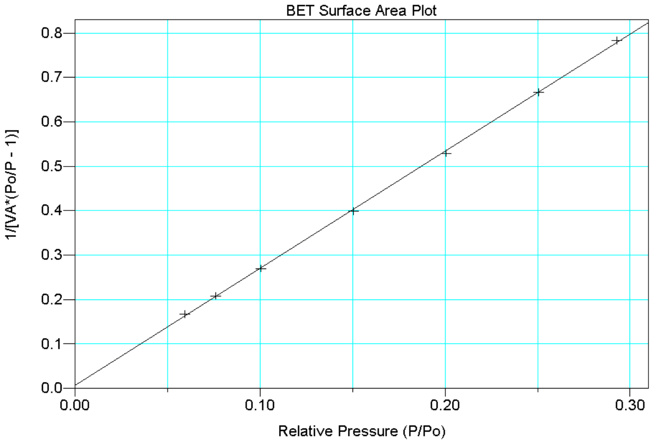

Sample CM02

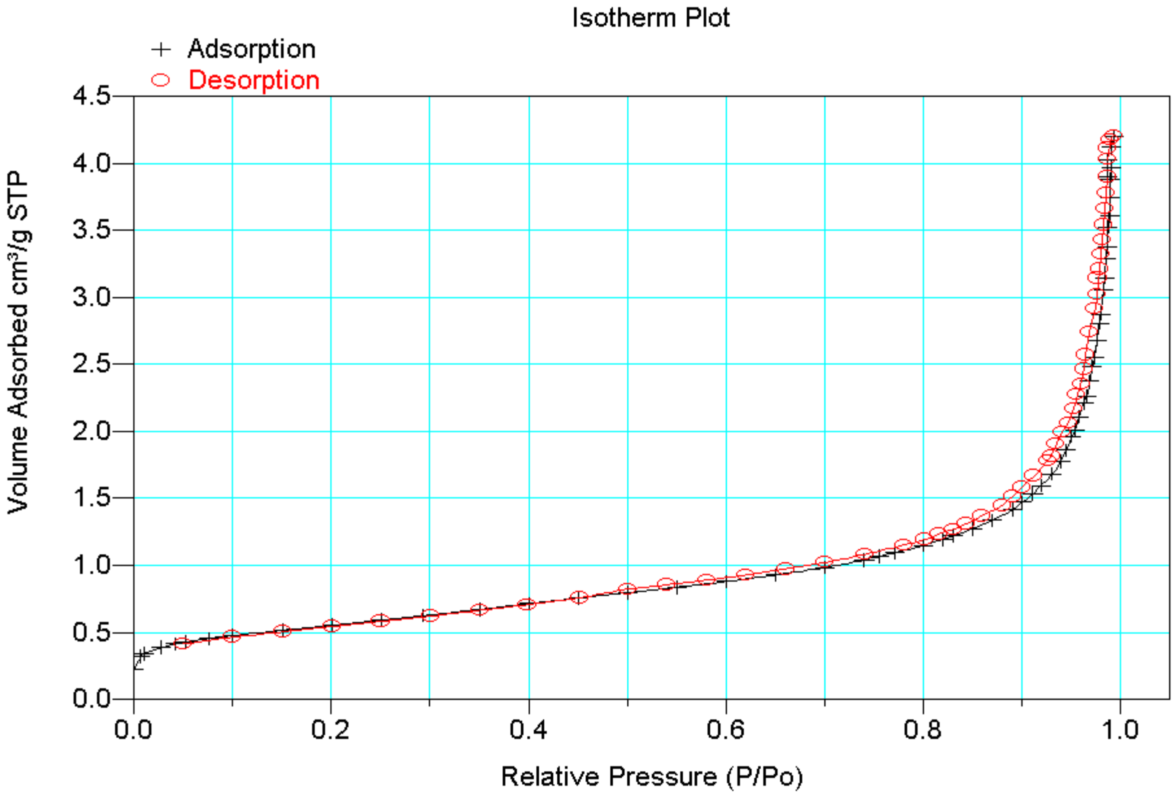

BET Surface Area Report

BET Surface Area : 2.005 ± 0.007916 m^2/g
Slope : 2.214853 ± 0.008869
Y-Intercept : 0.011535 ± 0.001607
c_0 : 193.015.317
V_M : 0.449158 cm^3/g STP
Correlation Coefficient: 9.999599e-01

Molecular Cross-section: 0.1620 nm^2

Relative Pressure	Vol Adsorbed (cm^3/g STP)	1/ [VA*(Po/P - 1)]
0.052319434	0.4285	0.128846
0.075679242	0.4545	0.180130
0.100279254	0.4779	0.233197
0.150429904	0.5159	0.343239
0.200460365	0.5534	0.453014
0.250577954	0.5909	0.565824
0.292744992	0.6246	0.662645

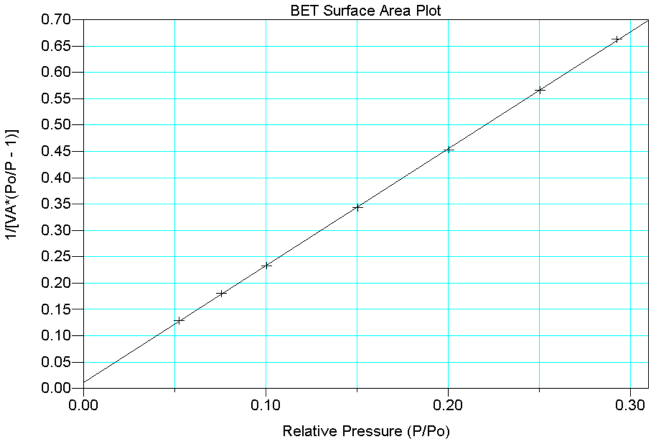

Sample CM03

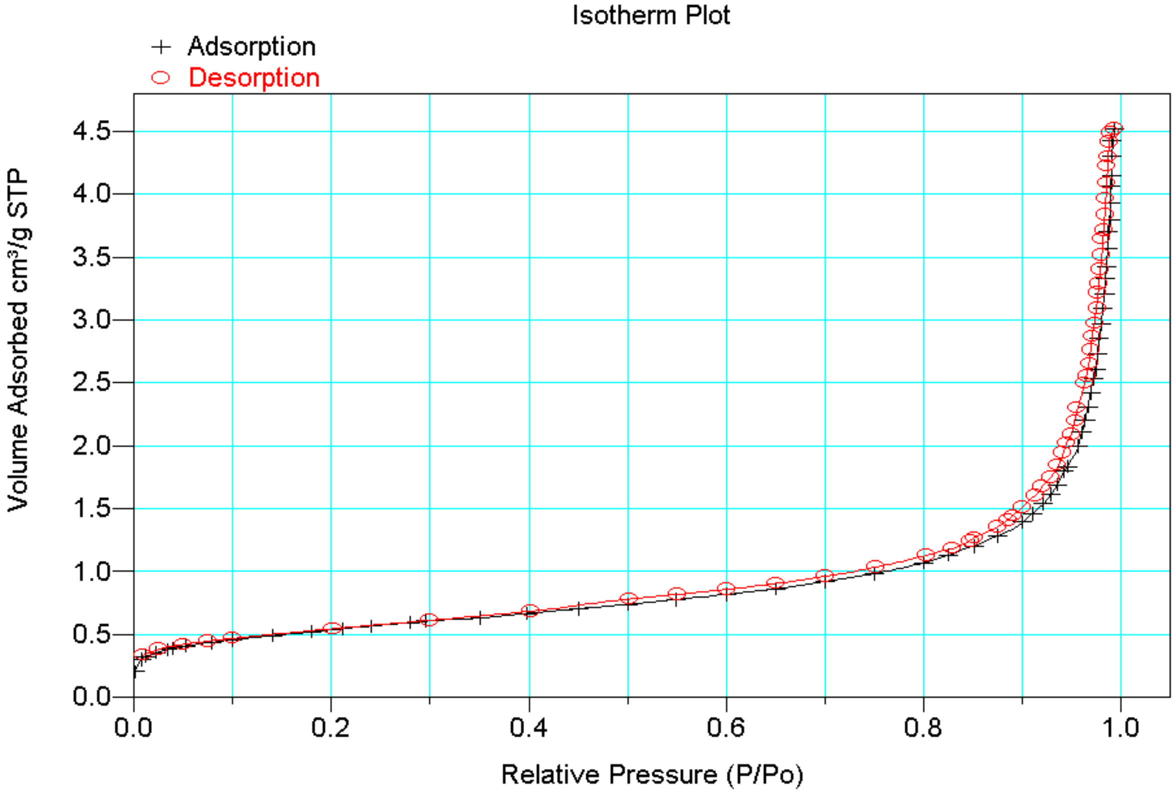

BET Surface Area Report

BET Surface Area	: 1.950 ± 0.01084 m^2/g
Slope	: 2.276977 ± 0.012834
Y-Intercept	: 0.013820 ± 0.002491
c_0	: 165.764.741
V_M	: 0.436529 cm^3/g STP

Correlation Coefficient: 9.998888e-01

Molecular Cross-section: 0.1620 nm^2

Relative Pressure	Vol Adsorbed (cm³/g STP)	1/ [VA*(Po/P - 1)]
0.052022125	0.4085	0.134324
0.079099734	0.4382	0.196016
0.100265078	0.4590	0.242797
0.140327122	0.4922	0.331670
0.180181448	0.5222	0.420870
0.211036288	0.5453	0.490506
0.240021599	0.5666	0.557410
0.279928545	0.5949	0.653452
0.295648841	0.6069	0.691610

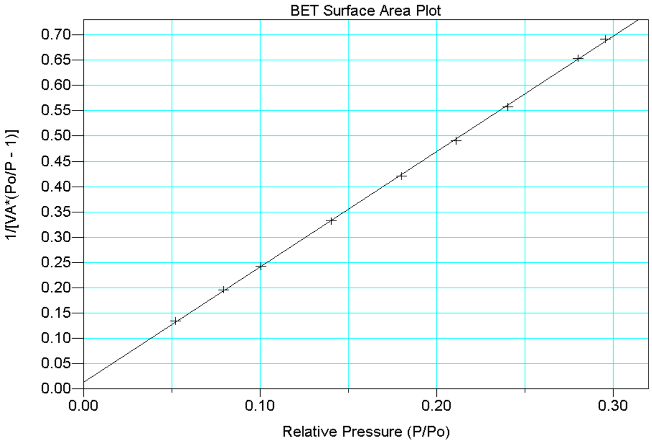

Sample CM04

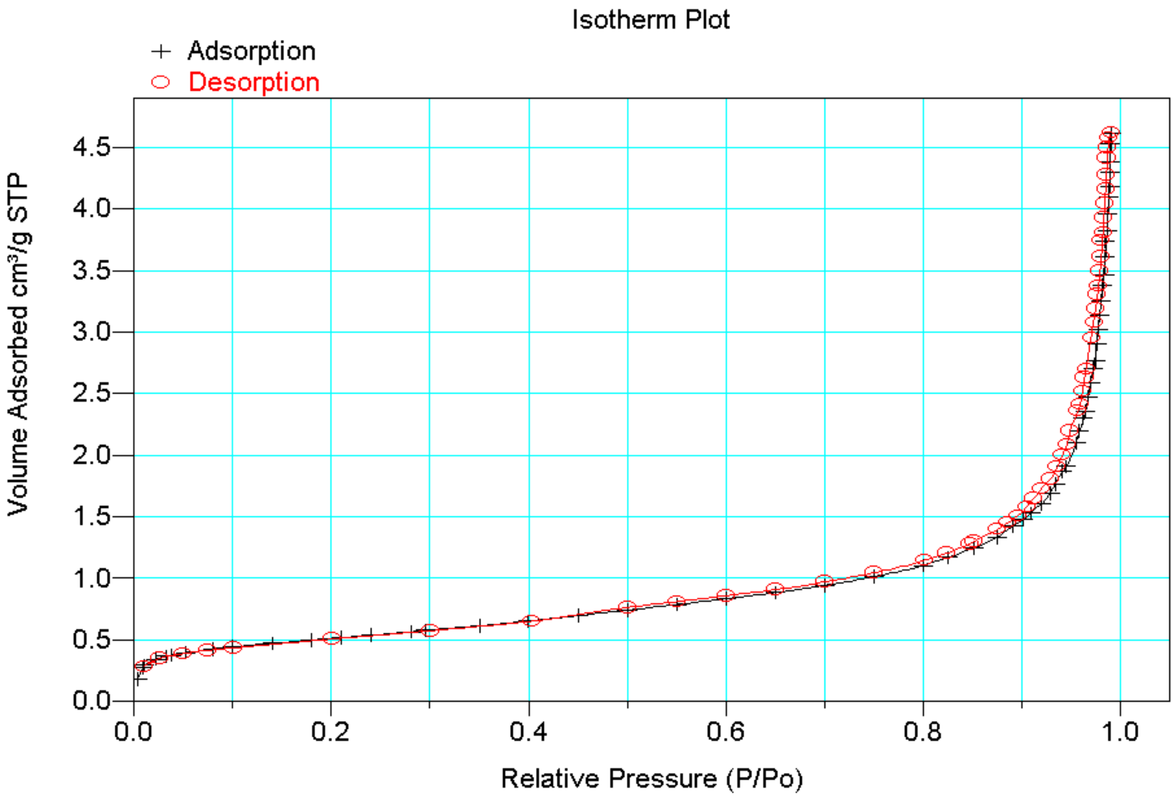

BET Surface Area Report

BET Surface Area : 1.900 ± 0.01057 m^2/g
Slope : 2.413740 ± 0.014001
Y-Intercept : 0.009460 ± 0.002719
c_0 : 256.160.481
V_M : 0.412677 cm^3/g STP
Correlation Coefficient: 9.998823e-01

Molecular Cross-section: 0.1620 nm^2

Relative Pressure	Vol Adsorbed (cm³/g STP)	1/ [VA*(Po/P - 1)]
0.052517607	0.3962	0.139900
0.079596219	0.4257	0.203157
0.100127889	0.4428	0.251304
0.140171398	0.4724	0.345107
0.180010597	0.4985	0.440373
0.210436576	0.5193	0.513273
0.240368374	0.5387	0.587395
0.280627574	0.5656	0.689755
0.295770798	0.5772	0.727683

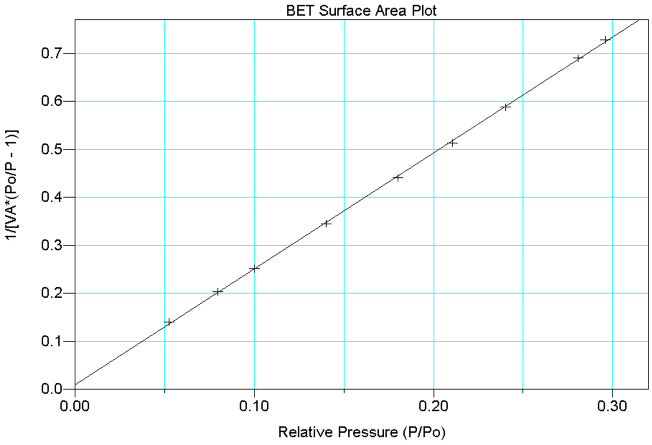

Sample CM05

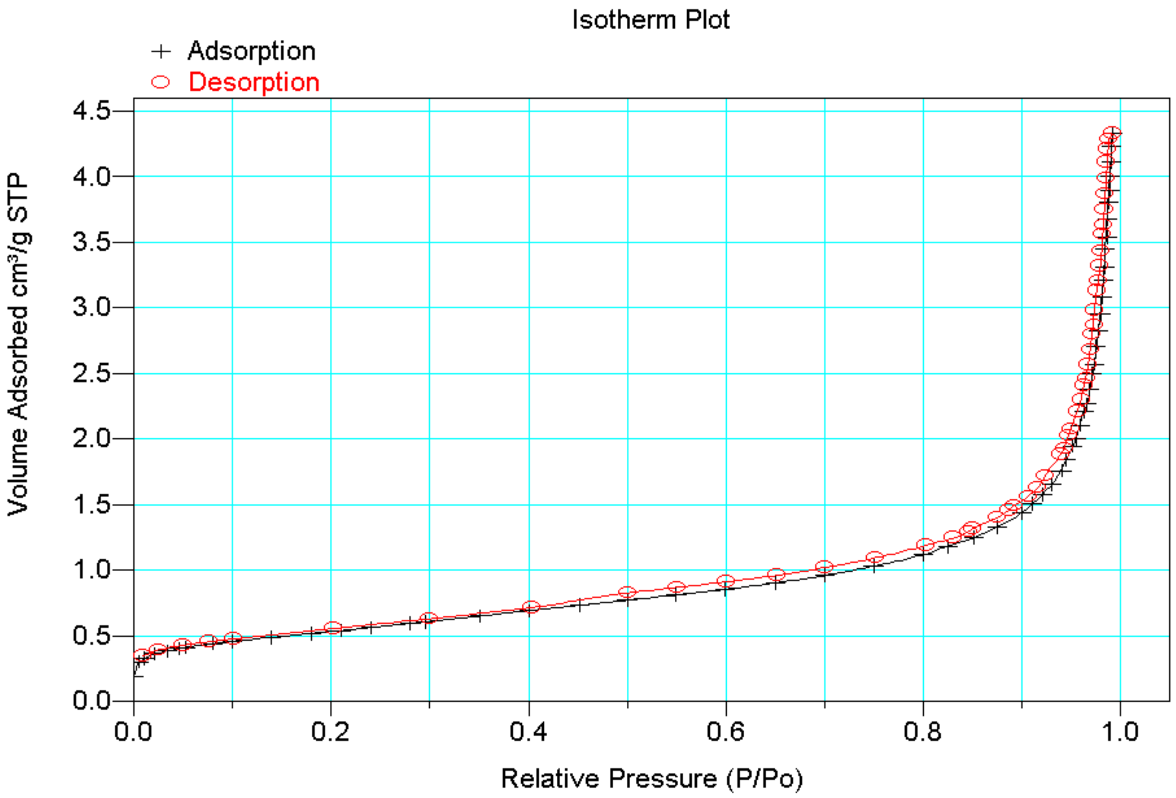

BET Surface Area Report

BET Surface Area : 1.945 ± 0.005233 m^2/g
Slope : 2.283764 ± 0.006229
Y-Intercept : 0.013663 ± 0.001209
c_0 : 168.150.598
V_M : 0.435270 cm^3/g STP
Correlation Coefficient: 9.999740e-01

Molecular Cross-section: 0.1620 nm^2

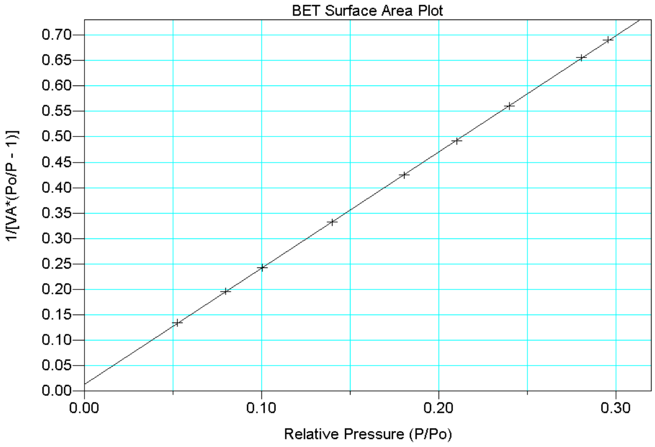

Relative Pressure	Vol Adsorbed (cm³/g STP)	1/ [VA*(Po/P - 1)]
0.052224153	0.4114	0.133938
0.079495354	0.4403	0.196120
0.100247564	0.4586	0.242936
0.139701576	0.4893	0.331907
0.180421115	0.5185	0.424552
0.210213672	0.5415	0.491578
0.240001565	0.5636	0.560271
0.280387689	0.5946	0.655254
0.295500864	0.6073	0.690632

Tuffeau limestone

Sample TL16

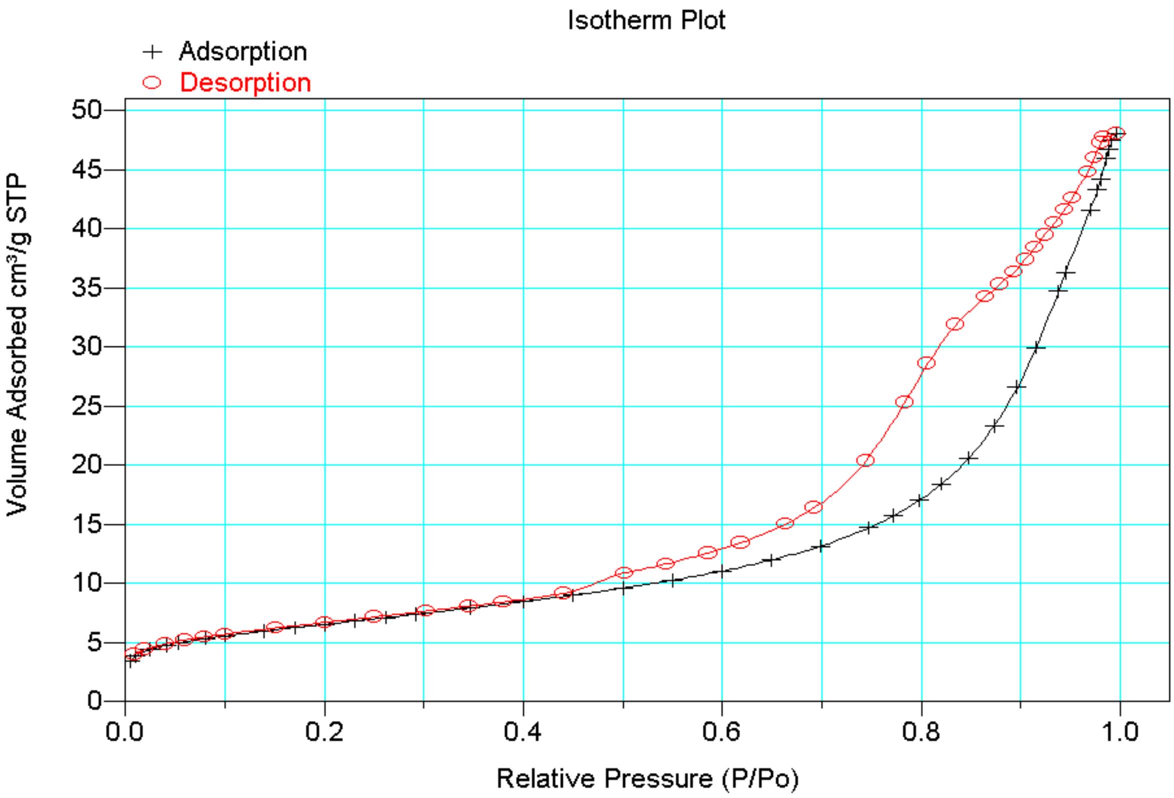

BET Surface Area Report

BET Surface Area : 23.4885 ± 0.0905 m²/g
Slope : 0.185432 ± 0.000714
Y-Intercept : 0.001413 ± 0.000133
c_0 : 132.260.103
V_M : 5.352038 cm³/g STP
Correlation Coefficient: 9.999482e-01

Molecular Cross-section: 0.1620 nm²

Relative Pressure	Vol Adsorbed (cm³/g STP)	1/ [VA*(Po/P - 1)]
0.053183801	49.517	0.011344
0.081153982	53.304	0.016569
0.099664050	55.435	0.019969
0.139465797	59.550	0.027215
0.170014777	62.462	0.032795
0.200223115	65.286	0.038347
0.230765441	68.099	0.044053
0.261300759	70.942	0.049862
0.292035720	73.838	0.055866

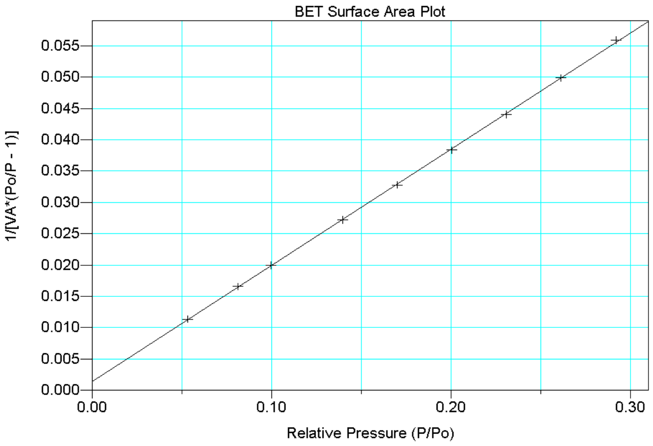

Sample TL19

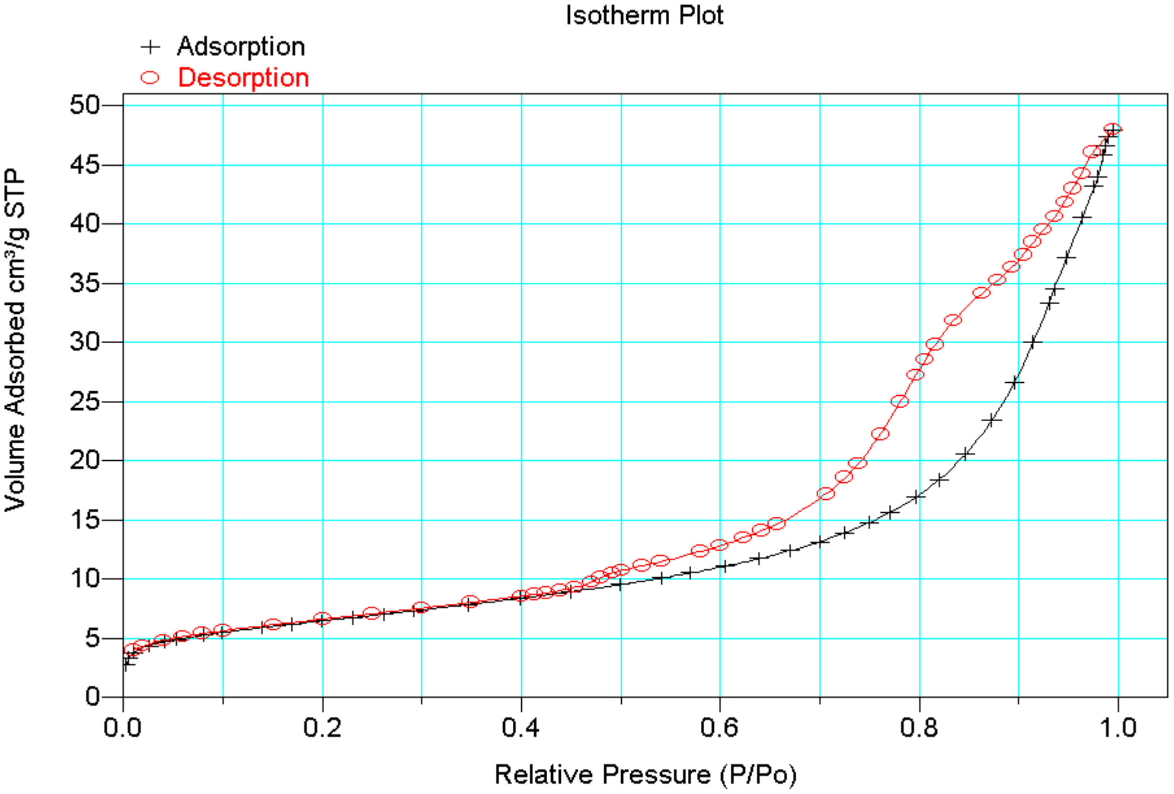

BET Surface Area Report

BET Surface Area : 23.0903 ± 0.0839 m²/g
Slope : 0.187066 ± 0.000673
Y-Intercept : 0.001464 ± 0.000126
c_0 : 128.809.248
V_M : 5.304216 cm³/g STP
Correlation Coefficient: 9.999547e-01

Molecular Cross-section: 0.1620 nm²

Relative Pressure	Vol Adsorbed (cm³/g STP)	1/ [VA*(Po/P - 1)]
0.052889296	48.919	0.011415
0.080931314	52.694	0.016711
0.099423602	54.837	0.020132
0.139361480	58.914	0.027486
0.169884951	61.820	0.033104
0.199700029	64.578	0.038640
0.230886924	67.457	0.044503
0.261380784	70.268	0.050361
0.292080230	73.177	0.056382

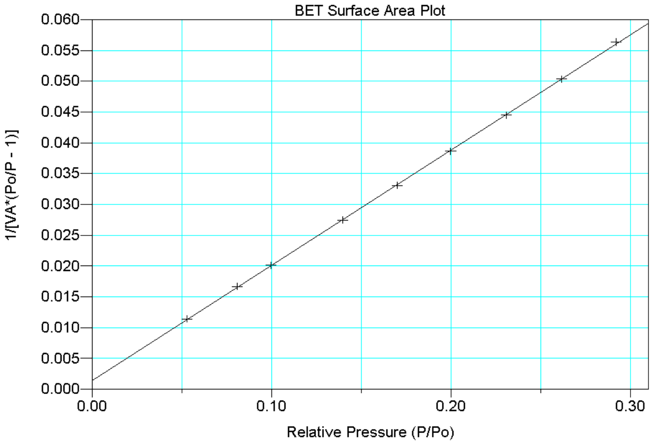

Sample TL23

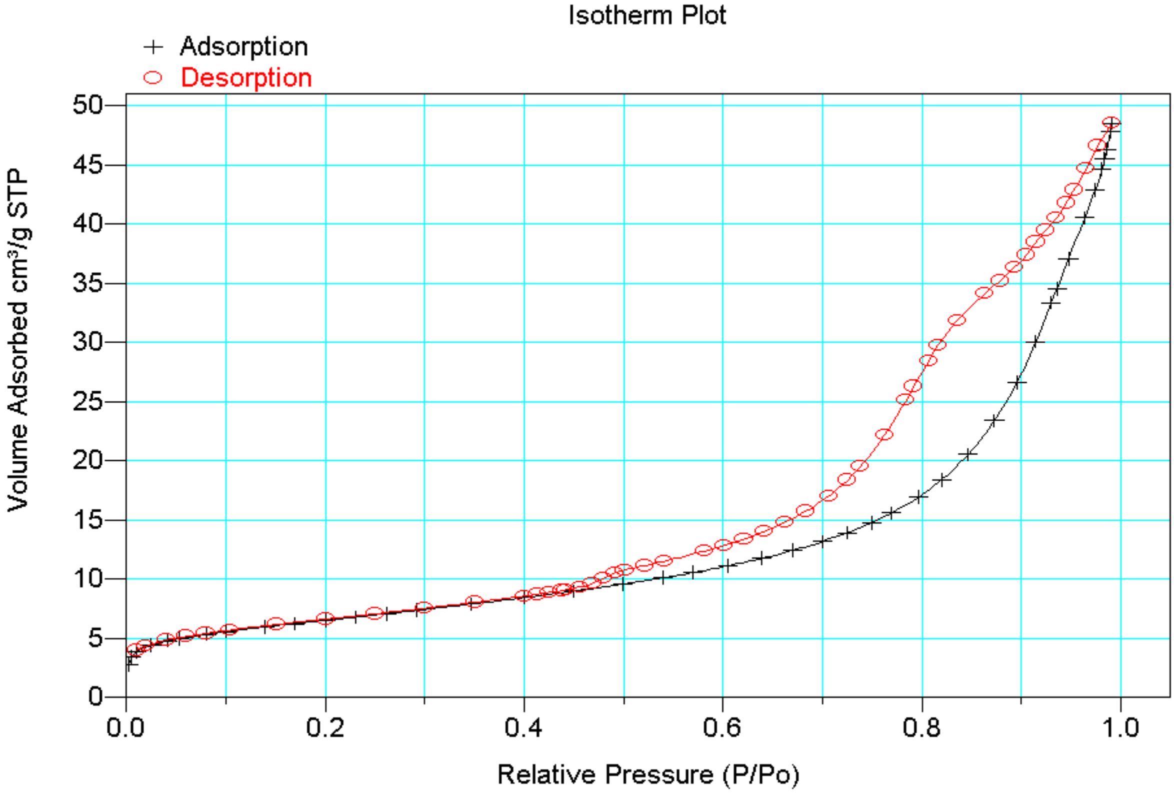

BET Surface Area Report

BET Surface Area : 23.1735 ± 0.0904 m²/g
Slope : 0.186538 ± 0.000721
Y-Intercept : 0.001314 ± 0.000135
c_0 : 142.927.007
V_M : 5.323338 cm³/g STP
Correlation Coefficient: 9.999478e-01

Molecular Cross-section: 0.1620 nm²

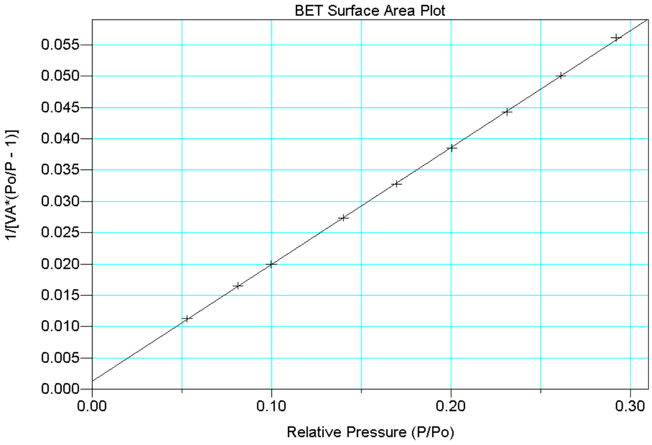

Relative Pressure	Vol Adsorbed (cm³/g STP)	1/ [VA*(Po/P - 1)]
0.052871804	49.560	0.011264
0.080997129	53.317	0.016531
0.099689913	55.435	0.019975
0.139962144	59.499	0.027352
0.169488650	62.253	0.032782
0.200302506	65.084	0.038484
0.230959015	67.869	0.044250
0.261309205	70.669	0.050057
0.292085119	73.544	0.056102

Sample TL26

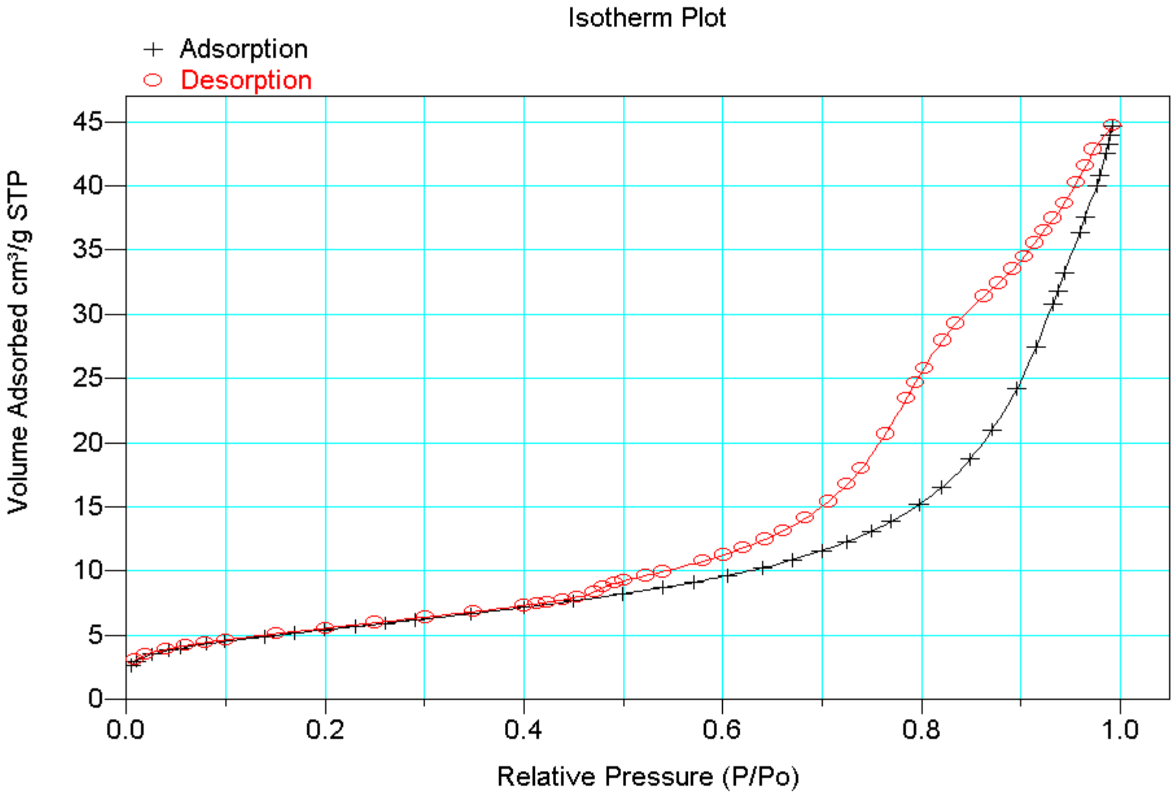

BET Surface Area Report

BET Surface Area : 19.7710 ± 0.0486 m²/g
Slope : 0.218314 ± 0.000536
Y-Intercept : 0.002582 ± 0.000100
c_0 : 85.564.599
V_M : 4.527034 cm³/g STP
Correlation Coefficient: 9.999789e-01

Molecular Cross-section: 0.1620 nm²

Relative Pressure	Vol Adsorbed (cm³/g STP)	1/ [VA*(Po/P - 1)]
0.053851798	39.968	0.014240
0.081169990	43.323	0.020391
0.099337028	45.212	0.024395
0.138702908	48.936	0.032908
0.169533425	51.612	0.039553
0.199666362	54.193	0.046035
0.230099809	56.736	0.052678
0.260533029	59.288	0.059426
0.290782222	61.890	0.066248

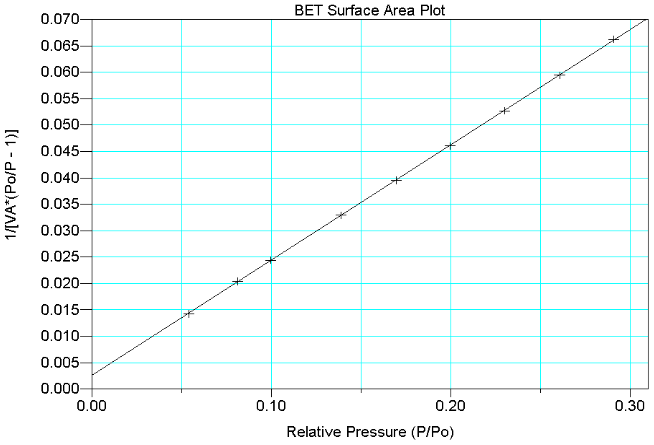

Sample TL29

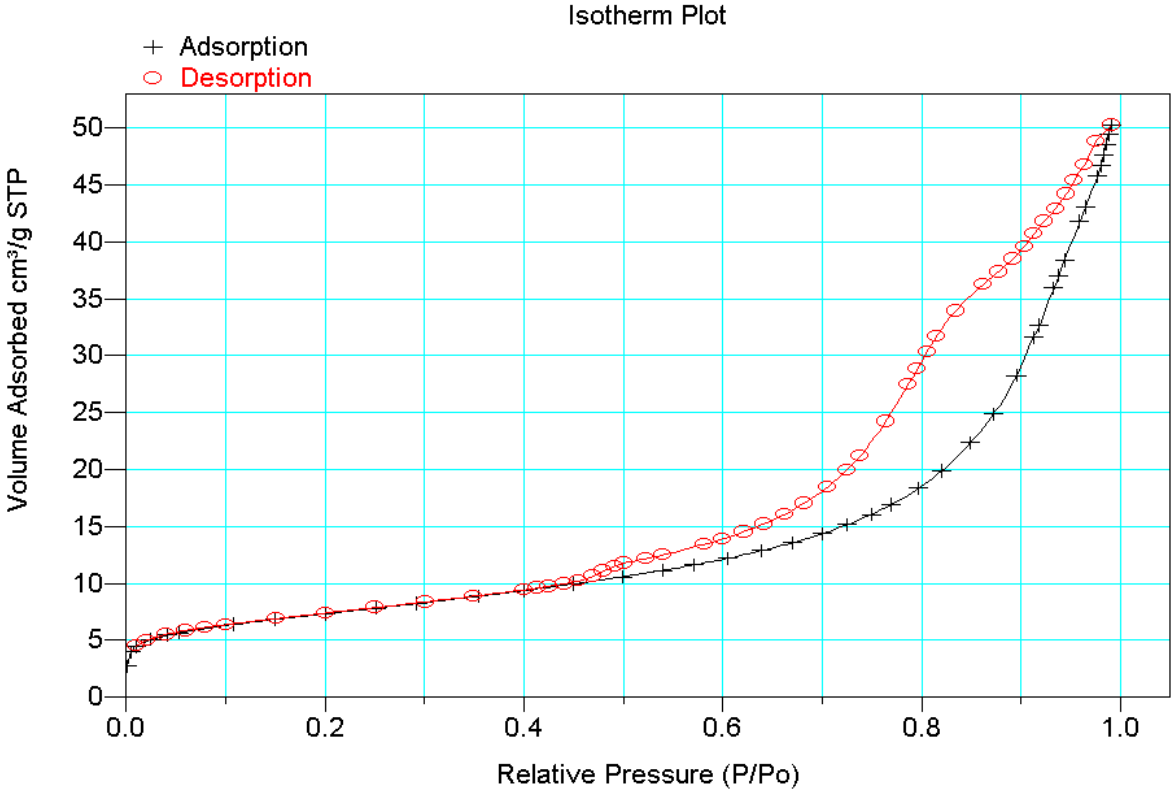

BET Surface Area Report

BET Surface Area : 25.8944 ± 0.1812 m²/g
Slope : 0.167749 ± 0.001161
Y-Intercept : 0.000802 ± 0.000225
c_0 : 210.170.922
V_M : 5.932916 cm³/g STP
Correlation Coefficient: 9.999043e-01

Molecular Cross-section: 0.1620 nm²

Relative Pressure	Vol Adsorbed (cm³/g STP)	1/ [VA*(Po/P - 1)]
0.053378614	56.725	0.009941
0.107875747	63.892	0.018926
0.149790356	68.358	0.025773
0.200663701	73.372	0.034214
0.251798196	78.374	0.042940
0.292603309	82.431	0.050179

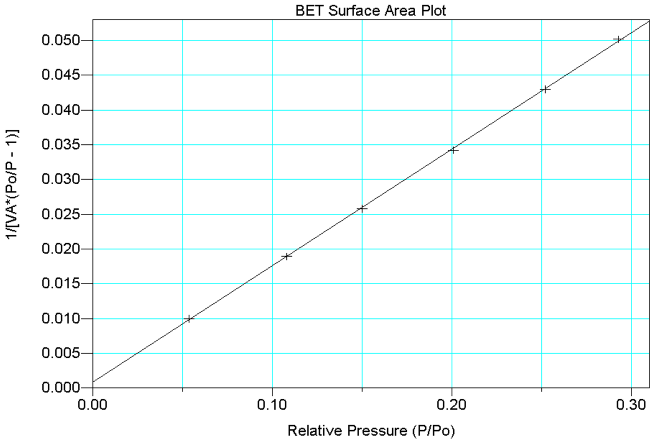

Vuillecin limestone

Sample VK211

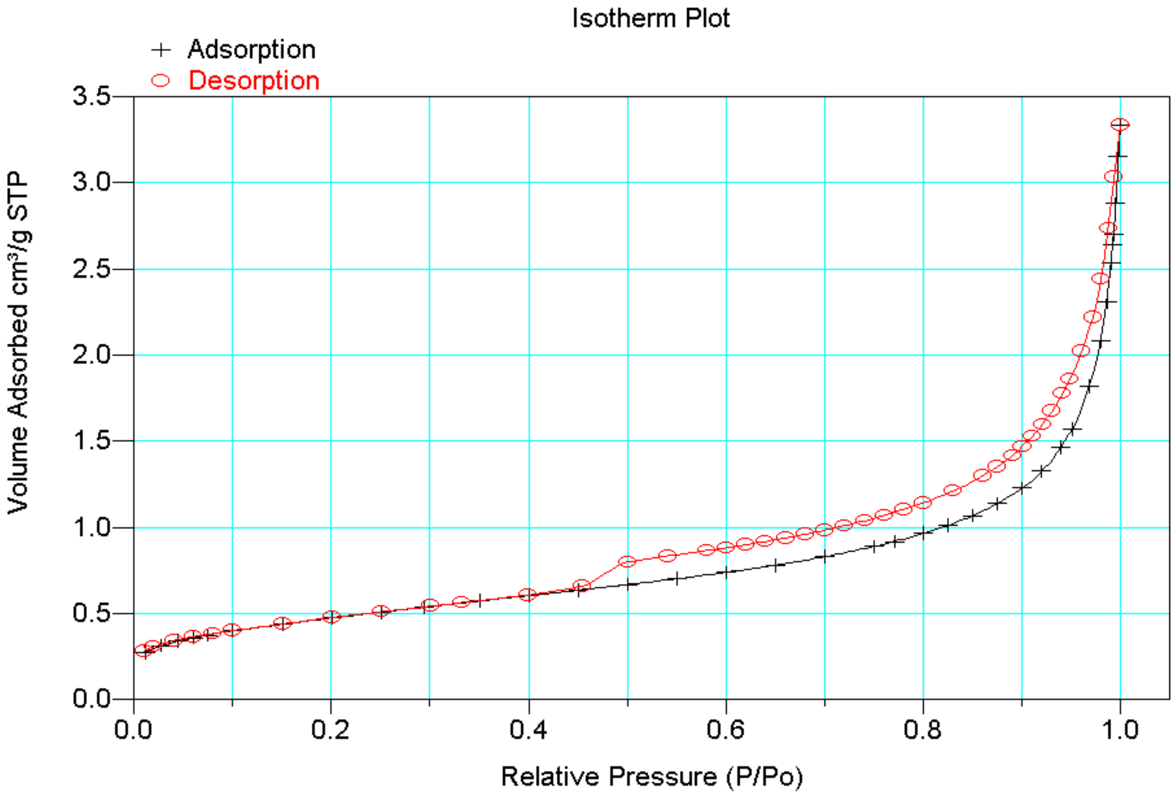

BET Surface Area Report

BET Surface Area : 1.6945 ± 0.0086 m²/g
Slope : 2.545127 ± 0.12855
Y-Intercept : 0.023933 ± 0.2335
c_0 : 107.344.743
V_M : 0.389247 cm³/g STP
Correlation Coefficient: 9.999362e-01

Molecular Cross-section: 0.1620 nm²

Relative Pressure	Vol Adsorbed (cm³/g STP)	1/ [VA*(Po/P - 1)]
0.060350985	0.3596	0.178598
0.074975542	0.3748	0.216275
0.099524044	0.3985	0.277321
0.150302202	0.4362	0.405516
0.200288257	0.4731	0.529374
0.250535229	0.5063	0.660254
0.293757231	0.5364	0.775507

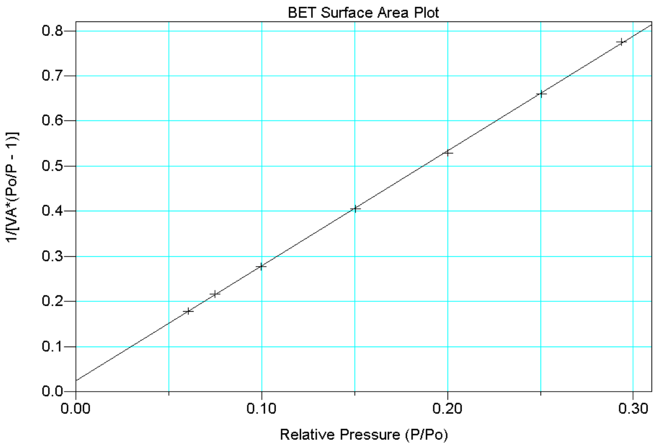

Sample VK212

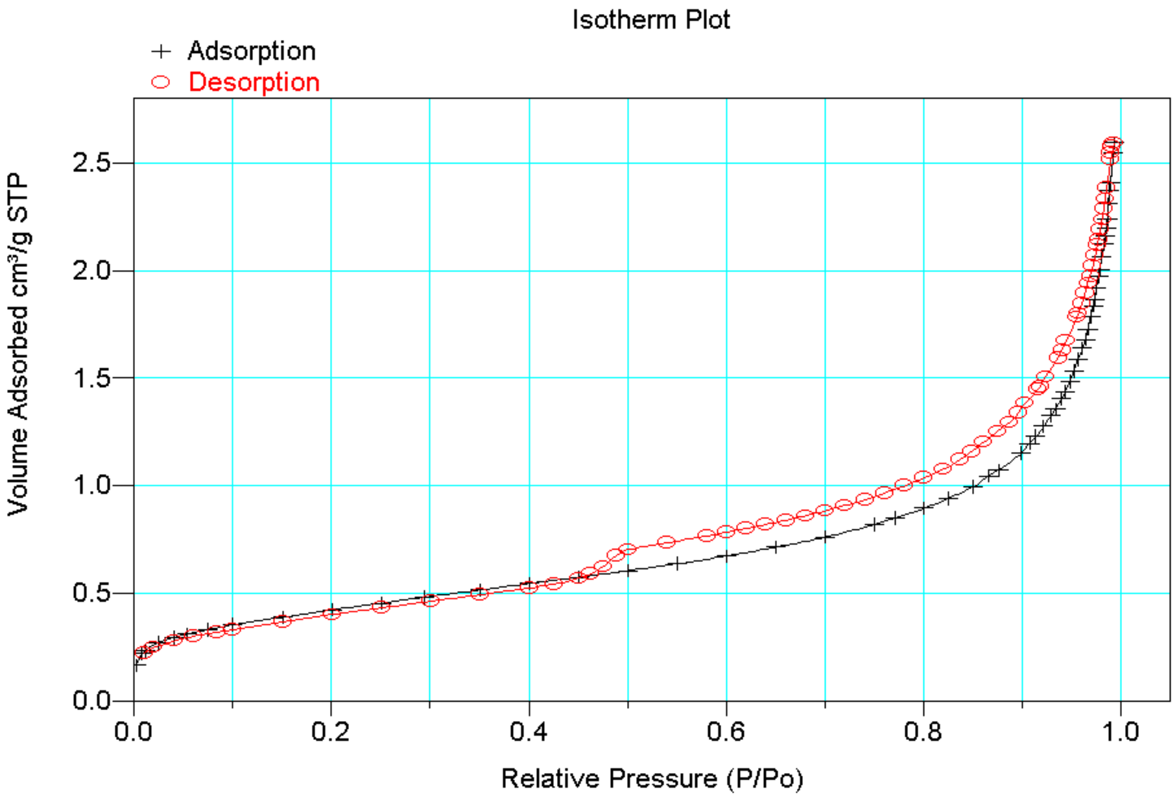

BET Surface Area Report

BET Surface Area : 1.5326 ± 0.0067 m²/g
Slope : 2.809391 ± 0.012181
Y-Intercept : 0.030932 ± 0.02209
c_0 : 91.826.025
V_M : 0.352073 cm³/g STP
Correlation Coefficient: 9.999530e-01

Molecular Cross-section: 0.1620 nm²

Relative Pressure	Vol Adsorbed (cm³/g STP)	1/ [VA*(Po/P - 1)]
0.053651540	0.3121	0.181670
0.074675650	0.3332	0.242238
0.100220342	0.3553	0.313448
0.150297730	0.3906	0.452804
0.200304604	0.4251	0.589260
0.250610813	0.4558	0.733727
0.293687105	0.4837	0.859577

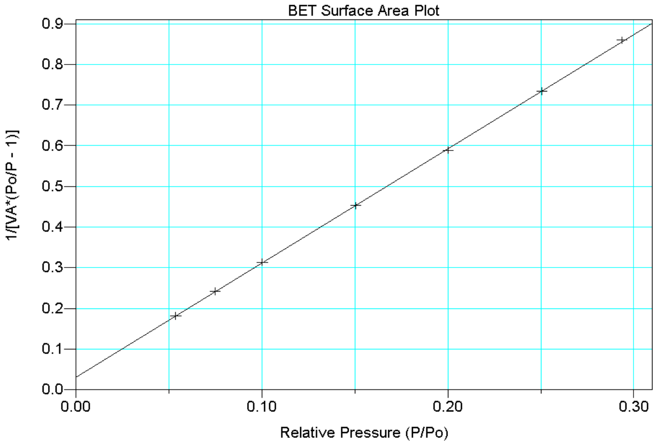

Sample VK213

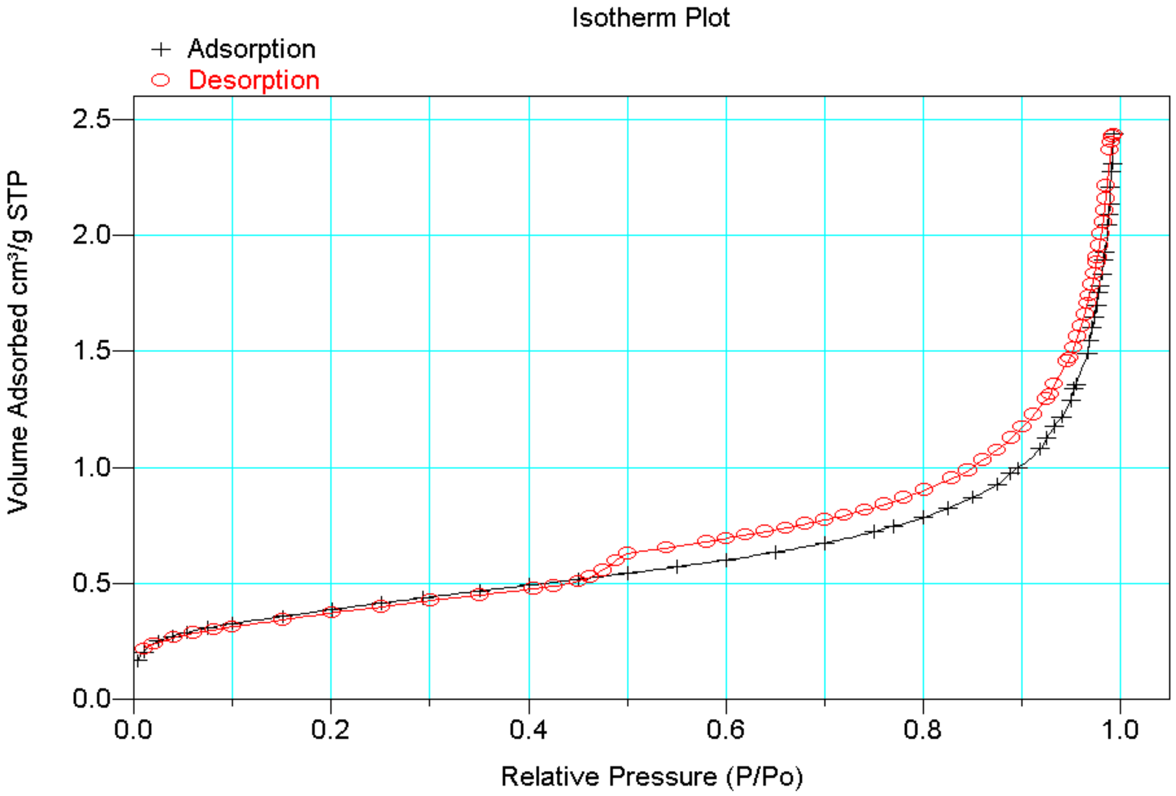

BET Surface Area Report

BET Surface Area : 1.3843 ± 0.0079 m^2/g
Slope : 3.117202 ± 0.017730
Y-Intercept : 0.027540 ± 0.003216
c_0 : 114.189.518
V_M : 0.317991 cm^3/g STP
Correlation Coefficient: 9.999191e-01

Molecular Cross-section: 0.1620 nm^2

Relative Pressure	Vol Adsorbed (cm³/g STP)	1/ [VA*(Po/P - 1)]
0.053724119	0.2887	0.196666
0.074789067	0.3079	0.262515
0.100386348	0.3279	0.340334
0.150435609	0.3573	0.495565
0.200334625	0.3877	0.646115
0.250476498	0.4145	0.806146
0.293579700	0.4382	0.948318

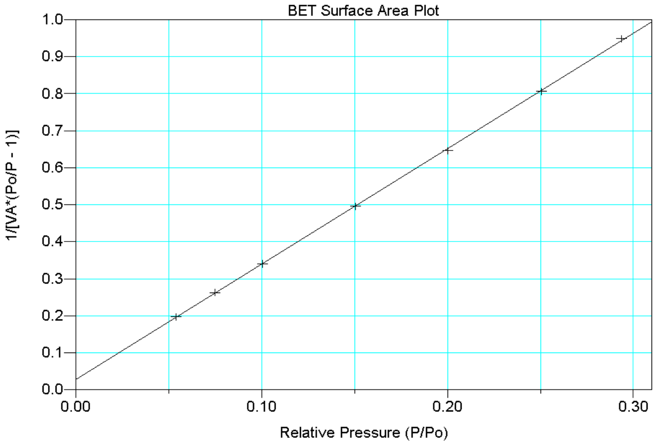

Sample VK214

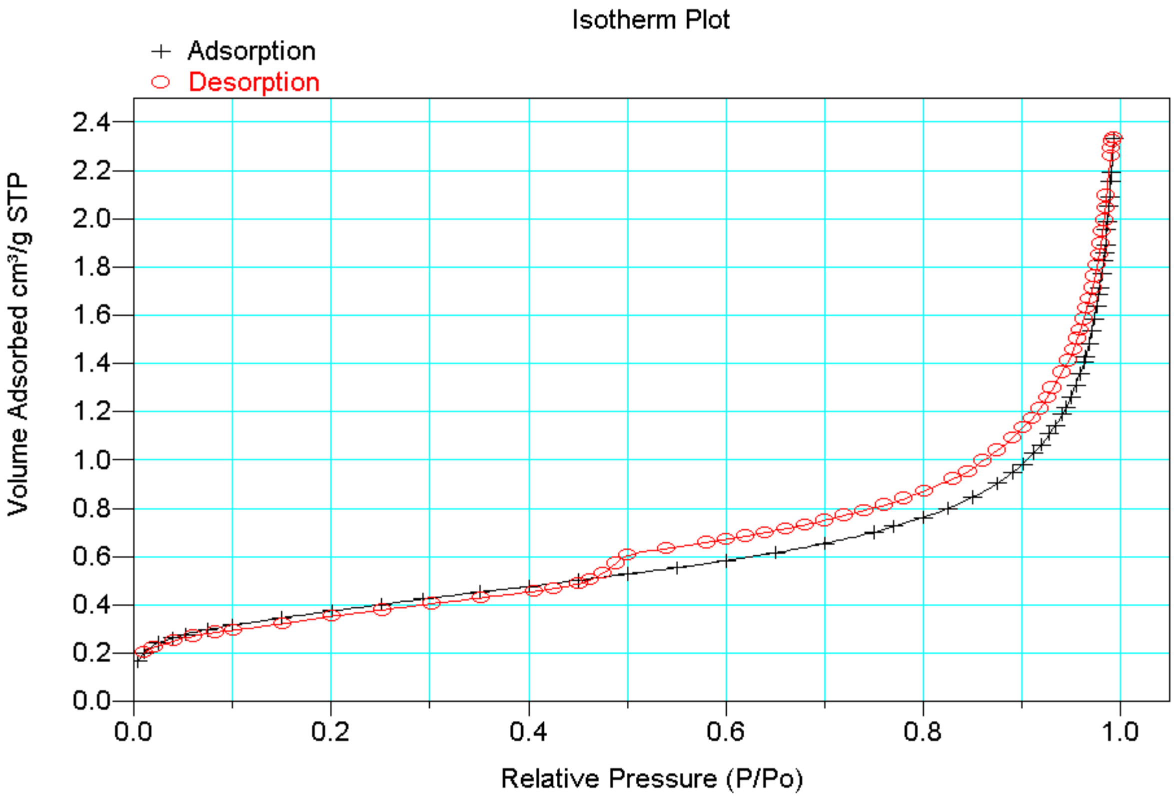

BET Surface Area Report

BET Surface Area : 1.3416 ± 0.0072 m^2/g
Slope : 3.215767 ± 0.17078
Y-Intercept : 0.029012 ± 0.3096
c_0 : 111.843.818
V_M : 0.308187 cm^3/g STP
Correlation Coefficient: 9.999295e-01

Molecular Cross-section: 0.1620 nm^2

Relative Pressure	Vol Adsorbed (cm^3/g STP)	1/ [VA*(Po/P - 1)]
0.052562628	0.2780	0.199583
0.074749977	0.2981	0.271014
0.100325560	0.3168	0.351957
0.150248472	0.3459	0.511142
0.200264502	0.3756	0.666677
0.250538055	0.4011	0.833528
0.293564076	0.4249	0.978085

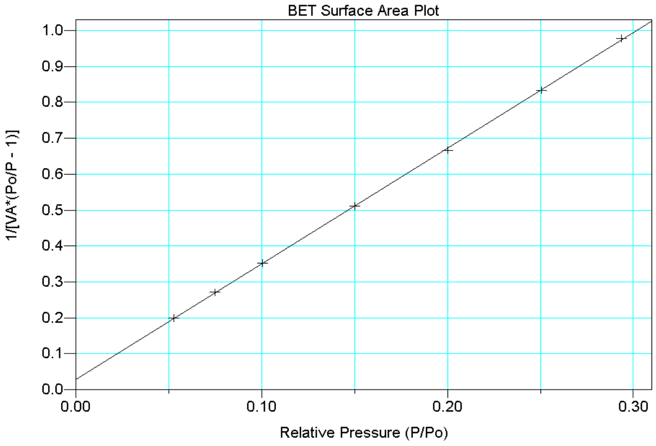

Sample VK215

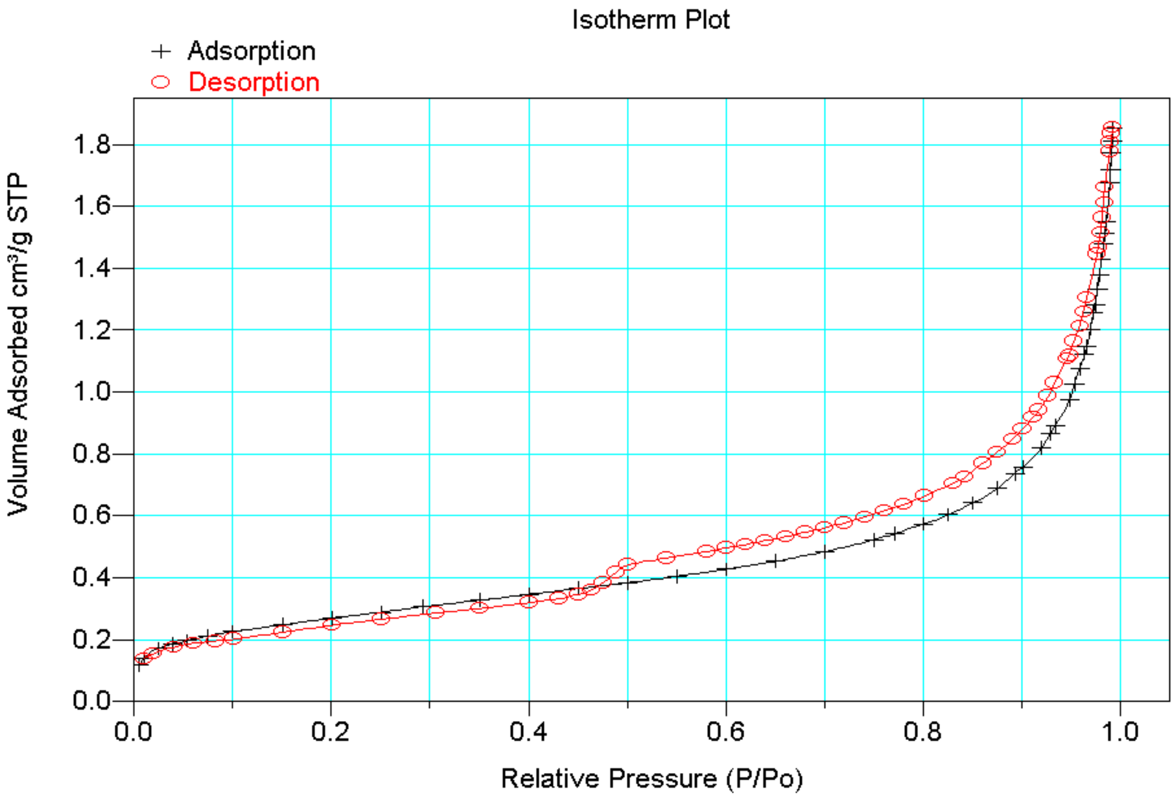

BET Surface Area Report

BET Surface Area : 0.9709 ± 0.0042 m²/g
Slope : 4.435111 ± 0.019211
Y-Intercept : 0.048524 ± 0.003484
c_0 : 92.401.005
V_M : 0.223033 cm³/g STP
Correlation Coefficient: 9.999531e-01

Molecular Cross-section: 0.1620 nm²

Relative Pressure	Vol Adsorbed (cm³/g STP)	1/ [VA*(Po/P - 1)]
0.053664471	0.1973	0.287445
0.074835436	0.2114	0.382632
0.100304570	0.2258	0.493844
0.150387773	0.2475	0.715205
0.200337717	0.2695	0.929637
0.250598065	0.2886	1.158.657
0.293553619	0.3065	1.355.899

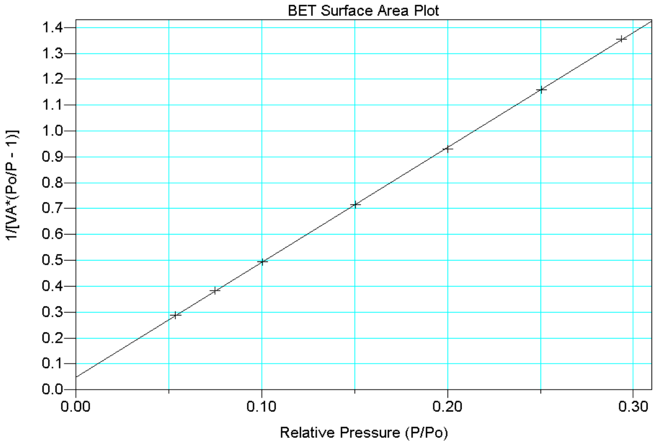

Appendix G:
Captured and analyzed BSE images

For all the images, the black areas represents the porous phase, and the white areas the mineral phase.

Fontainebleau sandstone

Transverse slice A

Original image

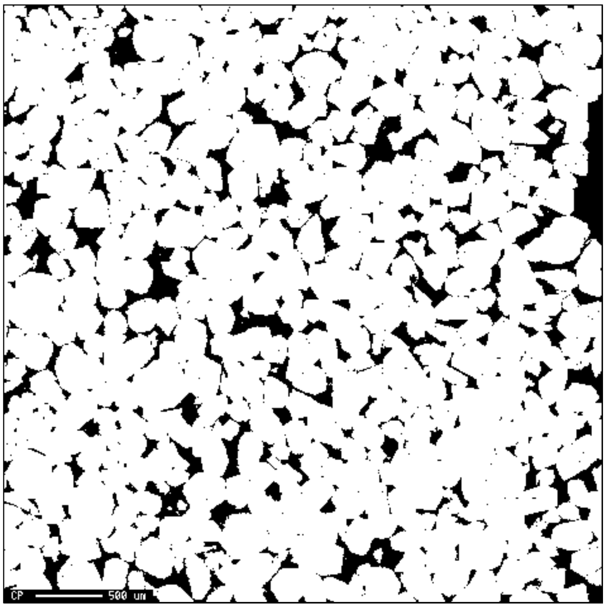

Analyzed image

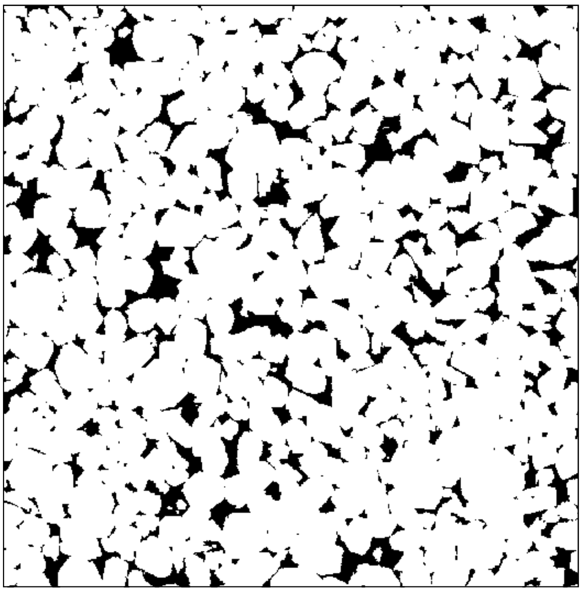

Porosity = 13.97 %
Mean Feret diameter D_F = 118.7 µm

Transverse slice B

Original image

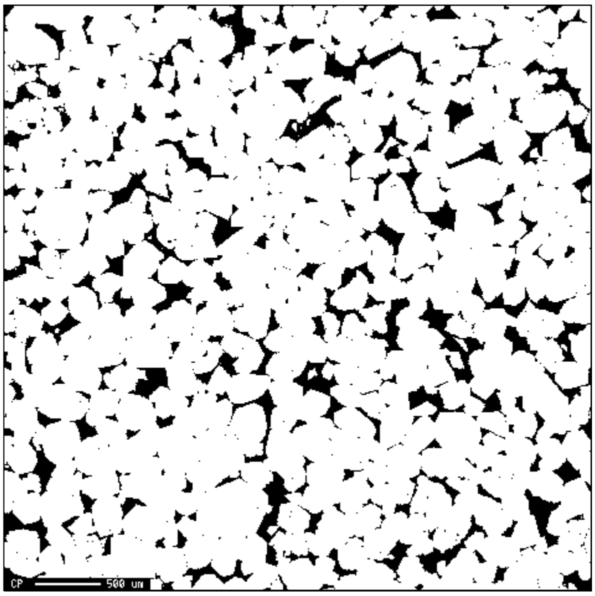

Analyzed image

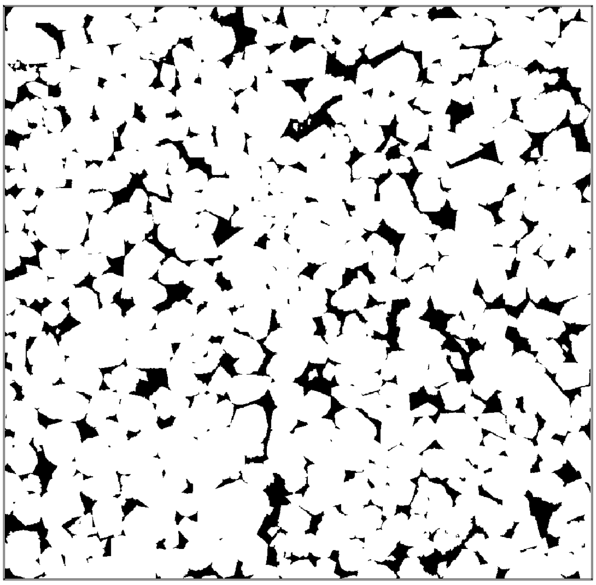

Porosity = 13.88 %
Mean Feret diameter D_F = 112.5 µm

Horizontal slice A

Original image

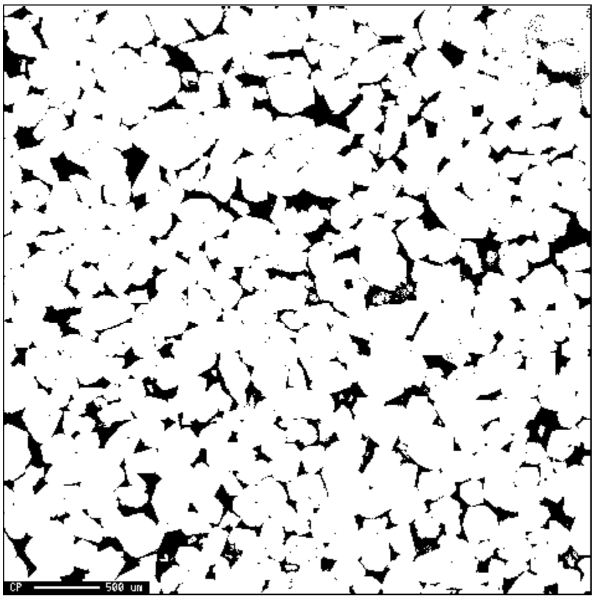

Analyzed image

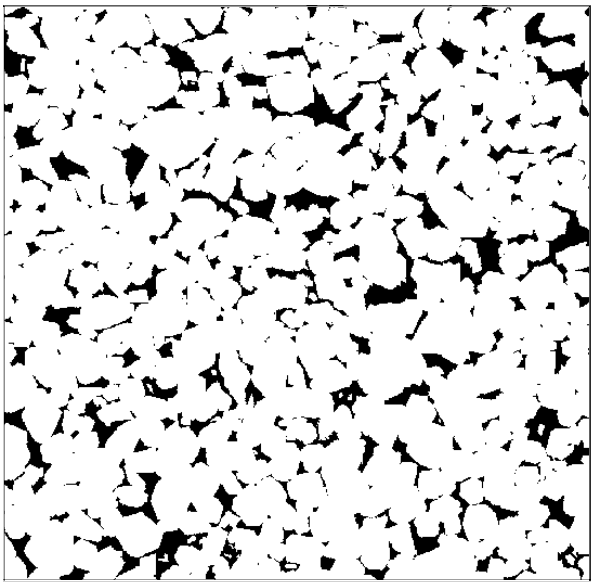

Porosity = 13.69 %
Mean Feret diameter D_F = 107.7 µm

Horizontal slice B

Original image

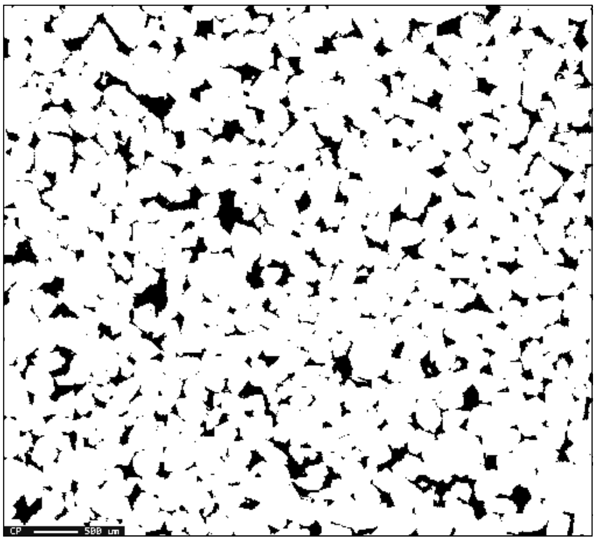

Analyzed image

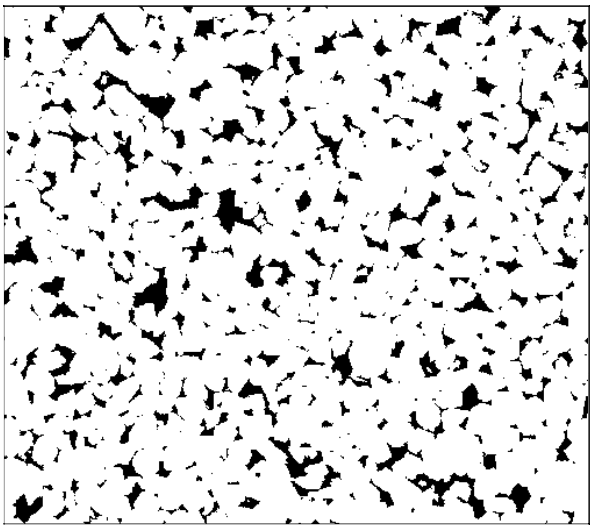

Porosity = 12.58 %
Mean Feret diameter D_F = 109.3 µm

Mons chalk

BSE image 1

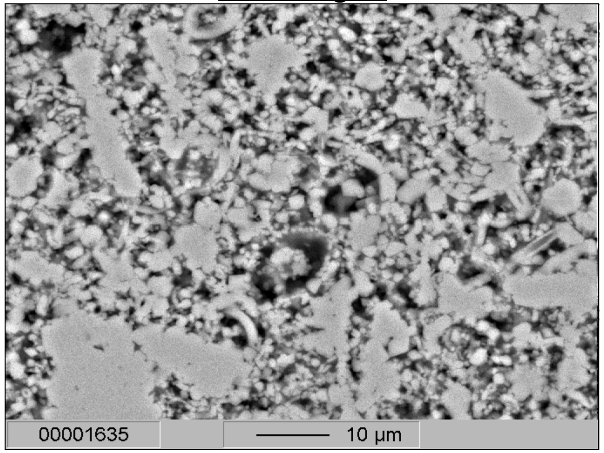

Image 1 after Binarisation 1

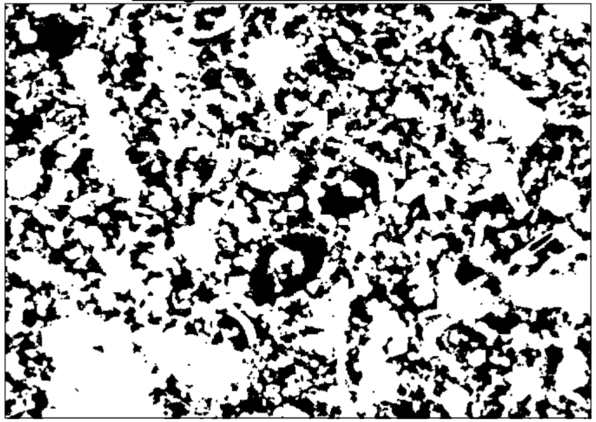

Threshold 147
Porosity = 35.64 %
D_F = 1.87 µm

Image 1 after Binarisation 2

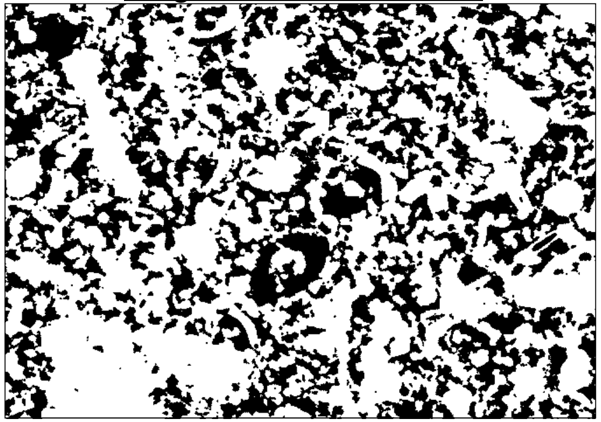

Threshold 157
Porosity = 37.36%
D_F = 1.96 µm

BSE image 2

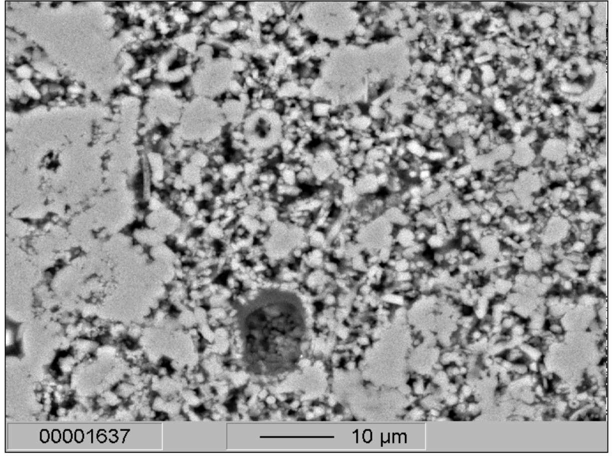

Image 2 after Binarisation 1

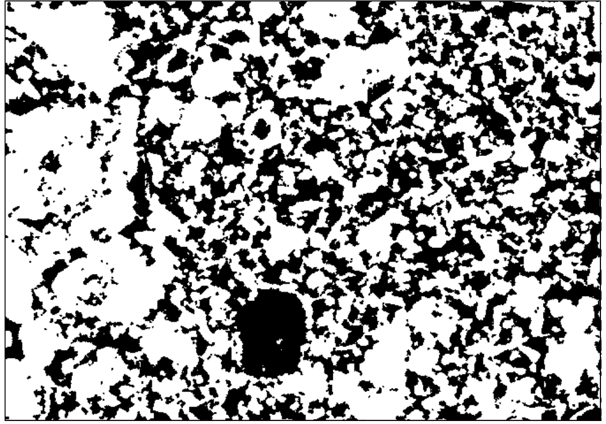

Threshold = 148
Porosity = 38.34 %
D_F = 1.86 µm

Image 2 after Binarisation 2

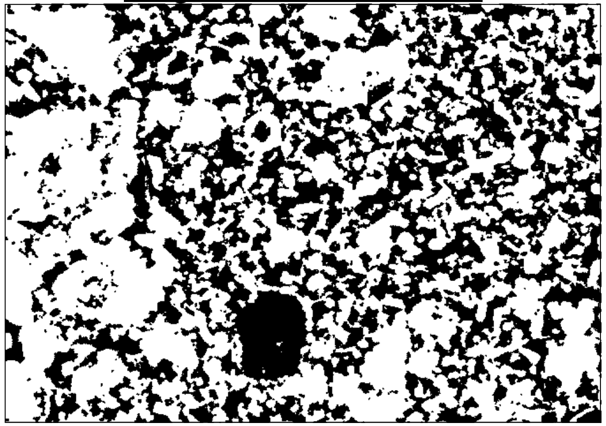

Threshold = 157
Porosity = 39.33 %
D_F = 1.78 µm

BSE image 3

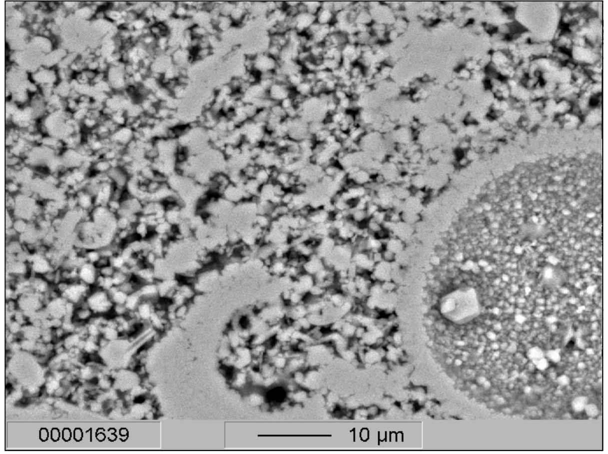

Image 3 after Binarisation 1

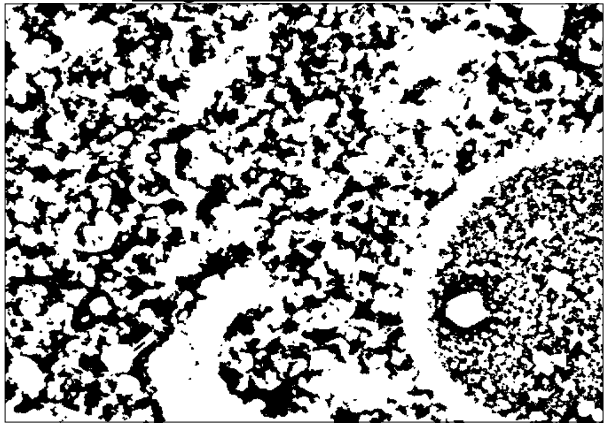

Threshold 147
Porosity = 37.72 %
D_F = 1.77 μm

Image 3 after Binarisation 2

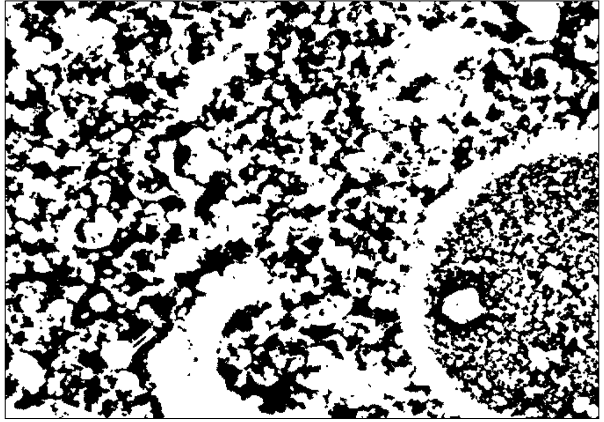

Threshold 157
Porosity = 40.35%
D_F = 1.78 μm

BSE image 4

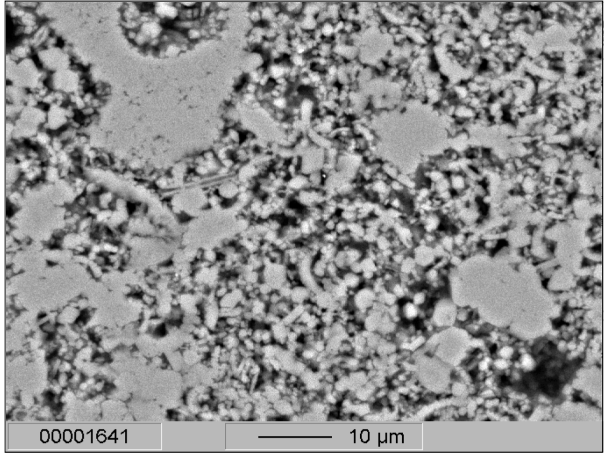

Image 4 after Binarisation 1

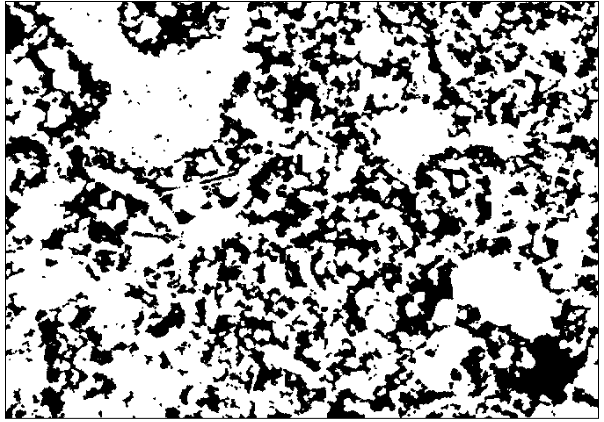

Threshold = 141
Porosity = 39.06 %
D_F = 1.73 μm

Image 4 after Binarisation 2

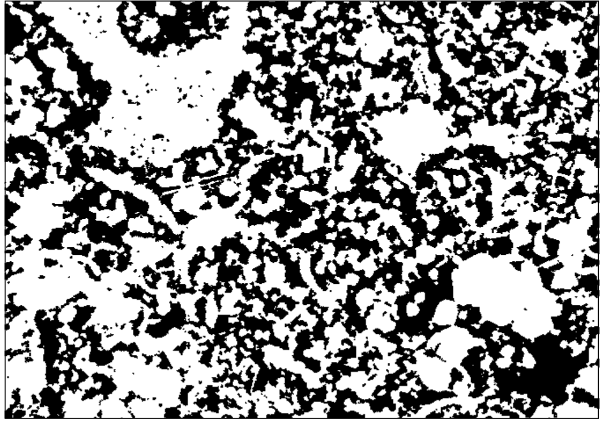

Threshold = 157
Porosity = 42.62 %
D_F = 1.68 μm

BSE image 5

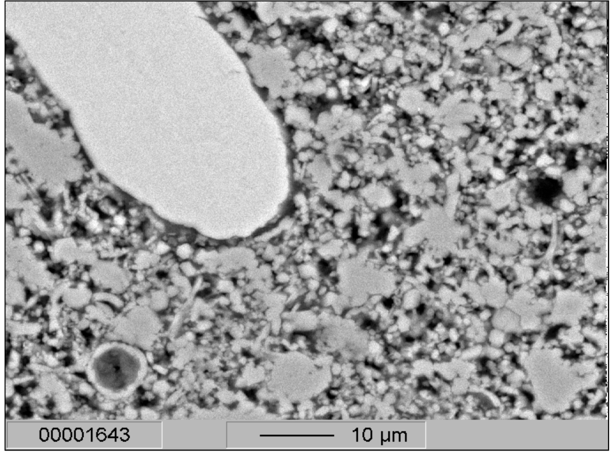

Image 5 after Binarisation 1

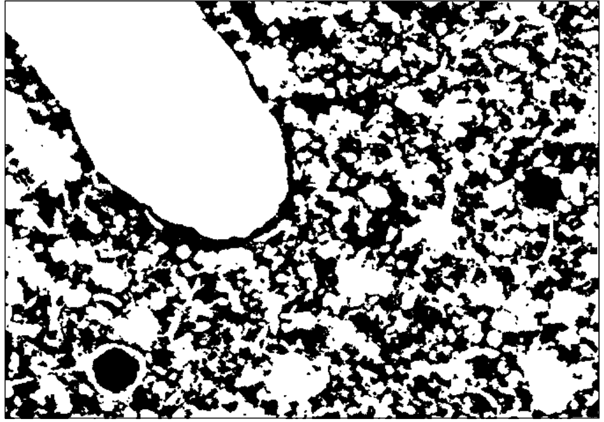

Threshold 159
Porosity = 35.33 %
D_F = 1.98 µm

Image 5 after Binarisation 2

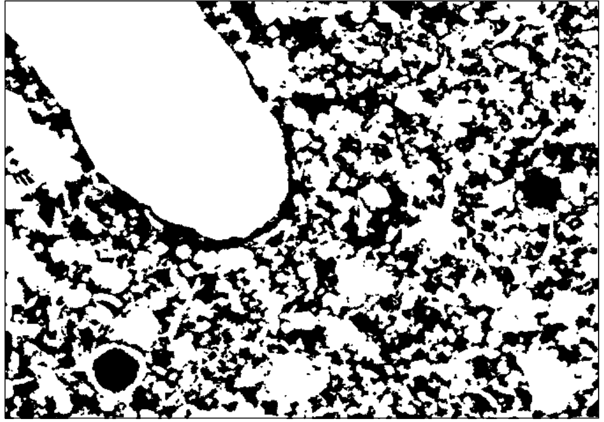

Threshold 157
Porosity = 34.78%
D_F = 1.97 µm

BSE image 6

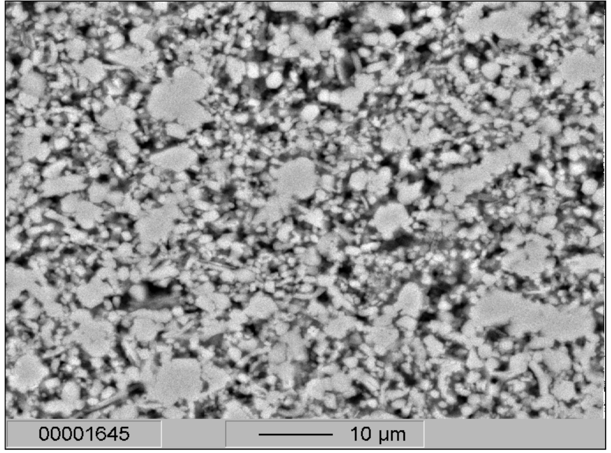

Image 6 after Binarisation 1

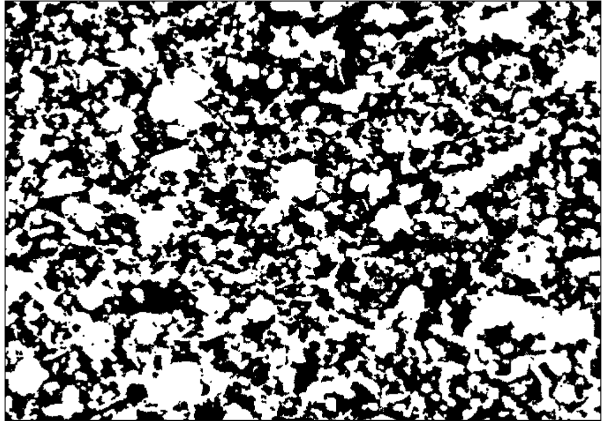

Threshold = 163
Porosity = 48.82 %
D_F = 1.99 µm

Image 6 after Binarisation 2

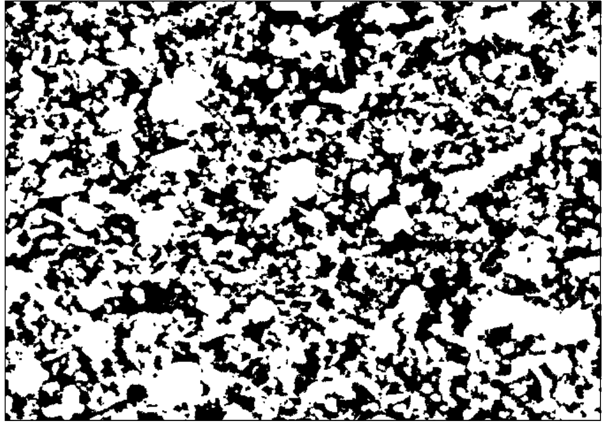

Threshold = 157
Porosity = 41.85 %
D_F = 2.08 µm

BSE image 7

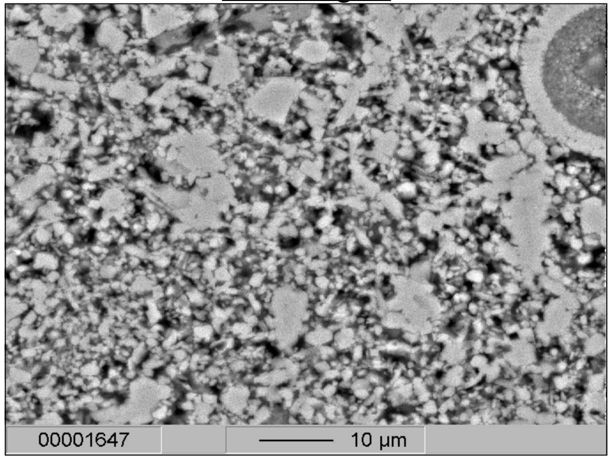

Image 7 after Binarisation 1

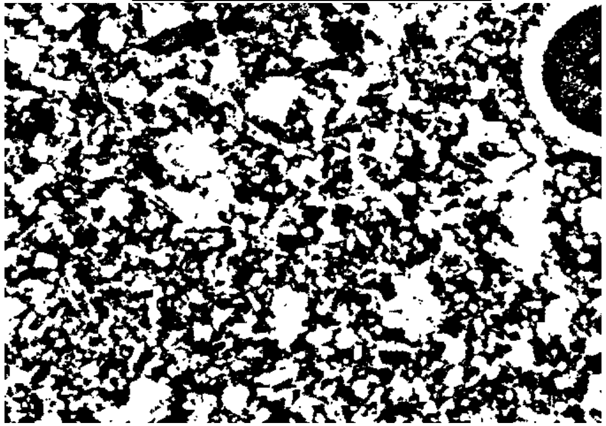

Threshold 158
Porosity = 49.59 %
D_F = 1.61 µm

Image 7 after Binarisation 2

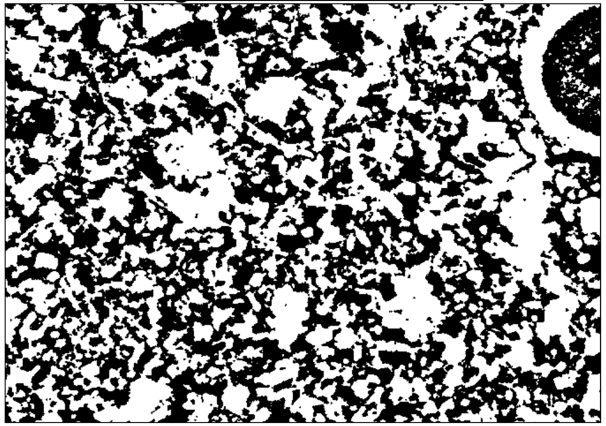

Threshold 157
Porosity = 47.06%
D_F = 1.63 µm

Appendix H:
Data of capillary water imbibition kinetics

Legend:

■	L (cm)
+	δW/s (g cm^{-2})
………	Mass increase from total porosity measurement
-.-.-.-.	Mass increase from free porosity measurement

B (cm $h^{-1/2}$): slope of the wet fringe rise curve obtained by capillary water imbibition kinetics.

A (g cm^{-2} $h^{-1/2}$): slope of the weight increase curve obtained by capillary water imbibition kinetics.

//: core drilled out from the block in a direction parallel to the stratification planes.

⊥: core drilled out from the block in a direction perpendicular to the stratification planes.

$d_{B,W}$ (g/cm³): bulk density determined by water porosimetry.

$d_{M,W}$ (g/cm³): mineral density determined by water porosimetry.

N_W (%): total water porosity determined by water porosimetry.

N_{48} (%): 48 hours porosity (or free porosity) determined by water porosimetry.

S_{48}: saturation coefficient (Hirschwald's coefficient) determined by water porosimetry.

Fontainebleau sandstone

Sample FONT1	
Length (cm)	5.72
Diameter (cm)	3.98
Section (cm²)	12.44
Sample volume (cm^3)	69.42
$d_{B,W}$ (g/cm^3)	2.32
$d_{M,W}$ (g/cm^3)	2.65
N_W (%)	12.37
N_{48} (%)	6.91
S_{48}	0.56
B (cm $h^{-1/2}$)	14.77
A (g cm^{-2} $h^{-1/2}$)	0.94

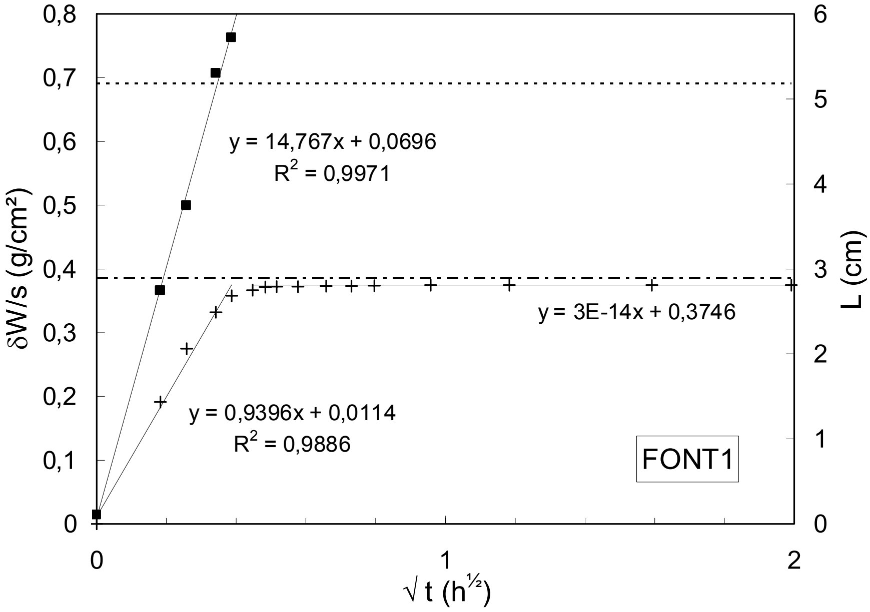

Sample FONT2	
Length (cm)	5.87
Diameter (cm)	3.98
Section (cm²)	12.44
Sample volume (cm^3)	71.63
$d_{B.W}$ (g/cm^3)	2.31
$d_{M,W}$ (g/cm^3)	2.65
N_W (%)	12.73
N_{48} (%)	7.48
S_{48}	0.59
B (cm $h^{-1/2}$)	14.24
A (g cm^{-2} $h^{-1/2}$)	0.99

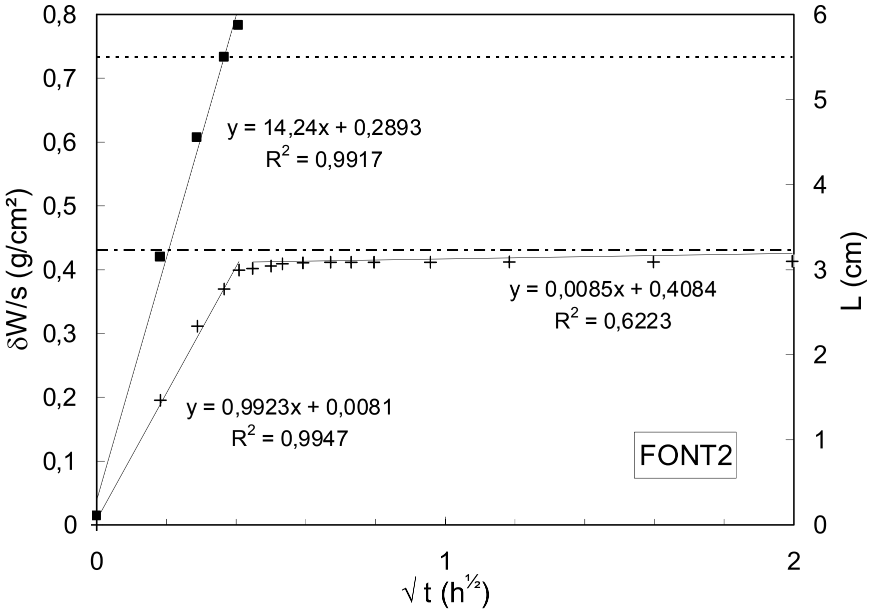

Sample FONT3	
Length (cm)	5.70
Diameter (cm)	3.98
Section (cm²)	12.44
Sample volume (cm^3)	69.15
$d_{B.\ W}$ (g/cm^3)	2.32
$d_{M,\ W}$ (g/cm^3)	2.65
N_W (%)	12.44
N_{48} (%)	7.04
S_{48}	0.57
B (cm $h^{-1/2}$)	13.83
A (g cm^{-2} $h^{-1/2}$)	1.03

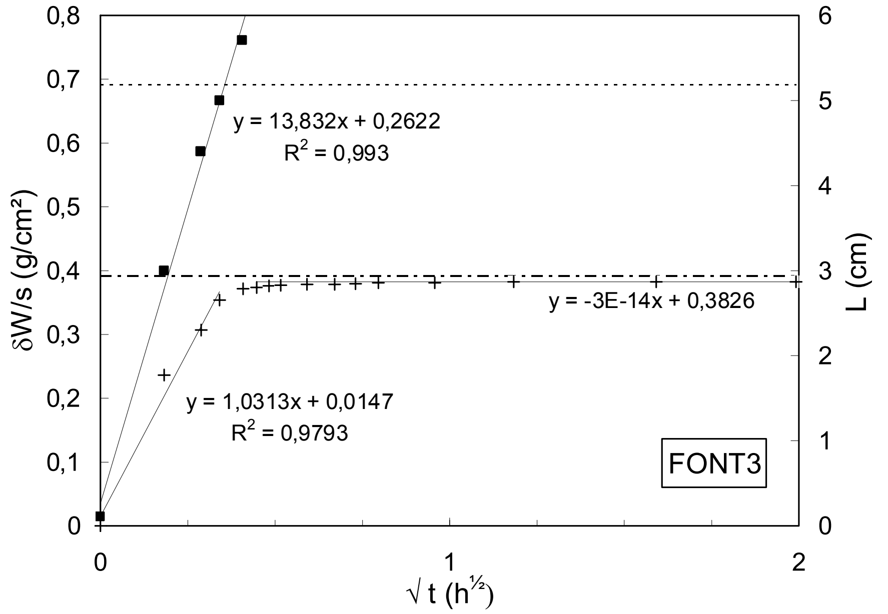

Sample FONT4	
Length (cm)	5.65
Diameter (cm)	3.98
Section (cm²)	12.44
Sample volume (cm^3)	71.34
$d_{B.\ W}$ (g/cm^3)	2.33
$d_{M,\ W}$ (g/cm^3)	2.65
N_W (%)	12.25
N_{48} (%)	6.50
S_{48}	0.53
B (cm $h^{-1/2}$)	15.29
A (g cm^{-2} $h^{-1/2}$)	0.95

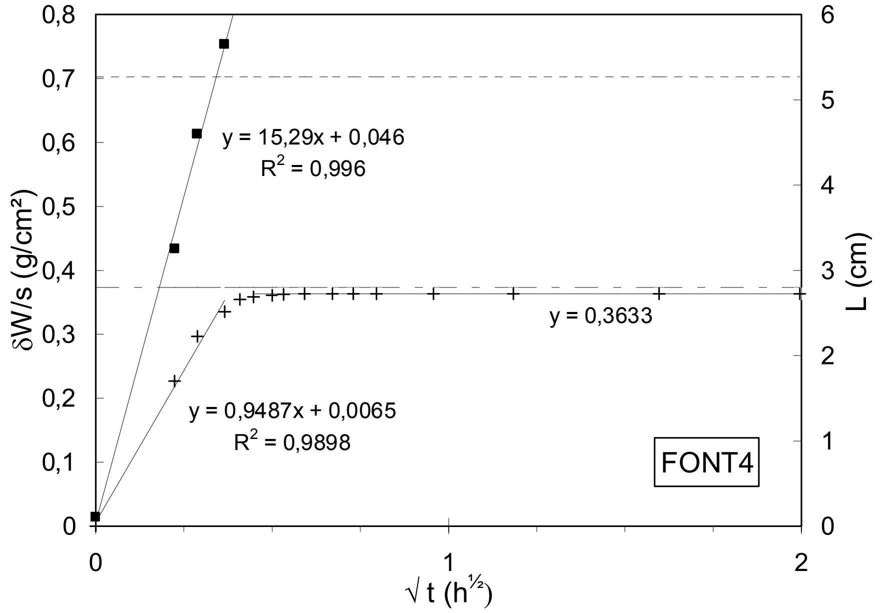

“Grès à Meules” sandstone

Sample SGM1 //	
Length (cm)	5.82
Diameter (cm)	3.99
Section (cm^2)	12.50
Sample volume (cm^3)	71.03
$d_{B.\,W}$ (g/cm^3)	2.10
$d_{M,\,W}$ (g/cm^3)	2.66
N_W (%)	21.01
N_{48} (%)	14.61
S_{48}	0.70
B (cm h$^{-1/2}$)	3.37
A (g cm^{-2} h$^{-1/2}$)	0.43

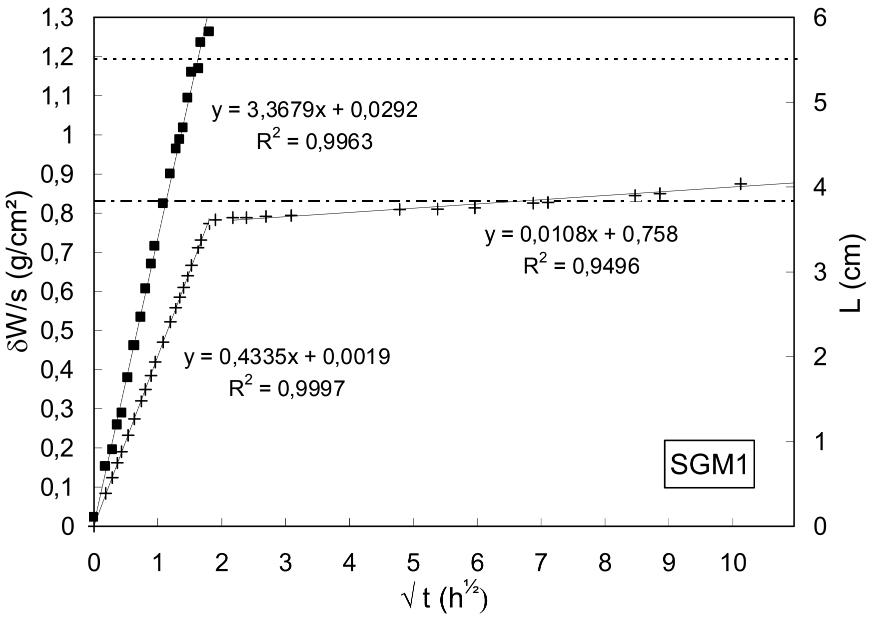

Sample SGM2 //	
Length (cm)	5.80
Diameter (cm)	3.99
Section (cm^2)	12.50
Sample volume (cm^3)	70.65
$d_{B.\,W}$ (g/cm^3)	2.10
$d_{M,\,W}$ (g/cm^3)	2.66
N_W (%)	21.08
N_{48} (%)	14.69
S_{48}	0.70
B (cm h$^{-1/2}$)	3.98
A (g cm^{-2} h$^{-1/2}$)	0.52

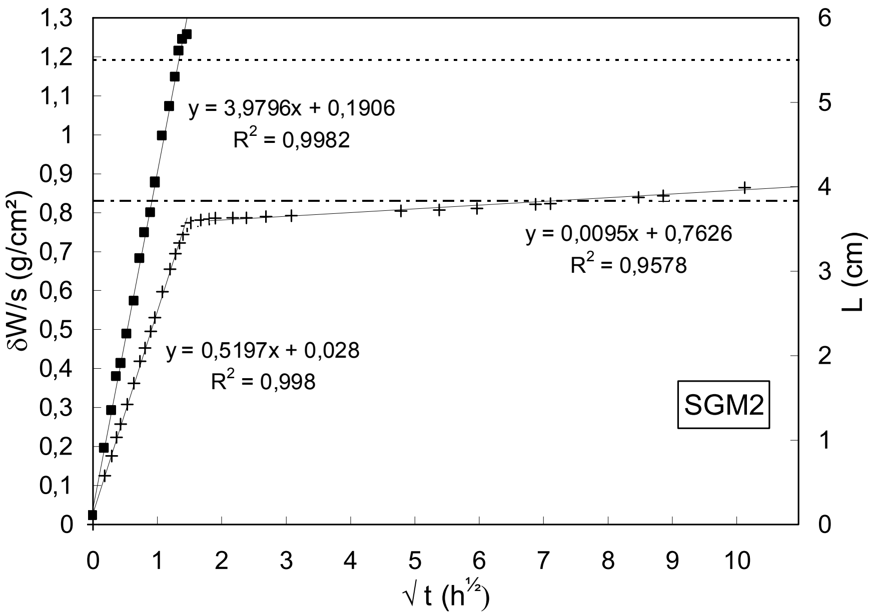

Sample SGM3 //	
Length (cm)	5.58
Diameter (cm)	3.99
Section (cm²)	12.50
Sample volume (cm^3)	72.44
$d_{B.\,W}$ (g/cm^3)	2.10
$d_{M,\,W}$ (g/cm^3)	2.66
N_W (%)	21.26
N_{48} (%)	13.94
S_{48}	0.66
B (cm h$^{-1/2}$)	4.17
A (g cm^{-2} h$^{-1/2}$)	0.53

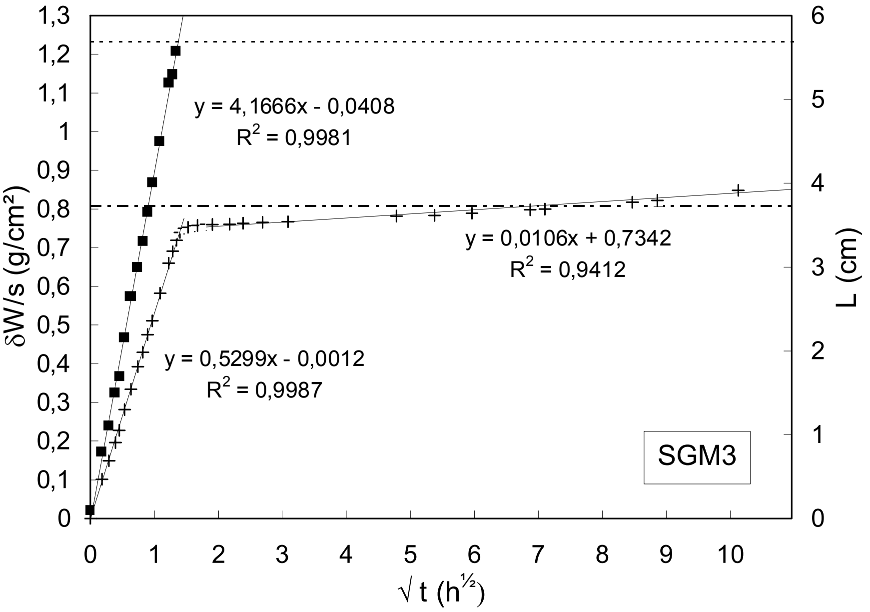

Sample SGM4 ⊥	
Length (cm)	5.47
Diameter (cm)	3.99
Section (cm²)	12.50
Sample volume (cm^3)	71.57
$d_{B.\,W}$ (g/cm^3)	2.09
$d_{M,\,W}$ (g/cm^3)	2.66
N_W (%)	21.48
N_{48} (%)	13.75
S_{48}	0.64
B (cm h$^{-1/2}$)	3.93
A (g cm^{-2} h$^{-1/2}$)	0.49

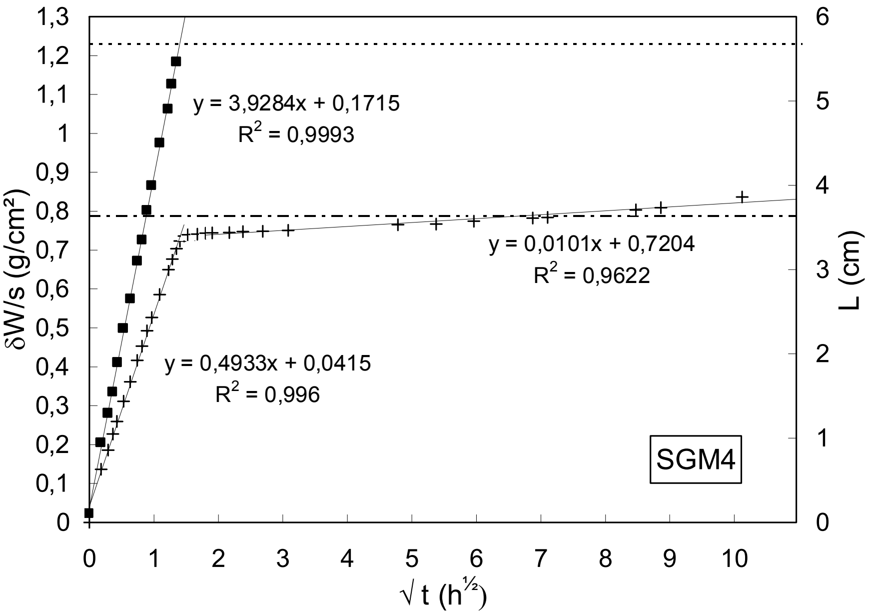

Mons chalk

Sample MS1		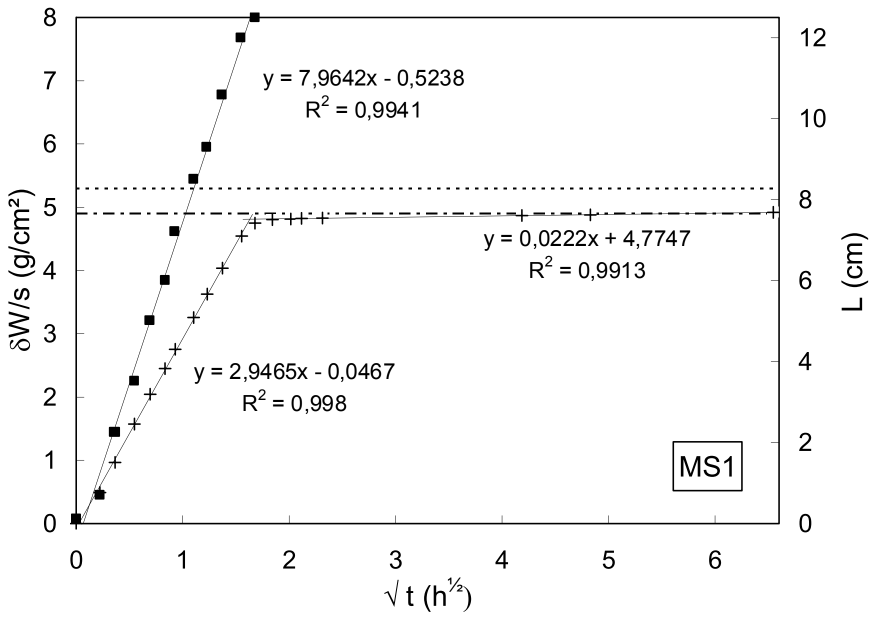
Length (cm)	12.49	
Diameter (cm)	3.88	
Section (cm²)	11.82	
Sample volume (cm^3)	143.91	
$d_{B.\,W}$ (g/cm^3)	1.53	
$d_{M,\,W}$ (g/cm^3)	2.71	
N_W (%)	43.45	
N_{48} (%)	40.24	
S_{48}	0.93	
B (cm h$^{-1/2}$)	7.96	
A (g cm^{-2} h$^{-1/2}$)	2.95	

Sample MS2		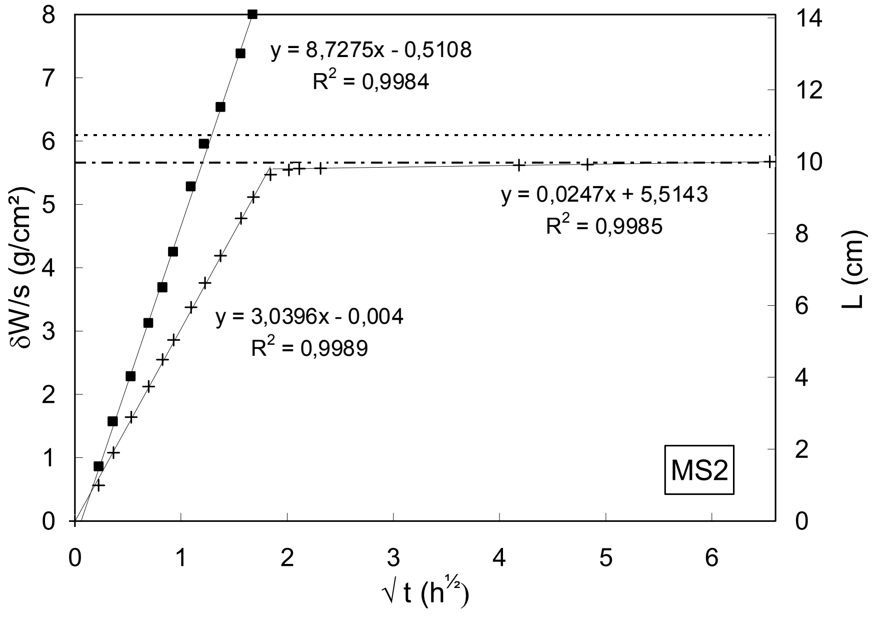
Length (cm)	14.04	
Diameter (cm)	3.85	
Section (cm²)	11.64	
Sample volume (cm^3)	162.00	
$d_{B.\,W}$ (g/cm^3)	1.53	
$d_{M,\,W}$ (g/cm^3)	2.71	
N_W (%)	43.78	
N_{48} (%)	40.67	
S_{48}	0.93	
B (cm h$^{-1/2}$)	8.73	
A (g cm^{-2} h$^{-1/2}$)	3.04	

Sample MS3	
Length (cm)	13.51
Diameter (cm)	3.87
Section (cm²)	11.76
Sample volume (cm^3)	156.22
$d_{B.\,W}$ (g/cm^3)	1.53
$d_{M,\,W}$ (g/cm^3)	2.71
N_W (%)	43.69
N_{48} (%)	40.29
S_{48}	0.92
B (cm h$^{-1/2}$)	8.62
A (g cm^{-2} h$^{-1/2}$)	2.81

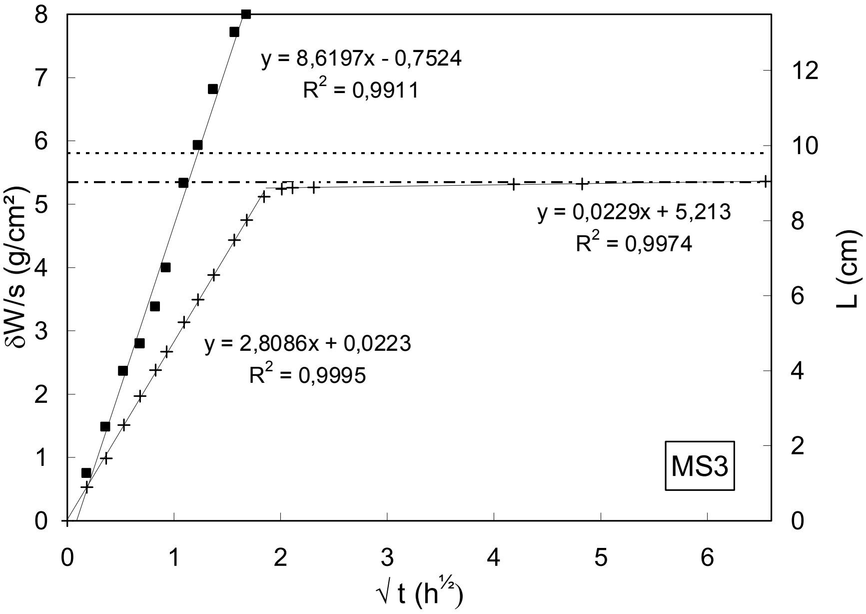

Sample MS4	
Length (cm)	13.35
Diameter (cm)	3.87
Section (cm²)	11.76
Sample volume (cm^3)	154.39
$d_{B.\,W}$ (g/cm^3)	1.52
$d_{M,\,W}$ (g/cm^3)	2.71
N_W (%)	43.60
N_{48} (%)	40.62
S_{48}	0.93
B (cm h$^{-1/2}$)	7.91
A (g cm^{-2} h$^{-1/2}$)	3.01

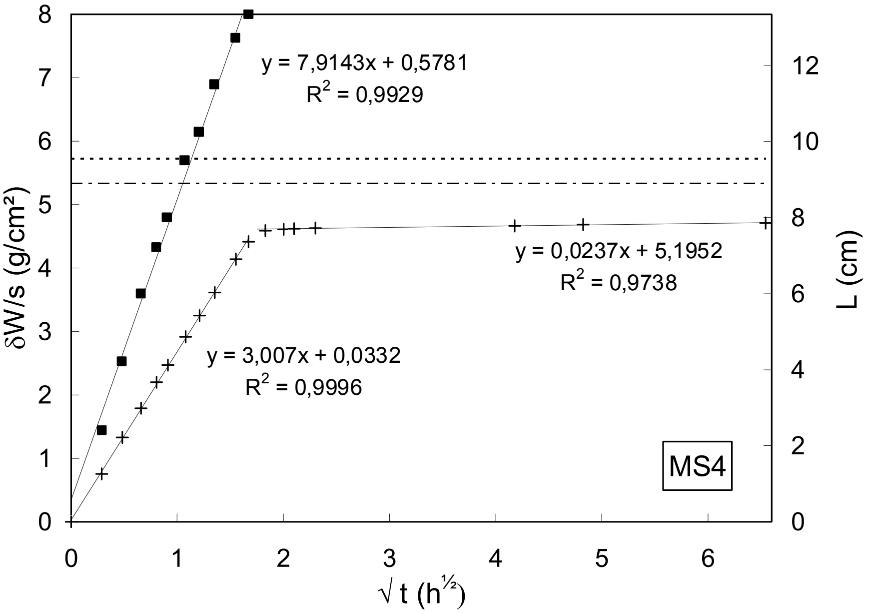

Sample MS5	
Length (cm)	10.70
Diameter (cm)	3.85
Section (cm²)	11.64
Sample volume (cm^3)	134.42
$d_{B.\,W}$ (g/cm^3)	1.53
$d_{M,\,W}$ (g/cm^3)	2.71
N_W (%)	43.72
N_{48} (%)	40.31
S_{48}	0.92
B (cm h$^{-1/2}$)	8.49
A (g cm^{-2} h$^{-1/2}$)	2.86

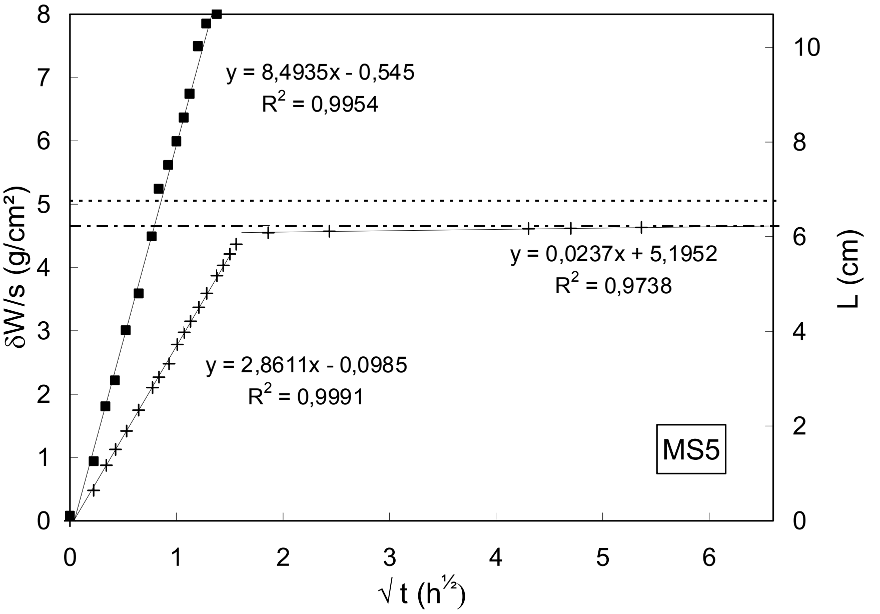

Sample MS6	
Length (cm)	7.04
Diameter (cm)	3.85
Section (cm²)	11.64
Sample volume (cm^3)	80.84
$d_{B.\,W}$ (g/cm^3)	1.53
$d_{M,\,W}$ (g/cm^3)	2.71
N_W (%)	43.46
N_{48} (%)	40.30
S_{48}	0.93
B (cm h$^{-1/2}$)	8.00
A (g cm^{-2} h$^{-1/2}$)	2.94

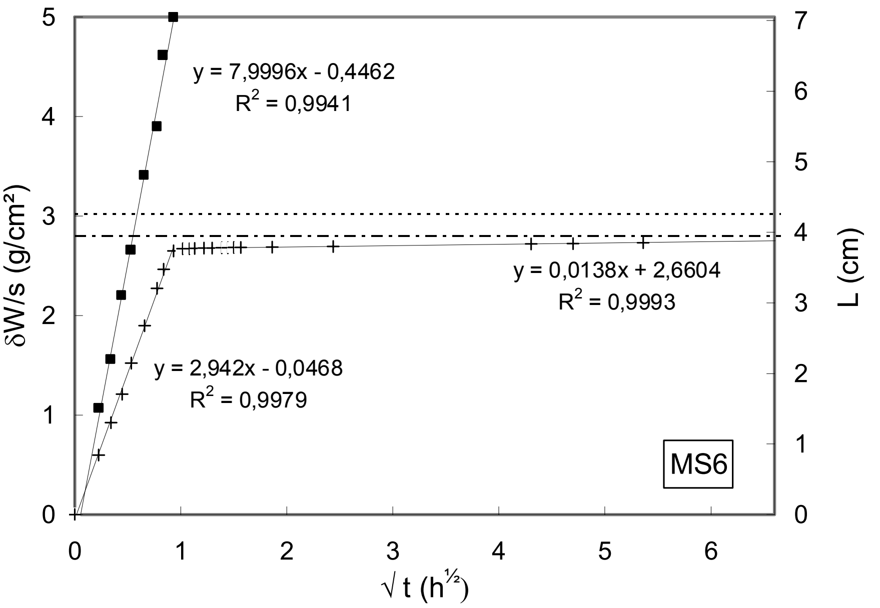

Sample MS7	
Length (cm)	10.45
Diameter (cm)	3.85
Section (cm²)	11.64
Sample volume (cm^3)	120.53
$d_{B,W}$ (g/cm^3)	1.53
$d_{M,W}$ (g/cm^3)	2.71
N_W (%)	43.67
N_{48} (%)	40.34
S_{48}	0.92
B (cm $h^{-1/2}$)	8.37
A (g cm^{-2} $h^{-1/2}$)	2.86

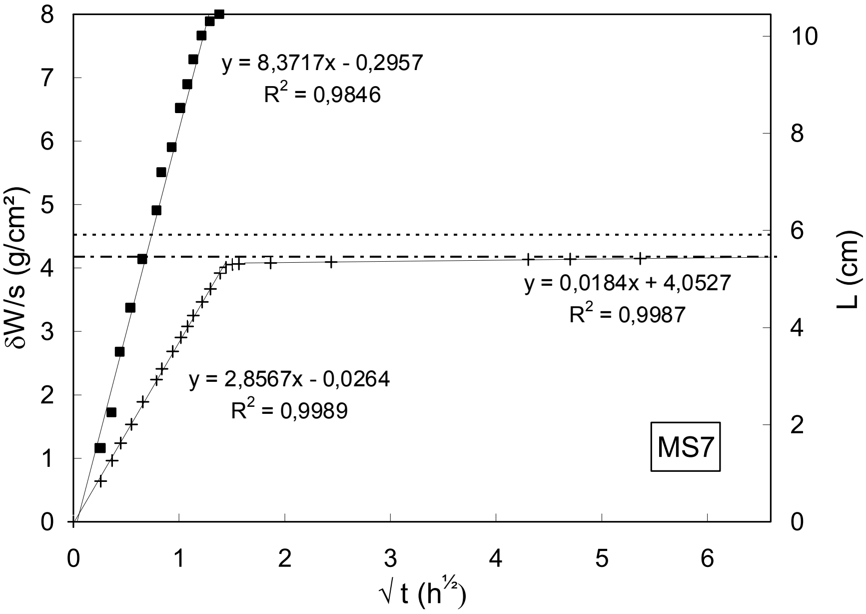

Sample MS8	
Length (cm)	7.79
Diameter (cm)	3.85
Section (cm²)	11.64
Sample volume (cm^3)	89.73
$d_{B,W}$ (g/cm^3)	1.52
$d_{M,W}$ (g/cm^3)	2.71
N_W (%)	43.79
N_{48} (%)	40.25
S_{48}	0.92
B (cm $h^{-1/2}$)	8.57
A (g cm^{-2} $h^{-1/2}$)	2.82

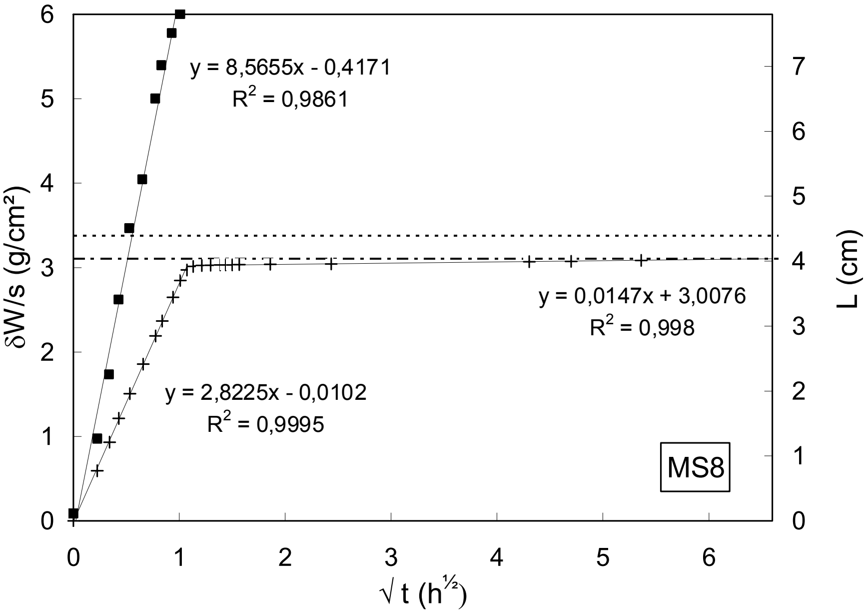

Sample MS9	
Length (cm)	6.30
Diameter (cm)	3.85
Section (cm²)	11.64
Sample volume (cm^3)	72.35
$d_{B.\ W}$ (g/cm^3)	1.52
$d_{M,\ W}$ (g/cm^3)	2.71
N_W (%)	43.83
N_{48} (%)	40.84
S_{48}	0.93
B (cm h$^{-1/2}$)	7.22
A (g cm^{-2} h$^{-1/2}$)	3.02

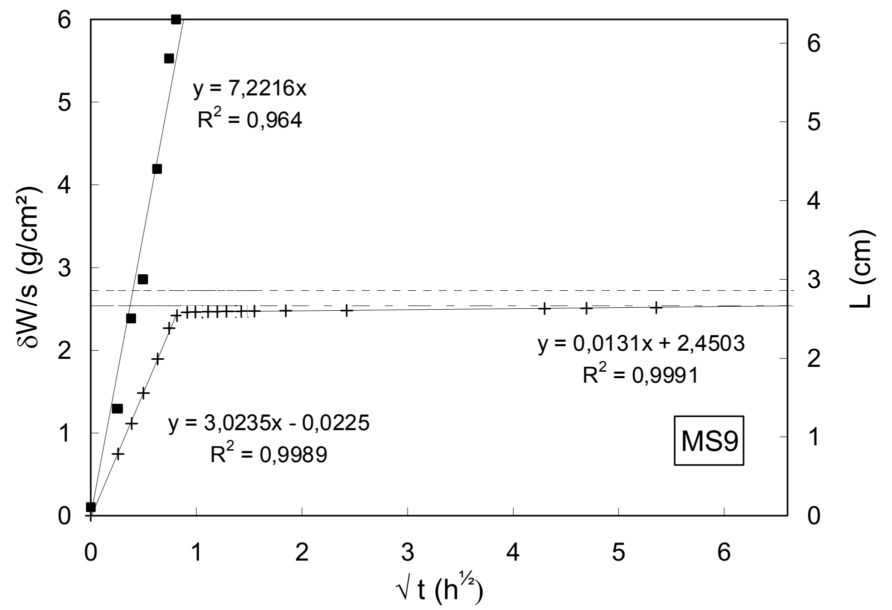

Sample MS10	
Length (cm)	9.98
Diameter (cm)	1.95
Section (cm²)	2.99
Sample volume (cm^3)	28.51
$d_{B.\ W}$ (g/cm^3)	1.52
$d_{M,\ W}$ (g/cm^3)	2.71
N_W (%)	43.74
N_{48} (%)	41.28
S_{48}	0.94
B (cm h$^{-1/2}$)	7.98
A (g cm^{-2} h$^{-1/2}$)	2.91

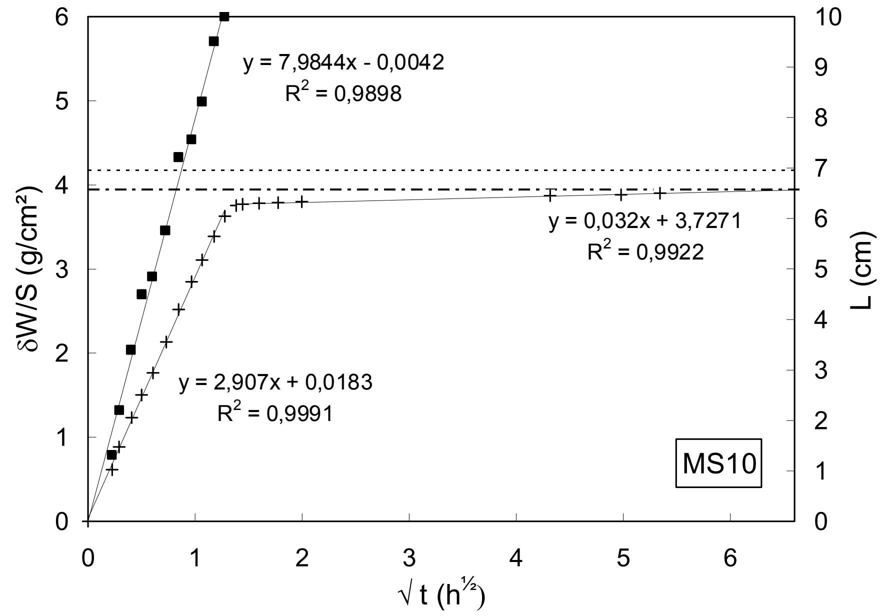

Sample MS11	
Length (cm)	9.35
Diameter (cm)	1.94
Section (cm²)	2.96
Sample volume (cm^3)	26.88
$d_{B.\,W}$ (g/cm^3)	1.53
$d_{M,\,W}$ (g/cm^3)	2.71
N_W (%)	43.68
N_{48} (%)	41.11
S_{48}	0.94
B (cm h$^{-1/2}$)	7.98
A (g cm^{-2} h$^{-1/2}$)	2.91

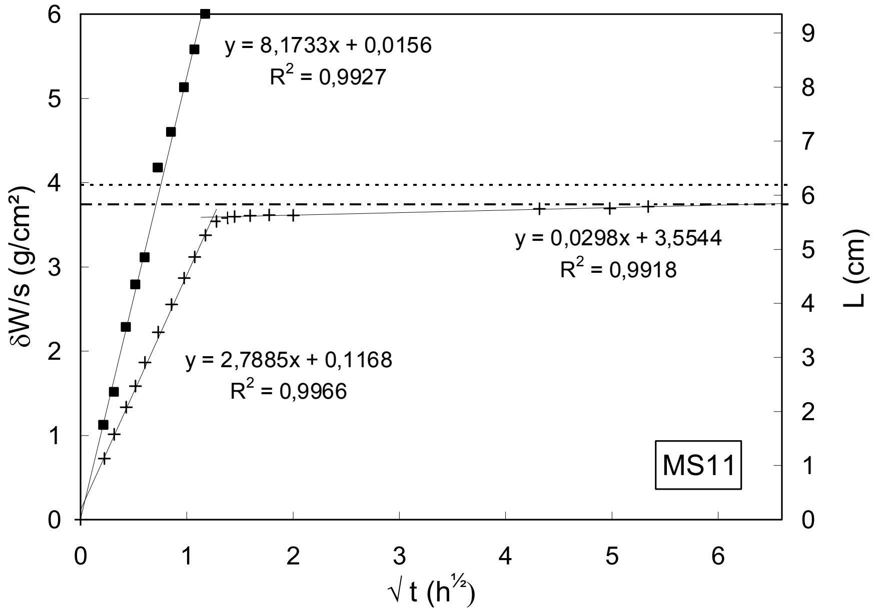

Tuffeau limestone

Sample TUF4	
Length (cm)	6.03
Diameter (cm)	3.8
Section (cm²)	11.34
Sample volume (cm^3)	67.63
$d_{B,W}$ (g/cm^3)	1.33
$d_{M,W}$ (g/cm^3)	2.55
N_W (%)	47.69
N_{48} (%)	40.19
S_{48}	0.84
B (cm h$^{-1/2}$)	5.82
A (g cm^{-2} h$^{-1/2}$)	2.34

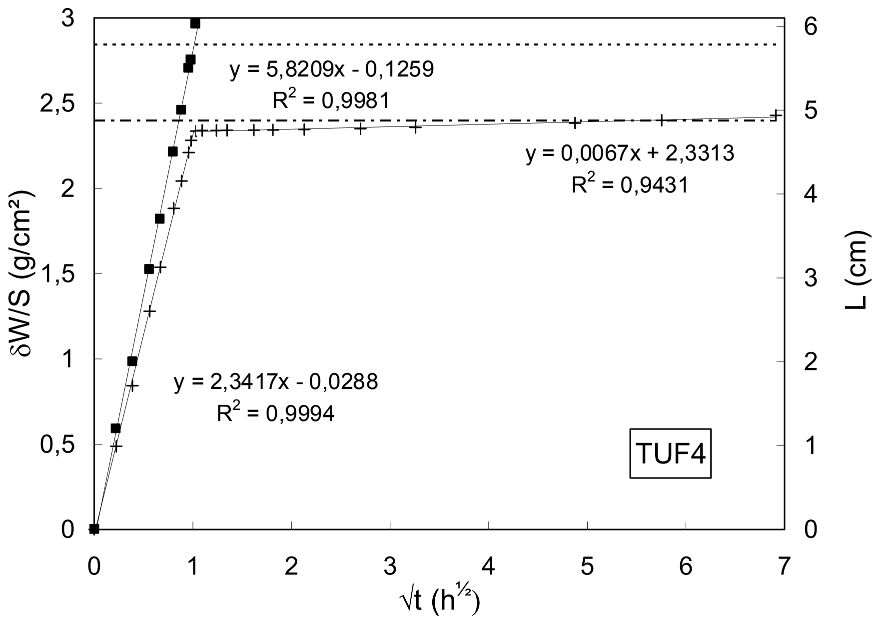

Sample TUF5	
Length (cm)	5.93
Diameter (cm)	3.82
Section (cm²)	11.46
Sample volume (cm^3)	67.85
$d_{B,W}$ (g/cm^3)	1.37
$d_{M,W}$ (g/cm^3)	2.55
N_W (%)	46.46
N_{48} (%)	36.39
S_{48}	0.78
B (cm h$^{-1/2}$)	5.65
A (g cm^{-2} h$^{-1/2}$)	2.19

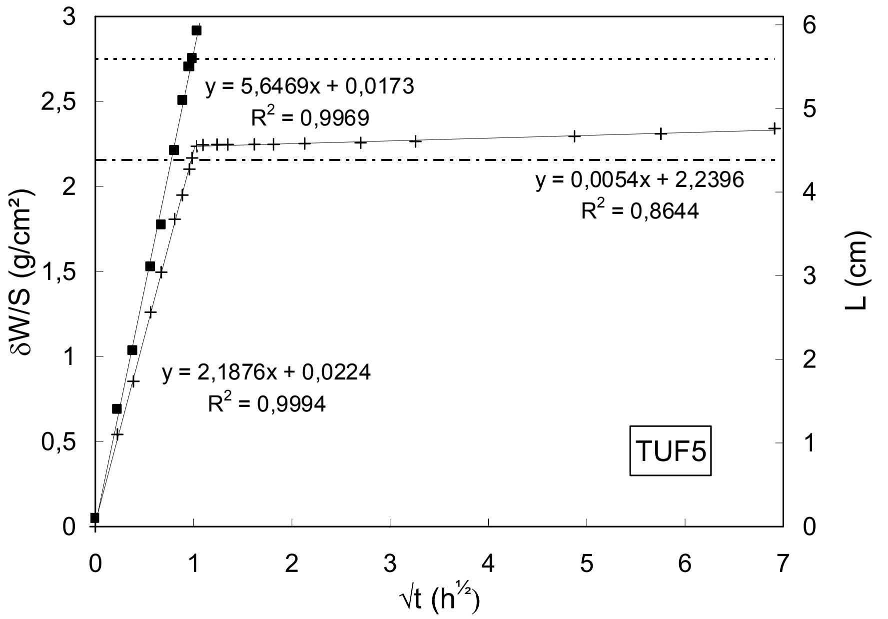

Sample TUF6	
Length (cm)	5.85
Diameter (cm)	3.87
Section (cm²)	11.77
Sample volume (cm^3)	66.46
$d_{B.\,W}$ (g/cm^3)	1.42
$d_{M,\,W}$ (g/cm^3)	2.57
N_W (%)	44.90
N_{48} (%)	37.15
S_{48}	0.83
B (cm h$^{-1/2}$)	5.31
A (g cm^{-2} h$^{-1/2}$)	1.14

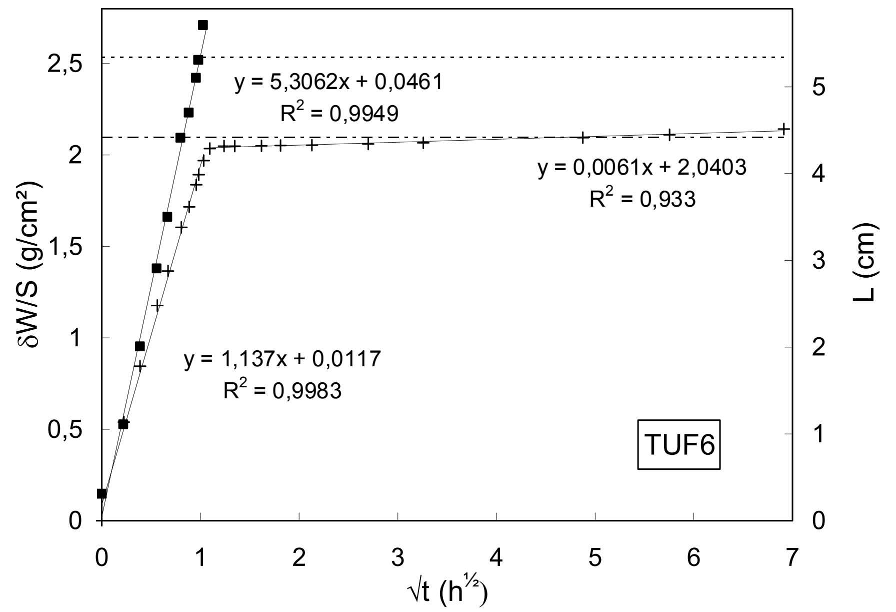

Sample TUF7	
Length (cm)	6.05
Diameter (cm)	3.88
Section (cm²)	11.82
Sample volume (cm^3)	68.88
$d_{B.\,W}$ (g/cm^3)	1.37
$d_{M,\,W}$ (g/cm^3)	2.55
N_W (%)	46.17
N_{48} (%)	38.25
S_{48}	0.83
B (cm h$^{-1/2}$)	5.32
A (g cm^{-2} h$^{-1/2}$)	1.92

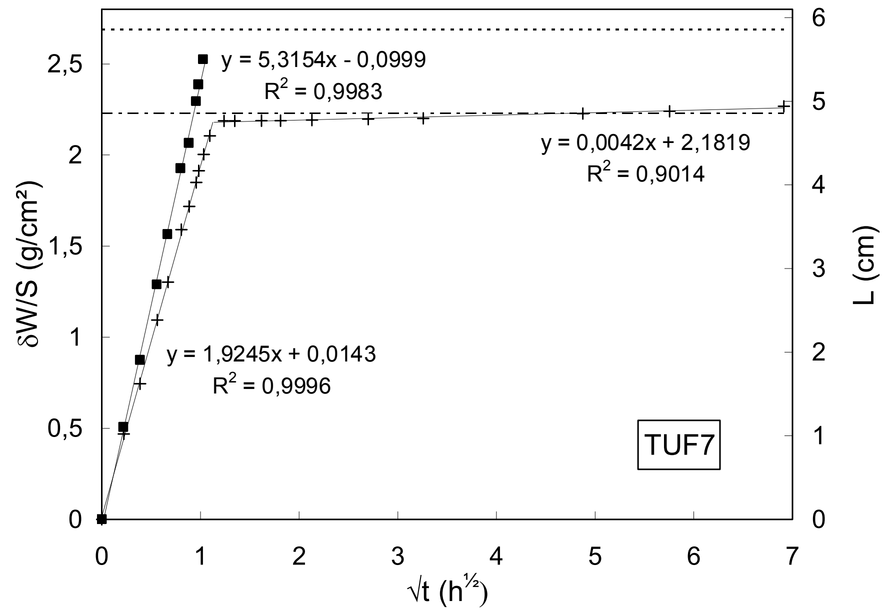

Vuillecin limestone

Sample VUI1 //	
Length (cm)	5.63
Diameter (cm)	3.95
Section (cm²)	12.25
Sample volume (cm^3)	67.96
$d_{B,W}$ (g/cm^3)	2.38
$d_{M,W}$ (g/cm^3)	2.71
N_W (%)	12.37
N_{48} (%)	8.67
S_{48}	0.70
B (cm h$^{-1/2}$)	0.83
A (g cm^{-2} h$^{-1/2}$)	0.07

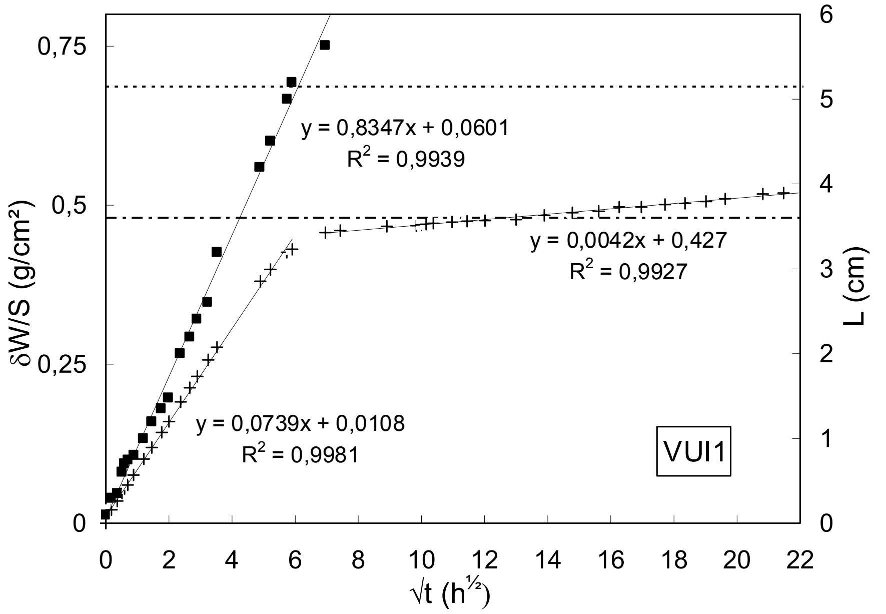

Sample VUI2 //	
Length (cm)	6.0
Diameter (cm)	3.96
Section (cm²)	12.32
Sample volume (cm^3)	69.78
$d_{B,W}$ (g/cm^3)	2.41
$d_{M,W}$ (g/cm^3)	2.71
N_W (%)	11.12
N_{48} (%)	7.82
S_{48}	0.70
B (cm h$^{-1/2}$)	0.68
A (g cm^{-2} h$^{-1/2}$)	0.05

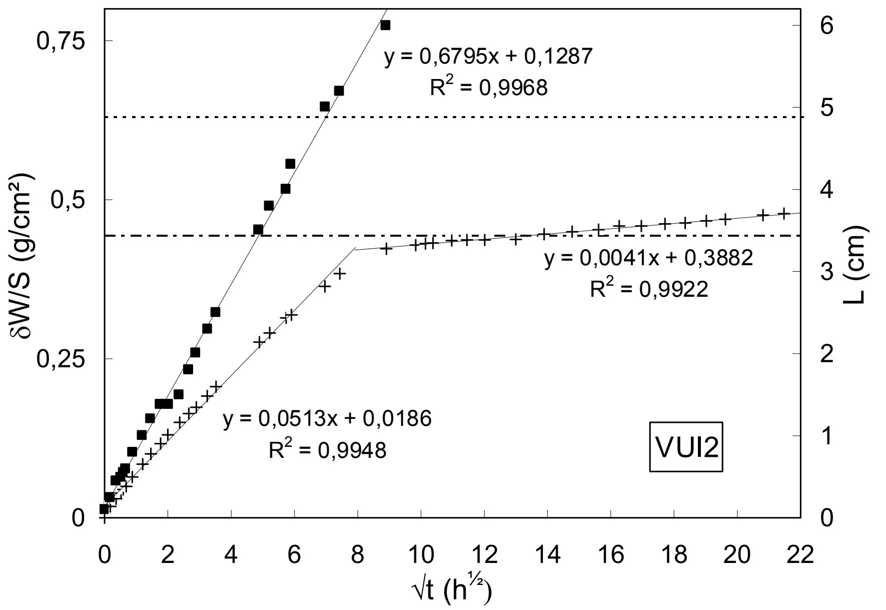

Sample VUI3 //	
Length (cm)	5.8
Diameter (cm)	3.96
Section (cm²)	12.32
Sample volume (cm^3)	69.04
d$_{B.\,W}$ (g/cm^3)	2.40
d$_{M,\,W}$ (g/cm^3)	2.71
N$_W$ (%)	11.43
N$_{48}$ (%)	8.31
S$_{48}$	0.73
B (cm h$^{-1/2}$)	0.74
A (g cm^{-2} h$^{-1/2}$)	0.06

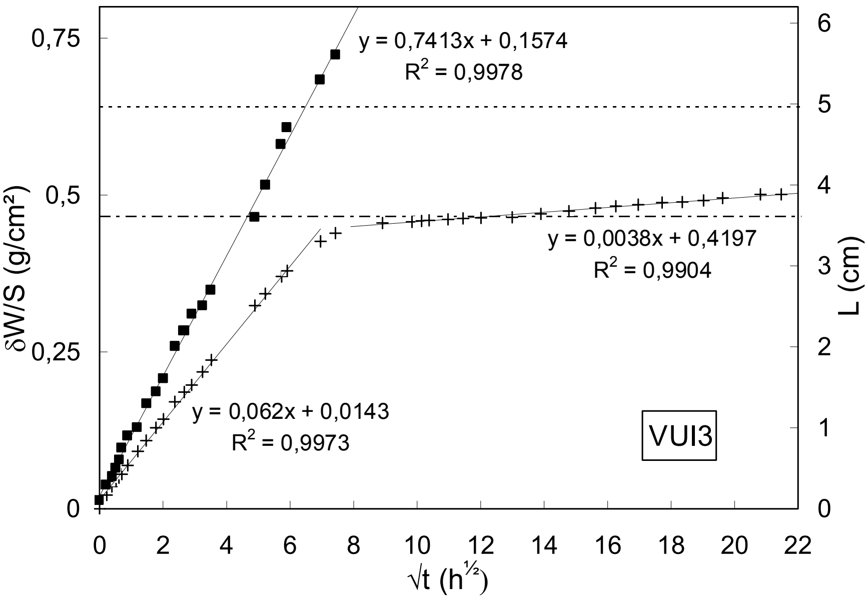

Sample VUI4 //	
Length (cm)	4.8
Diameter (cm)	3.96
Section (cm²)	12.32
Sample volume (cm^3)	57.78
d$_{B.\,W}$ (g/cm^3)	2.43
d$_{M,\,W}$ (g/cm^3)	2.71
N$_W$ (%)	10.54
N$_{48}$ (%)	7.51
S$_{48}$	0.71
B (cm h$^{-1/2}$)	0.84
A (g cm^{-2} h$^{-1/2}$)	0.06

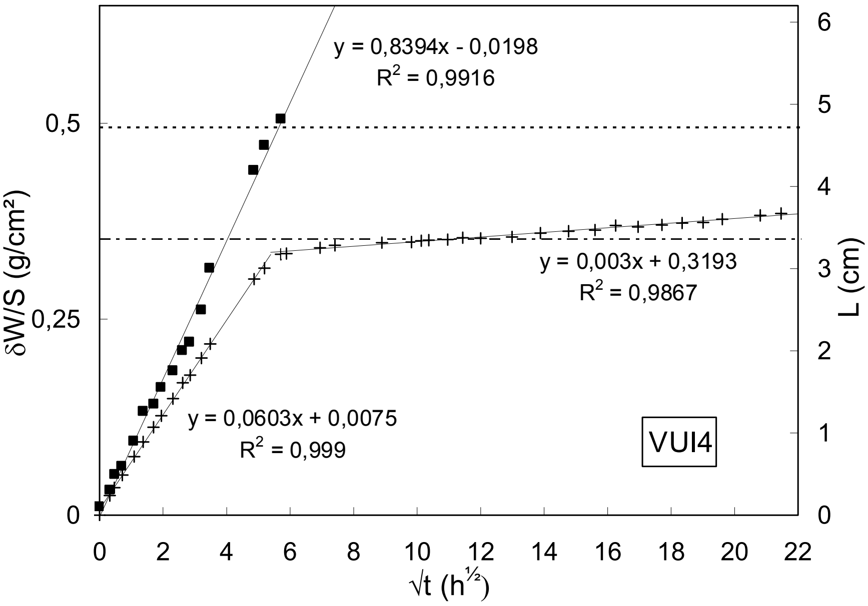

Sample VUI5 ⊥	
Length (cm)	5.7
Diameter (cm)	3.96
Section (cm²)	12.32
Sample volume (cm^3)	68.80
$d_{B.\,W}$ (g/cm^3)	2.39
$d_{M,\,W}$ (g/cm^3)	2.71
N_W (%)	11.89
N_{48} (%)	8.36
S_{48}	0.70
B (cm $h^{-1/2}$)	0.53
A (g cm^{-2} $h^{-1/2}$)	0.04

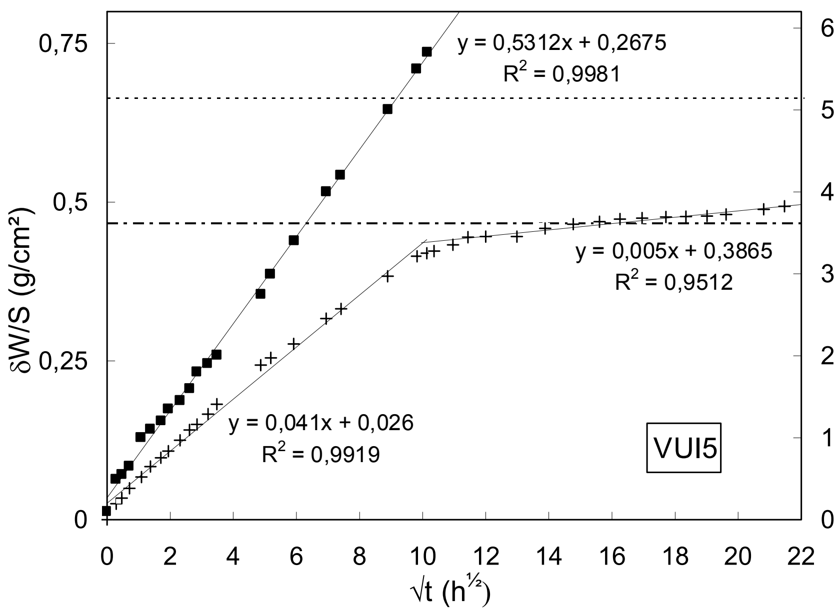

Sample VUI6 ⊥	
Length (cm)	5.3
Diameter (cm)	3.96
Section (cm²)	12.32
Sample volume (cm^3)	64.08
$d_{B.\,W}$ (g/cm^3)	2.39
$d_{M,\,W}$ (g/cm^3)	2.71
N_W (%)	11.77
N_{48} (%)	8.49
S_{48}	0.72
B (cm $h^{-1/2}$)	0.59
A (g cm^{-2} $h^{-1/2}$)	0.07

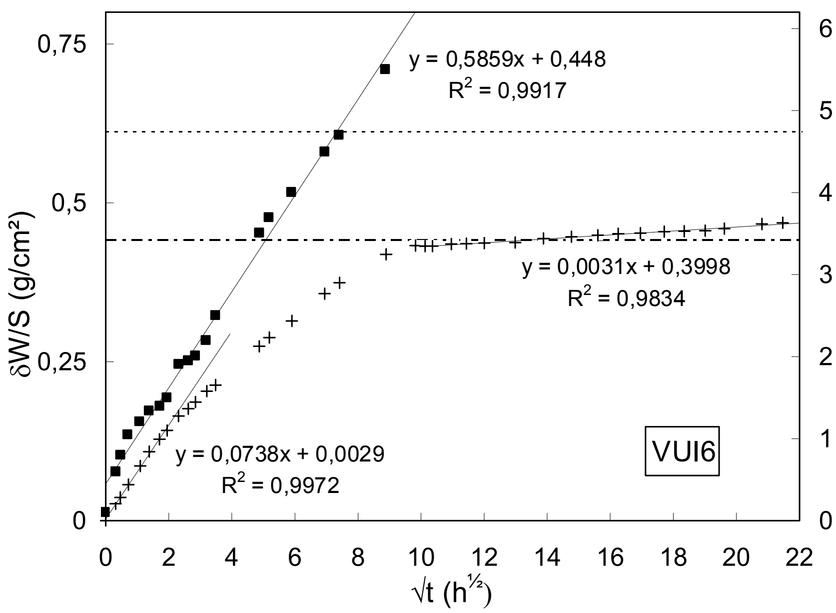

Sample VUI7 ⊥	
Length (cm)	5.7
Diameter (cm)	3.97
Section (cm²)	12.38
Sample volume (cm^3)	67.90
$d_{B.\,W}$ (g/cm^3)	2.37
$d_{M,\,W}$ (g/cm^3)	2.71
N_W (%)	12.37
N_{48} (%)	8.66
S_{48}	0.70
B (cm h$^{-1/2}$)	0.58
A (g cm^{-2} h$^{-1/2}$)	0.07

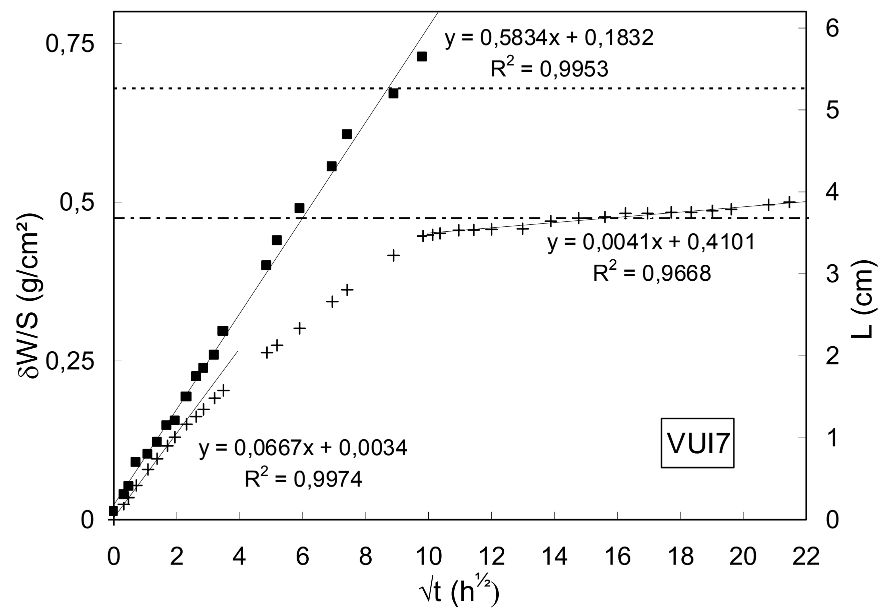

Sample VUI8 ⊥	
Length (cm)	5.8
Diameter (cm)	3.97
Section (cm²)	12,.80
Sample volume (cm^3)	69.31
$d_{B.\,W}$ (g/cm^3)	2.37
$d_{M,\,W}$ (g/cm^3)	2.71
N_W (%)	12.67
N_{48} (%)	8.64
S_{48}	0.68
B (cm h$^{-1/2}$)	0.55
A (g cm^{-2} h$^{-1/2}$)	0.04

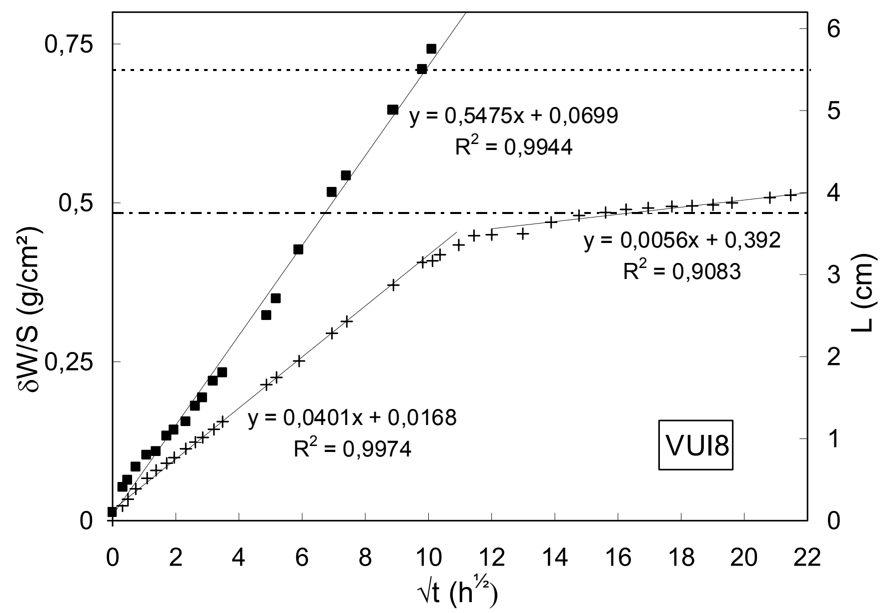

Sample VUI9 ⊥	
Length (cm)	5.9
Diameter (cm)	3.97
Section (cm²)	12.38
Sample volume (cm^3)	69.31
$d_{B. W}$ (g/cm^3)	2.37
$d_{M, W}$ (g/cm^3)	2.71
N_W (%)	12.67
N_{48} (%)	8.92
S_{48}	0.70
B (cm h$^{-1/2}$)	0.63
A (g cm^{-2} h$^{-1/2}$)	0.06

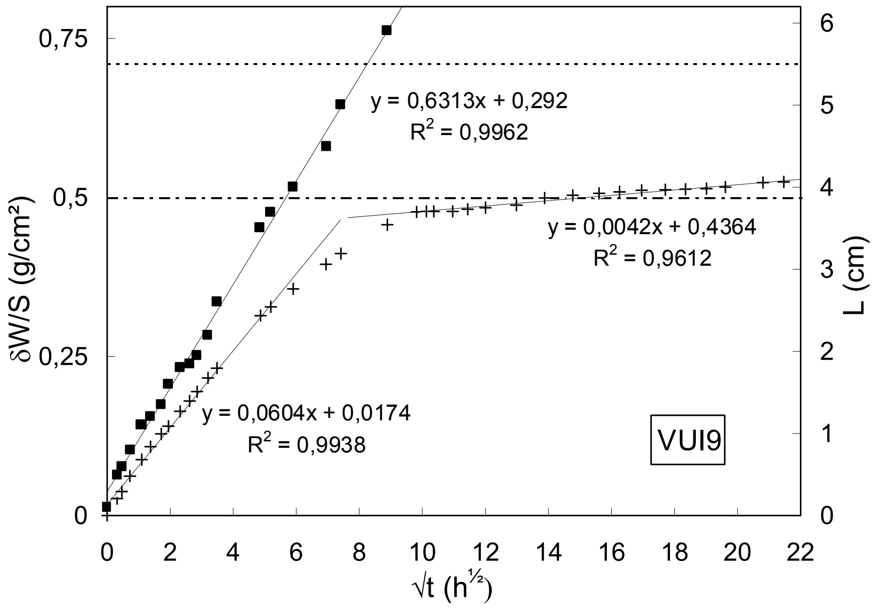

Appendix I:
Theory of a spherical pore model – Simulation of capillary water imbibition

Related bibliography: MERZ J.D. et al., 1988; HAMMECKER C.et al., 1989; HAMMECKER C.et al., 1993; HAMMECKER C., 1993

The problem of the correlation B-pore size of the capillary water imbibition kinetics led the authors to think about flow paths, which would be made of elementary spheres (see figure below). The authors have developed a model of spherical pores for the simulation of capillary imbibition in sedimentary rocks.

Spherical pores

Poiseuille's law expresses the water flow in a tube as a function of the radius R, the differential pressure ΔP and the length L of the cylinder:

$$Q = \frac{\pi R^4 \Delta P}{8\eta L} \qquad (I1)$$

with ΔP given by the relation:

$$\Delta P = \frac{2\gamma \cos\theta}{R} - \rho g L \qquad (I2)$$

Considering a vertical water imbibition in a sphere, the radius of the water section is a function of R, the radius of the sphere and L, height of water:

$$r(L) = \left(2RL - L^2\right)^{-1/2} \qquad (I3)$$

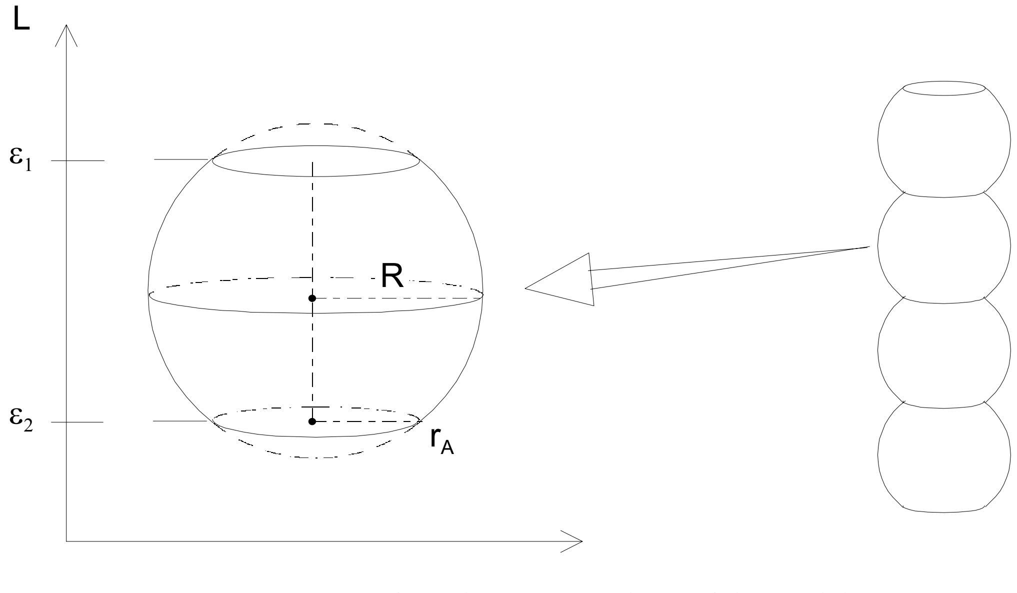

Representation of an elementary sphere of the model.

Then, the pressure difference expressed by Relation *I2* ($\cos\theta \approx 1$) becomes:

$$\Delta P = \frac{2\gamma}{r(L)} - \rho g L \quad (I4)$$

The same calculation as for the cylinder pore theory leads to the following expression of imbibition velocity:

$$\frac{dL}{dt} = \frac{R_A^4}{8\eta L\, r(L)^2}\left(\frac{2\gamma}{r(L)} - \rho g L\right) \quad (I5)$$

where R_A is the radius of the smaller section, through which water flows, that is the pore access size.

In order to obtain a direct relation between L and the time t, we consider the length of the water path given by the ordinates of the top and bottom points of the elementary sphere. The height of water is ε_2-ε_1 (Fig. A) with:

$$\varepsilon_1 = R - (R^2 - R_A^2)^{1/2} \quad (I6)$$

$$\varepsilon_2 = R + (R^2 - R_A^2)^{1/2} \quad (I7)$$

Then, the model needs the determination of only two geometrical parameters R and R_A, which correspond to D, pore diameter, and D_A, pore access diameter, respectively. The analytical determination of these parameters requires the application of a packing model of spherical particles.

Granular model: determination of the model parameters D and D_A

The mineral structure of the rock is reduced to uniform spherical grains, which can be packed in three ways: cubic, tetrahedral, octahedral. For each rock, the theoretical diameter D_S of these grains is determined from the experimental specific surface area (S_{BET}) and bulk density ($d_{B,\,Hg}$).

The external surface of a sphere is written:

$$S = \pi D_S^2 \quad (I8)$$

The fraction surface/volume is expressed by:

$$S/V = 6/D_S \quad (I9)$$

Introducing the bulk density (d_B) and the specific surface area (S_i), the diameter of the particles is determined with the following relation (LOWELL S. and SHIELDS J.E., 1984):

$$D_S = \frac{6}{d_B S_i} \quad (I10)$$

For each type of packing, the interspaces between the particles can be characterized by the diameter D of a sphere, which could be included in a pore between the particles, and the diameter D_A of a sphere, which could fill the access to the pore. Then, the size of the inter-particle spaces D and D_A can be geometrically determined from D_S as shown in the following table:

Expression of D and D_A *as a function of* D_S *according to the type of packing:*

	D	D_A
Cubic	$D_S/\sqrt{2}$	$D_S(\sqrt{8}-2)/2$
Tetrahedral	$D_S((2\sqrt{3}-\pi)/2\pi)^{-1/2}$	$D_S(2\sqrt{3}-3)/3$
Octahedral	$D_S(\sqrt{8}-2)/2$	$D_S(2\sqrt{3}-3)/3$

Empirical expression of B

For each type of particle packing, the authors have applied the spherical pore model to calculate B coefficients for an imbibition through a 10 cm-height L. They have plotted the values of B versus the specific surface area and came to the following empirical relation:

$$B = \frac{a}{\sqrt{d_B S_i}} \qquad (I11)$$

with the condition $0.1 < S_i < 50$ m²/g.

The model constant a depends on the type of particle packing:

- Cubic: $a = 28.91$
- Tetrahedral: $a = 23.07$
- Octahedral: $a = 9.882$

Appendix J:
Data from the simulations with the PORE-COR model

Legend:

N_{PC} (%): Simulated total porosity

$D_{A,PC}$ (µm): Simulated mean pore access diameter

S_{PC} ($m^2\ g^{-1}$): Simulated specific surface area

K_{PC} (mD): Simulated gas permeability

Γ_{PC}: Connectivity of the simulated porous network

N_{Hg} (%): Total porosity measured by mercury porosimetry

D_{50} (µm): Median pore access diameter from mercury porosimetry

S_{Hg} ($m^2\ g^{-1}$): Specific surface area measured by mercury porosimetry

σ_N: Porosity standard deviation between the simulation and the experiment

Fontainebleau sandstone

Sample Ftt1:

PORE-COR simulation		Experimental results (mercury porosimetry)	
N_{PC} (%)	10.8	N_{Hg} (%)	10.8
$D_{A,PC}$ (µm)	55.7	D_{50} (µm)	30.4
S_{PC} (m²/g)	$2\ 10^{-3}$	S_{Hg} (m²/g)	$12\ 10^{-3}$
K_{PC} (mD)	2760		
Γ_{PC}	4.3		

Porosity standard deviation $\sigma_N = 0.1\%$

Cumulative percent of total porosity curves

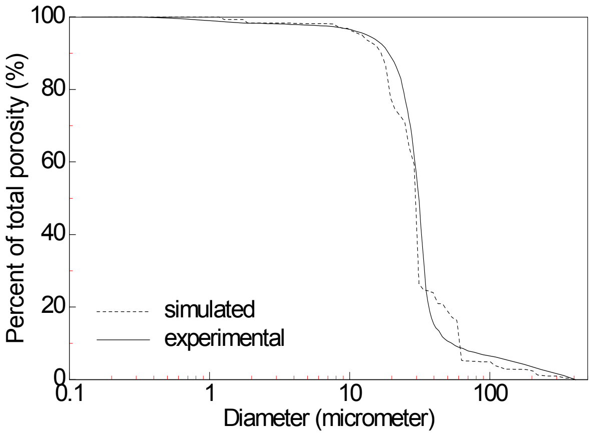

Pore and throat size distributions

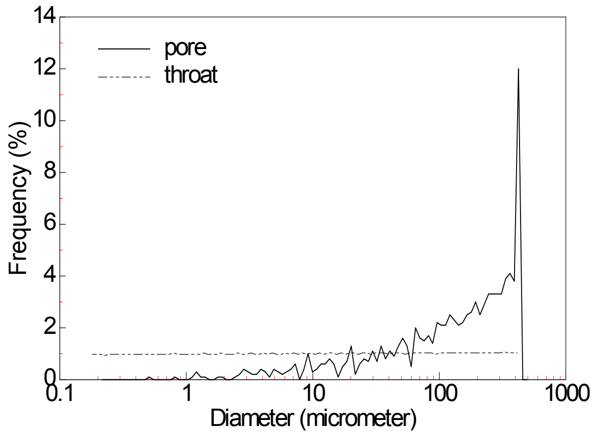

3D-simulated unit cell for Ftt1

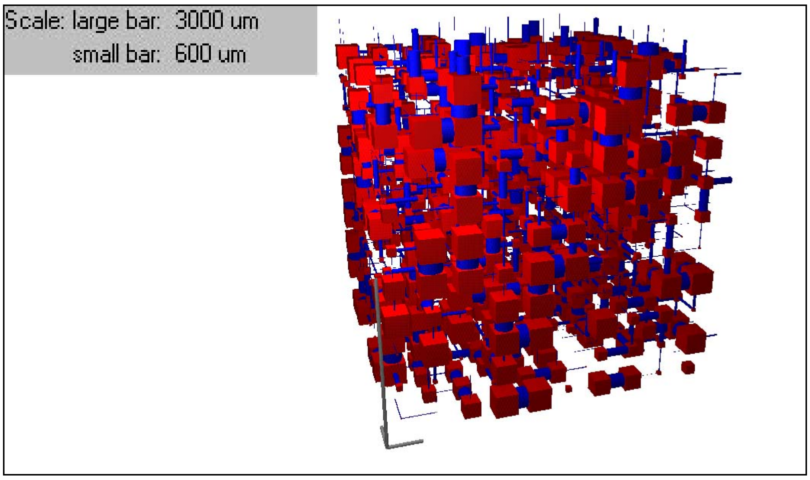

Sample FS19:

PORE-COR simulation		Experimental results (mercury porosimetry)	
N_{PC} (%)	13.2	N_{Hg} (%)	13.2
$D_{A,PC}$ (µm)	57.3	D_{50} (µm)	33.8
S_{PC} (m²/g)	$2\ 10^{-3}$	S_{Hg} (m²/g)	$11\ 10^{-3}$
K_{PC} (mD)	3277		
Γ_{PC}	4.3		

Porosity standard deviation $\sigma_N = 0.1\%$

Cumulative percent of total porosity curves

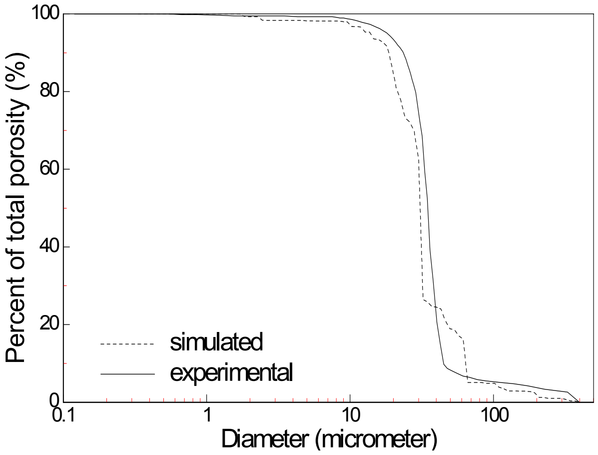

Pore and throat size distributions

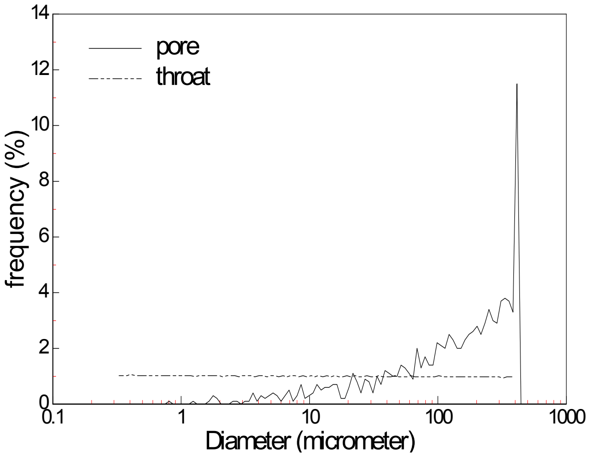

“Grès à Meules“ sandstone

Sample GMT0:

PORE-COR simulation		Experimental results (mercury porosimetry)	
N_{PC} (%)	23.0	N_{Hg} (%)	23.8
$D_{A,PC}$ (µm)	35.6	D_{50} (µm)	7.5
S_{PC} (m²/g)	$3\ 10^{-3}$	S_{Hg} (m²/g)	3.1
K_{PC} (mD)	2		
Γ_{PC}	3.4		

Porosity standard deviation σ_N = 1.4%

Cumulative percent of total porosity curves

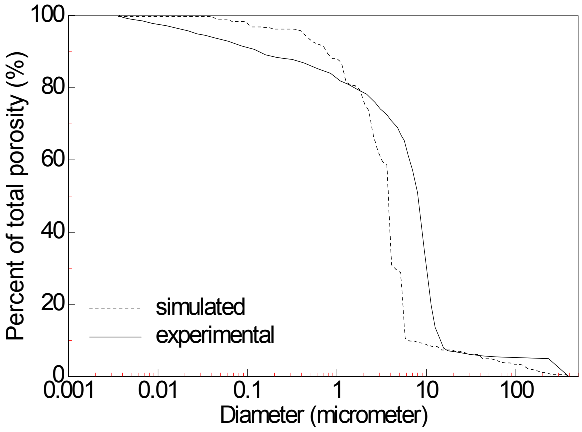

Pore and throat size distributions

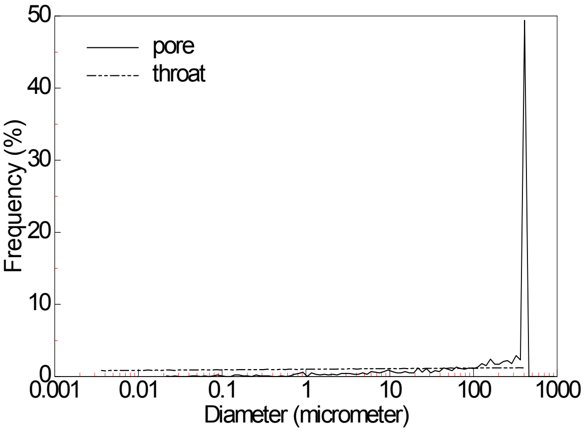

3D-simulated unit cell for GMT0

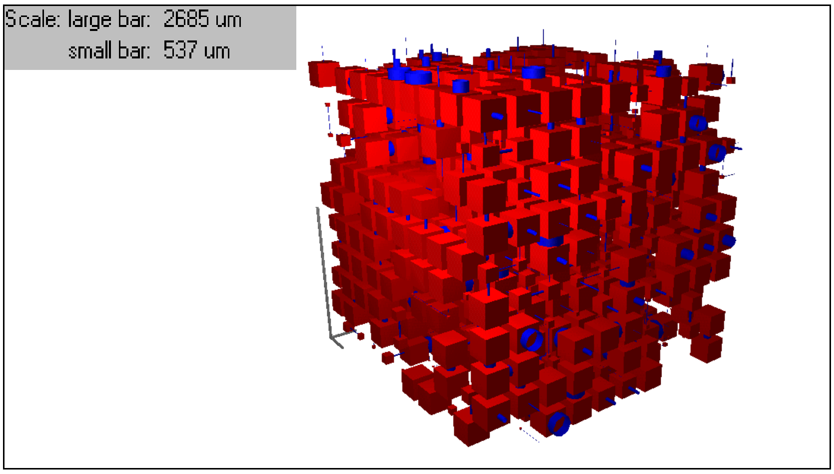

Sample S2GM28:

PORE-COR simulation		Experimental results (mercury porosimetry)	
N_{PC} (%)	21.1	N_{Hg} (%)	21.1
$D_{A,PC}$ (μm)	37.0	D_{50} (μm)	9.4
S_{PC} (m²/g)	$3\ 10^{-3}$	S_{Hg} (m²/g)	0.4
K_{PC} (mD)	63		
Γ_{PC}	4.4		

Porosity standard deviation σ_N = 2.7%

Cumulative percent of total porosity curves

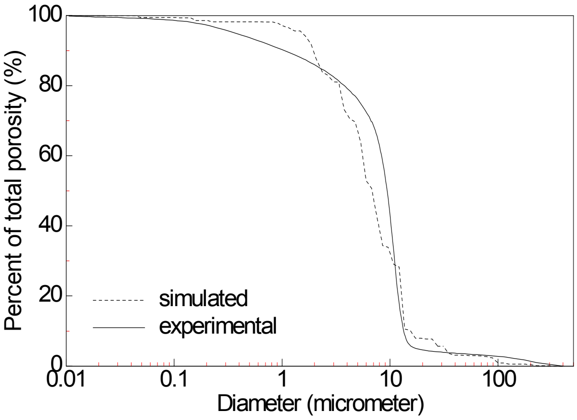

Pore and throat size distributions

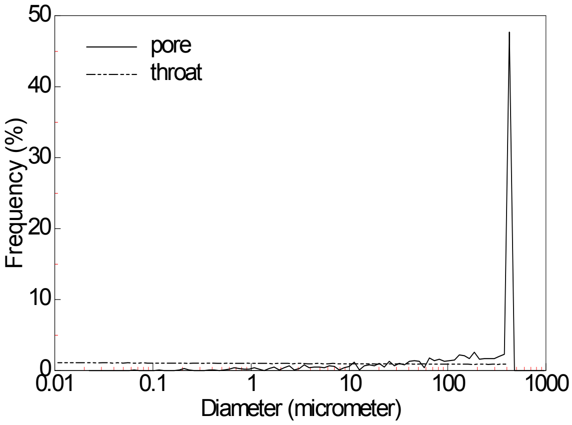

Mons chalk

Sample CM49:

PORE-COR simulation		Experimental results (mercury porosimetry)	
N_{PC} (%)	41.2	N_{Hg} (%)	41.2
$D_{A,PC}$ (μm)	2.0	D_{50} (μm)	0.7
S_{PC} (m²/g)	0.3	S_{Hg} (m²/g)	2.0
K_{PC} (mD)	1		
Γ_{PC}	3.3	Porosity standard deviation $\sigma_N = 0.1\%$	

Cumulative percent of total porosity curves

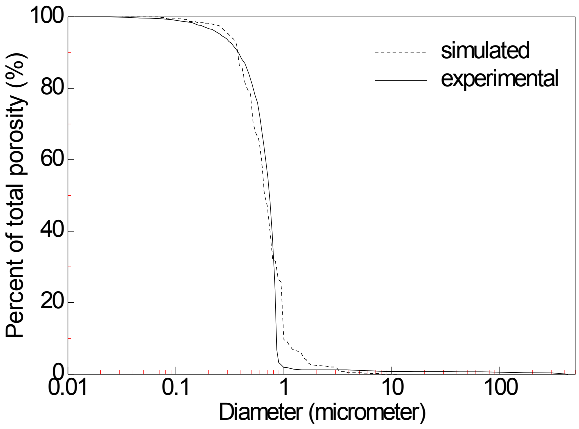

Pore and throat size distributions

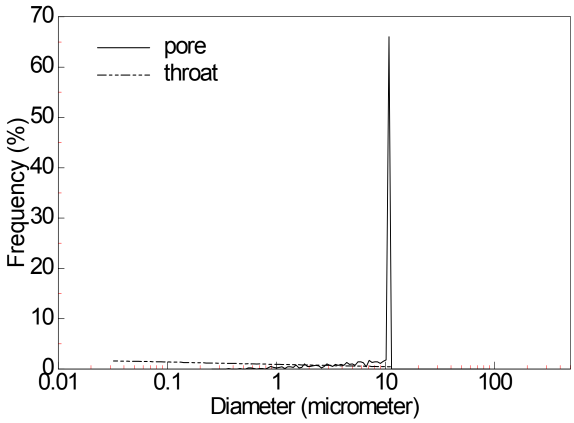

3D-simulated unit cell for CM49

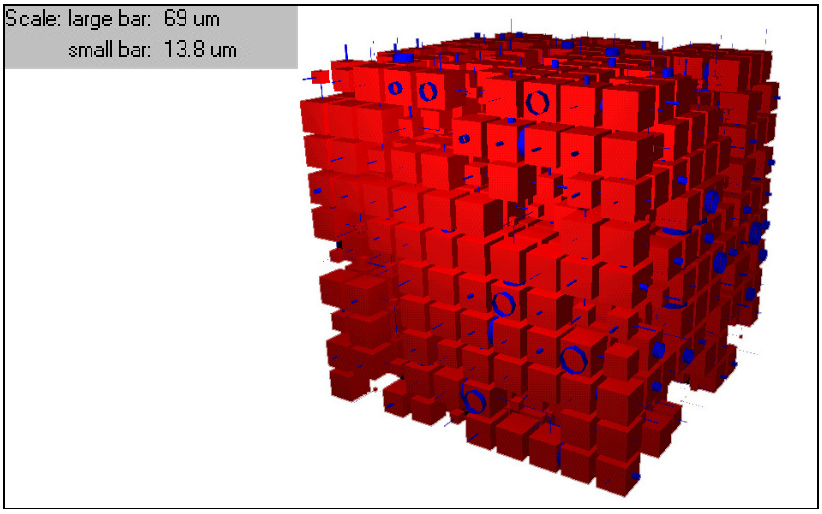

Sample CM68:

PORE-COR simulation		Experimental results (mercury porosimetry)	
N_{PC} (%)	38.8	N_{Hg} (%)	38.8
$D_{A,PC}$ (μm)	0.6	D_{50} (μm)	0.7
S_{PC} (m²/g)	0.9	S_{Hg} (m²/g)	1.7
K_{PC} (mD)	6		
Γ_{PC}	4.4		

Porosity standard deviation $\sigma_N = 0.0\%$

Cumulative percent of total porosity curves

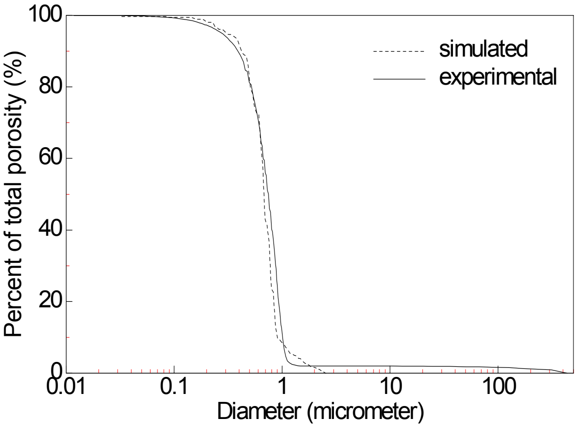

Pore and throat size distributions

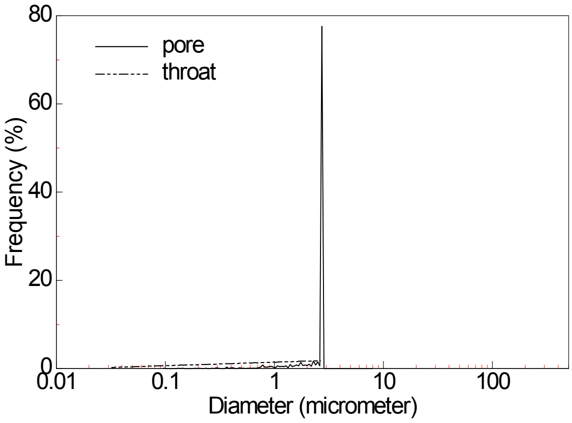

Tuffeau limestone

Sample TUF060:

PORE-COR simulation		Experimental results (mercury porosimetry)	
N_{PC} (%)	45.2	N_{Hg} (%)	45.2
$D_{A,PC}$ (µm)	34.5	D_{50} (µm)	3.4
S_{PC} (m²/g)	$10\ 10^{-3}$	S_{Hg} (m²/g)	23.0
K_{PC} (mD)	$10\ 10^{-3}$		
Γ_{PC}	3.3		

Porosity standard deviation $\sigma_N = 5.0\%$

Cumulative percent of total porosity curves

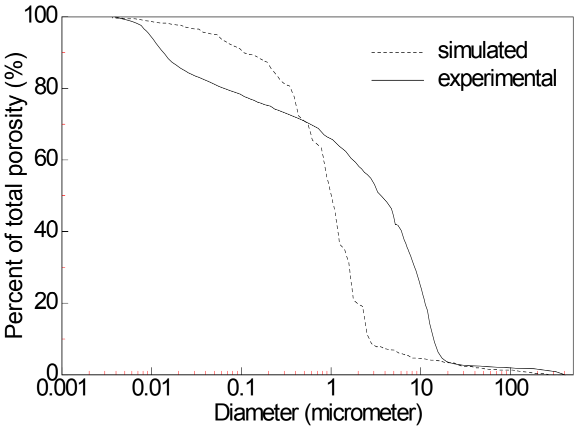

Pore and throat size distributions

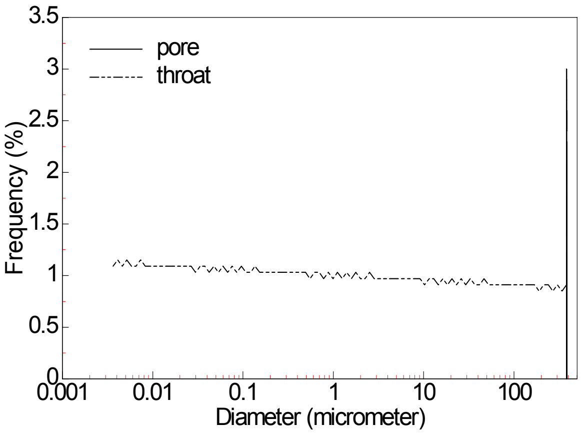

3D-simulated unit cell for TUF060

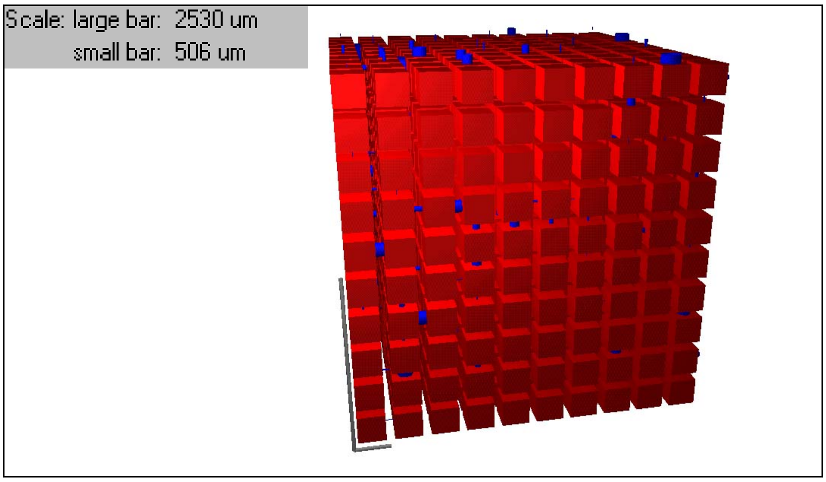

Sample TUF062:

PORE-COR simulation		Experimental results (mercury porosimetry)	
N_{PC} (%)	46.7	N_{Hg} (%)	46.7
$D_{A,PC}$ (µm)	35.4	D_{50} (µm)	3.9
S_{PC} (m²/g)	$10\ 10^{-3}$	S_{Hg} (m²/g)	24.9
K_{PC} (mD)	$20\ 10^{-3}$		
Γ_{PC}	3.3		

Porosity standard deviation σ_N = 5.2%

Cumulative percent of total porosity curves

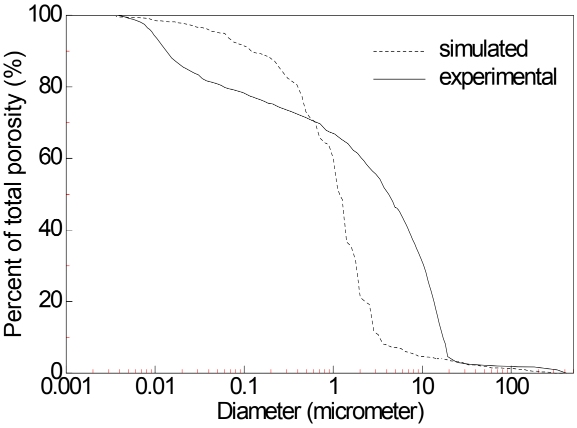

Pore and throat size distributions

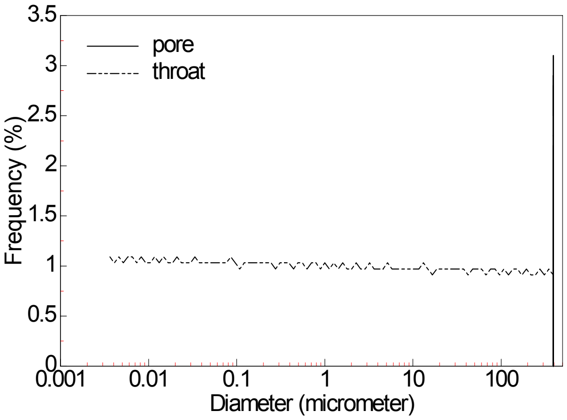

Vuillecin limestone

Sample NK03:

PORE-COR simulation		Experimental results (mercury porosimetry)	
N_{PC} (%)	12.0	N_{Hg} (%)	12.2
$D_{A,PC}$ (µm)	1.1	D_{50} (µm)	0.8
S_{PC} (m²/g)	0.1	S_{Hg} (m²/g)	1.2
K_{PC} (mD)	0.1		
Γ_{PC}	3.3		

Porosity standard deviation $\sigma_N = 0.5\%$

Cumulative percent of total porosity curves

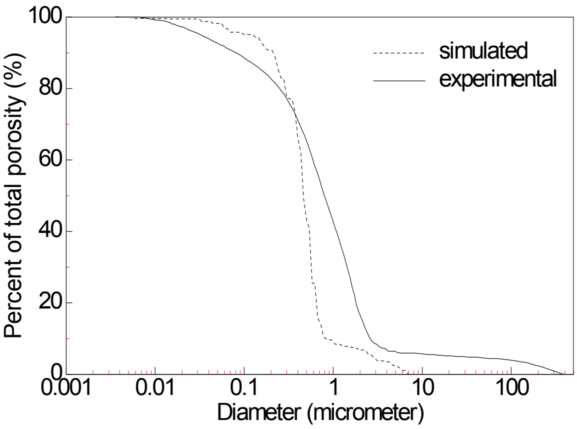

Pore and throat size distributions

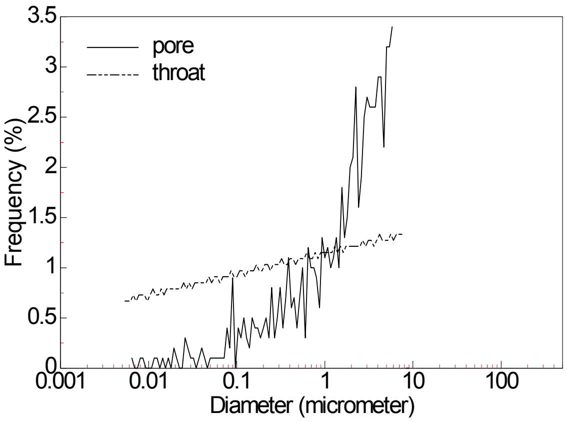

3D-simulated unit cell for NK03

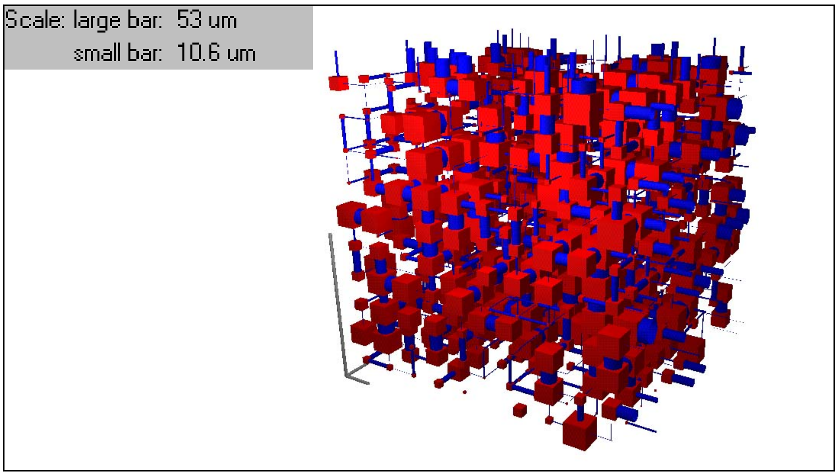

Sample NK12:

PORE-COR simulation		Experimental results (mercury porosimetry)	
N_{PC} (%)	12.0	N_{Hg} (%)	12.1
$D_{A,PC}$ (µm)	35.3	D_{50} (µm)	0.9
S_{PC} (m²/g)	$2\ 10^{-3}$	S_{Hg} (m²/g)	1.7
K_{PC} (mD)	$1\ 10^{-4}$		
Γ_{PC}	3.0		

Porosity standard deviation σ_N = 1.8%

Cumulative percent of total porosity curves

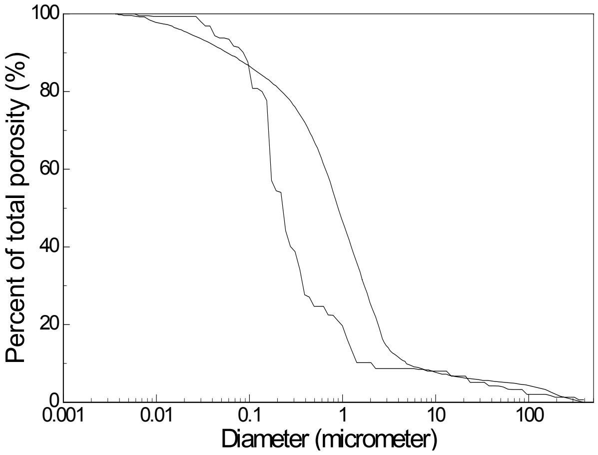

Pore and throat size distributions

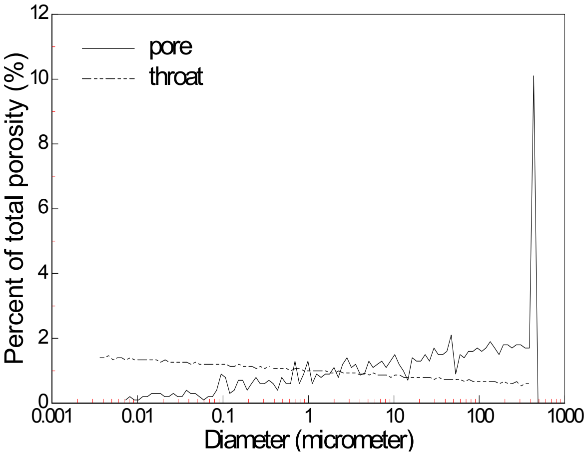

Appendix K:
Certificate example of a Certified Reference Material

The following certificate of CRM-BAM-P120 was provided by the Federal Institute for Materials Research and Testing (Berlin, Germany) using mercury porosimetry as certification method. The establishment of the certificates needs inter-laboratory analyses. The certificates contain information about:

- the certified properties (values and uncertainty range),
- the certified curves,
- instruction for the use of the reference material,
- declaration of conformity with standards and guides (e.g. ISO Guides 30-35)

Federal Institute for Materials Research and Testing

CERTIFIED REFERENCE MATERIAL
FOR MERCURY INTRUSION (HIGH PRESSURE RANGE)

CERTIFICATE OF ANALYSIS

CRM BAM-PM-120
Material: Beads of α-alumina

Certified properties:

A) **Pressure-volume curve between 0.1 MPa and 400 MPa (see Fig. A1 and A2 in Annex 1 and Table in Annex 2 for values at each data point)**

B) **Diameter-volume curve between 3.7 nm and 14708 nm (see Fig. A3 and A4 in Annex 1 and Table in Annex 2 for values at each data point)**

C) **Pore volume at selected intrusion pressure points as well as values for the pore diameter (see Table 1)**

Table 1 Single values of certified properties

Property	Unit	$\bar{\bar{x}}$	s	s/√n
Pore volume at 100 MPa	$mm^3 \cdot g^{-1}$	545,0	12,2	2.4
Pore volume at 195 MPa	$mm^3 \cdot g^{-1}$	546,7	12,7	2.5
Pore volume at 200 MPa	$mm^3 \cdot g^{-1}$	546,8	12,7	2.5
Pore volume at 395 MPa	$mm^3 \cdot g^{-1}$	548,1	13,1	2.6
Mean pore width d_{50}	nm	228,0	5,9	1.2
Most frequent pore width $d_{p,m}$	nm	232,2	8,8	1.8

$\bar{\bar{x}}$ average of laboratory averages (certified value)
s standard deviation of laboratory averages
n number of laboratories (outlier free) participating in the interlaboratory study (here 25)

Table 2 Non-certified property

	Unit	Value
Specific surface area*	$m^2 \cdot g^{-1}$	9,6

* only as additional information, given without uncertainty, calculated according to $A_{sp} = 4 \cdot V / d$ using the certified properties V_{200MPa} and d_{50} (diameter at 50 % specific pore volume)

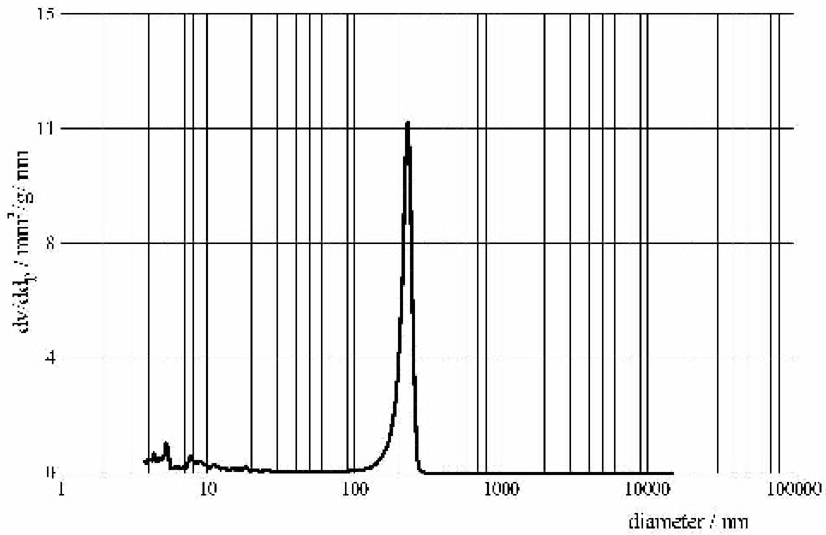

Figure 1 Pore size distribution of CRM BAM-PM-120

DESCRIPTION OF THE SAMPLE

The reference material consists of beads of α-alumina. The particles form stabile agglomerates. Mercury porosimetry measures the voids inside the agglomerates.

INSTRUCTION FOR USE

The reference material is intended for use in the calibration and checking of high pressure mercury porosimeters in the pressure range between 0.1 and 400 MPa.

The unopened bottle should be stored at normal ambient temperature in a dry place.

The recommended minimum sample intake is 0.3 g or more depending on the equipment used.

Use mercury with a purity of 99.9999 % (outgassed) or better.

Prior to the analysis, a heating procedure for drying the sample is necessary. Heat the reference material for 3 hours at 105 °C.

Because of the volume between the particles of the sample (intergranular volume with a more or less random character), the mercury filling procedure of the penetrometer (dilatometer) should be carried out with caution.

DATA EVALUATION

In order to obtain the certified values, the intergranular volume recorded during the filling procedure has to be subtracted from the intrusion curve at the beginning of the data evaluation. The transformation of the intrusion pressure data p_{Hg} into pore diameter values d_p according to the Washburn equation $d_p = 4\,\gamma \cos\theta / p_{Hg}$ (assuming a cylindric pore model) has to be carried out using the following values of the parameters: $\gamma = 0.48\ \mathrm{N\ m^{-1}}$ (surface tension of mercury) and $\theta = 140°$ (contact angle of mercury). The most frequent pore diameter is the maximum of the pore size distribution curve dv/dd (see Fig. 1)

SHELF LIFE

Provided the sample is stored and handled appropriately, the certification will remain valid for 24 months from the date of shipment.

PARTICIPATING LABORATORIES

Co-ordination

Bundesanstalt für Materialforschung und -prüfung, DE

Participants:

- Bundesanstalt für Materialforschung und -prüfung, Berlin, DE (5 equipments in 2 laboratories)
- Degussa AG, Hanau, DE
- Delft University of Technology, Delft, NL
- DMT - Gesellschaft für Lehre und Bildung mbH, Bochum, DE
- Dr. C. Otto Feuerfest GmbH, Bochum, DE
- Forschungsinstitut der Zementindustrie Düsseldorf, Düsseldorf, DE
- Forschungsinstitut für anorganische Werkstoffe - Glas/Keramik - GmbH, Höhr-Grenzhausen, DE
- Fraunhofer-Institut für Bauphysik, Valley-Oberlaindern, DE
- Grace GmbH, Worms, DE
- Hermsdorfer Institut für Technische Keramik e.V., Hermsdorf/Thür., DE
- Hüls Infracor GmbH, Marl, DE
- Materialprüfanstalt für das Bauwesen, Braunschweig, DE
- MBF Gesellschaft für Materialprüfung und Baustofforschung mbH, Berlin, DE
- Merck KG aA, Darmstadt, DE
- Micromeritics GmbH, Möchengladbach, DE
- Quantachrome GmbH, Odelzhausen, DE
- Rheinisch-Westfälische Technische Hochschule, Aachen, DE (2 laboratories)
- Technische Universität Dresden, Dresden, DE
- Technische Universität Hamburg-Harburg, Hamburg, DE
- ThermoQuest Italia S.p.A., CE Instruments, Rodano (Milan), IT
- Universität Gesamthochschule Siegen, Siegen, DE
- Universität Hannover, Hannover, DE
- Universität Karlsruhe, Karlsruhe, DE
- Universiteit van Amsterdam, Amsterdam, NL

ANALYTICAL METHODS USED

Mercury intrusion according to DIN 66 133

DOCUMENTATION

Guidelines for the production and certification of BAM reference materials

BCR/48/93 (1994)	Guidelines for the production and certification of BCR reference materials
ASTM D 4284-92	Standard test method for determining pore volume distribution of catalysts by mercury intrusion porosimetry
BS 7591-1 : 1992	Porosity and pore size distribution of materials. Method of evaluation by mercury porosimetry
DIN 66133 : 1993	Bestimmung der Porenvolumenverteilung und der spezifischen Oberfläche von Feststoffen durch Quecksilberintrusion (Determination of the pore volume distribution and the specific surface area of solids by mercury intrusion)
ISO/WD 155 901-1	Pore size distribution and porosity of solid materials – Evaluation by mercury porosimetry and gas sorption, Part 1: Mercury porosimetry (WG 3) July 1998

LEGAL NOTICE

Neither the Federal Institute for Materials Research and Testing (BAM) nor any person acting on its behalf make any warranty or representation, express or implied, that the use of any information, material, apparatus, method or process disclosed in this document may not infringe privately owned rights, or assume any liability with respect to the use of, or damages resulting from the use of any information, material, apparatus, method or process disclosed in this document.

Date of shipment: ....

BAM
for certified true copy

Prof Dr A. Zschunke	Prof Dr K. Meyer
Head of Department Analytical Chemistry, Reference Materials	Head of Division Inorganic Chemical Analysis; Reference Materials

Annex 1

CERTIFIED CURVES

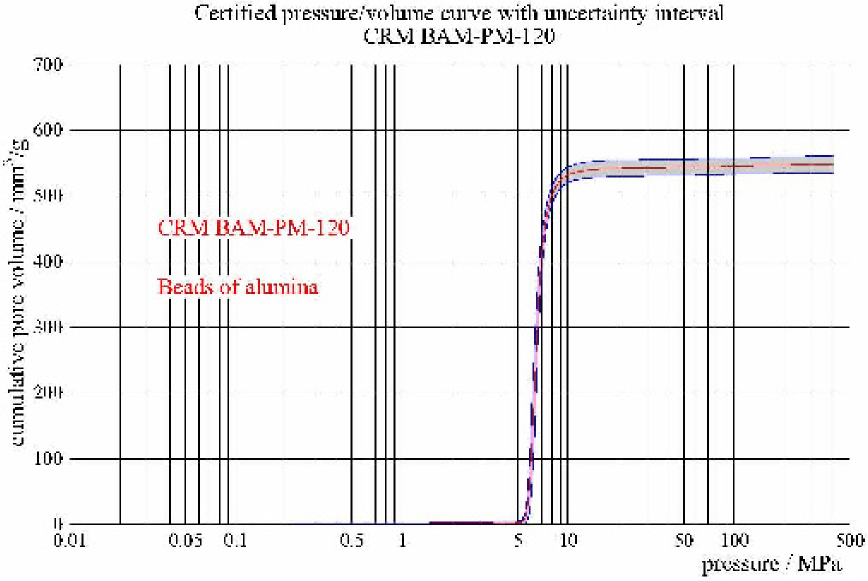

Figure A1

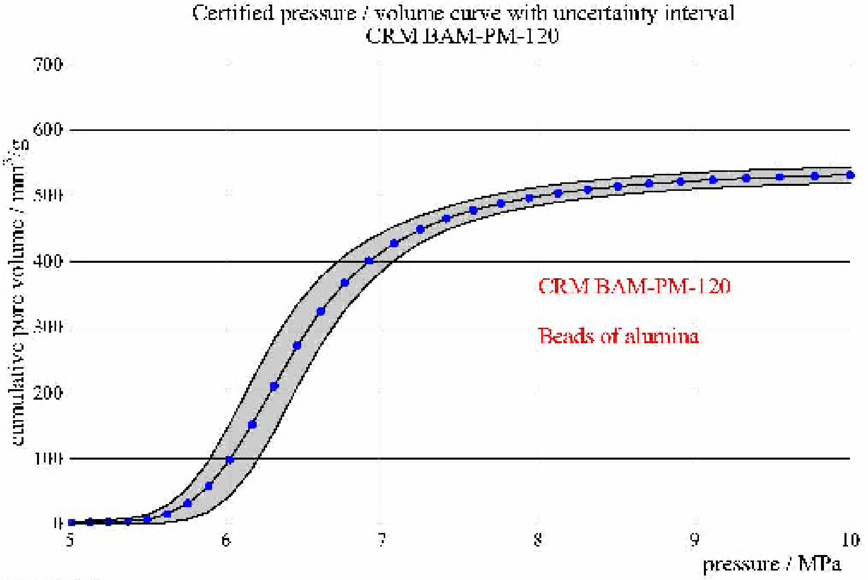

Figure A2

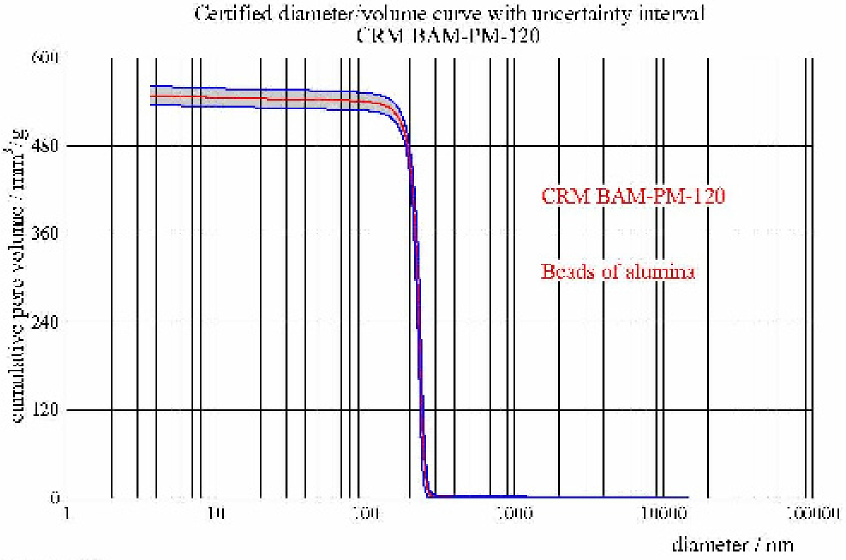

Figure A3

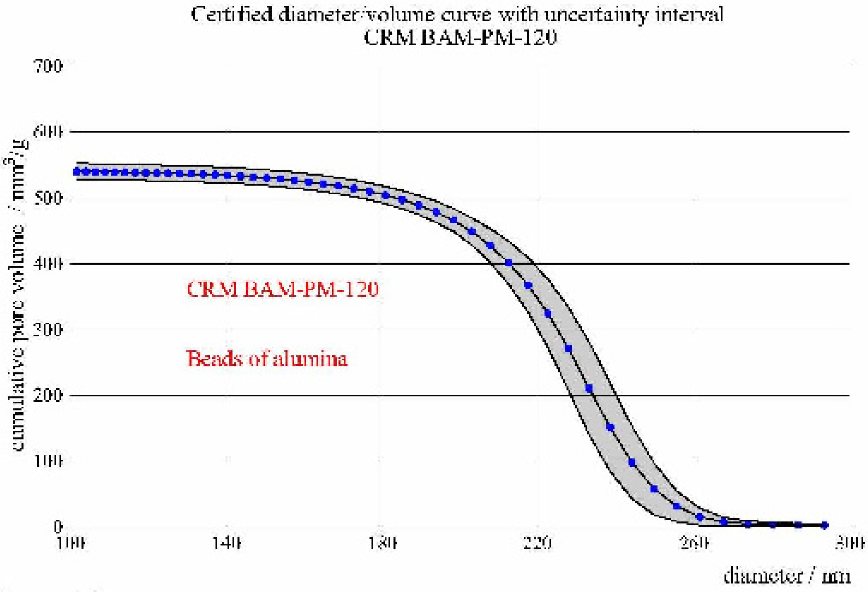

Figure A4

Annex 2

CRM BAM-PM-120

Certified values of the pressure-volume and the diameter-volume curves at each data point

Data point No.	p_{Hg} (MPa)	d_p (nm)	v_p (mm^3/g)	s (mm^3/g)	v_p+s (mm^3/g)	v_p-s (mm^3/g)
1	0.100	14708.063	0.000	0.210	0.210	-0.210
2	0.102	14372.299	0.004	0.219	0.223	-0.214
3	0.105	14046.062	0.011	0.216	0.227	-0.204
4	0.107	13726.545	0.021	0.215	0.236	-0.194
5	0.110	13412.962	0.035	0.216	0.251	-0.182
6	0.112	13106.549	0.054	0.226	0.280	-0.171
7	0.115	12810.219	0.074	0.236	0.310	-0.162
8	0.117	12516.559	0.092	0.243	0.335	-0.151
9	0.120	12233.671	0.110	0.253	0.363	-0.143
10	0.123	11955.143	0.132	0.263	0.394	-0.131
11	0.126	11683.979	0.156	0.275	0.431	-0.119
12	0.129	11417.080	0.182	0.293	0.475	-0.110
13	0.132	11157.772	0.204	0.306	0.510	-0.103
14	0.135	10902.254	0.221	0.316	0.537	-0.095
15	0.138	10655.076	0.239	0.327	0.566	-0.088
16	0.141	10412.466	0.266	0.347	0.613	-0.081
17	0.145	10175.465	0.292	0.369	0.660	-0.077
18	0.148	9943.954	0.314	0.384	0.698	-0.070
19	0.151	9717.572	0.340	0.401	0.741	-0.062
20	0.155	9496.296	0.364	0.421	0.785	-0.056
21	0.158	9280.173	0.385	0.435	0.820	-0.050
22	0.162	9068.913	0.415	0.444	0.859	-0.029
23	0.166	8862.462	0.437	0.455	0.892	-0.018
24	0.170	8660.762	0.459	0.469	0.928	-0.010
25	0.174	8463.605	0.481	0.481	0.961	0.000
26	0.178	8270.943	0.505	0.490	0.994	0.015
27	0.182	8082.880	0.525	0.505	1.029	0.021
28	0.186	7899.560	0.549	0.516	1.065	0.033
29	0.191	7719.990	0.575	0.534	1.109	0.041
30	0.195	7545.210	0.587	0.544	1.131	0.043
31	0.200	7377.497	0.600	0.554	1.154	0.046
32	0.204	7203.686	0.610	0.570	1.180	0.039
33	0.209	7039.704	0.618	0.584	1.202	0.034
34	0.214	6878.480	0.627	0.597	1.225	0.030
35	0.219	6722.882	0.639	0.615	1.254	0.023
36	0.224	6569.878	0.648	0.630	1.278	0.018
37	0.229	6420.292	0.659	0.648	1.307	0.011
38	0.234	6274.151	0.671	0.666	1.337	0.005
39	0.240	6131.545	0.682	0.681	1.363	0.000
40	0.245	5991.769	0.692	0.695	1.387	-0.003
41	0.251	5855.575	0.704	0.712	1.416	-0.008
42	0.257	5722.067	0.715	0.729	1.445	-0.015
43	0.263	5591.842	0.727	0.747	1.474	-0.020
44	0.269	5464.570	0.738	0.766	1.504	-0.028
45	0.275	5340.768	0.753	0.793	1.545	-0.040
46	0.282	5218.676	0.765	0.814	1.580	-0.049
47	0.288	5098.877	0.778	0.830	1.609	-0.052
48	0.295	4983.727	0.791	0.845	1.635	-0.054
49	0.302	4870.297	0.805	0.865	1.670	-0.060
50	0.309	4759.426	0.821	0.885	1.707	-0.064

p_{Hg} - mercury intrusion pressure
d_p - pore diameter
v_p - specific pore volume
s - uncertainty (see page 1)
v_p+s - upper limit of the uncertainty interval
v_p- s - lower limit of the uncertainty interval

Certified values of the pressure-volume and the diameter-volume curves

Data point No.	p_{Hg} (MPa)	d_p (nm)	v_p (mm³/g)	s (mm³/g)	v_p+s (mm³/g)	v_p-s (mm³/g)
51	0.316	4651.091	0.836	0.905	1.741	-0.069
52	0.324	4545.219	0.851	0.925	1.777	-0.074
53	0.331	4441.763	0.866	0.942	1.808	-0.076
54	0.339	4340.636	0.880	0.961	1.841	-0.080
55	0.347	4241.847	0.895	0.985	1.880	-0.090
56	0.355	4145.297	0.908	1.004	1.912	-0.096
57	0.363	4050.935	0.919	1.019	1.938	-0.100
58	0.372	3958.376	0.927	1.020	1.947	-0.094
59	0.380	3868.616	0.934	1.023	1.957	-0.089
60	0.389	3780.553	0.940	1.026	1.965	-0.086
61	0.398	3694.439	0.944	1.029	1.972	-0.084
62	0.407	3610.491	0.951	1.029	1.980	-0.077
63	0.417	3529.219	0.959	1.029	1.987	-0.069
64	0.427	3447.900	0.966	1.029	1.994	-0.062
65	0.437	3369.419	0.974	1.029	2.002	-0.054
66	0.447	3292.770	0.983	1.030	2.012	-0.047
67	0.457	3217.773	0.991	1.032	2.023	-0.040
68	0.468	3144.577	0.998	1.032	2.030	-0.034
69	0.479	3072.948	1.008	1.034	2.042	-0.026
70	0.490	3002.998	1.014	1.035	2.049	-0.020
71	0.501	2934.644	1.022	1.036	2.057	-0.014
72	0.513	2867.944	1.029	1.037	2.066	-0.009
73	0.525	2802.564	1.036	1.039	2.075	-0.003
74	0.537	2739.767	1.044	1.041	2.085	0.003
75	0.550	2676.425	1.051	1.043	2.094	0.008
76	0.562	2615.504	1.059	1.045	2.103	0.014
77	0.575	2555.965	1.066	1.047	2.113	0.019
78	0.589	2497.764	1.073	1.050	2.123	0.023
79	0.603	2440.978	1.081	1.053	2.134	0.028
80	0.617	2385.367	1.088	1.055	2.142	0.033
81	0.631	2331.071	1.094	1.057	2.151	0.038
82	0.646	2278.009	1.100	1.059	2.159	0.042
83	0.661	2226.155	1.106	1.061	2.167	0.045
84	0.676	2175.480	1.112	1.063	2.175	0.049
85	0.692	2125.960	1.120	1.066	2.186	0.054
86	0.708	2077.567	1.126	1.068	2.194	0.059
87	0.724	2030.276	1.133	1.068	2.201	0.065
88	0.741	1984.062	1.139	1.071	2.209	0.067
89	0.759	1938.999	1.144	1.073	2.217	0.071
90	0.776	1894.765	1.151	1.074	2.225	0.078
91	0.794	1851.635	1.158	1.076	2.234	0.082
92	0.813	1809.485	1.165	1.078	2.243	0.087
93	0.832	1768.296	1.174	1.078	2.252	0.096
94	0.851	1728.046	1.184	1.078	2.262	0.107
95	0.871	1689.710	1.195	1.077	2.272	0.117
96	0.891	1650.271	1.205	1.077	2.282	0.128
97	0.912	1612.796	1.216	1.077	2.293	0.139
98	0.933	1575.997	1.228	1.077	2.305	0.151
99	0.955	1540.122	1.240	1.077	2.317	0.163
100	0.977	1505.065	1.252	1.078	2.330	0.174

p_{Hg} - mercury intrusion pressure
d_p - pore diameter
v_p - specific pore volume
s - uncertainty (see page 1)
v_p+s - upper limit of the uncertainty interval
v_p- s - lower limit of the uncertainty interval

CRM BAM-PM-120

Certified values of the pressure-volume and the diameter-volume curves

Data point No.	p_{Hg} (MPa)	d_p (nm)	v_p (mm³/g)	s (mm³/g)	v_p+s (mm³/g)	v_p-s (mm³/g)
101	1.000	1470.905	1.260	1.080	2.340	0.181
102	1.023	1437.820	1.267	1.082	2.349	0.185
103	1.047	1404.806	1.273	1.085	2.358	0.188
104	1.072	1372.625	1.279	1.087	2.366	0.192
105	1.096	1342.388	1.285	1.090	2.375	0.195
106	1.122	1310.855	1.291	1.093	2.384	0.198
107	1.148	1281.072	1.298	1.096	2.394	0.202
108	1.175	1251.856	1.304	1.100	2.403	0.204
109	1.202	1223.367	1.312	1.102	2.414	0.210
110	1.230	1195.514	1.319	1.106	2.425	0.213
111	1.259	1168.239	1.327	1.111	2.438	0.216
112	1.288	1141.709	1.335	1.116	2.451	0.219
113	1.318	1115.717	1.343	1.121	2.464	0.222
114	1.349	1090.325	1.352	1.127	2.479	0.225
115	1.380	1065.869	1.361	1.132	2.493	0.229
116	1.413	1041.249	1.372	1.138	2.510	0.234
117	1.445	1017.549	1.383	1.144	2.527	0.239
118	1.479	994.385	1.396	1.150	2.546	0.246
119	1.514	971.752	1.408	1.157	2.565	0.251
120	1.549	949.630	1.418	1.162	2.580	0.256
121	1.585	928.077	1.429	1.167	2.596	0.262
122	1.622	906.891	1.441	1.172	2.613	0.269
123	1.660	886.246	1.454	1.177	2.631	0.277
124	1.698	866.076	1.466	1.182	2.647	0.284
125	1.738	846.361	1.479	1.186	2.664	0.293
126	1.776	827.994	1.490	1.191	2.681	0.299
127	1.820	808.266	1.503	1.197	2.700	0.306
128	1.862	789.966	1.515	1.202	2.717	0.313
129	1.906	771.890	1.527	1.207	2.734	0.319
130	1.950	754.321	1.540	1.212	2.752	0.328
131	1.995	737.150	1.553	1.217	2.770	0.336
132	2.042	720.369	1.566	1.223	2.789	0.343
133	2.089	703.970	1.579	1.229	2.808	0.350
134	2.138	687.948	1.592	1.237	2.829	0.355
135	2.188	672.296	1.604	1.245	2.849	0.359
136	2.239	656.985	1.616	1.252	2.869	0.364
137	2.291	642.029	1.630	1.260	2.890	0.370
138	2.344	627.515	1.644	1.268	2.912	0.376
139	2.399	613.134	1.659	1.276	2.934	0.383
140	2.455	599.147	1.674	1.283	2.957	0.391
141	2.512	585.537	1.689	1.290	2.980	0.399
142	2.570	572.339	1.705	1.297	3.003	0.408
143	2.630	559.184	1.724	1.304	3.028	0.420
144	2.692	546.457	1.744	1.311	3.055	0.433
145	2.754	534.027	1.765	1.319	3.084	0.446
146	2.818	521.882	1.785	1.328	3.113	0.456
147	2.884	509.992	1.806	1.338	3.144	0.467
148	2.951	498.474	1.827	1.349	3.176	0.479
149	3.020	487.053	1.849	1.360	3.209	0.489
150	3.090	475.942	1.870	1.371	3.241	0.499

p_{Hg} - mercury intrusion pressure
d_p - pore diameter
v_p - specific pore volume

s - uncertainty (see page 1)
v_p+s - upper limit of the uncertainty interval
v_p- s - lower limit of the uncertainty interval

CRM BAM-PM-120

Certified values of the pressure-volume and the diameter-volume curves

Data point No.	p_{Hg} (MPa)	d_p (nm)	v_p (mm^3/g)	s (mm^3/g)	v_p+s (mm^3/g)	v_p-s (mm^3/g)
151	3.162	465.109	1.934	1.342	3.276	0.592
152	3.236	454.522	1.916	1.391	3.307	0.526
153	3.311	444.176	1.939	1.401	3.340	0.537
154	3.388	434.066	1.961	1.412	3.374	0.549
155	3.467	424.185	1.985	1.425	3.410	0.560
156	3.548	414.530	2.008	1.438	3.446	0.570
157	3.631	405.092	2.030	1.451	3.481	0.579
158	3.715	395.873	2.055	1.467	3.523	0.588
159	3.802	386.860	2.082	1.482	3.564	0.599
160	3.890	378.053	2.109	1.499	3.609	0.611
161	3.981	369.450	2.140	1.515	3.655	0.624
162	4.074	361.040	2.173	1.534	3.707	0.639
163	4.169	352.822	2.215	1.550	3.765	0.664
164	4.266	344.790	2.259	1.569	3.828	0.691
165	4.365	336.942	2.304	1.587	3.891	0.717
166	4.467	329.271	2.361	1.602	3.963	0.759
167	4.571	321.777	2.420	1.619	4.039	0.801
168	4.677	314.452	2.479	1.638	4.117	0.841
169	4.786	307.295	2.540	1.658	4.198	0.883
170	4.898	300.300	2.606	1.697	4.303	0.909
171	5.012	293.464	2.826	1.847	4.673	0.979
172	5.129	286.784	3.140	2.277	5.417	0.862
173	5.248	280.256	3.739	3.210	6.949	0.529
174	5.370	273.877	4.795	4.434	9.229	0.361
175	5.495	267.642	7.614	7.102	14.716	0.512
176	5.623	261.550	16.662	12.901	29.563	3.761
177	5.754	255.597	31.477	22.183	53.660	9.295
178	5.888	249.776	57.722	38.151	95.873	19.571
179	6.026	244.090	98.332	55.179	153.511	43.153
180	6.166	238.537	151.561	67.289	218.850	84.272
181	6.310	233.107	210.735	70.461	281.196	140.274
182	6.457	227.801	271.768	62.623	334.391	209.145
183	6.607	222.616	324.151	52.140	376.291	272.011
184	6.761	217.548	367.548	41.453	409.001	326.095
185	6.918	212.596	400.976	32.760	433.736	368.216
186	7.079	207.757	427.293	25.619	452.912	401.674
187	7.244	203.026	446.606	20.328	466.934	426.278
188	7.413	198.406	465.671	17.497	483.168	448.174
189	7.586	193.890	478.269	15.853	494.122	462.416
190	7.762	189.476	488.551	14.630	503.181	473.921
191	7.943	185.163	496.967	13.899	510.866	483.068
192	8.128	180.948	503.873	13.272	517.145	490.601
193	8.318	176.830	509.601	12.861	522.462	496.740
194	8.511	172.805	514.174	12.595	526.769	501.578
195	8.710	168.871	518.048	12.377	530.424	505.671
196	8.913	165.027	521.217	12.120	533.336	509.096
197	9.120	161.271	524.063	12.117	536.180	511.946
198	9.333	157.600	526.432	11.959	538.391	514.472
199	9.550	154.012	528.443	11.870	540.314	516.573
200	9.772	150.507	530.194	11.857	542.051	518.337

p_{Hg} - mercury intrusion pressure
d_p - pore diameter
v_p - specific pore volume

s - uncertainty (see page 1)
v_p+s - upper limit of the uncertainty interval
v_p- s - lower limit of the uncertainty interval

Certified values of the pressure-volume and the diameter-volume curves

Data point No.	p_{Hg} (MPa)	d_p (nm)	v_p (mm³/g)	s (mm³/g)	v_p+s (mm³/g)	v_p-s (mm³/g)
201	10.000	147.091	531.636	11.856	543.492	519.780
202	10.232	143.752	532.896	11.709	544.605	521.187
203	10.471	140.481	533.874	11.773	545.647	522.101
204	10.715	137.282	534.626	11.954	546.580	522.672
205	10.966	134.139	535.567	11.983	547.550	523.584
206	11.220	131.085	536.200	12.043	548.243	524.157
207	11.482	128.107	536.761	12.063	548.825	524.698
208	11.749	125.196	537.304	12.054	549.357	525.250
209	12.020	122.372	537.759	12.071	549.830	525.688
210	12.303	119.551	538.152	12.094	550.246	526.058
211	12.599	116.750	538.522	12.100	550.622	526.422
212	12.883	114.171	538.847	12.104	550.951	526.743
213	13.183	111.572	539.120	12.125	551.245	526.995
214	13.490	109.032	539.387	12.161	551.547	527.226
215	13.804	106.551	539.613	12.171	551.783	527.442
216	14.125	104.135	539.817	12.192	552.009	527.625
217	14.454	101.765	540.024	12.202	552.226	527.822
218	14.791	99.449	540.228	12.201	552.429	528.027
219	15.136	97.178	540.400	12.272	552.672	528.128
220	15.488	94.971	540.558	12.224	552.782	528.334
221	15.849	92.807	540.706	12.226	552.932	528.480
222	16.218	90.699	540.842	12.226	553.068	528.616
223	16.596	88.633	540.985	12.233	553.218	528.752
224	16.982	86.616	541.094	12.245	553.339	528.849
225	17.376	84.652	541.192	12.247	553.439	528.945
226	17.783	82.714	541.294	12.262	553.556	529.032
227	18.197	80.833	541.384	12.277	553.661	529.107
228	18.621	78.993	541.466	12.290	553.756	529.176
229	19.055	77.193	541.560	12.300	553.860	529.260
230	19.498	75.439	541.655	12.310	553.965	529.345
231	19.953	73.719	541.745	12.318	554.063	529.427
232	20.417	72.043	541.819	12.324	554.143	529.495
233	20.893	70.402	541.886	12.331	554.217	529.555
234	21.380	68.798	541.946	12.334	554.280	529.612
235	21.878	67.233	542.009	12.338	554.347	529.671
236	22.387	65.704	542.061	12.345	554.406	529.716
237	22.909	64.207	542.117	12.355	554.472	529.762
238	23.442	62.745	542.197	12.363	554.560	529.834
239	23.988	61.319	542.246	12.369	554.615	529.877
240	24.547	59.922	542.301	12.378	554.679	529.923
241	25.119	58.557	542.367	12.387	554.754	529.980
242	25.704	57.225	542.412	12.394	554.806	530.017
243	26.303	55.922	542.462	12.398	554.860	530.064
244	26.915	54.650	542.516	12.405	554.921	530.111
245	27.542	53.406	542.571	12.406	554.977	530.164
246	28.184	52.190	542.619	12.414	555.033	530.204
247	28.840	51.002	542.666	12.419	555.085	530.247
248	29.512	49.841	542.718	12.421	555.139	530.297
249	30.200	48.706	542.766	12.426	555.192	530.340
250	30.903	47.598	542.809	12.426	555.235	530.383

p_{Hg} - mercury intrusion pressure
d_p - pore diameter
v_p - specific pore volume
s - uncertainty (see page 1)
v_p+s - upper limit of the uncertainty interval
v_p- s - lower limit of the uncertainty interval

Certified values of the pressure-volume and the diameter-volume curves

Data point No.	p_{Hg} (MPa)	d_p (nm)	v_p (mm³/g)	s (mm³/g)	v_p+s (mm³/g)	v_p-s (mm³/g)
251	31.632	46.511	542.858	12.415	555.273	530.443
252	32.359	45.452	542.917	12.419	555.336	530.498
253	33.113	44.426	542.954	12.422	555.376	530.532
254	33.894	43.407	542.999	12.419	555.418	530.580
255	34.677	42.428	543.034	12.424	555.457	530.610
256	35.481	41.453	543.070	12.428	555.498	530.641
257	36.308	40.509	543.111	12.428	555.539	530.683
258	37.154	39.597	543.150	12.428	555.578	530.722
259	38.079	38.636	543.191	12.432	555.623	530.759
260	38.904	37.808	543.231	12.437	555.668	530.794
261	39.811	36.945	543.272	12.433	555.706	530.840
262	40.736	36.104	543.312	12.434	555.746	530.877
263	41.697	35.282	543.351	12.435	555.786	530.916
264	42.656	34.479	543.391	12.435	555.826	530.956
265	43.652	33.694	543.434	12.444	555.877	530.990
266	44.668	32.937	543.481	12.446	555.927	531.034
267	45.709	32.178	543.515	12.459	555.974	531.056
268	46.777	31.445	543.554	12.459	556.013	531.094
269	47.860	30.729	543.587	12.459	556.046	531.128
270	48.978	30.039	543.619	12.457	556.075	531.162
271	50.119	29.346	543.652	12.455	556.107	531.197
272	51.296	28.676	543.685	12.451	556.136	531.234
273	52.491	28.028	543.717	12.450	556.167	531.266
274	53.702	27.396	543.746	12.449	556.195	531.297
275	54.956	26.764	543.783	12.450	556.233	531.334
276	56.234	26.155	543.829	12.445	556.274	531.384
277	57.544	25.563	543.881	12.435	556.316	531.445
278	58.894	24.978	543.941	12.424	556.365	531.517
279	60.250	24.419	543.991	12.423	556.414	531.567
280	61.660	23.857	544.045	12.419	556.464	531.626
281	63.096	23.311	544.076	12.420	556.496	531.655
282	64.565	22.788	544.095	12.424	556.519	531.671
283	66.069	22.267	544.113	12.422	556.535	531.691
284	67.608	21.755	544.160	12.406	556.566	531.754
285	69.193	21.260	544.187	12.408	556.594	531.779
286	70.795	20.776	544.256	12.401	556.657	531.854
287	72.444	20.302	544.272	12.391	556.663	531.881
288	74.131	19.841	544.341	12.369	556.710	531.972
289	75.858	19.393	544.368	12.364	556.731	532.004
290	77.625	18.948	544.403	12.356	556.759	532.047
291	79.433	18.516	544.461	12.345	556.806	532.115
292	81.283	18.099	544.560	12.284	556.843	532.276
293	83.176	17.688	544.621	12.266	556.887	532.355
294	85.114	17.285	544.678	12.245	556.923	532.433
295	87.096	16.891	544.725	12.235	556.959	532.490
296	89.125	16.502	544.776	12.226	557.004	532.551
297	91.201	16.127	544.833	12.210	557.043	532.623
298	93.325	15.760	544.878	12.207	557.085	532.671
299	95.499	15.401	544.932	12.209	557.141	532.723
300	97.724	15.051	544.971	12.205	557.176	532.765

p_{Hg} - mercury intrusion pressure
d_p - pore diameter
v_p - specific pore volume

s - uncertainty (see page 1)
v_p+s - upper limit of the uncertainty interval
v_p- s - lower limit of the uncertainty interval

CRM BAM-PM-120

Certified values of the pressure-volume and the diameter-volume curves

Data point No.	p_{Hg} (MPa)	d_p (nm)	v_p (mm³/g)	s (mm³/g)	v_p+s (mm³/g)	v_p-s (mm³/g)
301	100.000	14.706	545.021	12.200	557.221	532.821
302	102.329	14.372	545.067	12.190	557.256	532.875
303	104.713	14.046	545.104	12.187	557.291	532.917
304	107.152	13.726	545.142	12.185	557.327	532.956
305	109.648	13.414	545.176	12.192	557.368	532.984
306	112.202	13.109	545.231	12.204	557.434	533.027
307	114.815	12.810	545.278	12.209	557.487	533.068
308	117.490	12.519	545.324	12.217	557.541	533.107
309	120.226	12.234	545.360	12.226	557.586	533.134
310	123.027	11.955	545.407	12.237	557.644	533.169
311	125.893	11.682	545.478	12.262	557.740	533.216
312	128.825	11.417	545.522	12.284	557.806	533.238
313	131.826	11.157	545.593	12.300	557.893	533.293
314	134.896	10.902	545.654	12.320	557.974	533.334
315	138.038	10.655	545.708	12.341	558.049	533.366
316	141.254	10.412	545.762	12.359	558.121	533.403
317	144.544	10.175	545.799	12.377	558.176	533.422
318	147.911	9.944	545.847	12.398	558.245	533.449
319	151.356	9.718	545.910	12.417	558.327	533.493
320	154.882	9.496	545.972	12.438	558.410	533.534
321	158.489	9.280	546.037	12.460	558.497	533.577
322	162.181	9.069	546.112	12.485	558.597	533.627
323	165.959	8.862	546.196	12.504	558.700	533.692
324	169.824	8.661	546.261	12.526	558.786	533.735
325	173.780	8.464	546.326	12.550	558.877	533.776
326	177.828	8.271	546.390	12.579	558.969	533.811
327	181.970	8.083	546.465	12.612	559.077	533.853
328	186.209	7.899	546.542	12.651	559.193	533.891
329	190.546	7.719	546.613	12.685	559.298	533.928
330	194.984	7.543	546.715	12.712	559.427	534.003
331	199.526	7.372	546.783	12.737	559.520	534.046
332	204.174	7.204	546.829	12.726	559.555	534.103
333	208.930	7.040	546.864	12.723	559.587	534.141
334	213.796	6.879	546.889	12.718	559.607	534.171
335	218.776	6.723	546.922	12.716	559.638	534.206
336	223.872	6.570	546.944	12.711	559.655	534.233
337	229.087	6.420	546.967	12.708	559.675	534.259
338	234.423	6.274	547.005	12.712	559.717	534.293
339	239.883	6.131	547.026	12.711	559.737	534.315
340	245.471	5.992	547.052	12.707	559.759	534.345
341	251.189	5.855	547.080	12.707	559.787	534.373
342	257.040	5.722	547.103	12.702	559.805	534.401
343	263.027	5.592	547.125	12.700	559.825	534.425
344	269.153	5.465	547.158	12.704	559.861	534.454
345	275.423	5.340	547.266	12.750	560.017	534.516
346	281.838	5.219	547.387	12.802	560.189	534.585
347	288.403	5.100	547.494	12.837	560.330	534.657
348	295.121	4.984	547.546	12.927	560.473	534.619
349	301.995	4.870	547.609	12.971	560.580	534.638
350	309.030	4.759	547.655	12.994	560.649	534.661

p_{Hg} - mercury intrusion pressure
d_p - pore diameter
v_p - specific pore volume
s - uncertainty (see page 1)
v_p+s - upper limit of the uncertainty interval
v_p- s - lower limit of the uncertainty interval

CRM BAM-PM-120

Certified values of the pressure-volume and the diameter-volume curves

Data point No.	p_{Hg} (MPa)	d_p (nm)	v_p (mm³/g)	s (mm³/g)	v_p+s (mm³/g)	v_p-s (mm³/g)
351	316.228	4.651	547.715	13.029	560.744	534.685
352	323.594	4.545	547.755	13.050	560.805	534.705
353	331.131	4.442	547.791	13.063	560.854	534.728
354	338.844	4.341	547.845	13.087	560.932	534.758
355	346.737	4.242	547.914	13.096	561.010	534.818
356	354.813	4.145	547.946	13.099	561.046	534.849
357	363.078	4.051	547.992	13.099	561.091	534.892
358	371.535	3.959	548.032	13.081	561.113	534.951
359	380.189	3.869	548.073	13.090	561.163	534.983
360	389.045	3.781	548.100	13.092	561.192	535.007
361	398.107	3.694	548.135	13.096	561.231	535.039

p_{Hg} - mercury intrusion pressure
d_p - pore diameter
v_p - specific pore volume
s - uncertainty (see page 1)
v_p+s - upper limit of the uncertainty interval
v_p- s - lower limit of the uncertainty interval

in addition data on disk

List of the symbols and abbreviations

Symbols:

a	constant
$\bar{a}$	floor space of one molecule of gas (e.g. nitrogen or krypton)
A	coefficient of the weight increase with time from capillary water imbibition kinetics
B	coefficient of the water migration with time from capillary water imbibition kinetics
C	pore circumference
c_0	apparatus constant
$C_{X\text{-}AR}$	X-ray refraction coefficient
χ	sample thickness
$d_{B,i}$	bulk density determined using the method i (i= W or Hg)
$d_{M,i}$	mineral or skeletal density determined using the method i (i= W; Hg or He)
D	mean pore diameter
D_F	mean Feret diameter
D_{APD}	average pore access diameter
D_{50}	median pore access diameter
D_H	hydraulic diameter
D_s	mean grain diameter
E	energy
f	pore shape factor
F	force
γ	fluid surface tension
Γ	porous network connectivity
h	height
η	fluid viscosity
I	intensity
I_A	transmitted X-ray intensity after absorption
I_R	transmitted X-ray intensity after refraction
K	permeability
K_A	mean permeability measured using nitrogen
$K_A{}^*$	sample permeability measured using nitrogen
K_i	permeability calculated using the pore model i (i=DP; KC; M or PC)
K_{PI}	permeability calculated using Pittman's empirical equation
L	length, height of water (or of the wet fringe) in the sample analyzed by capillary water imbibition kinetics
λ	correlation factor between the pore-to-throat-size ratio R_P/T and the ratio $N_{TR,W}/N_{TR,Hg}$
Max[X]	measured maximum value of the parameter X
Min[X]	measured minimum value of the parameter X

MIL	mean internal line (parameter determined by image analysis)
μ	linear attenuation coefficient
$\mathcal{N}$	Avogrado's constant
N	total porosity
N_{Hg}	total porosity measured by mercury porosimetry
$N_{X\text{-}AR}$	total porosity measured by X-ray refraction
N_W	total porosity measured by water porosimetry
N_{48}	48 hours porosity measured by water porosimetry
N_C	closed porosity
N_F	free porosity
N_O	open porosity
N_{TR}	trapped porosity
$N_{TR,i}$	trapped porosity measured using the method i (i=W or Hg)
$N^*_{TR,i}$	percentage of trapped porosity measured using the method i (i=W or Hg)
$N_{Macro,Hg}$	macroporosity measured by mercury porosimetry
$N_{Micro,Hg}$	microporosity measured by mercury porosimetry
P	pressure
Q	fluid flow
θ	fluid/material contact angle
R or r	fixed or variable pore radius
$R_{P/T}$	pore-to-throat-size ratio
Re	Reynold's number
ρ	fluid density (g cm^{-3})
s	surface area
S	pore surface area
S_i	specific surface area measured using the method i (i=W; Hg; IA or X-AR)
S_0	specific surface area divided by the specific volume of the solid phase
Σ	inner surface density (pore surface area per volume unit)
S_{48}	Hirschwald's or water saturation coefficient
σ_X	standard deviation of the measured parameter X; for n measured values X_i (i=1,…,n) $\sigma_X = \sqrt{\frac{1}{n-1}\sum_{i=1}^{n}\left(X_i - \overline{X}\right)^2}$ with $\overline{X} = \frac{1}{n}\sum_{i=1}^{n}\left(X_i\right)$ the mean value of X
$\sigma_{R,X}$	relative standard deviation of the measured parameter X; $\sigma_{R,X} = \frac{\sigma_X}{\overline{X}}$
t	time
T	porous network tortuosity
U	fluid velocity
V	volume
V_B	sample bulk volume
V_p	porous volume
V_p^{tot}	total porous volume
$V^*_{p,i}$	total specific pore volume measured using the method i (i=W or Hg)

V_R	residual volume of mercury measured at the pressure 0.1 MPa
V_a	volume of gas adsorbed at pressure P
V_m	volume of a mono-layer of gas molecules adsorbed
V_M	molecular gas volume at standard pressure and temperature
w_s	dry sample weight
w_1	weight of the immersed water-saturated sample
w_2	water-saturated sample weight
w_{48}	weight of the imbibed sample after 48 hours
Z	atomic number

Abbreviations:

BET	Brunauer-Emmett-Teller theory
BSE	back-scattered electron
Clst	cluster
CRM(s)	certified reference material(s)
CT	X-ray computed tomography
DP	Debye-Poiseuille's pore model
Geo-RM(s)	reference geomaterial(s)
He	helium pycnometry
Hg	mercury porosimetry
IA	image analysis
KC	Kozeny-Carman's pore model
M	Marshall's pore model
MP	macropore
µP	micropore
Opal-CT	opal-cristobalite-tridymite
PC	PORE-COR model
RM(s)	reference material(s)
SAXS	small angle X-ray scaterring
SEM	scanning electron microscopy
W	water porosimetry
XRD	X-ray diffraction
X-AR	X-ray adsorption/refraction

List of the tables and figures

Glossary of geology

Allochem

Allochemichal components or allochems are carbonate sediments, which have formed within the basin of deposition. They include **ooliths**, **bioclasts**, **intraclasts** and **pelloids**. Allochems, micrite and sparite are the three most important components of carbonate rocks.

Bioclast

Bioclasts, or skeletal particles, are the remains, complete or fragmented of carbonate-secreting organisms. There are many varieties in the mineralogy (**molluscs**, **bryozoans**, **echinoderms**, **foraminifera**…).

Biotite See **mica**.

Bryozoan

Widespread in marine limestones, bryozoans had calcite hard parts and a laminar wall structure is preserved.

Calcareous

A descriptive term used for rocks and other earth materials that have an abundance of calcium carbonate ($CaCO_3$). For example, a calcareous sandstone has up to 50% calcium carbonate.

Calcite

Mineral made of calcium carbonate ($CaCO_3$), generally white and easily scratched with knife. Most seashells are made of calcite or related minerals. This is the *lime* of limestone. Calcite elements can have different sizes. These elements are classified in two groups according to their grain size:

- sparitic calcite (or **sparite**): elements of grain sizes over 2 µm;
- micritic calcite (or **micrite**): elements of grain sizes under 2 µm.

Cementation

One of the processes that works together to turn sediment into **sedimentary rock**. Mineral-laden water percolates through sediment with open pore spaces. The spaces are gradually filled by minerals precipitating from the water, binding the grains together.

Chalcedony

This is a very general name for all fine grained **quartz**.

Chlorite

Family of platy silicate minerals that contain various amounts of magnesium, iron, aluminium, water, and small amounts of other elements. Some mineralogists include chlorites in the **mica** family because the crystals form small flakes.

Clast

A fragment of a pre-existing rock (extraclast) or **fossil** (**bioclast**) embedded within another rock. Some are often reworked later to form new sediment grains (**intraclasts**).

Clay

A family of platy silicate minerals that commonly form as a product of rock weathering. Also, any particle smaller than 1/256 of a millimeter in diameter.

Clinoptilolite

Hydrated sodium potassium calcium aluminium tecto-silicate. Clinoptilolite forms as a devitrification product (the conversion of glass to crystalline material) of volcanic glass in tuffs. Tuffs are consolidated pyroclastic rocks.

Coccolith

A coccolith is a single disc-like plate which is secreted by the algal organism and held in combination with several other, sometimes varying shaped plates by an organic coating to form the coccosphere (calcareous **fossil**). The organism, which creates the coccosphere, is called a coccolithophore; it is phytoplankton. The calcareous skeletons of coccolithophores are found in marine deposits often in vast numbers, sometimes making up the major component of a rock, such as the chalk of England.

Cristobalite

Cristobalite is a polymorph of **quartz** (crystal system: tetragonal). It is believed to form under high temperature in volcanic rocks. There is a high temperature phase called beta-cristobalite that crystallises in the isometric crystal system, creating octahedral crystals. When the temperature goes down, the internal structure transforms into cristobalite but the crystal form is not changed; therefore the most cristobalite crystals are pseudomorphs of beta-cristobalite. Cristobalite is crystallized from molten rock at temperatures above 1470 degrees Celsius. If the temperature is lower, silica crystallizes as **tridymite** (870-1470 degrees Celsius) or beta-quartz (below 870 degrees Celsius).

Crystallization

Growth of minerals (crystalline solids) from a liquid or gas.

Diagenesis

A group of processes that cause physical and chemical changes in sediment after it has been deposited and buried under another layer of sediment.

Echinoderm

Kind of **bioclast** easy to identify because it break down into plates which, although they may exhibit a wide variety of shapes, are single calcite crystal with uniform extinction.

Feldspar

Family of silicate minerals containing varying amounts of potassium, sodium and calcium along with aluminium, silicon and oxygen. Potassium-feldspars (K-feldspars) contain considerable potassium. Plagioclase feldspars contain considerable sodium and calcium. Feldspar crystals are stubby prisms, generally white, grey, or pink.

Foliation

Aligned layers of minerals. Foliation forms when pressure squeezes flat or elongates minerals so that they become aligned. These rocks develop a platy or sheet-like structure that reflects the direction that pressure was applied.

Foraminifera

Calcite **bioclasts**, which show a variety of shapes and wall structures.

Fossil

Mineralized remains or traces of organisms.

Geothermal energy
Power generation using natural steam derived from the Earth's internal heat.

Glauconite
Hydrous potassium aluminum iron magnesium silicate, which forms exclusively in marine environments. It commonly occurs as rounded pellets which are aggregates of many very small crystals.

Goethite
Hydrogen iron oxide mineral (orthorhombic crystal system).

Illite
A potassium-rich **clay** mineral, formed during the alteration of silicate minerals such as **mica** and **feldspar** and commonly found in marine shales.

Intraclast see **clast**

Kaolinite
A mineral derived from aluminium silicates in the soil that has altered from feldspar in granite and pegmatite. Clay beds.

Limestone
A sedimentary rock made mostly of the mineral **calcite** (calcium carbonate). Limestone is usually formed from shells of once-living organisms or other organic processes, but may also form by inorganic precipitation.

Matrix
Fine-grained material surrounding larger grains in a **sedimentary rock**.

Mica
Group of silicate minerals composed of varying amounts of aluminium, potassium, magnesium, iron and water. All micas form flat, plate-like crystals. Crystals cleave into smooth flakes. **Biotite** is dark, black or brown mica; **Muscovite** is light-coloured or clear mica.

Micrite
Carbonate sediments in the form of grains less than 2 μm in diameter. Much of it forms in the basin of deposition, either as a precipitate from seawater or from the disintegration of the hard part of organisms.

Mollusc
Common components of **limestones**. Most bivalves and gastropods were made of aragonite, so although there are a diversity of structures. Most originally aragonitic molluscs are preserved as **clasts** – that is the aragonite dissolved out during the diagenesis leaving a mould, which later became filled with a **sparite** cement.

Muscovite see **mica**

Oncholith
Carbonate grain, which is larger than 2 mm in diameter and have an outer layer with concentric laminae.

Oolith

Spherical or ellipsoidal carbonate grain, less than 2 mm in diameter, having regular concentric laminae developed around a nucleus.

Opal

Hydrated amorphous **quartz** created by silica-rich solutions at low temperatures.

Packstone

Carbonate grain supported rock; the grains have shapes that allow for small amounts of mud to occur in the interstices (Dunham's classification).

Phyllite

A very fine-grain, foliated metamorphic mineral. Phyllites are usually black or dark grey; the **foliation** is commonly crinkled or wavy. Phyllite differs from less re-crystallized slate by its sheen, which is produced by barely visible flakes of muscovite.

Quartz

One of the most common minerals in the Earth's crust (and in some new-age boutiques), made up of silicon dioxide (SiO_2), also called silica, and commonly in white masses. Crystals are clear, glassy 6-sided prisms.

Quartzarenite

Sandstone with 95% of greater Quartz (Q-pole material).

Sandstone

Sedimentary rock mainly made of sand-sized grains.

Sedimentary rock

Sedimentary rocks are formed from pre-existing rocks or pieces of once-living organisms. They form from deposits that accumulate on the Earth's surface. Sedimentary rocks often have distinctive layering or bedding.

Smectite

A group of fine-grained **clays** which can incorporate water. They swell significantly upon water absorption and can absorb large cations.

Sparite

Carbonate sediments in the form of grains more than 2 μm in diameter. It is usually pore-filling cement and thus may form in a rock a long time after deposition of the original **allochems** and **micrite**.

Sublitharenite

Sandstone with recycled orogen provenances spread along the Quartz-Feldspar sideline (Folk's classification – Quartz content over 75% and ratio of feldspar to rock fragments less than 1).

Tridymite

Member of the Quartz Group, which also includes **cristobalite**, tridymite is a polymorph of **quartz** (crystal system: monoclinic). It forms from a melt at low pressures and at temperatures of approximately 870 degrees to 1470 degrees Celsius; above 1470 degrees Celsius, **cristobalite** is stable.

Acknowledgements

First of all, I would like to express my gratitude to Prof. A. Zschunke and Prof. C. Dubois for supervising this PhD thesis.

The realization of this study came within the framework of a practice work at the BAM (Federal Institute for Materials Research and Testing, Germany). Special thanks to Prof. K. Meyer, and also to Dr P. Klobes, for managing this study and for their support inside the Federal Institute.

The LMN (Laboratory of Nuclear Microanalysis) and the Geosciences Department of the University of Besançon (France) assisted in the realization of this study through an opportune collaboration with the BAM. I would like to give special thanks again to Prof. C. Dubois who has warmly received me and supported me during my stays in Besançon; also many thanks to Dr J-P. Sizun (from the Geosciences Department), who brought much scientific support to this study, sharing with me what I personally consider as to be his great knowledge of the substance "rock".

Furthermore, I want to thank some people who contributed in one way or another to this study. I think in particular about Dr J. Goebbels who made the X-ray computed tomography measurements. I also think about Dr U. Mücke who was responsible for the capture of the backscattered electron images and who had a share in the analysis of the images. In this context, I would also like to thank Dr T. Moelders for the preparation of the samples and his suggestions during the analysis. I would like to extend my thanks to Dr K.-W. Harbich for the X-ray absorption and refraction measurements and for his critical looks about the interpretation of the results. I also thank Mrs. A. Zimathies, for her large and precious contribution in the measurements using gas adsorption and mercury porosimetry.

Last but not least, I am also grateful to the personnel of the Laboratory I.13, for receiving and supporting me during my practice work at the BAM and for participating at far or close range in the discussion of the results, and to members of the LMN and the Geosciences Department for their support during my stays in Besançon.

Lebenslauf

von Rodolphe Robert
geboren am : 06.01.1974 in Dôle (Frankreich)
Nationalität : französisch
Adresse : Tietzenweg 14, D-12203 Berlin
Telefon : 030 83226779
E-Mail : rodolphe.robert@freenet.de

Ausbildung

09.1991 - 06.1992	Abitur; Gymnasium Charles Nodier, Dôle, Frankreich
09.1992 - 06.1995	Diplom „DEUG“, Fachgebiet Mathematik-Physik-Chemie; Universität Besançon, Frankreich
09.1995 - 06.1997	Licence, Physik-Chemie; Universität Besançon
09.1997 - 06.1998	Magister, Physik-Chemie; Universität Besançon
09.1998 - 06.1999	Diplomarbeit, Physik-Chemie der Grenzfläche; Universität Besançon
09.1999 - 09.2004	Promotion zum Grad Dr. rer. nat. im Fach Chemie; Humboldt-Universität Berlin, Deutschland

Berufserfahrung

07.93, 07.94, 08.97	Solvay S.A. Chemie Industrie (Tavaux, Frankreich); Angestellter, Fachtätigkeit
01.09.99 -31.08.02	Bundesanstalt für Materialforschung und –prüfung; Laboratorium „Elementarspurenanalytik; Spektralanalyse“ (Berlin, Deutschland); wissenschaftlicher Angestellter, Fachtätigkeit

Praktika / Seminare

01.03 - 31.05.1998	Praktikum im Laboratorium für Materialmikroanalyse EA 473 LCR-CEA M07 (Besançon, Frankreich) Aufgabe: *Mitentwicklung einer Bildanalyse-Technik zur Untersuchung der Porenstruktur von Kreide*
01.01 - 30.06.1999	Praktikum im Laboratorium für Materialmikroanalyse EA 473 LCR-CEA M07 Aufgabe: *Strukturcharakterisierung des Granits der Vogesen - Relation Porosität/Mineralogie*
01.04 - 30.04.1999	Praktikum im Laboratorium HYDR´ASA, UMR 6532 CNRS (Poitiers, Frankreich) Aufgabe: *Chemische Farbverarbeitung der Mineralphase des Granits der Vogesen*
29 - 30.10.2001	Seminar DAP (Deutsches Akkreditierungssystem Prüfwesen GmbH) Tätigkeit: *Akkreditierungs- und Begutachtungstechnik für Prüflaboratorien*

19.01 - 13.02.2004 Trainingsmaßnahme vom ceuss.com Personaltraining GmbH
Tätigkeit: *EDV-Kenntnisse*

Veröffentlichung / Publikationen

21.19.2000 R. Robert, P. Sardini, S. Sammartino, C. Dubois, L. Guillot, M. Rossy, P. Gaviglio, and A. Meunier

Poster: "*Porosity changes in a granite over time: Identification from 14C-PMMA autoradiographs and mineral cartographs*"

The Second International TRI/Princeton Workshop "Characterization of Porous Materials: from Angstroms to Millimeters", Princeton, NJ (USA), June 19-21, 2000

19.04.2001 R. Robert

Vortrag: "*Porosity characterization of selected sedimentary rocks regarding their possible application as Geo-CRMs*"

Seminar der Bundesanstalt für Materialforschung und -prüfung

29.11.2002 R. Robert, P. Sardini, S. Sammartino, C. Dubois, L. Guillot, M. Rossy, P. Gaviglio, and M. Siitari-Kauppi

"*Porosity changes in a granite close to quarry faces: identification from 14C-PMMA autoradiographs and mineralogical cartographies*"

Eur. Phys. J. AP 21, 127-136 (2003)

Sonstige Kenntnisse

Sprachen
Französisch: Muttersprache
Deutsch: in Wort und Schrift („Zertifikat Deutsch“ des Goethe Institut)
Englisch: in Wort und Schrift (Universitätsausbildung)

EDV:
Betriebssystemen: WIN 98, 2000 und XP
Anwendung: Word, Excel, Access, PowerPoint
Bildanalyse: Image C, NIH Image
Programmierung: FORTRAN, BASIC (Grundkenntnisse)
Sonstige: Adobe Photoshop, COREL Draw

Führerschein: Klasse B

Hobbys

Sport: Jogging, Fußball, Tennis
Literatur: Originalromane und wissenschaftliche Lektüre in französisch, deutsch und englisch
Sonstige: Schachspiel, Zeichnen

Selbstständigkeitserklärung

Hiermit erkläre ich, dass die vorliegende Dissertation selbstständig und nur unter Verwendung der angegebenen Literatur und Hilfsmittel von mir, Rodolphe Robert, angefertigt wurde.

Berlin, den 3. März 2004

Rodolphe Robert